Combined scanning probe microscopy studies
on
self-assembled porphyrin monolayers

Michiel Coenen

ISBN/EAN 978-90-9027473-7

Printed by: Proefschriftmaken.nl || Uitgeverij BOXPress

Combined Scanning Probe Microscopy Studies on Self-Assembled Porphyrin Monolayers

Proefschrift

ter verkrijging van de graad van doctor
aan de Radboud Universiteit Nijmegen
op gezag van de rector magnificus prof. mr. S.C.J.J. Kortmann,
volgens besluit van het college van decanen
in het openbaar te verdedigen op vrijdag 13 september 2013
om 10:30 uur precies

door

Martinus Jacobus Johannes Coenen

geboren op 18 december 1981
te Venray

Promotor	: Prof. dr. S.E. Speller (University of Rostock)
Copromotoren	: Dr. J.A.A.W. Elemans
	: Dr. B.L.M. Hendriksen

Manuscriptcommissie:

Prof. dr. A.E. Rowan
Prof. dr. E. Vlieg
Dr. M.A. Stöhr (Rijksuniversiteit Groningen)

The work described in this thesis was financially supported by NanoNed, the Dutch nanotechnology programme of the Ministry of Economic Affairs.

ISBN: 978-90-9027473-7

Contents

CHAPTER 1

Introduction

This thesis describes the structure of self-assembled porphyrin monolayers and the influence that structure has on the physicochemical properties of those monolayers and the molecules that constitute them. This chapter aims to provide a scientific justification for performing this research.

1.1 Structure versus Function

There is a strong relation between the structure of an object and its function. At the macroscopic scale this statement is trivial, as it is obvious that the same pile of bricks can function as a road when assembled in a horizontal manner, and as a wall when stacked vertically, and that the same piece of steel can be turned into a fork, a spoon or a knife. The concept of isomerism, the fact that molecules consisting of the same collection of atoms but in different structural arrangements, have different properties, is already known since the work of Friedrich Wöhler and Justus von Liebig in the 1820s. They found that isocyanic acid and fulminic acid, two compounds with an atomic composition of HNCO but with different structural arrangements of these atoms, as shown in Figure 1.1, have very different properties: the former is a stable substance while the other is highly explosive[1]. Molecules with the same collection of atoms can differ in the locations of their functional groups, be mirror images of one another, have their substituents at different orientations with respect to non-rotatable bonds, and all these different isomers generally have different physical and

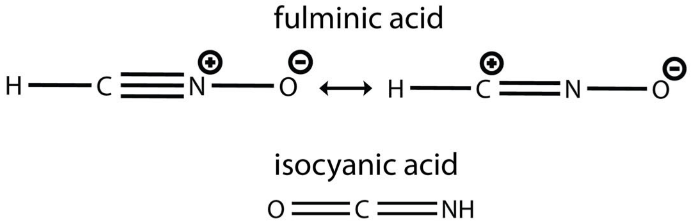

Figure 1.1: Chemical structures of fulminic acid and isocyanic acid, the two molecules that lead to the discovery of isomerism.

chemical properties. For organic molecules, with typical length scales of less than a few nanometers, it has thus been known for nearly 200 years that the structure of a molecule is the key to its properties. Another beautiful example of the strong relationship between chemical structure and function is carbon. Both graphite and diamond are materials composed of only carbon atoms. In graphite, depicted in Figure 1.2a, the carbon atoms are arranged in sheets within which they are connected through strong, covalent bonds, but the sheets themselves are only bound to each other through much weaker Van der Waals forces and π–π interactions. The electronic structure of graphite makes that it absorbs light over a wide spectral range and this material is therefore black. The weak bonds between the different sheets make that these sheets can easily be separated, causing graphite to be soft enough for use as pencil leads and as lubricant. Graphite furthermore conducts electricity. Diamond could not have been more different: it is one of the hardest materials known to man, it is optically transparent and an electrical insulator. This is all the result of the structure of diamond, in which the carbon atoms are strongly bound to all their direct neighbours (Figure 1.2b). Recently discovered structures formed by carbon atoms, such as nanotubes[2], buckyballs[3] (Figure 1.2c, d) and graphene[4], which is a single graphite layer, further widen the range of properties of pure carbon materials, and new structural variations of carbon hold great promise for a range of future applications[5]. Also for more complex systems such as proteins, which constitute thousands of atoms of various different elements, structure-function relationships play a myriad of important roles. The 3-dimensional structure of a protein is key to its function[6]. The manner in which a long protein chain folds into the correct structure is highly complex, and a large number of so-called chaperone molecules is employed by living cells to guide these folding processes[7]. The large number of diseases that are ascribed to the misfolding of proteins, such as Alzheimer's and Huntington's disease, stresses the great influence the structures of the involved proteins have on their function[7]. Not

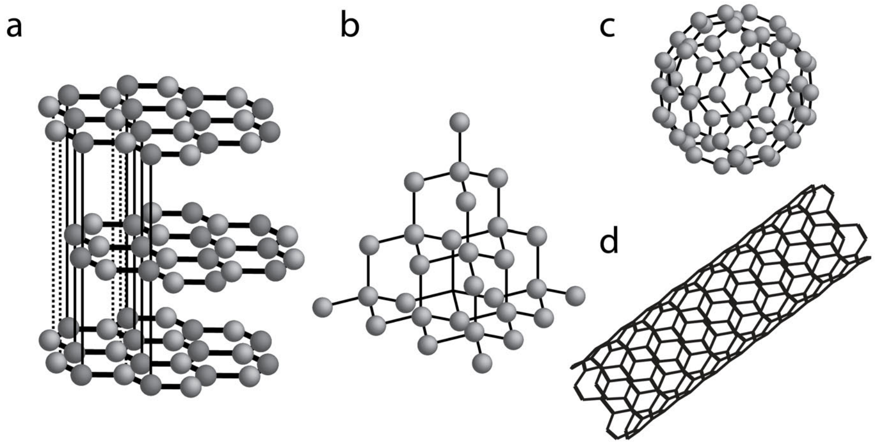

Figure 1.2: Overview of the crystal and molecular structures of different forms of pure carbon: graphite (a), diamond (b), C_{60}, also known as the buckyball (c) and a nanotube (d).

just the structure of a protein itself, but also the influence it has on the shape of its active components, so-called cofactors, was found to have great influence on the properties and functionality of the protein. The heme group, which is an iron-containing porphyrin ring (see Section 2.3), has many different functions in the human body and elsewhere in biology. Peroxidase proteins were found to have a profound influence on the shape of the heme factor they accommodate[8]. The heme group was reported to be strongly bent in a saddle-like shape conformation. This bending was ascribed to the presence of the protein, since the isolated heme protoporphyrin is flat. Such structural deformations of porphyrin rings have great influence on their properties, such as solvation[9], redox potential[10,8,11], optical properties[10,8,11,12], spin delocalization[10], axial ligation[9,13,8] and π–π interactions[8]. The same heme group can therefore perform a wide variety of biological functions as different proteins differently alter its planarity and thereby its properties.

Over the last decade many nanoscopic objects have been created that are inspired by their macroscopic counterparts, like nanocars[14], molecular motors[15] and nanoelevators[16]. Besides demonstrating that chemistry has advanced to such an extent that virtually all imaginable stable configurations of atoms can now be synthesized, this development shows that the initial steps towards creating nanoscale devices are not seldom based on duplicating macroscopic structures, with the implicit rationale that properties and function will follow structure.

The notion that structure and function are strongly related is therefore clearly established at length scales ranging from meters to nanometers, and an obvious way to gain more control over the properties and function of an object, be it of macroscopic size or mere nanometers long, is to gain more control over its structure.

1.2 Self-assembly

This thesis focusses on one particular type of structures: highly ordered molecular layers that spontaneously form when a solution containing those molecules is applied to a surface. This spontaneous formation process is called self-assembly. Molecular self-assembly is the process in which a number of pre-existing molecules arrange themselves into larger structures. The arrangement is guided by a combination of weak interactions between the constituents such as Van der Waals interaction, π–π interaction, hydrogen bonding and dipole-dipole interactions[17,18]. Control over these interactions, most importantly through the design of the molecular components, allows one to guide the resulting assemblies. The study of the self-assembly of molecules into large structures is called supramolecular chemistry and a plethora of assemblies has been created, from finite structures such as cages[19] to supramolecular polymers[20] and nano-ribbons[21]. The soft interactions that govern supramolecular chemistry can also be employed to create well-defined layers of molecules on solid surfaces. The preparation of these so-called self-assembled monolayers is remarkably simple. By simply applying a droplet of a solution containing the molecules of interest on a surface, these will assemble themselves into regular patterns at nanometer sized intervals. Because of their easy fabrication, self-assembled monolayers are interesting for a wide range of possible applications. Since the molecules are positioned at regular spacings on a solid support, they are promising candidates for the next generations of data storage and other electronic devices[22–24]. They are specifically promising for areas where electronics and chemistry meet, such as biosensors[25,26]. Furthermore, self-assembled monolayers of catalytically active molecules combine the high specificity that can be achieved with molecular, homogeneous catalysts, with the advantages of heterogeneous catalysts, such as the ease with which the catalyst can be separated from the reaction mixture after the process is completed.[27,28].

Many molecules have been found to self-assemble on solid surfaces into highly ordered patterns. Figure 1.3a shows a scanning tunneling microscopy (STM, Section 2.2.1) image of a self-assembled monolayer of stearic acid on highly oriented pyrolytic graphite (HOPG, Section 2.4) reported by Rabe *et al.*[29]. This image shows that these molecules form a well-ordered monolayer, in which the stearic acid molecules are aligned in lamellar arrays. The molecules interact with each other *via* hydrogen bonding between the carboxylic acid head groups and Van der Waals interactions between the tails, and they are bound to the HOPG substrate via Van der Waals interactions. Alkyl chains are frequently employed to enhance the self-assembly of molecules on HOPG surfaces. The STM image in Figure 1.3b shows a self-assembled mono-

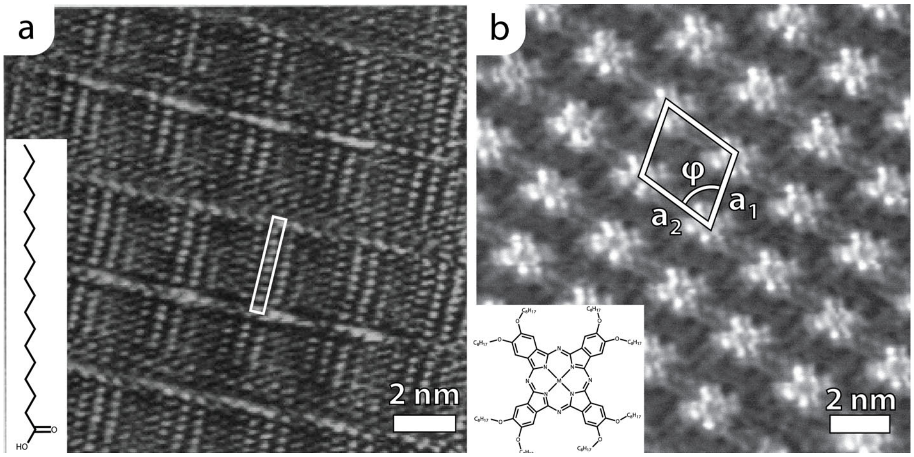

Figure 1.3: STM image of stearic acid ($C_{17}H_{35}COOH$) at the HOPG/1-phenyloctane interface as reported by Rabe *et al.*[29] (a) and an STM image of an alkyl-functionalized copper phthalocyanine (CuPcOC8) at the HOPG/1-phenyloctane interface, reproduced from[30] (b).

layer of copper(II) 2,3,9,10,16,17,23,24-octakis(octyl-oxy)-29H,31H- phthalocyanine (CuPcOC8). The phthalocyanine adsorbates form a highly ordered, 2-dimensional crystalline lattice which is built up from the regular repetition of a unit cell. A possible unit cell for this monolayer, which is sketched in the image, consists of two vectors, $\mathbf{a}_1$ and $\mathbf{a}_2$ with an angle ϕ between them. Every molecule displayed in the STM image can be found at integer multiples of these two unit cell vectors. The properties of unit cell vectors and how they are used to describe self-assembled monolayers is more extensively described in Section 2.5. Some molecules are able to self-assemble at the solid/liquid interface in more than one crystalline structure. An example of this, so-called, 2–dimensional polymorphism is given in Figure 1.4. These STM images, reported by Tahara *et al.*[31], show that the drawn rhombic-shaped bis-dehydrobenzo[12]annulene (bisBDA) can form at least four different polymorphs at the HOPG/1,2,4-trichlorobenzene interface. The occurrence of these polymorphs could by guided by the choice of concentration of the molecules in the supernatant solvent, and even more different surface structures could be obtained by creating structural variations of this molecule, *e.g.* by variation of the length of the alkyl tails. This example demonstrates that the same molecular building block can be used to build different monolayer structures, and understanding and control over these structures is a prerequisite to exploit the full capabilities of self-assembled monolayers.

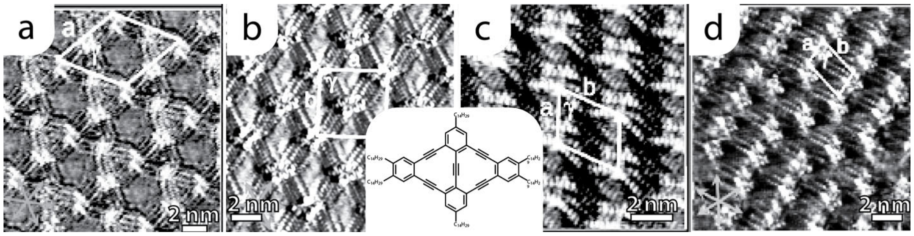

Figure 1.4: Four different polymorphs formed by rhombic-shaped bis-dehydrobenzo[12]annulene molecules equipped with six $C_{14}H_{29}$ tails, as reported by Tahara *et al.*[31]. Several different porous (a,b) and non-porous (c,d) surface polymorphs were observed at the HOPG/1,2,4-trichlorobenzene interface.

1.3 2-Dimensional crystal engineering

Over the past decade tremendous progress has been made in the understanding and control of self-assembled monolayers, and the term 2-dimensional crystal *engineering* is used to indicate the wealth of possibilities that are emerging for the creation of well-defined, functional monolayers[32–34]. An overview of some of the tools and buildings blocks for the control of self-assembled monolayers, that have been reported in the literature is given in Figure 1.5. Lackinger *et al.*[35], demonstrated that the structure of a self-assembled monolayer trimesic acid can form either a "chickenwire" or a "flower" pattern on the HOPG surface, depending on the carboxylic acid that was used as solvent (Figure 1.5a). Control over monolayer structures has also already been demonstrated by changing the temperature and the concentration of the solution from which the monolayer was created[36,35,37]. Monolayers of multiple molecular components have also been created. Figure 1.5b shows a crystalline self-assembled monolayer of four different molecular species[38], as was reported by De Feyter and coworkers. An example of the binding of molecules in a porous network is given in Figure 1.5c. After deposition of a porous network of melanine (1,3,5-triazine-2,4,6-triamine) and PTCDI (perylene tetra-carboxylic di-imide) on a silver-terminated silicon surface, C_{60} molecules could be trapped in the pores of this structure[39]. The fourth example (Figure 1.5d), shows that self-assembled molecular layers are not confined to 2-dimensions. In this case, molecules of hexa-peri-hexabenzocoronene, were found to self-assemble in a second layer on top of a layer of pentacontane ($C_{50}H_{102}$) at the HOPG/*n*-tetradecane interface[40]. These examples are all beautiful demonstrations of different types of monolayer structures that can be created and, to some extent, controlled. Prediction and thereby true engineering or design of the structure of self-assembled monolayers is however still beyond reach, and this thesis therefore aims to contribute to the understanding of the structure of self-assembled monolayers and of the control over the polymorphic composition of these monolayers. The motivation for carefully investigating these structures is the hypothesis that the structure of a monolayer will influence its properties and ultimately its function.

1.3.1 Monolayer structure and function

Few studies on the relationships between the structure and function of a monolayer have already been performed and various types of structures of self-assembled monolayers have been found to influence their properties. The influence of surface density of an adlayer on its properties was demonstrated by Burke *et al*[41] who showed that the opto-electronic characteristics of 3,4,9,10-perylene tetracarboxylic dianhydride (PTCDA) molecules on a NaCl (001) surface were more bulk-like for denser adlayer structures, and resembled more closely the properties of the isolated molecule for more spacious packing geometries. The influence of molecular orientation on the properties of adsorbates was demonstrated by Nikiforov *et al.*[42], who showed that 5,15-bis(2',6'-bis(3,3-dimethyl-1-butyloxy)phenyl)porphyrin can form two different surface structures on HOPG surfaces (Figure 1.6b,c). A difference in work function was found between an orientation in which the porphyrin plane was perpendicular to the surface and one in which it was parallel. Self-assembled 2-D porous networks demonstrate that the structure of self-assembled monolayers can not only alter the existing properties of the interface or molecules, but that new properties can also emerge upon self-assembly, as these networks can act as hosts for binding of guest molecules[43,44]. The ability to bind these guests is not present in the individual molecules constituting the monolayer and only arises upon assembling in the network surface structure. This thesis aims to make a contribution to the understanding of the possibly myriad of manners in which the structure of self-assembled monolayers influences their properties and thereby function, as a whole and of their molecular constituents.

1.4 Outline of this thesis

This thesis describes the structure and properties of self-assembled 5,10,15,20-tetraundecylporphyrins at the interfaces of HOPG and a range of organic solvents, as well as at HOPG surfaces in Ultra High Vacuum. An introduction of the used experimental techniques and more detailed information on the used porphyrin molecules, the graphite substrate and the mathematical description of self-assembled monolayers will be provided in Chapter 2. The four different 2-D polymorphs that are formed by self-assembly of these molecules on the graphite surface are described in Chapter 3, where also is described how the polymorphic composition of a given surface can be controlled during the initial stages of self-assembly, what the geometrical relationship between the different polymorphs is, and how the lattice structure of the polymorphs relates to the structural conformations of the porphyrin constituents. The influence

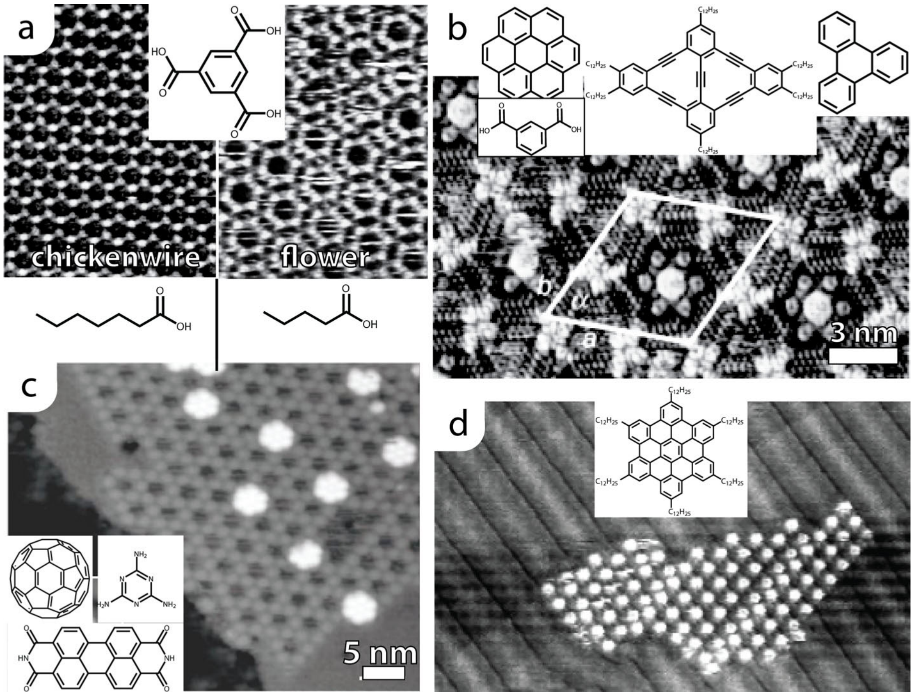

Figure 1.5: Examples of complex self-assembled monolayers that have already been engineered. The STM images in (a) show that the structure of self-assembled monolayers of trimesic acid can be controlled by forming the layer from either a 1-heptanoic acid (left) or 1-pentanoic acid (right) solution[35]. Image (b) shows that crystalline monolayers of multiple components, four in this case, can also be formed from solution[38]. The STM measurement depicted in (c) shows the binding of several C_{60} guest molecules in a porous network of melanine[39] and PTCDI and the fourth example (d) shows that self-assembled layers are not confined to 2-dimensions, but that multiple layers can be stacked on top of each other in a controllable fashion[40].

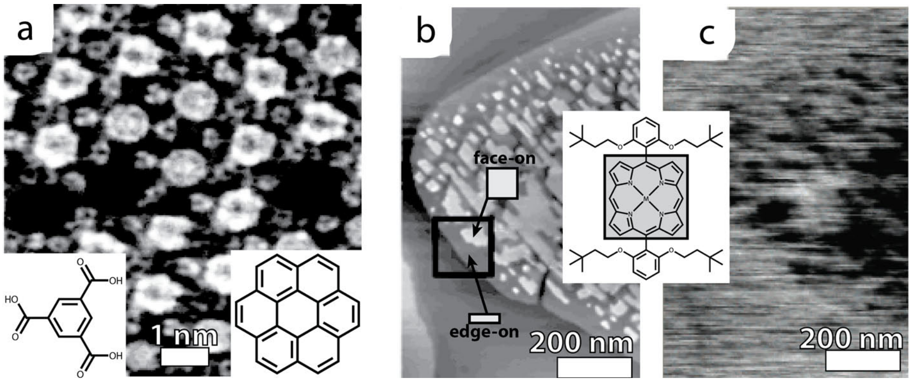

Figure 1.6: Two examples from the literature in which the properties of molecules in a monolayer depend on their arrangement on the surface. Figure (a) shows an STM image of a 2-dimensional porous network of 1,3,5-trimesic acid on the HOPG/1-heptanoic acid interface reported by Griessl *et al.*[44]. Some of the pores are filled with coronene guest molecule. The nc-AFM and SKFM measurements in (b) and (c) respectively, are reproduced from a paper by Nikiforov *et al.*[45]. They report that 5,15-bis(2',6'-bis(3,3-dimethyl-1-butyloxy)phenyl)porphyrin can assemble at the HOPG surface in both an edge-on and a face-on orientation and they showed that there is a difference in work function between these two orientations.

of the 2-dimensional polymorphism on the physical properties of the porphyrin adsorbates is the topic of Chapter 4, where different physical and chemical properties of these layers will be determined locally, using a combination of SPM techniques. STM studies on dynamical transitions from low density to higher density polymorphs, is the topic of Chapter 5. In this Chapter also local control over the surface structure by employing nanomanipulation with an STM or AFM tip well be described. Finally, in Chapter 6, the attention is shifted to the formation of redox species of copper 5,10,15,20-tetraundecylporphyrins, created by voltage pulses applied with an STM tip. Finally, in Chapter 7, the development of an electrochemical STM is described which will allow for more detailed investigation of the redox species of self-assembled porphyrin monolayers.

References

1. http://www.chemheritage.org/discover/chemistry-in-history/themes/molecular-synthesis-structure-and-bonding/liebig-and wohler.aspx

2. Ajayan P.M. *Chem. Rev.*, 99 (7):1787–1800, **1999**

3. Kroto H.W., Heath J.R., OBrien S.C., Curl R.F. and Smalley R.E. *Nature*, 318 (6042):162–163, **1985**

4. Novoselov K.S., Geim A.K., Morozov S.V., Jiang D., Zhang Y., Dubonos S.V., Grigorieva I.V. and Firsov A.A. *Science*, 306 (5696):666–669, **2004**

5. Delgado J.L., Herranz M.A. and Martin N. *J. Mater. Chem.*, 18:1417–1426, **2008**

6. Dobson C.M. *Nature*, 426:884–890, **2003**

7. Hartl F.U. and Hayer-Hartl M. *Science*, 295 (5561):1852–1858, **2002**

8. Shelnutt J.A., Song X.Z., Ma J.G., Jia S.L., Jentzen W. and J. Medforth C. *Chem. Soc. Rev.*, 27 (1):31–42, **1998**

9. Berezin D., Semeikin A. and Berezin M. *Rus. J. Phys. Chem.*, 83 (8):1315–1320, **2009**

10. Medforth C.J., Senge M.O., Smith K.M., Sparks L.D. and Shelnutt J.A. *J. Am. Chem. Soc.*, 114 (25):9859–9869, **1992**

11. Senge M.O. *Chem. Commun.*, 3:243–256, **2006**

12. Röder B., Büchner M., Rückmann I. and Senge M.O. *Photochem. Photobiol. Sci.*, 9 (8):1152–1158, **2010**

13. Jentzen W., Song X.Z. and Shelnutt J.A. *J. Phys. Chem. B*, 101 (9):1684–1699, **1997**

14. Vives G. and Tour J.M. *Acc. Chem. Res.*, 42 (3):473–487, **2009**

15. Michl J. and Sykes E.C.H. *ACS Nano*, 3 (5):1042–1048, **2009**

16. Badjić J.D., Balzani V., Credi A., Silvi S. and Stoddart J.F. *Science*, 303 (5665):1845–1849, **2004**

17. Lindsey J.S. *New J.Chem.*, 15 (2-3):153–180, **1991**

18. Whitesides G.M., Mathias J.P. and Seto C.T. *Science*, 254 (5036):1312–1319, **1991**

19. Chakrabarty R., Mukherjee P.S. and Stang P.J. *Chem. Rev.*, 111 (11):6810–6918, **2011**

20. Brunsveld L., Folmer B.J.B., Meijer E.W. and Sijbesma R.P. *Chem. Rev.*, 101 (12):4071–4098, **2001**

21. Maune H.T., Han S.P., Barish R.D., Bockrath M., Goddard III W.A., Rothemund P.W.K. and Winfree E. *Nat. Nanotechnol*, 5 (1):61–66, **2010**

22. Smits E.C.P., Mathijssen S.G.J., van Hal P.A., Setayesh S., Geuns T.C.T., Mutsaers K., Cantatore E., Wondergem H.J., Werzer O., Resel R., Kemerink M., Kirchmeyer S., Muzafarov A.M., Ponomarenko S.A., de Boer B., Blom P.W.M. and de Leeuw D.M. *Nature*, 455 (7215):956–959, **2008**

23. Joachim C., Gimzewski J.K. and Aviram A. *Nature*, 408 (6812):541–548, **2000**

24. Ciesielski A., Palma C.A., Bonini M. and Samorì P. *Adv. Mater.*, 22 (32):3506–3520, **2010**

25. Andringa A.M., Spijkman M.J., Smits E.C.P., Mathijssen S.G.J., van Hal P.A., Setayesh S., Willard N.P., Borshchev O.V., Ponomarenko S.A., Blom P.W.M. and de Leeuw D.M. *Org. Elec.*, 11 (5):895–898, **2010**

26. Chaki N.K. and Vijayamohanan K. *Biosens. Bioelectron.*, 17 (1-2):1–12, **2002**

27. Corma A. *Catal. Rev.*, 46 (3-4):369–417, **2004**

28. de Almeida M.P. and Carabineiro S.A.C. *ChemCatChem*, 4 (1):18–29, **2012**

29. Rabe J.P. and Buchholz S. *Science*, 253 (5018):424–427, **1991**

30. Qiu X., Wang C., Yin S., Zeng Q., Xu B. and Bai C. *J. Phys. Chem. B*, 104 (15):3570–3574, **2000**

31. Tahara K., Okuhata S., Adisoejoso J., Lei S., Fujita T., Feyter S.D. and Tobe Y. *J. Am. Chem. Soc.*, 131 (48):17583–17590, **2009**

32. Champness N.R. and De Feyter S. *CrystEngComm*, 13:5531–5531, **2011**

33. Furukawa S., Uji-i H., Tahara K., Ichikawa T., Sonoda M., De Schryver F.C., Tobe Y. and De Feyter S. *J. Am. Chem. Soc.*, 128 (11):3502–3503, **2006**

34. Palma C.A., Bonini M., Breiner T. and Samorí P. *Adv. Mater.*, 21 (13):1383–1386, **2009**

35. Lackinger M., Griessl S., Heckl W.M., Hietschold M. and Flynn G.W. *Langmuir*, 21 (11):4984–4988, **2005**

36. Gutzler R., Sirtl T., Dienstmaier J.F., Mahata K., Heckl W.M., Schmittel M. and Lackinger M. *J. Am. Chem. Soc.*, 132 (14):5084–5090, **2010**

37. Lei S.B., Tahara K., De Schryver F.C., Van der Auweraer M., Tobe Y. and De Feyter S. *Angew. Chem.-Int. Ed.*, 47 (16):2964–2968, **2008**

38. Adisoejoso J., Tahara K., Okuhata S., Lei S., Tobe Y. and De Feyter S. *Angew. Chem.-Int. Ed*, 121 (40):7489–7493, **2009**

39. Theobald J.A., Oxtoby N.S., Phillips M.A., Champness N.R. and Beton P.H. *Nature*, 424 (6952):1029–1031, **2003**

40. Piot L., Marchenko A., Wu J., Müllen K. and Fichou D. *J. Am. Chem. Soc.*, 127 (46):16245–16250, **2005**

41. Burke S.A., LeDue J.M., Topple J.M., Fostner S. and Grütter P. *Adv. Mater.*, 21 (20):2029–2033, **2009**

42. Nikiforov M.P., Zerweck U., Milde P., Loppacher C., Park T.H., Uyeda H.T., Therien M.J., Eng L. and Bonnell D. *Nano Letters*, 8 (1):110–113, **2007**

43. Stepanow S., Lingenfelder M., Dmitriev A., Spillmann H., Delvigne E., Lin N., Deng X., Cai C., Barth J.V. and Kern K. *Nat. Mater.*, 3 (4):229–233, **2004**

44. Griessl S.J.H., Lackinger M., Jamitzky F., Markert T., Hietschold M. and Heckl W.M. *Langmuir*, 20 (21):9403–9407, **2004**

45. Nikiforov M.P., Zerweck U., Milde P., Loppacher C., Park T.H., Uyeda H.T., Therien M.J., Eng L. and Bonnell D. *Nano Lett.*, 8 (1):110–113, **2008**

CHAPTER 2

Background of the research

2.1 Introduction

The topic of this thesis is the relationship between the structure and the physicochemical properties of porphyrin molecules in a self-assembled monolayer on graphite surfaces. In this chapter the different concepts and techniques that underlie research described in this thesis will be discussed. First the working principles of the employed scanning probe microscopy (SPM) techniques will be described. This will include Scanning Tunneling Microscopy (STM), Atomic Force Microscopy (AFM) and Scanning Kelvin Probe Microscopy (SKPM). The chemical and physical properties of porphyrins, the molecules studied in this thesis, will be treated, which should explain our interest in these particular molecular systems. The structure of the graphite substrate on which the self-assembled monolayers will form, will be discussed next, and finally the required conventions and mathematics to describe the structure of self-assembled molecular monolayers on graphite will be explained.

2.2 Scanning Probe Microscopy

Scanning Probe Microscopy (SPM) presents a class of microscopes that all rely on the same underlying principle. A sharp needle, called *tip*, is scanned at a short distance over the area of interest of a given sample. Movement relative to the sample can be controlled very accurately by mounting either the tip or the sample on a piezo–

electric element. Piezo–electric materials expand or shrink if an external voltage is applied across them, and this allows for controlled movement in the range of several picometers. By placing orthogonal electrodes at a tubular piezo–electric element or by employing multiple piezo–electric elements, tip and sample can be moved in all three orthogonal directions (x,y,z) relative to each other with sub–nanometer precision[1]. While scanning over the area of interest of a given sample, a local property of the sample surface is continuously probed. Several different SPMs exist which all probe a different local property of the sample. In scanning tunneling microscopy (STM) the local density of states of the sample is probed, while atomic force microscopy (AFM) locally measures forces between tip and sample. Other implementations exist, such as magnetic force microscopy (MFM), which locally measures the magnetic field of the sample[2,3], and Scanning Near Field Optical Microscopy (SNOM)[4,5], which locally maps its optical properties. The tip can also be used to manipulate the sample at the nanoscopic scale. Their ability to both image and manipulate matter at the nanoscale has made SPMs among the most important tools in nanoscience and nanotechnology. The examples shown in Figure 2.1 give an overview of the capabilities of Scanning Probe Microscopies. One of the most famous examples of the capabilities of STM is shown in Figure 2.1a. This image shows an STM image from an experiment by Eigler and co-workers[6] in which they wrote the letters "IBM" by positioning xenon atoms on a nickel (110) surface with the help of the STM tip. Each character is 5 nm from bottom to top, demonstrating the incredible precision of scanning probe microscopes. Figure 2.1b shows that AFM can be employed to measure the forces between individual molecules. Gaub *et al.*[7] chemically attached biotin to the tip of an AFM cantilever and to an agarose bead that served as the sample surface. Avidin, a protein that specifically binds four biotin molecules, was added to the system and the approach of the tip to the sample leads to the formation of a avidin-biotin complex. When the tip is subsequently retracted, this complex breaks again and the forces required for this breaking can be measured from the deflection of the AFM cantilever. The unbinding of single biotin-avidin complexes could be studied using this technique. As a final example, the real-time imaging of a catalytic reaction, as reported by Hulsken *et al.*[8], is depicted in Figure 2.1c. The red dots represent adsorbed manganese porphyrins that appear significantly higher than the majority of the porphyrin adsorbates. These apparently higher species have catalytically split an oxygen molecule and bound its oxygen atoms. This process could be observed in real-time in STM with molecular resolution, showing that single steps of a complex catalytic reaction mechanism can be elucidated with this technique.

2.2.1 Scanning Tunneling Microscopy

The Scanning Tunneling Microscope (STM) was the first scanning probe microscope to be invented[1,9]. STM allowed for the first time the imaging of individual atoms

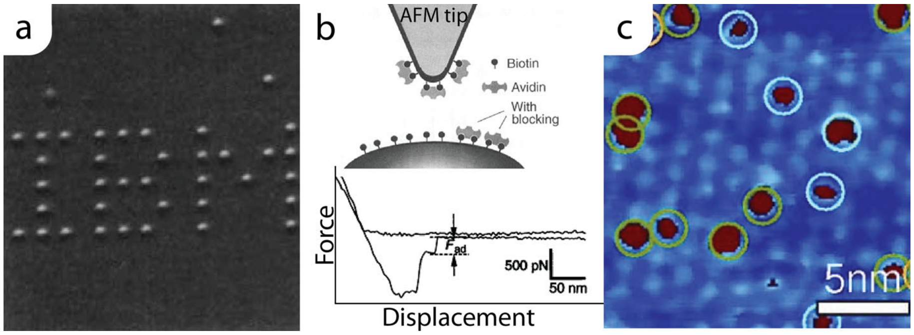

Figure 2.1: Three examples demonstrating the capabilities of scanning probe microscopy for imaging and manipulation at the nanoscale. The STM image in (a) shows the word "IBM" written by the placement of xenon atoms at the nickel (110) surface using a low temperature STM[6]. Each character measures 5 nm from top to bottom. Figure (b) shows an example of AFM force spectroscopy. Gaub *et al.*[7] attached biotin molecules to both tip and an agarose bead, and when avidin was allowed to bind to biotin units on both tip and sample, the force required to separate single biotin-avidin bonds could be measured upon retraction of the tip. The STM image in (c) shows the real-time, real-space dissociation and binding of oxygen to surface bound manganese porphyrins at the single catalyst level as measured by Hulsken and co-workers[8].

in real–time and real-space. The importance of the invention was acknowledged by awarding its inventors, Binnig and Rohrer, with the Nobel Prize in physics in 1986, a mere 4 years after the invention. The working principle of STM is explained in Figure 2.2. An atomically sharp needle (I), usually called tip, is attached to the bottom of a hollow cylindrical piezo electric element (II). The outer electrode of this piezo tube is segmented into four sections, and by applying voltages to these sections the piezo element can be bent independently in both the X and Y direction, allowing the tip to be moved along the sample surface. By applying an additional voltage to the inner wall of the piezo element, the entire piezo element is extended or contracted, allowing for movement normal to the sample surface, *i.e.* in the Z direction. Several other geometries of piezo elements can be used to perform the same three-axis movement of tip relative to sample. The sample, rather than the tip, can for instance be attached to the tubular piezo element, and separated piezo elements can be employed for movement along each of the three orthogonal directions. The general principle is, however, always the same. Using the piezoelement, the tip is scanned in consecutive lines along the region of interest of the sample surface (III). A small bias voltage (V_{bias}), with typical values of a few millivolts to a few volts at most, is applied between the tip and the surface. Because of the quantummechanical

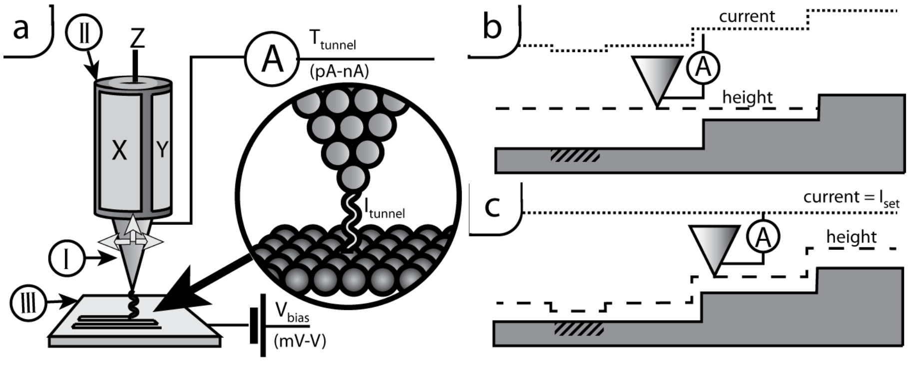

Figure 2.2: Schematic drawing of a Scanning Tunneling Microscope (a) and two sketches depicting constant-height (b) and constant-current (c) STM operation modes. In the depicted STM setup, an atomically sharp tip (I) is mounted at the bottom of a segmented piezo tube (II). By applying voltages at the four electrodes on the outer shell and the one at the inner wall of the tube, the tip can be moved both laterally (X,Y) as vertically (Z) with respect to the sample surface (III). The tip is scanned, line by line, over the area of interest of the sample. A bias voltage (V_{bias}) is applied between tip and sample and a small tunneling current (I_{tunnel}) flows between the two when they are brought at short distances of a few nanometers. In constant height mode (b), the extension of the piezo element (height) is not adjusted throughout the scan line and the tunneling current is measured at each location of the scan line. In constant current mode (c), the operation mode most commonly used in STM, a feedback system is used to adjust the height such that the tunneling current is kept constant. The tips then nicely tracks a constant-current contour above the sample surface.

tunneling effect, the wave-functions of electrons in the tip have a non-zero amplitude throughout the small gap between the tip apex and the sample surface and *vice versa*.[1] When the sample is negatively biased, electrons will mostly tunnel from the occupied states of the sample to unoccupied states of the tip, and when the sample is placed at a more positive electrical potential than the tip, the electrons will predominantly move from occupied tip states to unoccupied sample states. At distances in the order of a few nanometers, this nonzero amplitude leads to a large enough probability for an electron to move between the tip and the sample to create a detectable tunneling current (I_{tunnel}). This tunneling current is typically in the order of picoamperes to nanoamperes, but because the tunneling probability decays exponentially with increasing tip-sample separation, it is a very accurate measure of that distance, despite its small magnitude. The tunneling current is not a mere reflection of the distance between the most protruding atom of the STM tip and the sample surface. Because the electrons tunnel between states in tip and sample, the local electronic structure of both tip and sample influence the resulting tunneling current. By scanning the tip over the area of interest of a sample, one can make a map of the local tunneling current. This is sketched in Figure 2.2b. The tunneling current, of which the profile is sketched by the dotted line, is a reflection of both the topography of the sample, and the spatial variation in the electronic states of the sample surface. The dashed area of the sketched sample surface represents an area where the electronic structure of the sample is different from its surroundings in such a way that the measured tunneling current through this area is lower than that through the surrounding surface. The operation mode sketched in Figure 2.2b is referred to as "constant-height" mode, since the height, *i.e.* the extension or contraction of the piezo, is not varied throughout the measurement, as is sketched by the dashed line profile. A problem that arises from not adjusting the height of the tip, is that the moving tip may crash into large topographical features of the sample. The microscope would furthermore fail to image a sample surface which is sloped with respect to the tip. These problems are overcome by measuring in "constant current" mode. Rather than measuring the tunneling current everywhere within the area of interest and making a map of the obtained values, a feedback system is used to adjust the tip-sample separation such that the tunneling current is maintained at a constant, preset, value (I_{set}). This operation mode is sketched in Figure 2.2c. The tip now tracks an iso-current contour of the sample at a safe and constant distance. The height map that is obtained in this mode, is typically referred to as a topography image, but since it is actually an iso-current contour, it depict a superposition of the true topography and variations in the local electronic structure of the sample. The dashed area, in which the tunneling conductivity is lower than in the surrounding layer, therefore appears as a depression in such STM topography images.

Ambient STM measurements, *i.e.* at room temperature and an air pressure of 1 bar, were performed on a home-built Nijmegen Ambient STM. The ambient STM measurements performed in Chapters 3 and 5 were performed using a home-built controller and software[10]. This controller does not allow for delivering well-defined bias voltage pulses to the STM junction and the measurements in Chapter 6 were therefore performed on a similar home-built STM but then operated using an Omicron Scala Controller[11]. All STM tips were mechanically cut from $Pt_{0.8}Ir_{0.2}$ wire, with a diameter of 0.5 mm. STM measurements in Ultra High Vacuum were performed using a JEOL JSPM 4500A. These measurements, which are described in Chapter 4, were performed to compare results obtained in STM measurements with those acquired using Atomic Force Microscopy and the used tips were therefore Pt-coated AFM cantilevers. These tips can be used for both STM and AFM measurements and images using both techniques can therefore be obtained at the exact same location of the sample surface.

2.2.2 Atomic Force Microscopy

AFM was invented in 1986[12] and it is presently the most widely used form of Scanning Probe Microscopy. A major drawback of STM is the requirement that the sample needs to be conductive. This means that its field of application is limited to metallic or semi-conducting substrates, which are optionally covered with a non-conducting adlayer that is at most a few nanometers thick. Because Atomic Force Microscopy (AFM) relies on the local determination of forces between a tip and the sample, this technique does not have this requirement. The working principle of AFM is depicted in Figure 2.3a. In AFM a very sharp tip is mounted at the end of a flexible cantilever (I). When this tip is brought in close proximity to the surface (II), forces between tip and sample cause the cantilever to bend. The amount of bending is determined by measuring the deflection of a laser beam (III) that is aimed at the very end of the cantilever, using a segmented photodiode (IV). The deflection of the cantilever is proportional to the forces between the apex of the tip and the sample substrate. The tip and the sample can be moved relative to each other by a piezo electric element(V), which in this case is sketched below the sample surface, but different practical implementations are possible. Like in STM, one typically does not make a map of the interaction force over the surface, but rather uses a feedback loop to adjust the tip-sample distance such that the force is constant throughout the scanning. The simplest operation mode of AFM is called contact mode. In this mode the tip is scanned across the sample surface such that the deflection, and thereby the interaction force, is kept constant. In contact mode AFM the tips touches the sample surface and this may, on soft surfaces such as the monolayers examined in this research, damage the sample. To minimize this damage, dynamic force microscopy modes (Tapping Mode AFM, and non-contact AFM) can be used[13]. In these dynamic modes the cantilever is made to oscillate close to or at its mechanical resonance frequency by an oscillating piezo (VI in Figure 2.3a) and the forces between the tip and the sample are probed by determining variations in the cantilever oscillations. The general working principle of the dynamic AFM modes is sketched in Figure 2.3b. The tip oscillates with a certain frequency ν, amplitude A and phase shift ϕ relative to the drive piezo. If the force between tip and sample varies, for instance by encountering a topographical feature such as a step edge, the oscillation of the cantilever is affected. In Figure 2.3b it is sketched that the amplitude of the tip oscillation decreases upon encountering a step edge. The tip–sample distance is subsequently adjusted using a feedback loop, such that the oscillation amplitude reaches its previous, preset value. The method sketched here is thus based on keeping the amplitude of the tip-oscillation constant, but dynamic AFM measurements can also be based on tracking the surface at a constant frequency or phase shift. In Tapping Mode AFM (tm-AFM) the cantilever is driven with a constant excitation amplitude and at a constant frequency which is typically chosen to be about 5% below its resonance frequency. The cantilever therefore oscillates at the driving frequency and its resulting amplitude is measured from the

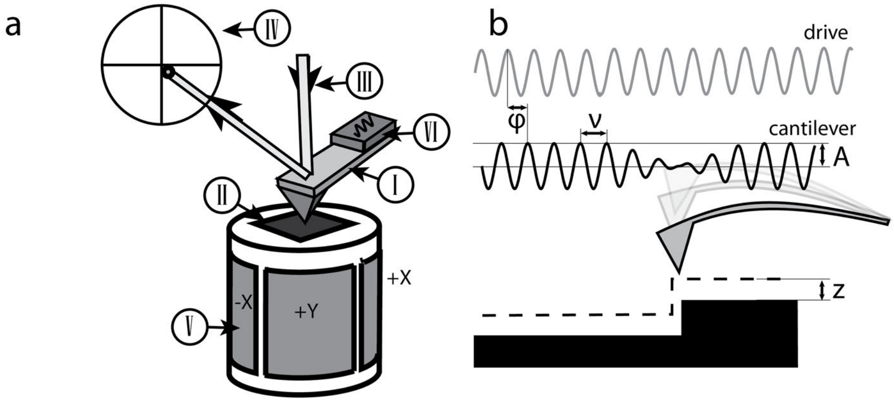

Figure 2.3: Schematic drawing of the working principle of AFM (a). The sharp tip with which the sample is probed is mounted at the bottom of a flexible, reflective cantilever (I). A laser beam (III) is aimed at the very end of the cantilever and the reflected beam shines on a four-quadrant photodetector (IV). Bending of the cantilever, because of interaction between the tip and the sample (II), also deflects the reflected laser beam and this deflection can be measured by the location of the laser spot on the photodiode. Tip and sample can be moved relative to each other by a piezo element (V). For dynamical AFM measurements, such as tm-AFM and nc-AFM, a second piezo element (VI) is used to drive the tip oscillation. The operation principle of dynamic AFM modes is explained in (b), using amplitude modulated AFM, such as tm-AFM, as an example. The cantilever is driven with an oscillation of constant amplitude and frequency. As a result of forces between tip and sample, the amplitude of the cantilever oscillation varies with the topography of the sample. The tip-sample separation is adjusted to keep the resulting cantilever oscillation constant. In other modes the phase shift (ϕ) between the drive and cantilever oscillations or the change in tip frequency (ν) are measured or used as feedback parameter.

deflection of the laser beam on the photo-detector using a Lock-In amplifier. When the tip is brought close to the sample, forces acting between the tip and the sample will damp the oscillation of the cantilever and thereby reduce its amplitude. Two different processes can alter the amplitude of the tip. Besides the normal, dissipative damping, which lowers the amplitude of the cantilever directly, the interaction with the surface can cause the resonant frequency of the cantilever to shift. Since the tip is driven at a constant frequency, the difference between the driving and the resonant frequency changes in this process. When the cantilever is driven at a frequency further away from its resonance frequency, its response to the driving oscillation will diminish and its amplitude will decrease. In tm-AFM the amplitude of the cantilever oscillation is kept constant by adjusting the vertical distance between the tip and the sample. This feedback loop responds to the decline in amplitude caused by the shift of the cantilever resonance frequency as well as to the direct damping. These two processes can to some extend be analysed independently by examining the phase shift of the cantilever oscillation versus the drive oscillation. tm-AFM is a form of amplitude modulated AFM (am-AFM). tm-AFM is widely applied to study nanoscopic samples under ambient conditions. In tm-AFM the tip touches the sample only at the very downward part of its oscillation and since the cantilever oscillation is generally much faster (300 kHz) than the scanning movement over the sample (10 Hz), the cantilever can be considered to have no lateral movement with respect to the sample as they touch. Therefore it does not scratch or influence the sample surface to the same extent as contact mode AFM does. In UHV, a different implementation of AFM is more commonly applied in which there is no contact between tip and sample during any part of the oscillation cycle. In principle am-AFM-based non-contact AFM measurements can be performed in UHV, but since the energy stored in an oscillating cantilever in UHV is generally very large, as is apparent from its high Q-factor, a large number of oscillating cycles are required for the cantilever to obtain a noticeable change in amplitude[14]. This technique is therefore very slow at low pressure atmospheres. For the majority of AFM measurements performed in this thesis a different dynamic AFM operation was used, which is commonly referred to as non-contact AFM (nc-AFM). In nc-AFM it is not the amplitude that is kept fixed by adjusting the tip-sample distance, but the cantilever's resonance frequency. This is thus a form of frequency-modulated AFM (fm-AFM). In nc-AFM the cantilever is always driven at its current resonance frequency. Allowing the tip to come in close proximity to the sample surface will cause the resonance frequency to shift towards lower values. A downward shift of typically 10-500 Hz of the original resonance frequency (which typically is 100-300 kHz) is used as a setpoint for the feedback system, which determines the actual resonance frequency using a phase locked loop (PLL) and adjusts the tip-sample distance such that it matches the frequency setpoint. Atomic[15,13] and molecular resolution[16,17] images have been obtained with nc-AFM . The nc-AFM measurements described in this thesis were performed on a JEOL JSPM 4500A, while ambient tapping mode AFM images were conducted on a Veeco Nanoscope IV or Veeco Dimension 3100.

2.2.3 Kelvin Probe Microscopy

Scanning Kelvin Probe Force Microscopy (SKFM) is an AFM-based microscopy technique with which the local electronic properties of a sample can be investigated. SKFM, which is also referred to by the abbreviations KPFM, KPM, SKPM and KFM, can be implemented in several different ways in the different AFM modes. The underlying working principle was discovered by Lord Kelvin, long before AFM was invented. Consider two materials with different Fermi levels (ϵ_1 and ϵ_2) and different

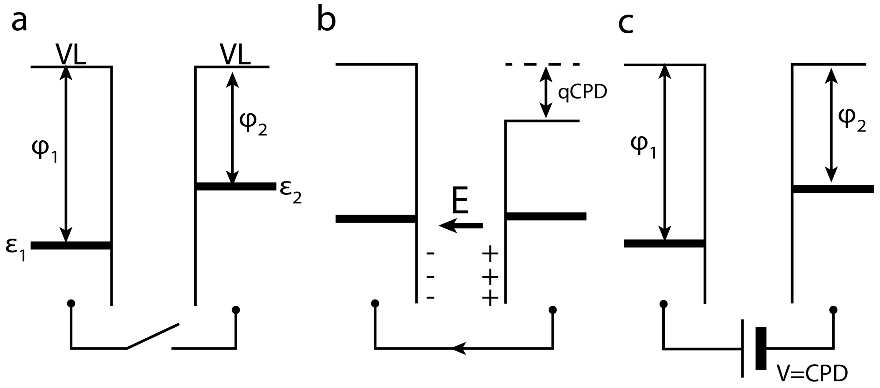

Figure 2.4: Schematic representation of the working principle of Kelvin Probe Microscopy. Two different materials generally have their respective Fermi levels (ϵ_1, ϵ_2) at different distances from their energy level of a motionless electron in free space, called vacuum level (VL) (a). This implies that they have different work functions (ϕ_1, ϕ_2). When two materials with different work functions are electrically connected or otherwise allowed to reach thermodynamic equilibrium, the Fermi levels will align by the transfer of electrons from the material with the highest Fermi level to the one with lowest (b). Since charge is transferred between two initially neutral materials, an electric field (E) now exists between the two materials. When a voltage is applied between the two materials the energy levels can be shifted relative to each other. If the levels are shifted to such an extent that the electric field between the two materials is cancelled, the levels are again at the original positions of the isolated materials (c). The voltage required to perform this cancellation is the difference in work function between the two materials. This quantity is also referred to as the contact potential difference (CPD). (Adapted from Palermo *et al.*[18]).

work functions (ϕ_1 and ϕ_2) as sketched in Figure 4.15a. The work function is defined as the lowest amount of energy required to remove an electron from the material to the vacuum level (VL). When two materials are brought into electrical contact or otherwise allowed to reach thermodynamic equilibrium, the Fermi levels of the two materials will align: electrons will migrate from the material with the highest Fermi level to the material with the lowest Fermi level until the two are aligned (Figure 4.15b). Because charge is transferred between two initially neutral materials, an electric field (**E**) now exists between them. The difference in work function between the two materials, also referred to as the contact potential difference (CPD), can be determined from this electric field. When a voltage with a value of $V = qCPD$ (q being the elementary charge) is applied between the two materials, the Fermi levels are shifted back to their original positions, and the electric field between the two materials is cancelled (Figure 4.15c). Determining the voltage at which the electric field is cancelled thus yields the difference in work function between the two materials. AFM-based Kelvin probe microscopy is performed by applying a modulated voltage between the tip and sample[19]. The potential difference between tip and sample is then given by

$$\Delta V = \Delta\Phi - V_{dc} + V_{ac}\sin(\omega t) \tag{2.1}$$

In which $\Delta\Phi$ is the difference in work function between the tip and the sample, V_{dc} is the dc-component of the applied bias voltage, and V_{ac} is the oscillating component of this bias voltage with frequency ω. The tip—sample system can be approximated as a parallel plate capacitor, and the energy stored in this system can then be expressed as:

$$U = \frac{1}{2}C\Delta V^2 \tag{2.2}$$

The force between the tip and the sample is then given by

$$F = -\frac{\partial U}{\partial z} = -\frac{1}{2}\frac{\partial C}{\partial z}\Delta V^2 = -\frac{1}{2}\frac{\partial C}{\partial z}[F_{dc} + F_{\omega} + F_{2\omega}] \tag{2.3}$$

which has components at dc, the modulation frequency ω and twice the modulation frequency, 2ω of:

$$\begin{aligned} F_{dc} &= (\Delta\Phi - V_{dc})^2 - \frac{V_{ac}^2}{2} && (2.4)\\ F_{\omega} &= 2V_{ac}(\Delta\Phi - V_{dc})\sin(\omega t) && (2.5)\\ F_{2\omega} &= \frac{1}{2}V_{ac}^2\cos(2\omega t) && (2.6) \end{aligned}$$

From these equations it is apparent that if V_{dc} is adjusted such that $V_{dc} = \Delta\Phi$, the component at ω becomes zero. In Kelvin Probe Microscopy this property is exploited by applying a modulated bias voltage with frequency ω, measuring the response of the cantilever at this frequency using a Lock–In amplifier and then adjusting the value of V_{dc} using a feedback loop such that F_{ω} is minimized. The required V_{dc} then yields the desired difference in the work function. The description above is common for all Kelvin Probe Microscopy techniques, but these underlying principles can be implemented in AFM techniques in a variety of ways. The first major distinction is whether the Kelvin Probe measurement is performed simultaneously with the AFM topography measurement or that these two measurements are performed in rapid succession[20]. The latter method is performed by scanning each scan-line of the image twice in succession, the first time while measuring the topography, and the second time with the tip lifted a specific distance over the image, while tracking a contour of the topography and measuring the Contact Potential Difference. This so-called "lift"-mode is generally applied for ambient Kelvin Probe Microscopy measurements

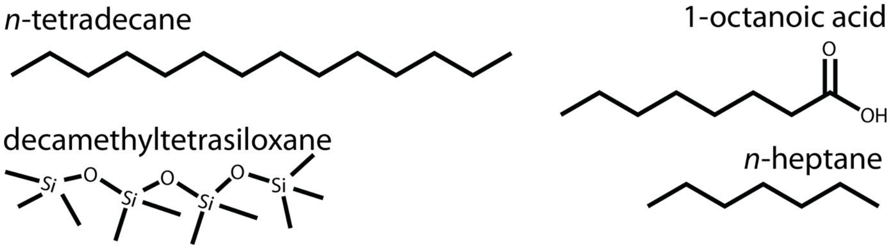

Figure 2.5: Molecular structures of the solvents used in the research described in this Thesis.

based on tm-AFM. In nc-AFM, the Kelvin Probe Measurement is generally performed simultaneous to the topography measurement. The applied bias voltage modulation frequency (ω) is chosen far away from the mechanical resonance frequency of the tip, such that the two oscillating signals do not interfere. In general, the response of the cantilever to the modulated bias voltage is measured by detecting the amplitude at the bias voltage modulation frequency. A disadvantage of this technique is that, since the cantilever should have a detectable mechanical response to the bias voltage modulation, implies that one generally has to use cantilevers with a rather low stiffness which leads to lower resolution topography images. To overcome this problem the Kelvin Probe Microscopy measurements performed in this research are based on a principle developed by Kitamura *et al.*[21]. Instead of measuring the amplitude of the cantilever at the modulation frequency, one measures the variation of the mechanical resonance frequency at the bias voltage modulation frequency. In the nc-AFM techniques in which the CPD measurements are performed simultaneously with the topography signal, in general local differences in contact potential are not only measured, but they are locally corrected for by adjusting the bias voltage such that the electrostatic interaction is cancelled. One therefore not only *measures* Φ at every point of the surface, but locally corrects for it and measure a clean topography signal.

2.2.4 Experimental environments

In this research, both STM and AFM have been applied in several different environments, ranging from Ultra High Vacuum (*i.e.* pressures lower than 10^{-6} mbar) to apolar solvents and aqueous electrolytes. Scanning Tunneling Microscopy can easily be applied in a wide variety of apolar solvents. The molecular structures and most relevant physical parameters of the solvents used in the research of this thesis are given in Figure 2.5 and Table 2.1, respectively. The main restrictions for choosing a

Table 2.1: Overview of selected physical properties of the solvents used in this Thesis.

Solvent	density (g/cm^3)	ϵ	mp (°C)	bp (°C)
1-octanoic acid	0.910	2.4	16.7	237
n-tetradecane	0.763	1.9	5.5	253
n-heptane	0.684	1.9	-90.6	98.4
decamethyltetrasiloxane	0.854	2.3	-68	194
water	1	80	0	100

suitable solvent are the low electrical conductivity to prevent any currents other than the one originating from the tunneling between the tip apex and the surface, and a low vapour pressure. The first requirement is to make sure we only measure the quantum mechanical tunneling current, and no electrochemical or polarizing currents due to electrochemical reactions or migrating ions, respectively. The second requirement is to prevent solvent evaporation, which would increase the concentration of solutes during the measurement and cause thermal drift by the decrease in temperature of the evaporating solvent. Finally some solvents are known to co-deposit on certain substrates[22]. This coadsorption can be used to guide the adsorption of molecules and to create different polymorphs[23], but is regarded as an undesired feature in this research.The main solvents used in this research are *n*-tetradecane (99+%, Aldrich), decamethyltetrasiloxane (97%, Aldrich) and 1-octanoic acid (98%, Aldrich). All solvents were used as received, unless otherwise stated. Aside from measurements performed at the solid/liquid interface, the monolayers described in this thesis have also been studied as *dry* layers under an ambient atmosphere and in UHV. For this purpose, monolayers were prepared by immersing a freshly cleaved HOPG sample in a *n*-heptanic solution of the molecule under investigation. The sample was typically left in this solution for 15-30 minutes, after which it was excessively rinsed with clean heptane, to prevent crystallisation and the formation of multilayers. Finally, the sample was dried in a gentle flow of nitrogen gas. Samples prepared as such could be imaged under an ambient atmosphere using STM and tm-AFM and in UHV using STM, nc-AFM and SKFM.

2.3 Porphyrins

A porphyrin is a heterocyclic macrocyclic tetrapyrrole: it consists of four pyrrole rings that are linked to form a larger ring structure. Tetrapyrroles, including porphyrins, can be found in a myriad of proteins where they act as cofactors[24], and perform a wide range of different functions. The general structure of a porphyrin is depicted in Figure 2.6a. The four pyrrole rings (one of them is encircled) are connected to each other *via* methine bridges at their α-carbon atoms. The carbon atom in this bridge is referred to as the *meso* carbon atom. The nitrogen atoms point inwards and together form a ligand that can bind virtually any transition metal ion (M) in its center. The heme–group (Figure 2.6a), a cofactor for the hemoglobin and myoglobin proteins, is an iron-containing porphyrin. In these proteins this porphyrin is responsible for the binding, transport and release of oxygen in animals and humans. The same iron-porphyrin is also part of the protein cytochrome P450, which is a monooxygenase, and its function is to insert a single oxygen atom from molecular oxygen into a variety of organic substrates[25]. The application of the same iron-porphyrin derivative for two such distinct functionalities nicely exemplifies the versatility of metallo-porphyrins. When the central metal ion is replaced by another transition metal, the range of functionalities of tetrapyrrolic macrocycles can be even further expanded. An example from biology is chlorophyll-b . This magnesium-containing macrocycle, depicted in Figure 2.6, is an element of the light harvesting complex of green plants in which sunlight is adsorbed as a first step towards converting this light into chemically stored energy[24]. Porphyrins are stable molecules and the size of the gap between their highest occupied molecular orbital (HOMO) and their lowest unoccupied molecular orbital (LUMO) makes that they strongly absorb light in the visible region, thereby giving them an intense color[26,27]. Because of this property porphyrins are used as dyes in a variety of paints and inks. Porphyrins have rich electrochemical behavior[28,29], several oxidations and reductions can occur on the porphyrin itself and, depending on the central metal, additional redox states are available on the metallo-center. Again depending on the central metal atom, a variety of axial ligands can bind to porphyrins. The affinity of zinc porphyrins for nitrogen ligands is, for instance, widely used to create supramolecular assemblies[30]. Porphyrins with metallo-centers that can attain more than one oxidation state are often catalytically active. Manganese and chromium porphyrins, for instance, catalyze the epoxidation of alkenes[31–33], while cobalt porphyrins are electrocatalysts for the reduction of water to hydrogen gas[34]. Because of these interesting physical and chemical properties, porphyrins have been extensively investigated for use in applications ranging from organic semiconductors[35–37,26]and light emitting diodes[38] to sensors[39] and catalysts[40–43]. The porphyrins used in the research described in this thesis are functionalized with an undecyl tail at each of the four *meso*-positions. Such alkyl chains are known to facilitate the binding of molecules on graphite surfaces[44]. These 5,10,15,20-tetraundecylporphyrins were kindly supplied by Prof. Dr. Maxwell J. Crossley of the University of Sydney and the synthesis and characterization has been recently published[45].

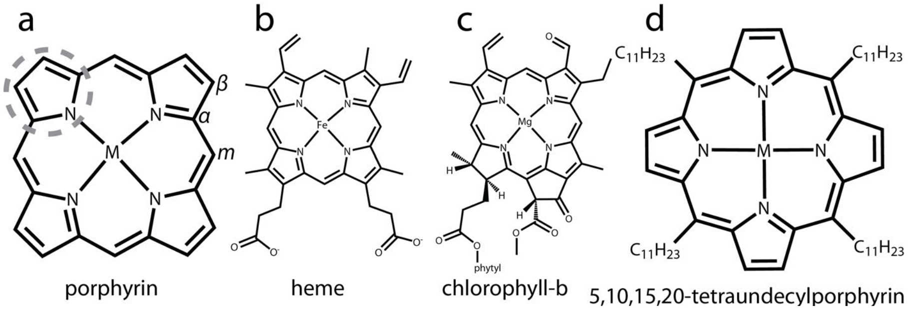

Figure 2.6: Molecular structure of a porphyrin macrocycle (a). This heterocycle constists of four pyrrole rings (encircled) that are attached to each other via methine bridges. The carbon atoms of the macrocycle are named α, β and *meso* (m). The central metal atom M, can be virtually any transition metal atom. Two occurences of porphyrins in biological systems, heme (b) and chlorophyll-b (c) are depicted, as well as the alkyl-functionalized porphyrin used in this research (d).

2.4 Graphite

Graphite is one of the allotropes of carbon[46]. Besides the 3-dimensional bulk materials graphite and diamond, carbon can also form individual 2-dimensional layers called graphene[47] sheets, 1-dimensional nanotubes[48], and *quasi* 0-dimensional buckyballs[49] These forms of carbon are very promising for the creation of novel nano-electronic materials[50], and given the high degree of similarity between their structures and that of graphite, graphite presents an interesting platform to study the adsorption of molecules to this class of materials. The crystal structure of graphite consists of sheets in which the carbon atoms are arranged in a hexagonal lattice with two carbon atoms per unit cell as is shown in Figure 2.7. These carbon atoms are all in sp^2 hybridized orbitals, and form strong covalent bonds between each other within the individual sheets. The sheets themselves are only connected by the much weaker Van der Waals and $\pi - \pi$ interactions. The distance between neighbouring carbon atoms within each of the planar sheets is 142 pm, and the distance between the sheets is 335 pm[51].The sheets are arranged in an alternating "ABAB" stacking pattern, as has been sketched in Figures 2.7a and b. The sheets are shifted such that two types of atoms exist at the graphite surface. The atoms labeled "α" in Figure 2.7b, are positioned exactly above a carbon atom in the next graphite layer, while the atoms labelled "β" are above the center of a hexagon in the next layer, and therefore not directly above another carbon atom. The inequivalence of the two types of atoms is reflected by the fact that often only the β atoms are visible in STM images as a result of a complex interplay between mechanical and electronic effects[52,53]. A typical STM image of a highly ori-

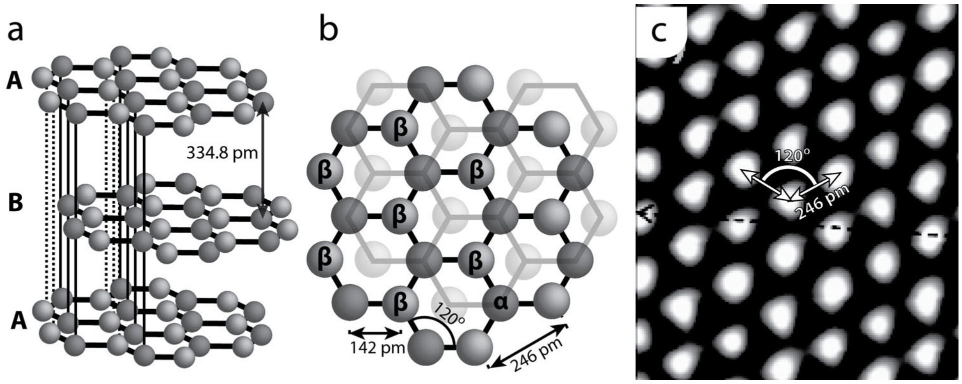

Figure 2.7: The crystal structure of graphite. (a) 3-Dimensional structure of the alternating stacked sheets of hexagonal graphene sheets with the interlayer distance indicated. (b) Top view of a single sheet, which is the surface structure on which the self–assembled monolayers, described in this thesis, form. (c) Typical literature example from Khara *et al.*[52] of an STM image of an HOPG surface. V_{bias} = -70 mV, I_{set} = 200 pA.

ented pyrolytic graphite (HOPG) surface taken from literature, is depicted in Figure 2.7c. The protrusions of the β atoms are spaced at 246 pm, at angles of 120°. The most commonly used type of graphite used in STM experiments, and the one that is also used throughout this thesis, is HOPG because of its high degree of crystallinity and the low spread in the orientation of the different polycrystalline grains of the material. For all STM experiments described in this thesis, commercially available HOPG samples (NT-MDT, ZYB) have been used. Because the layers of graphite are merely bound together by weak Van der Waals interactions, and the individual layers within each HOPG sample are oriented nearly parallel, they can be easily separated by cleaving using adhesive tape, leaving an atomically flat, clean and chemically inert surface, making it an ideal substrate for ambient STM studies. The recent discovery of graphene, a single sheet of graphite, might open some interesting possibilities to transfer the extensive knowledge acquired on monolayers on graphite, to which this thesis aims to contribute, to industrial applications. It has been demonstrated that graphene can be incorporated within the current framework of top-down nanofabrication[54,55]. The interactions between adsorbed molecules and graphene should to a large extend be similar to those with graphite, since they are governed by dispersive forces such as Van der Waals and π-π interactions. Several molecules, such as perylene-3,4,9,10-tetracarboxylic dianhydride(PTCDA)[56], pentacene and C60[57], have been shown to form self-assembled monolayers on graphene layers in UHV.

2.4.1 Graphite unit cell vectors

The unit cell vectors of molecular overlayers are conventionally described in terms of the unit cell vectors of the underlying substrate. The unit cell vectors of the graphite (0001) surface will be referred to as $\mathbf{g}_1$ and $\mathbf{g}_2$ throughout this thesis, and they are drawn in Figure 2.8. These vectors coincide with the 3–index Miller vectors [100] and [010], respectively. In this system the [001] direction is normal to the honeycomb planes. These 3–index Miller vectors are not commonly used to describe hexagonal lattices, such as graphite. The $\mathbf{g}_3$ vector would be written as $[\bar{1}\bar{1}0]$ and its crystallographic equivalence to the [100] and [010] directions is not immediately apparent in this description. This apparent asymmetry can be solved by using the 4–index Miller-Bravais system[58]. In this system, three indices are used to describe a honeycomb plane. Since this plane was already completely defined by two Miller indices, the third vector is not independent from the other two. If the Miller indices are given by $[uvw]$, the Miller-Bravais indices $[UVTW]$ are given by:

$$\begin{aligned} U &= 2u - v \\ V &= 2v - u \\ T &= -u - v \\ W &= w \end{aligned} \tag{2.7}$$

which are then converted to the set having the smallest possible integer coefficients. The indices of the graphite directions are shown in Figure 2.8b. The vectors $\mathbf{g}_1$, $\mathbf{g}_2$ and $\mathbf{g}_3$ are now written as $[2\bar{1}\bar{1}0]$, $[\bar{1}2\bar{1}0]$ and $[\bar{1}\bar{1}20]$, respectively, and their equivalence is now much clearer. The vector normal to the honeycomb plane is the [0001] direction, which makes this the (0001) plane. Throughout this thesis only two vectors ($\mathbf{g}_1$ and $\mathbf{g}_2$) will be used to describe the unit cell vectors of the molecular overlayer, but for comparison to literature some directions will also be given in the four–index notation.

2.5 The structure of self-assembled monolayers

The research described in this thesis focusses on the study of porphyrin monolayers on graphite surfaces. These monolayers are highly ordered structures that form via a processes called self-assembly: through an interplay of intermolecular forces and forces between the molecules and the graphite substrate, the molecules assemble into large 2-dimensional periodic structures without any external guidance or interference. The porphyrin molecules described in this thesis form physisorbed layers on graphite. These layers are characterized by weak, non-covalent, interactions between the molecules in the overlayer and the underlying substrate. This is in contrast to, for instance, monolayers formed by thiols on gold surfaces[59], which are chemisorbed,

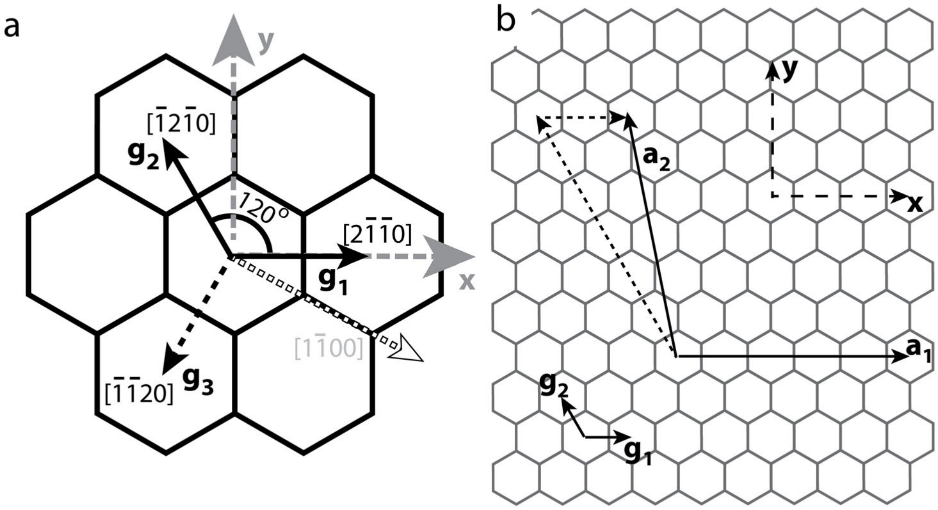

Figure 2.8: Definition of the graphite lattice unit cell vectors (a). $\mathbf{g_1}$ and $\mathbf{g_2}$ indicate the two graphite unit vectors used to characterized the adlayers in this thesis, which span a right-handed coordinate system. The third equivalent vector $\mathbf{g_3}$ is also depicted. The relationship between the used vectors and the four-coordinate Miller-Bravais indices is also sketched for comparison to literature. In (b) an example is given how to describe the unit cell vectors of a molecular overlayer ($\mathbf{a_1}$, $\mathbf{a_2}$) in terms of the graphite coordinates. An x,y-coordinate system is defined to transform vectors in graphite coordinates to real-space coordinates so their angles and lengths can be determined.

and strong, covalent, Au–S bonds exist between the thiol groups and the gold surface. The same strong bonding type can be found for silane derivatives on a variety of silicon-based substrates[60,61]. The unit cell vectors of the porphyrin monolayers in this thesis have been determined and will be described in terms of the unit cell vectors of the underlying HOPG substrate surface. There are two main reasons to express the unit cell vectors in terms of the vectors of the underlying substrate. The first is that the substrate is used as an internal calibration grid during the STM measurements. During an STM measurement of a molecular monolayer, it is possible to image the atomic corrugation of the underlying substrate surface in the same image as the molecular overlayer, by varying the distance between the tip and sample. By increasing the tunneling current setpoint or lowering the applied bias voltage the tip comes closer to the sample surface and the atomic corrugation of the substrate surface can be measured even when a molecular monolayer is present. The lattice constants of the substrate surface are known with high precision from diffraction experiments. The unit cell vectors of the overlayer can then be determined in terms of these known

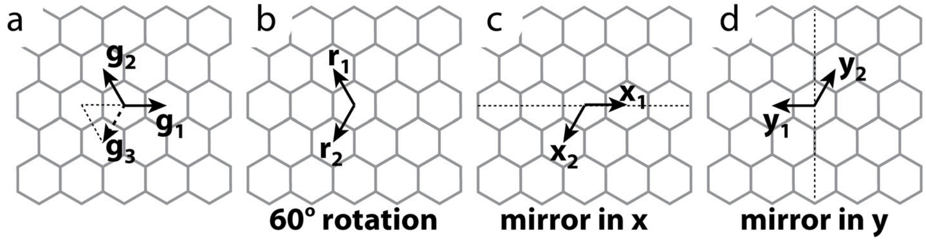

Figure 2.9: Overview of the results of a 60° rotation (b), mirroring in the x-axis (c) and the y-axis (d) on the graphite unit cell vectors $\mathbf{g_1}$ and $\mathbf{g_2}$ as drawn in (a)

dimensions. When the image is distorted, for instance due to thermal drift, the atomic calibration grid is distorted in the same way as the molecular overlayer. The unit cell vectors of the monolayer described in terms of the underlying substrate are therefore unaffected, even though in the real-space STM image the vectors seem distorted. The second reason, which will be discussed in more detail in Section 2.5.3, is that the coefficients of the vectors numbers give valuable information about the interactions between the molecules and the surface.

2.5.1 Unit cell vectors

The unit cell vectors of the monolayers will be described in terms of the $\mathbf{g}_1$ and $\mathbf{g}_2$ unit cell vectors. An example of this is given in Figure 2.9a. The two overlayer vectors $\mathbf{a}_1$ and $\mathbf{a}_2$ are, in terms of $\mathbf{g}_1$ and $\mathbf{g}_2$ given by:

$$\mathbf{a}_1 = 5\mathbf{g}_1 \quad \text{and} \quad \mathbf{a}_2 = 2\mathbf{g}_1 + 6\mathbf{g}_2 \tag{2.8}$$

We will write these vectors in column vector form:

$$\mathbf{a}_1 = \begin{pmatrix} 5 \\ 0 \end{pmatrix} \quad \text{and} \quad \mathbf{a}_2 = \begin{pmatrix} 2 \\ 6 \end{pmatrix} \tag{2.9}$$

In general, unit cell vectors $\mathbf{v}_1$ and $\mathbf{v}_2$ can thus be written on the $\mathbf{g}_1$, $\mathbf{g}_2$ basis as:

$$\mathbf{v}_1 = \begin{pmatrix} v_{11} \\ v_{12} \end{pmatrix} \quad \text{and} \quad \mathbf{v}_2 = \begin{pmatrix} v_{21} \\ v_{22} \end{pmatrix} \tag{2.10}$$

It is important to note that v_{11},v_{12},v_{21} and v_{22} are not necessarily integers. The difference between integer and non-integer values is more extensively discussed in Section 2.5.3. Figure 2.9a shows that the $\mathbf{g}_3$ vector, which is crystallographically equivalent to $\mathbf{g}_1$ and $\mathbf{g}_2$, is given by:

$$\mathbf{g}_3 = \begin{pmatrix} -1 \\ -1 \end{pmatrix} \tag{2.11}$$

Figures 2.9b—d show the effect of symmetry operations on the graphite unit cell vectors. The effect of a 60° rotation, R_{60} maps $\mathbf{g}_1$ and $\mathbf{g}_2$ on $\mathbf{r}_1$ and $\mathbf{r}_2$ respectively. These vectors are given by:

$$\mathbf{r}_1 = \begin{pmatrix} 1 \\ 1 \end{pmatrix} \quad \text{and} \quad \mathbf{r}_2 = \begin{pmatrix} -1 \\ 0 \end{pmatrix} \tag{2.12}$$

so that the matrix representation of a 60° rotation on the graphite basis is given by

$$\mathbf{R_{60}} = \begin{pmatrix} 1 & -1 \\ 1 & 0 \end{pmatrix} \tag{2.13}$$

Equivalently, mirroring in the x– and y–axis can be expressed by

$$\mathbf{M_x} = \begin{pmatrix} 1 & -1 \\ 0 & -1 \end{pmatrix} \quad \text{and} \quad \mathbf{M_y} = \begin{pmatrix} 1 & -1 \\ 1 & 0 \end{pmatrix} \tag{2.14}$$

If a unit cell vector $\mathbf{v}$ is expressed in terms of $\mathbf{g}_1$ and $\mathbf{g}_2$, one can easily find its symmetry equivalent and, for chiral monolayers, their enantiomeric counterparts by multiplication by a combination of the matrices of equations 2.13 and 2.14. The above vectors and matrices express overlayer vectors in terms of the underlying substrate. It is also useful to express the lengths of the unit cells and the angle between them in euclidean, x and y, coordinates. The transformation from graphite to x, y–coordinates is given by:

$$\mathbf{E} = \begin{pmatrix} \mathbf{e}_1 & \mathbf{e}_2 \end{pmatrix} = G \begin{pmatrix} 1 & -\frac{1}{2} \\ 0 & \frac{\sqrt{3}}{2} \end{pmatrix} \tag{2.15}$$

where $\mathbf{e}_1$ and $\mathbf{e}_2$ are column vectors containing the x, y–coordinates of $\mathbf{g}_1$ and $\mathbf{g}_2$ and in which G is the graphite lattice constant of 246 pm.

2.5.2 Unit cell matrices

Throughout this thesis, the unit cell vectors of the molecular adlayers will be expressed in terms of column vectors on a basis spanned by $\mathbf{g}_1$ and $\mathbf{g}_2$. To emphasize the fact that these vectors span a 2–dimensional unit cell and belong together, one can concatenate these vectors in a matrix:

$$\mathbf{V} = \begin{pmatrix} v_{11} & v_{21} \\ v_{12} & v_{22} \end{pmatrix} \tag{2.16}$$

where v_{nm} are components as defined in equation 2.10. $\mathbf{V}$ is then transformed to real-space coordinates by multiplying by $\mathbf{E}$:

$$\mathbf{B} = \mathbf{EV} \tag{2.17}$$

or equivalently:

$$\begin{pmatrix}\mathbf{b}_1 & \mathbf{b}_2\end{pmatrix} = \begin{pmatrix}\mathbf{e}_1 & \mathbf{e}_2\end{pmatrix}\begin{pmatrix}v_{11} & v_{21} \\ v_{12} & v_{22}\end{pmatrix} \tag{2.18}$$

Applying the following property of the transpose of matrices:

$$(\mathbf{AB})^T = \mathbf{B}^T\mathbf{A}^T \tag{2.19}$$

It is deduced that:

$$\mathbf{B}^T = \mathbf{V}^T\mathbf{E}^T \tag{2.20}$$

which leads to:

$$\begin{pmatrix}\mathbf{b}_1{}^T \\ \mathbf{b}_2{}^T\end{pmatrix} = \begin{pmatrix}v_{11} & v_{12} \\ v_{21} & v_{22}\end{pmatrix}\begin{pmatrix}\mathbf{e}_1{}^T \\ \mathbf{e}_2{}^T\end{pmatrix} \tag{2.21}$$

so that the *rows* of the "v"-matrix are the unit cell vectors on the graphite basis and the other two matrices are also built up from *row* vectors. The relationship in equation 2.21 is the common[62–64], and IUPAC recommended[65], method to describe unit cells in the field of surface science. The symmetry relationships shown before can also be used in this system when one takes the property of equation 2.19 into account.

2.5.3 Commensurism

The structure of a self-assembled monolayer on a solid surface is determined by a balance between interactions between the molecules within the layer (E_{intra}) and interactions between the monolayer and the substrate (E_{inter})[66,67]. This balance can lead to different types of epitaxial relations between the monolayer and the substrate. In Figure 2.10 the difference between commensurate, coincident and incommensurate adlayer structures is explained. First, consider a free floating molecular monolayer, confined to two dimensions but without any surface in its vicinity. This monolayer may be difficult to realize in practice, but in theoretical calculations it should be accessible. In such a monolayer, the molecules will form a lattice in which the lattice constants are purely defined by interactions between the molecules. The sketched example is a one-dimensional monolayer to simplify the explanation, but the same reasoning would apply in a two-dimensional system. The single unit cell vector of the free floating one-dimensional molecular monolayer is referred to as $\mathbf{m}$. When a monolayer of these molecules is allowed to form on a solid substrate, three different types of epitaxial relationships between the two are possible. When the atomic corrugation is very weak, by which it is here meant that the interaction between the molecules (E_{intra}) is much stronger than the local variation of the interaction of the molecules with the substrate (E_{inter}), the monolayer will be completely unaffected by the atomic corrugation of the surface. The lattice constant of the monolayer ($\mathbf{a}$) is the same as it would be for the free floating monolayer ($\mathbf{m}$) and is not altered by the lattice

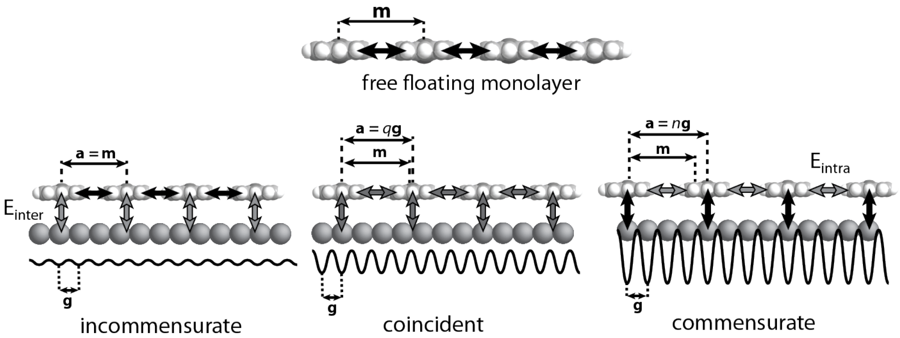

Figure 2.10: Explanation of the three different epitaxial relationships a self-assembled monolayer can have with the surface of the substrate. In an incommensurate layer the distances between the molecules in the layer are completely governed by the interactions between the molecules within the layer (E_{intra}). In commensurate layers the interaction between the surface and the molecules (E_{inter}) dictates the adlayer structures, as is apparent from the fact that each molecule is adsorbed at the same point within the substrate unit cell. Coincident layers present the intermediate case between these two extremes. The balance between E_{intra} and E_{inter} is such that the influence of the substrate on the monolayer is significant but not strong enough to enforce commensurism.

constant of the underlying surface ($\mathbf{g}$). In this case, the layer is incommensurate to the underlying substrate. In the complete opposite, commensurate, case, when the atomic corrugation of the surface is very strong, each molecule will preferably adsorb at the same energetic minimum of the energy landscape. Therefore commensurism is also referred to as point-on-point epitaxy. The lattice constants of the monolayer ($\mathbf{a}$) are then completely governed by the substrate lattice vectors and one will find that the unit cell vectors of the monolayers are integer multiples of the unit cell vectors of the substrate:

$$\mathbf{a} = n * \mathbf{g} \quad \text{with} \quad n \in \mathbb{Z} \tag{2.22}$$

Many molecular monolayers formed on metallic surfaces are commensurate. In such systems the molecule–substrate interaction is strong and stiff compared to the molecule–molecule interaction and this therefore leads to the formation of commensurate layers[64]. Between these two extreme scenarios is the coincident epitaxial mode. The interaction between the molecules and the substrate is not strong enough to enforce commensurism, but strong enough to influence the structure of the monolayer. Mathematically, the unit cell vector of the overlayer is a non-integer but rational multiple of the underlying substrate unit cell vector:

$$\mathbf{a} = q * \mathbf{g} \quad \text{with} \quad q \in \mathbb{Q} \wedge q \notin \mathbb{Z} \tag{2.23}$$

In the example in Figure 2.10 the coincident overlayer has a lattice constant $\mathbf{a} = \frac{7}{2}\mathbf{g}$. Which implies that the overlayer and the substrate have a superstructure with a periodicity of 2 overlayer unit cell vectors or 7 substrate unit cell vectors. In 2-dimensional coincident monolayers, the symmetry elements of the substrate are also reflected in the self-assembled monolayer: domains with the same overlayer structure can be found along all symmetry equivalent axes of the underlying substrate. Fritz *et al.* further subdivided different forms of coincidence in point-on-line, geometrical[66] and line-on-line[68] coincidence, and these distinctions differentiate how integer and non-integer coefficients are distributed over the matrix $\mathbf{V}$ (eq. 2.21) in 2-dimensional monolayers. Such a distinction is not made in this thesis. The most important information for the work presented here is whether the substrate–molecule interaction is such that it enforces commensurism or not, since this yields information on whether the interaction between the monolayer and the substrate or the interaction between the molecules within the monolayer contributes most to the structure of the molecular monolayer. To be able to make the distinction between these different types of epitaxy, using distance measurements obtained from STM images requires very high precision. Fortunately, the superstructures formed by coincident monolayers layers can in many cases directly be observed in STM images. The fact that adjacent molecules are adsorbed at slightly different locations within the unit cell of the substrate affects the electronic coupling between the two, and thereby the tunneling probability. In STM images, the superstructures caused by non-commensurate monolayers are therefore visible as an additional topographic feature called a Moiré pattern. An example of such a Moiré pattern is shown in Figure 2.11a, which depicts a self-assembled monolayer of stearic acid on HOPG[69]. Besides the atomically resolved stearic acid molecules, a periodic structure with a periodicity of several molecules can be observed (white arrows). From this Moiré pattern it can immediately be deduced, without the need for high precision distance measurements, that the molecular overlayer is not commensurate to the underlying substrate. HOPG itself can also display Moiré pattern, an example of which is depicted in Figure 2.11b. Besides the atomically resolved HOPG surface, a much larger hexagonal structure can be observed. This structure is caused by a slight rotation of the top-most graphite sheet with respect to the directly underlying layer. This rotation causes a spatial variation in the electronic coupling between the two layers and therefore a spatial variation in tunneling current[70]. The occurrence of Moiré patterns and the lack of commensurism that can be deduced from this, thus contains important information about the delicate balance between interactions between **CuP** molecules within the monolayer and interactions between the substrate and the monolayer. The occurrence of such superstructures in STM will therefore be used to identify the importance of different interactions in the monolayer structures that are topic of this thesis.

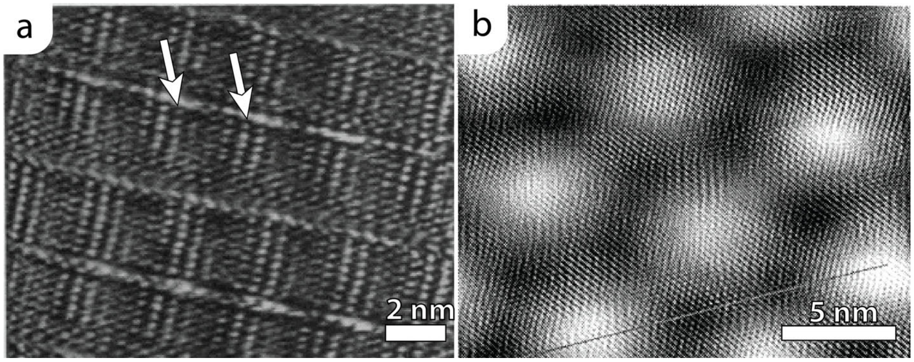

Figure 2.11: STM image of stearic acid at the HOPG/1-phenyloctane interface, as reported by Rabe and co-workers[69]. A periodic structure with a periodicity of several molecules can be observed in the apparent height of the overlayer. This superstructure (indicated by the two arrows) is ascribed to a mismatch in the periodicity of the molecular overlayer and the underlying substrate. The graphite surface itself can also display such a periodic superstructure, as is shown in (b)[70].

References

1. Bai C. *Scanning tunneling microscopy and its applications.* Springer, second, revised edition, **1992**
2. Rugar D., Mamin H.J., Guethner P., Lambert S.E., Stern J.E., McFadyen I. and Yogi T. *J. Appl. Phys.*, 68 (3):1169–1183, **1990**
3. Saenz J.J., Garcia N., Grutter P., Meyer E., Heinzelmann H., Wiesendanger R., Rosenthaler L., Hidber H.R. and Guntherodt H.J. *J. Appl. Phys.*, 62 (10):4293–4295, **1987**
4. Durig U., Pohl D.W. and Rohner F. *J. Appl. Phys.*, 59 (10):3318 –3327, **1986**
5. Pohl D.W., Fischer U.C. and Durig U.T. *J. Microsc.*, 152:853–861, **1988**
6. Eigler D.M. and Schweizer E.K. *Nature*, 334:524–526, **1990**
7. Florin E.L., Moy V.T. and Gaub H.E. *Science*, 264:415–417, **1994**
8. Hulsken B., Van Hameren R., Gerritsen J.W., Khoury T., Thordarson P., Crossley M.J., Rowan A.E., Nolte R.J.M., Elemans J.A.A.W. and Speller S. *Nat. Nanotech.*, 2 (5):285–289, **2007**
9. Binnig G. and Rohrer H. *Helv. Phys. Acta*, 55:726–735, **1982**
10. Gerritsen J.W., Boon E.J.G., Janssens G. and van Kempen H. *Appl. Phys. A: Mater. Sci. Proc.*, **1998**
11. Hulsken B. *STM in Liquids.* Ph.D. thesis, **2008**
12. Binnig G., Quate C. and Gerber C. *Phys. Rev. Lett.*, 56 (9):930–933, **1986**
13. Giessibl F.J. *Rev. Mod. Phys.*, 75:949–983, **2003**
14. Albrecht T.R., Grutter P., Horne D. and Rugar D. *J. Appl. Phys.*, 69 (2):668–673, **1991**
15. Allers W., Schwarz A., Schwarz U.D. and Wiesendanger R. *Europhys. Lett.*, 48 (3):276, **1999**
16. Fujii S. and Fujihira M. *Nanotechnology*, 17 (7):S112, **2006**
17. Pfeiffer O., Gnecco E., Zimmerli L., Maier S., Meyer E., Nony L., Bennewitz R., Diederich F., Fang H. and Bonifazi D. *J. Phys.: Conf. Ser.*, 19 (1):166, **2005**
18. Palermo V., Palma M. and Samorí P. *Adv. Mater.*, 18 (2):145–164, **2006**

19. Nonnenmacher M., O'Boyle M.P. and Wickramasinghe H.K. *J. Appl. Phys.*, 58 (25):2921–2923, **1991**

20. Liscio A., Palermo V., Gentilini D., Nolde F., Müllen K. and Samorí P. *Adv. Func. Mater.*, 16 (11):1407–1416, **2006**

21. Kitamura S. and Iwatsuki M. *Appl. Phys. Lett.*, 72 (24):3154–3156, **1998**

22. Hulsken B., Elemans J.A.A.W., Gerritsen J.W., Khoury T., Crossley M.J., Rowan A.E., Nolte R.J.M. and Speller S. *New J. Phys.*, 11, **2009**

23. Lackinger M., Griessl S., Heckl W.M., Hietschold M. and Flynn G.W. *Langmuir*, 21 (11):4984–4988, **2005**

24. Shelnutt J.A., Song X.Z., Ma J.G., Jia S.L., Jentzen W. and Medforth J.C. *Chem. Soc. Rev.*, 27 (1):31–42, **1998**

25. Feiters M.C., Rowan A.E. and Nolte R.J.M. *Chem. Soc. Rev.*, 29 (375-384), **2000**

26. Jurow M., Schuckman A.E., Batteas J.D. and Drain C.M. *Coord. Chem. Rev.*, 254 (19-20):2297–2310, **2010**

27. Senge M.O., Fazekas M., Notaras E.G.A., Blau W.J., Zawadzka M., Locos O.B. and Ni Mhuircheartaigh E.M. *Adv. Mater.*, 19 (19):2737–2774, **2007**

28. Fuhrhop J.H., Kadish K.M. and Davis D.G. *J. Am. Chem. Soc.*, 95 (16):5140–5147, **1973**

29. Liao M.S. and Scheiner S. *J. Chem. Phys.*, 117 (1):205–219, **2002**

30. Beletskaya I., Tyurin V.S., Tsivadze A.Y., Guilard R. and Stern C. *Chem. Rev.*, 109 (5):1659–1713, **2009**

31. Friedermann G.R., Halma M., Aparecida Dias de Freitas Castro K., Benedito Flávio L., Doro F.G., Drechsel M.S., Mangrich A.S., das Dores Assis M. and S. N. *Appl. Catal. A: General*, 308:172 – 181, **2006**

32. Jørgensen K.A. *Chem. Rev.*, 89 (3):431–458, **1989**

33. Traylor T.G. and Miksztal A.R. *J. Am. Chem. Soc.*, 111 (19):7443–7448, **1989**

34. Losse S., Vos J.G. and Rau S. *Coord. Chem. Rev.*, 254 (21-22):2492 – 2504, **2010**

35. Reid I., Zhang Y., Demasi A., Blueser A., Piper L., Downes J.E., Matsuura A., Hughes G. and Smith K.E. *Appl. Surf. Sci.*, 256 (3):720 – 725, **2009**

36. Ma P., Chen Y., Cai X., Wang H., Zhang Y., Gao Y. and Jiang J. *Synth. Met.*, 160 (5-6):510 – 515, **2010**

37. Checcoli P., Conte G., Salvatori S., Paolesse R., Bolognesi A., Berliocchi A., Brunetti F., D'Amico A., Di Carlo A. and Lugli P. *Synth. Met.*, 138 (1-2):261–266, **2003**

38. Kwong R.C., Sibley S., Dubovoy T., Baldo M., Forrest S.R. and Thompson M.E. *Chem. Mater.*, 11 (12):3709–3713, **1999**

39. Biesaga M., Pyrzyńska K. and Trojanowicz M. *Talanta*, 51 (2):209–224, **2000**

40. Yamazaki S., Senoh H. and Yasuda K. *Electrochem. Commun.*, 11 (6):1109 – 1112, **2009**

41. Curet-Arana M.C., Emberger G.A., Broadbelt L.J. and Snurr R.Q. *J. Mol. Catal. A: Chem.*, 285 (1-2):120 – 127, **2008**

42. Chung T.D. and Anson F.C. *J. Electroanal. Chem.*, 508 (1-2):115 – 122, **2001**

43. Yamazaki S., Yamada Y., Ioroi T., Fujiwara N., Siroma Z.Z., Yasuda K. and Miyazaki Y. *J. Electroanal. Chem.*, 576 (2):253 – 259, **2005**

44. Qiu X., Wang C., Yin S., Zeng Q., Xu B. and Bai C. *J. Phys. Chem. B*, 104 (15):3570–3574, **2000**

45. Kadish K.M., Ou Z., Zhan R., Khoury T. W.E. and Crossley M.J. *J. Porphyrins Phthalocyanines*, **2010**

46. Girifalco L.A., Hodak M. and Lee R.S. *Phys. Rev. B*, 62:13104–13110, **2000**

47. Novoselov K.S., Geim A.K., Morozov S.V., Jiang D., Zhang Y., Dubonos S.V., Grigorieva I.V. and Firsov A.A. *Science*, 306 (5696):666–669, **2004**

48. Ajayan P.M. *Chem. Rev.*, 99 (7):1787–1800, **1999**

49. Kroto H.W., Heath J.R., OBrien S.C., Curl R.F. and Smalley R.E. *Nature*, 318 (6042):162–163, **1985**

50. Delgado J.L., Herranz M.A. and Martin N. *J. Mater. Chem.*, 18:1417–1426, **2008**

51. Reynolds W.N. *Physical properties of graphite.* Elsevier Publishing Co. Ltd., **1968**

52. Khara G.S. and Choi J. *J.Phys.:Condens. Matter*, 21 (195402), **2009**

53. Atamny F., Spillecke O. and Schögl R. *Phys. Chem. Chem. Phys.*, 1:4113–4118, **1999**

54. Gu G., Nie S., Feenstra R.M., Devaty R.P., Choyke W.J., Chan W.K. and Kane M.G. *Appl. Phys. Lett.*, 90 (25), **2007**

55. Kedzierski J., Hsu P.L., Healey P., Wyatt P.W., Keast C.L., Sprinkle M., Berger C. and de Heer W.A. *IEEE Transactions on Electron Devices*, 55 (8):2078 –2085, **2008**

56. Wang Q.H. and Hersam M.C. *Nat. Chem.*, 1 (3):206–211, **2009**

57. Zhou H.T., Mao J.H., Li G., Wang Y.L., Feng X.L., Du S.X., Muellen K. and Gao H.J. *Appl. Phys. Lett.*, 99 (15), **2011**

58. Frank B.C. *Acta. Cryst.*, 18:862–866, **1965**

59. Ulman A. *Chem. Rev.*, 96 (4):1533–1554, **1996**

60. Haensch C., Hoeppener S. and Schubert U.S. *Chem. Soc. Rev.*, 39:2323–2334, **2010**

61. Wasserman S.R., Tao Y.T. and Whitesides G.M. *Langmuir*, 5 (4):1074–1087, **1989**

62. Merz L. and Ernst K.H. *Surf. Sci.*, 604 (11-12):1049 – 1054, **2010**

63. Park R.L. and Madden Jr. H. *Surf. Sci.*, 11 (2):188 – 202, **1968**

64. Barlow S.M. and Raval R. *Surf. Sci. Rep.*, 50 (6-8):201–341, **2003**

65. Bradshaw A.M. and Richardson N.V. *Pure Appl. Chem.*, 68 (2):457–467, **1996**

66. Hooks D.E., Fritz T. and Ward M.D. *Adv. Mater.*, 13 (4):227–241, **2001**

67. Last J.A., Hooks D.E., Hillier A.C. and Ward M.D. *J. Phys. Chem. B*, 103 (32):6723–6733, **1999**

68. Mannsfeld S., Leo K. and Fritz T. *Phys. Rev. Lett.*, 94:056104, **2005**

69. Rabe J.P. and Buchholz S. *Science*, 253 (5018):424–427, **1991**

70. Rong Z.Y. and Kuiper P. *Phys. Rev. B*, 48:17427–17431, **1993**

CHAPTER 3

The structure of tetraundecylporphyrin monolayers

3.1 Introduction

Because of their rich photo-physical[1,2], electronic[3] and chemical properties, porphyrins are very interesting molecules for use in a wide range of applications, for example as catalysts[1,4,5], chemical sensors[6], photosensitizers[7,8], light emitting diodes[9], photovoltaic cells[10] , molecular wires[11,12], transistors[13,14] and organic semiconductors[15]. In many cases a prerequisite for the effective application of porphyrins in an actual device is the self–organization of these molecules into ordered arrays on a solid support. Porphyrin–based assemblies have been used as a constituent of many self–organized materials both in solution[16] as on surfaces[1,12,17–20]. The arrangement of the molecules in self–assembled structures is governed by weak supramolecular interactions[18,21]. These interactions, such as Van der Waals (VdW) interactions, dipole–dipole interactions, π–π interactions, hydrogen bonding and the Coulomb forces between ions are much weaker than the covalent bonds between the atoms that constitute the porphyrin molecules. The weak nature of the interactions allows for the structure formation to be reversible and can be exploited for self-healing of damages to the layer[22]. Scanning tunneling microscopy (STM)[23] provides an excellent tool to study the structure of self–assembled monolayers on solid surfaces and many porphyrins have been investigated using this technique[17]. Studies range from those of simple porphyrins equipped with alkyl tails[24,25] or carboxylic acids[26], to those of more complex covalently linked networks[27], rings[28] and wheels[29] consisting of tens of porphyrins. Despite the numerous studies on the self–assembly of molecules on sur-

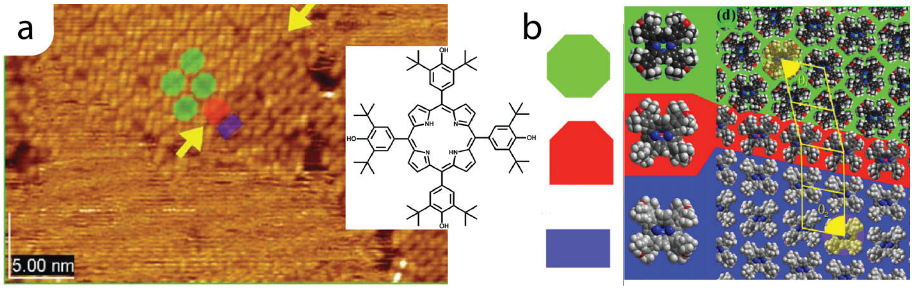

Figure 3.1: STM image of a self-assembled monolayer of 5,10,15,20-tetrakis(3,5-di-*t*-butylphenyl)porphyrin at the Cu(111) surface in UHV (a), its the molecular structure (inset) and a schematic representation of the hexagonal (green) and square (blue) polymorphs formed by this molecule at this surface and the molecules with a 'mixed' conformation (red) that are found at the border of the two polymorphs. Image parameters I_{set} = 80 pA, V_{bias} = +1.0 V, reproduced from Ariga *et al.*[37].

faces, the understanding of the relationship between the structure of a molecule and the structure of the monolayers it forms on a given surface is still rather limited. In order to use molecules as building blocks for functional devices, controlled bottom–up fabrication is of paramount importance[22,30]. One aspect of molecular self–assembly on surfaces which is receiving increasing attention, is 2–dimensional (2D) polymorphism: the ability of one compound, or combination of compounds[31–33], to form several different 2–dimensional surface structures. The existence of 2D-polymorphs of alkyl–functionalized dyes has been reported for small[34] and extended phthalocyanine derivatives[35], as well as for porphyrin–based macromolecules[36]. Not just the existence of the 2–D polymorphs themselves, but some interesting structural relationships between the polymorphs of a given molecule have also been reported. Ariga *et al.*[37] showed that 5,10,15,20-tetrakis(3,5-di-*t*-butylphenyl)porphyrin (inset Figure 3.1) can form polymorphs with hexagonal or square lattices when evaporated onto Cu(111) in ultra high vacuum (UHV) (Figure 3.1). They proposed that adsorbed molecules in the hexagonal polymorph (green) have a different molecular conformation than the porphyrins in the square polymorph (blue) and the difference between these conformations is in the rotation of the phenyl rings. At the border of domains of these two polymorphs, porphyrins can be found that are part of both these domains (red). These bordering porphyrins have a 'mixed' molecular conformation. Having the same molecular conformation as the porphyrins in the hexagonal polymorph on one side, and the molecular conformation as the porphyrins in the square lattice on the other side. These mixed conformations nicely explained the smooth connection between the hexagonal and square domains. The relationship between the molecular conformation and polymorphism that were reported by Ariga *et al.* shows that molecules can not only form several different 2–D polymorphs but that interesting structural relationships can exist between these different polymorphs. Such structural relationships between polymorphs will be discussed extensively in this Chapter, particularly because polymorphism might present opportunities to tune the physical and chemical properties of the adsorbate layers.

For several types of macrocycles it was shown that molecules in different 2D-polymorphs can exhibit different properties. Lei *et al.* showed that, depending on the concentration, alkoxylated dehydrobenzo[12]annulenes can form either a close–packed linear polymorph or a nanoporous network[32]. Such a network can be used to bind guest molecules[38] and the different polymorphs were found to induce different complexation behaviour of these guests. Burke *et al.* showed that the self–assembly into different polymorphs can affect the optoelectronic properties of 3,4,9,10-perylene tetracarboxylic dianhydride (PTCDA) molecules on a NaCl(001) substrate[39]. In etch pits, created in the NaCl surface, the PTCDA molecules were found to form a more densely packed p2×4 adlayer structure than on terraces (p3×3).The photoinduced shift of the local contact potential difference (CPD) between the probe and the surface, as measured with non-contact AFM (NC-AFM) and scanning Kelvin probe force microscopy (SKFM), was different for the two adlayer structures upon irradiation with different wavelengths of visible light. The optoelectronic properties of the monolayer were more bulk-like for the denser p2×4 structure and more monomer-like for the more weakly interacting p3×3 monolayers. These examples show that 2D-polymorphism can present interesting opportunities to create and modify functionality in self–assembled monolayers.

3.1.1 meso–5,10,15,20-tetraundecylporphyrin

In this chapter the 2–dimensional polymorphism of simple, symmetric alkyl–functionalized porphyrins on the HOPG/organic solvent interface will be discussed. This highly symmetric porphyrin derivative, provides a good starting point for such studies as the alkyl tails are chemically and electrochemically inert and therefore do not complicate the study of the very rich physical and chemical properties of the porphyrin ring itself. After the behaviour of these simple porphyrins is understood, these studies can of course be expanded to more complicated structures such as tetraphenyl porphyrins (TPP), or porphyrins with asymmetric functionalization of the porphyrin ring. The general structure of the molecule studied in this thesis, *meso*–5,10,15,20-tetraundecylporphyrin, is shown in Figure 3.2. The actual porphyrin is the organic ring drawn in black. Because the π–electrons in the alternating double bonds are delocalized over the entire ring, the molecule has a disk–like, almost flat shape. The porphyrin is equipped with four $C_{11}H_{23}$ saturated alkyl chains (blue). The strong Van der Waals interactions of these tails with the graphite facilitates adsorption of these molecules on the surface[17,40]. The **M** in the center of the porphyrin ring de-

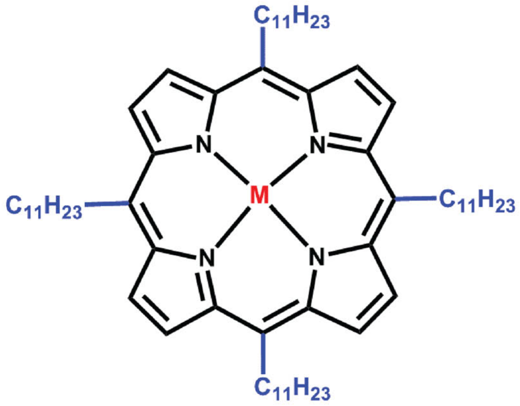

Figure 3.2: Molecular structure of *meso*–5,10,15,20-tetraundecylporphyrin. The actual porphyrin is the cyclic, aromatic part drawn in black. It can coordinate two protons (M = 2 H) or a variety of metal ions (M = Ni, Cu, Zn, Pt, Mn, ...). To facilitate binding to graphite substrates, the porphyrin is equipped with four $C_{11}H_{23}$ tails indicated in blue. Throughout this thesis this molecule will simply be referred to as **MP**, substituting M with the metal under discussion.

notes a metal ion coordinated to the porphyrin by the four nitrogen atoms of the pyrrole groups. One of the most interesting properties of porphyrins is that **M** can be virtually any transition metal atom (*e.g.* Ni, Cu, Zn, Mn, Pt, Mg, Fe, Co), and the physical and chemical properties of the molecules strongly depend on the metal center. Zinc porphyrins have a strong affinity for nitrogen ligands that bind axially to the metal center, making them a commonly used building block in supramolecular metal–ligand complexes[16,41]. Manganese[4,42,43] and cobalt[44–46] porphyrins are versatile catalysts, whereas platinum porphyrins are used in organic light emitting diodes[9]. These different metal centers are inserted in the final steps of the organic synthesis, making porphyrins very convenient for the creation of structurally similar, but functionally different molecules. In this chapter, the organic part of the molecules, *i.e.* the porphyrin macrocycle and the alkyl chains, is always the same and we will refer to the molecules simply as **MP**, replacing **M** with the specific metal under discussion. Besides transition metals, the porphyrin center can also be occupied by two hydrogen atoms. This, so called, free base porphyrin will be denoted **2HP**. Several STM studies have been performed on monolayers of similar *meso*–tetra–alkylporphyrins. Chin *et al.*[47] have reported a detailed study on self–assembled monolayers formed by *meso*–5,10,15,20-tetranonadecylporphyrin ($C_{19}H_{39}$ alkyl chains) on the graphite surface, while the adlayer structure of *meso*–5,10,15,20-tetradodecylporphyrin ($C_{12}H_{25}$

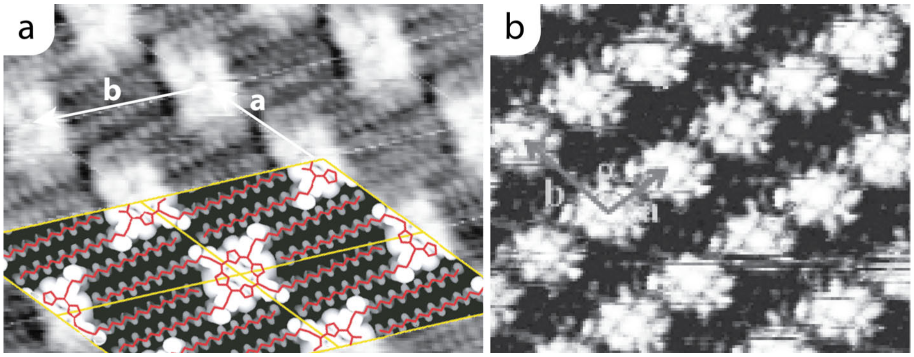

Figure 3.3: Reported STM images of *meso*–5,10,15,20-tetranonadecylporphyrin ($C_{19}H_{39}$ alkyl tails, free base) at the HOPG/1–phenyloctane interface[47] (a) and of *meso*–5,10,15,20-tetradodecylporphyrin ($C_{12}H_{25}$ alkyl tails, free base) at the HOPG/n–tetradecane interface[48] (b). The unit cell vectors of the structure in image (a) are $\mathbf{a} = 2.17 \pm 0.05$ nm and $\mathbf{b} = 3.38 \pm 0.06$ nm at an angle of $49.4 \pm 1.8°$. The inset displays the calculated (DFT) molecular structure of the monolayer, the tails are kinked to align to the underlying HOPG lattice. The porphyrin plus the kinked region of the tails appear much brighter than the extended parts of the tails. The unit cell vectors of the adlayer in image (b) are $\mathbf{a} = 1.4 \pm 0.1$nm and $\mathbf{a} = 1.9 \pm 0.2$nm at an angle of $80 \pm 6°$. Image parameters:V_{bias}=-683 mV, I_{set} =8 pA (a) and V_{bias}=-355 mV, I_{set} =17 pA (b).

alkyl chains) has been reported by Visser *et al.*[48]. Part of their results are shown in Figure 3.3. Both these studies make no report of polymorphism.

The surface structures formed by **MP** on HOPG, reported in this Chapter, have been studied using a home-built STM[49] capable of imaging surfaces under ambient conditions at the solid/liquid interface. Atomically sharp $Pt_{0.8}$-$Ir_{0.2}$ tips were mechanically cut using nail scissors. The HOPG samples were cleaned in toluene and subsequently cleaved using adhesive tape prior to use. All used solvents (toluene, 1–octanoic acid, *n*-tetradecane and decamethyltetrasiloxane) were used as received. STM images were recorded after a small droplet of the porphyrin-containing solution was applied between the tip and the sample. Further details were given in Chapter 2.

The majority of this chapter is devoted to STM studies of **CuP**, the copper derivative of the tetraundecylporphyrins. This chapter will start with a description of the different polymorphs formed by **CuP** on the HOPG surface in terms of their unit cell vectors. It will be shown that the surface coverage of the different polymorphs can be controlled by selecting the concentration and solvent of the supernatant **CuP** solution. A short extrapolation of the studies on **CuP** to other metal derivatives of **MP** will be made, demonstrating that all studied porphyrin derivatives show similar behavior and form the same type of adlayer structures. After this excursion, attention

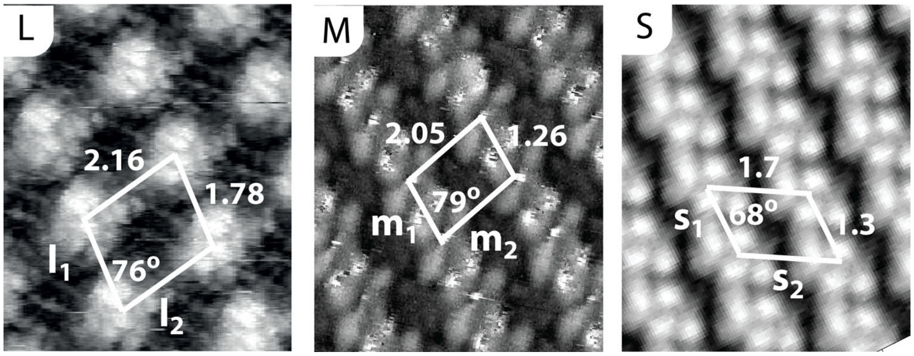

Figure 3.4: STM images of the three different polymorphs formed by **CuP** at the solvent/HOPG interface. The symbols used for the naming of the unit cell vectors (*i.e.* ($\mathbf{l}_1$,$\mathbf{l}_2$) for **L**, ($\mathbf{m}_1$,$\mathbf{m}_2$) for **M** and ($\mathbf{s}_1$,$\mathbf{s}_2$) for **S**) used throughout this thesis, are indicated. 5.5 × 6.5 nm^2, V$_{bias}$ $= 470$ mV, I$_{set}$ $= 13$ pA, HOPG/1-octanoic acid interface (L), 6.5 × 8.0 nm^2, V$_{bias}$ $= -710$ mV, I$_{set}$ $= 15$ pA, HOPG/1-octanoic acid interface (M), 6.0 × 7.5 nm^2, V$_{bias}$ $= -890$ mV, I$_{set}$ $= 8$ pA, HOPG/decamethyltetrasiloxane, correlation averaged image (S).

is shifted back to the description of the adlayer stuctures of **CuP**. The main finding is the observation that the unit cells of some of the adlayer structures formed by **CuP** on HOPG 'share' unit cell vectors. Its implications on the geometry of the layer will be discussed and an explanation of this behaviour in terms of the molecular conformations of the adsorbates is proposed.

3.2 Geometric description of the adlayer structures of CuP

Our STM experiments revealed that **CuP** can form three different 2-dimensional polymorphs on the HOPG surface (Figure 3.4). Because these polymorphs differ in the surface area of their unit cells, they will be referred to as Large (**L**), Medium (**M**) and Small (**S**), in accordance with the unit cell size. The unit cell vectors of the **L**, **M** and **S** polymorphs are summarized in Table 3.1 The values of these unit cell vectors were determined by co-imaging the molecular overlayers with the underlying graphite. The relationship between the unit cell vectors of the different polymorphs and the relationship of these vectors with the lattice of the underlying HOPG substrate will be discussed Section 3.3. When the geometries of the obtained unit cells are compared with those reported in literature for other alkyl-functionalized porphyrins, one finds that the **L** polymorph has great similarity to the monolayer structure observed by Chin *et al.*[47] for tetra-*meso*-$C_{19}H_{39}$ free base porphyrin, as is shown in Figure 3.3a, while

Table 3.1: Unit cell vectors of the three 2–dimensional polymorphs **S**,**M**,**L**, formed by **CuP** on the HOPG surface. Values are reported as $mean \pm S.D.$

Polymorph	Vector	Length (nm)	Angle	Area (nm^2)
L	$\mathbf{l}_1$	1.74 ±0.08	76° ±5°	3.65±0.30
	$\mathbf{l}_2$	2.16 ±0.14		
M	$\mathbf{m}_1$	1.26 ±0.05	79° ±4°	2.54±0.12
	$\mathbf{m}_2$	2.05 ±0.05		
S	$\mathbf{s}_1$	1.26 ±0.05	68° ±4°	2.07±0.16
	$\mathbf{s}_2$	1.70 ±0.15		

the monolayer structure found by Visser *et al.*[48] (Figure 3.3b) for the related tetra-*meso*-$C_{12}H_{25}$ free base porphyrin, shows great resemblance to the **M** polymorph. (See Section 3.5). There is a peculiar relationship between the unit cells of the different polymorphs, which can be observed in the STM image in Figure 3.5. A domain of the **S** polymorphs meets a domain of the **M** polymorph, and the boundary between the two polymorphs is very smooth; there is a perfect, seamless connection between the two domains. The unit cells, which are sketched in Figure 3.5, show that this smooth connection is caused by the fact that the unit cell vector parallel to the border of the two domains is shared between the two polymorphs. To be more specific:

$$\mathbf{m}_1 = \mathbf{s}_1$$

The statement that the unit cell vector is 'shared' between the two polymorphs not only implies that both unit cells have one vector that is identical, both in length and direction, it also implies that this shared unit cell vector can be part of both an **M** and an **S** unit cell at the same time. This in turn implies that **CuP** molecules at the border of the two domains are in both **M** and **S** unit cells at the same time. These molecules are indicated by $\mathcal{MS}$ in Figure 3.5. The sharing of unit cell vectors is not unique to the **M** and **S** adlayer structures of **CuP**, as will be discussed in the following.

3.2.1 The B unit cell

Besides the possibility to share one of its unit cell vectors with the unit cell of the **S** polymorph, the **M** polymorph can share its other unit cell vector with a fourth surface

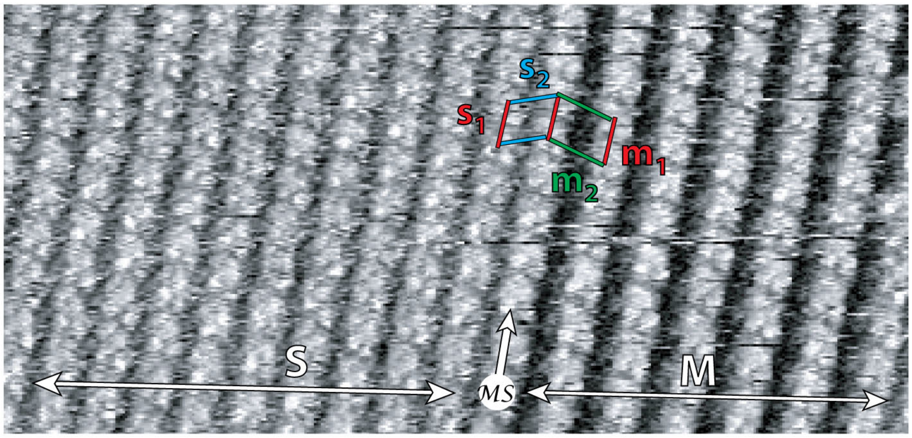

Figure 3.5: STM image of a monolayer of **CuP**, showing that the **M** and **S** polymorphs share one of their unit cell vectors. A unit cell of each of the two polymorphs is shown at the border of a domain of the two unit cells. Vectors $\mathbf{m}_2$ and $\mathbf{s}_2$ are different for the two structures, but the shortest vector of the **M** polymorph ($\mathbf{m}_1$) is identical to the shortest vector of the **S** polymorph ($\mathbf{s}_1$). This shared $\mathbf{m}_1 = \mathbf{s}_1$ vector is drawn in red. The molecules at the border between the two domains are truly within both an **M** and an **S** unit cell ($\mathcal{MS}$). Image parameters: decamethyltetrasiloxane/HOPG interface V$_{bias}$ $= -890$ mV, I$_{set}$ $= 7$ pA, 13×25 nm^2.

structure in which **CuP** was found to self-assemble at the HOPG surface. In Figure 3.6, two STM images of self-assembled monolayers of **CuP** can be observed, which consist of lamellar arrays of two distinct unit cells. One of these unit cells is that of the **M** polymorph, while the other presents a fourth possible unit cell, which will be referred to as '**B**'. Its unit cell vectors are $\mathbf{b}_1$=1.92 ± 0.09 nm and $\mathbf{b}_2$=2.05 ± 0.05 nm, which are at an angle of $71° \pm 4°$. The longest unit cell vector of the **M** polymorph is shared with the unit cell of the **B** adlayer structure:

$$\mathbf{m}_2 = \mathbf{b}_2$$

The **B** surface structure is different from the **L**, **M** and **S** polymorphs, because arrays consisting only of this unit cell were never observed to cover entire terraces on the HOPG surface. The **B** unit cell was only encountered in lamellar arrays in conjunction with lamellae of the **M** polymorph, as can, for instance, be observed in Figure 3.6. The fact that **B** and **M** unit cells share one of their unit cell vectors is again apparent from the seamless connection between the different lamellae. The ratio in which the lamellae of the **M** and **B** unit cells covered a given terrace depended on the concentration of the supernatant solution (Section 3.2.3). The STM image in Figure 3.6a

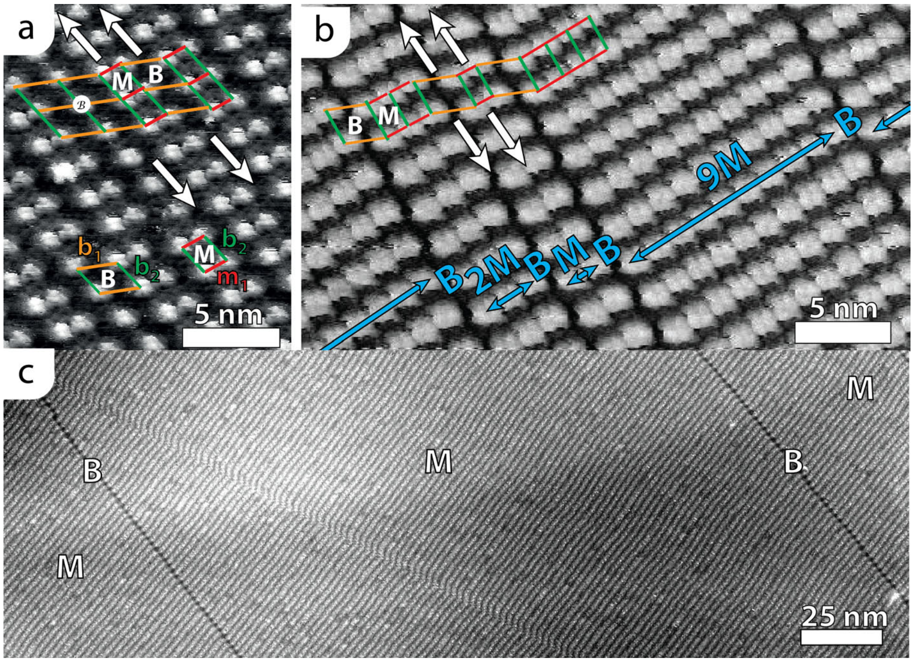

Figure 3.6: STM images in which the fourth possible unit cell in which **CuP** can self-assemble, is observed. This unit cell, named '**B**', only occurs in linear arrays in coexistence with linear arrays of the **M** polymorph. These two lamellae can occur in virtually all ratios: from the near one–to–one ratio in Figure (a), to ratios in which the **M** lamellae are slightly more abundant (b) and also on terraces nearly fully covered with the **M** polymorph, in which a lamella of **B** unit cells only rarely intersects patches of the **M** polymorph. The **M** and **B** unit cells share a unit cell vector. Image parameters: V$_{bias} = -760$ mV, I$_{set} = 21$ pA (a), V$_{bias} = -850$ mV, I$_{set} = 9$ pA (b), V$_{bias} = -760$ mV, I$_{set} = 21$ pA (c).

shows a packing in which lamellae of **M** and **B** unit cells appear almost alternatingly in a one–to–one ratio. Terraces with a perfect one–to–one ratio of **M** and **B** lamella were frequently observed at low supernatant solution concentrations, just as domains in which the coverage ratio of the **M** polymorph was larger than that of the **B** unit cells (Figure 3.6b). Adlayer structures in the STM image in Figure 3.6a, in which the **B** lamellea are more abundant than those of **M**, were observed only occasionally. The existence of this type of domain does however provide valuable information about the **B** surface structure. The fact that two adjacent lammelae of **B** unit cells are present in this image, shows that the **B** structure should be regarded as a stable unit cell formed by **CuP** on the HOPG surface, rather than phase boundaries between patches of the **M** polymorph. The STM image in Figure 3.6a shows that **CuP** can adsorb in single rows of molecules, marked '$\mathcal{B}$' with **B** lamellae on either side, and these molecules are therefore not part of any **M** unit cell, and thus not part of any **M** domain. From these observations it is concluded that **B** unit cells should be regarded as a fourth polymorph in which **CuP** can self-assemble on the HOPG surface, albeit with the additional constraints that it is only encountered in conjunction with unit cells of the **M** polymorph. In domains in which the lamellae of **M** unit cells are more prevalent than those of **B** unit cells, **M** unit cells can form patches of only one lamella wide (henceforth referred to as **MB** domains), patches containing a small number of **M** lamellae (Figure 3.6b, **M**≈**B**) and very large continuous areas, only occasionally intersected by a single lamella of the **B** polymorph (Figure 3.6c, **M**>**B**). Regardless of the ratio of **M** and **B** lamellae, these lamellae connect seamlessly, without any distortion of the layer. The collection of all types of domains comprising **M** and **B** unit cells will be referred to as **M**,**B**.

3.2.2 Shared unit cell vectors

The validity of the claims that $\mathbf{m}_2 = \mathbf{s}_2$ and $\mathbf{m}_1 = \mathbf{b}_1$ can be assessed without the use of high precision length measurements. The STM image in Figure 3.7a shows a domain composed primarily of the **S** polymorph, which is intersected by a single line of molecules adsorbed in the **M** polymorph. The black reference lines were drawn parallel to the $\mathbf{s}_2$ unit cell vector, and passing right through the middle of two adjacent rows of **CuP** molecules in the **S** domain. Note that these lines pass right through the centres of the **CuP** molecules in the **M** array. Even after translating over 60 $\mathbf{s}_1$ unit cell vectors in the **S** domain, no discernible phase shift is present with respect to the 60 $\mathbf{m}_1$ unit cell vectors in the **M** domain. Already a length difference of as little as 10 pm, between the $\mathbf{m}_1$ and $\mathbf{s}_1$ vectors, would influence the periodicity in the two patches to such an extend that it would cause a phase shift of half a unit cell vector over these distances. Such a phase shift would be easily recognizable, even without well-calibrated measurements. The same argument is valid for the equality of the $\mathbf{m}_2$ and $\mathbf{b}_2$ vectors in the STM images in Figures 3.7b and 3.7c. In the former

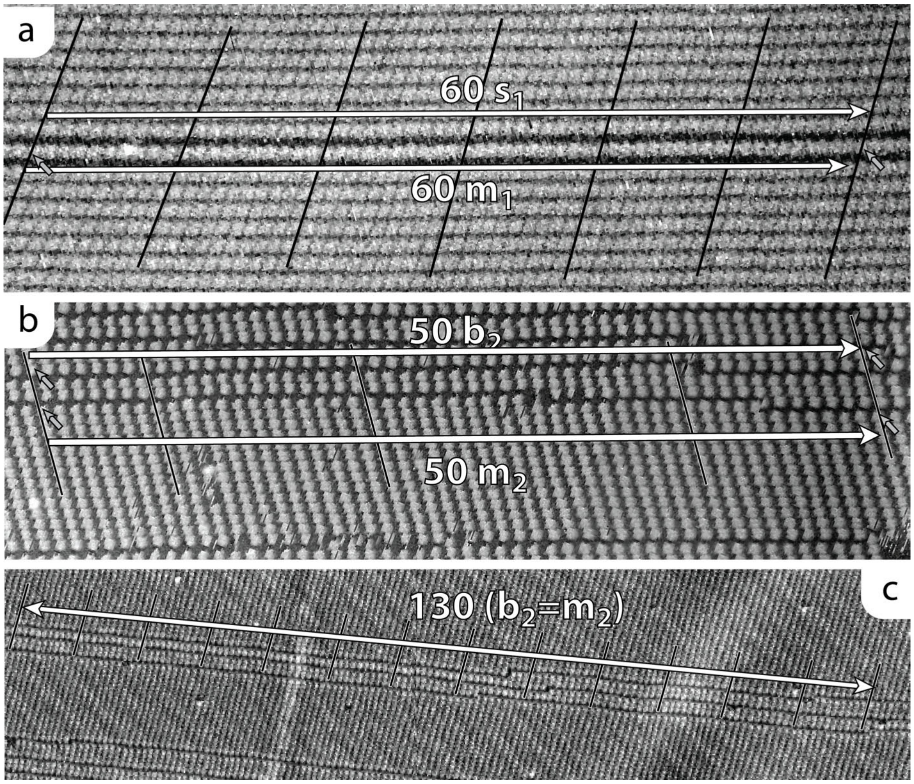

Figure 3.7: STM images of **CuP** at the HOPG/*1*-octanoic acid interface in which the equality of the shared unit cell vectors can be assessed. In image (a) it is shown for the shared $\mathbf{m}_1 = \mathbf{s}_1$ unit cell vectors that upon translating over 50 $\mathbf{s}_1$ unit cell vectors (white arrow), the registry of molecules in the **S** domain compared to the molecules in the single array of the **M** polymorph is the same. The black lines are visual guides which pass exactly between the molecules in the **S** domain, and go right through the center of a molecule in the **M** array. This is not only the case at the endpoints of the white vector, as indicated by small grey arrows, but throughout the entire domain. The same argument is applied to domains in which the **M** polymorph coexists with the **B** polymorph (images (b) and (c)) to demonstrate the equality of $\mathbf{m}_2$ and $\mathbf{b}_2$. Image parameters: 30 × 90 nm^2, V$_{bias}$ = -890mV, I$_{set}$ = 7pA (a), 37 × 125 nm^2, V$_{bias}$ = -780mV, I$_{set}$ = 8pA (b) 75 × 315 nm^2, V$_{bias}$ = -870mV, I$_{set}$ = 13pA (c).

image the resolution is high enough to resolve individual molecules, and it can be observed that after 50 translations over the shared $\mathbf{m}_2 = \mathbf{b}_2$ vector no discernible loss of registry between the two polymorphs can be observed. In Figure 3.7c, albeit at lower resolution, even over 130 translations of this shared vector no phase shift can be observed. Such numbers place the maximum possible discrepancy between the $\mathbf{b}_2$ and $\mathbf{m}_2$ vectors in the order of a few picometers. For that reason even without reference to their actual values, there is confidence about the shared nature of the aforementioned unit cell vectors. Actually, since the accuracy with which the equality of the shared unit cell vectors can be determined is well beyond the accuracy one can obtain using length measurements in ambient STM, the claim that the unit vectors are the same is stronger than their acclaimed values. It should be noted that there is another interesting geometrical relationship between the unit cells of the **M** and **B** polymorph in terms of sublattices. This relationship is explained in Appendix A.

3.2.3 Control by concentration

Before focussing on the further implications of the shared unit cell vectors, a means to control the ratio of the coverage of the different polymorphs of **CuP** on a given HOPG surface is presented. The difference in area of the different unit cells of the adlayer structures presents an opportunity to gain thermodynamic control over the surface coverage of the polymorphs. Understanding of the thermodynamics and kinetics of the formation of self–assembled monolayers is an important step in making the engineering of 2–dimensional surface structures an exact science[22]. In recent years the dependence of the structure of self–assembled monolayers on the temperature[50], the concentration[32,33,50–52] and the nature of the solvents from which the molecules are deposited on the surface[50,52] has been investigated in terms of thermodynamical quantities. In Chapter 5 of this thesis it will be advocated that the self-assembled monolayers of **CuP** on HOPG are not necessarily in thermodynamic equilibrium with the supernatant solvent at all times, since certain surface structures can remain trapped in thermodynamically unfavoured situations. Despite this fact, it is possible to test whether the results obtained by De Feyter and coworkers that at a solid/liquid interface higher density polymorphs form at high solute concentrations of tetrahydrobenzo[12]annulene derivatives[32], also apply qualitatively for self-assembled **CuP** monolayers. The surface areas of the unit cells of the polymorphs of **CuP** are plotted in Figure 3.8, both in absolute values and relative to the molecular surface area of the **L** polymorph. The surface area of the **B** unit cell is included despite the fact that this polymorph was never observed to solely cover entire terraces. The molecular area of the **MB** packing is included in Figure 3.8 and the region between the area of this packing and that of the **S** polymorph is shaded to indicate that a given substrate terrace can be covered by a seamlessly connected mixture of the **B**, **M** and **S** polymorphs because of the shared unit cell vectors, to yield all the *average*

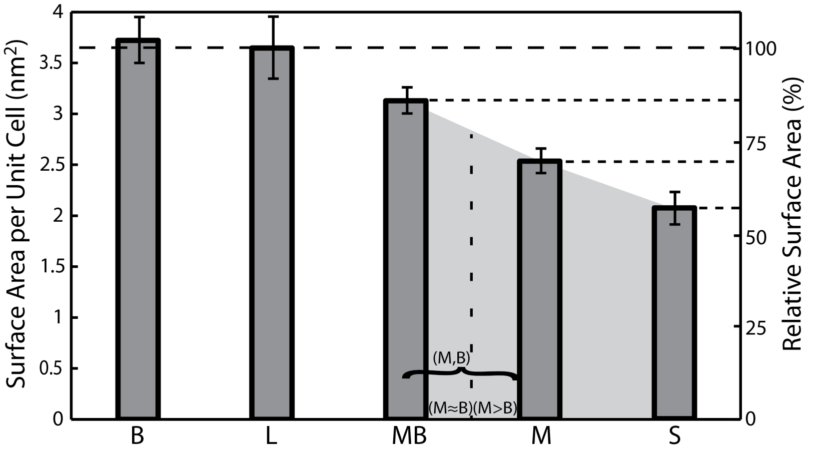

Figure 3.8: Overview of the surface densities of the four polymorphs **B**, **L**, **M** and **S** and of the **MB** packing. The values and error bars are based on those in Table 3.3. On the left vertical axis the absolute unit cell areas of each of the surface structures is set out while the right axis shows the unit cell area relative to the unit cell area of the **L** polymorph. The area reported for **MB** is the mean of that of the **M** and **B** unit cells. The shaded area between **MB** and **S** indicates that, because of the coexistence of those polymorphs, a given terrace can contain all these *average* unit cell areas. The further classification of domains comprising **M** and **B** unit cells (*i.e.* **M**,**B**, **M**≈**B** and **M**>**B**) are also indicated.

unit cell areas. The surface area of the unit cell of **S** is only about 57% of that of the **L** polymorph, showing that there is a 75% difference in surface coverage between the lowest and the highest density polymorph of **CuP** on HOPG. Given the fact that the polymorphs of **CuP** strongly differ in surface area, it would be expected that when the surface is in contact with a highly concentrated solution of the molecules the structure with the highest surface concentration (*i.e.* the lowest unit cell area) would primarily be obtained, and *vice versa*. The STM images in Figure 3.9 show that the polymorph formation can indeed be controlled by varying the concentration of **CuP** in the supernatant 1–octanoic acid solution. By applying solutions with concentations in the range of 10^{-7}M to 10^{-3}M, the surface can be covered with the pure **L** polymorph, domains comprising mixtures of the **B** and **M** unit cells, terraces fully covered with the **M** polymorphs and domains comprising up to 70 % of the **S** polymorph. It should be emphasized that these concentrations should only be taken as rough estimates and that the surface fraction of the different polymorphs also depends on the history of the self-assembled monolayer; not only the actual concentration of the solution to which the monolayer is exposed determines which polymorphs are present and in which ratio, also the concentrations to which the sample was exposed during

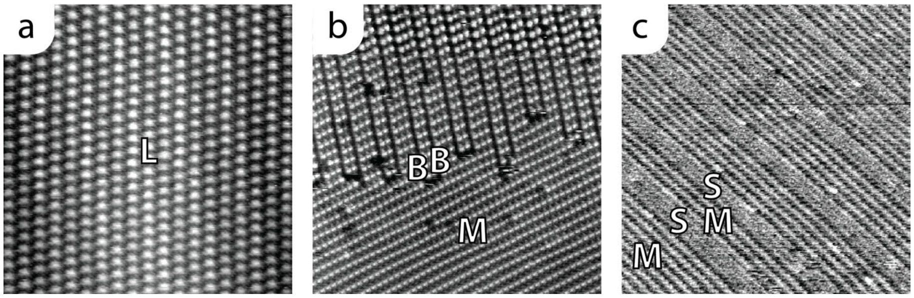

Figure 3.9: Three typical STM images of monolayers of **CuP** at the interface of HOPG and a supernatant solution of 1-octanoic acid with concentrations of 10^{-6}M (a), 10^{-4}M (b) and 10^{-3}M (c) of **CuP**. In (a) a domain of the most spacious polymorph, **L**, is visible. Image (b) shows a large **M** domain in the bottom which meets a mixed domain of **M** and **B** in the top. At even higher concentrations the mixing of **S** and **M** is observed (c). $V_{bias} = 380$ mV, $I_{set} = 4$ pA, 50 × 50 nm^2 (a), $V_{bias} = -1200$ mV, $I_{set} = 3$ pA, 60 × 60 nm^2 (b) and $V_{bias} = -820$ mV, $I_{set} = 9$ pA, 65 × 65 nm^2.

the formation of the monolayer influence its current polymorphic composition. This behaviour will be topic of Chapter 5 where transformations of the monolayer upon *in situ* changing the concentration of the supernatant solution will be discussed.

3.2.4 Control by solvent type

Throughout this chapter, STM images are shown of **CuP** monolayers at the interface of HOPG and *n*-tetradecane, 1-octanoic acid or decamethyltetrasiloxane and it is proposed that at the interfaces of HOPG with all these solvents, the same adlayer structures are formed. The dependence on the solvent of the formation and the stability of 2-dimensional polymorphs has also been previously investigated[31] and described in terms of thermodynamics[50] for molecules that form porous networks. The influence of the solvent in these cases was rather complex, since it was found to coadsorb in the pores of the lowest density polymorph. Because of the compact nature of the polymorphs found for **CuP** and the fact that the same structures form in all investigated solvents (*i.e.* *n*-tetradecane, 1-octanoic acid and decamethyltetrasiloxane), it is expected that solvent coadsorption is not a factor in the formation of **CuP** monolayers on the HOPG surface. Despite the very diverse nature of the used solvents, which could in principle have influenced the surface structures in various ways[53], such as coadsorption[53] and by acting as a templating layer[54], the structures that formed were always the same. Even in high resolution STM images, no indications were ever found for the coadsorption of solvent molecules or for the solvent molecules acting as a templating layer, which was previously observed in STM studies of **MnP** at the *n*-tetradecane/Au(111) interface[55]. The ratio in which the 2D-polymorphs cover the surface, however, does depend on the solvent, but it is proposed that this occurs in a rather straightforward manner.

The driving force for the formation of the higher density polymorphs is not only expected to be dependent on the concentration of the molecules in the supernatant solution, but also on the capacity of the solvent to dissolve those molecules. The chemical potentials of **CuP** molecules in a solution (μ_{sol}) that is in equilibrium with their precipitated solid (μ_s) are given by:

$$\mu_s = \mu_{sol}(sat) = \mu^0_{sol} + kT \ln [\mathbf{CuP}]_{sat} \tag{3.1}$$

Therefore:

$$\mu^0_{sol} = \mu_s - kT \ln [\mathbf{CuP}]_{sat} \tag{3.2}$$

The chemical potential of a **CuP** molecule in any solution is therefore given by:

$$\mu_{sol} = \mu_s + kT \ln \frac{[\mathbf{CuP}]}{[\mathbf{CuP}]_{sat}} \tag{3.3}$$

Since μ_s is the chemical potential of the pure solid phase of **CuP**, it does not depend on the solvent and therefore this equation shows that the difference in chemical potential of a porphyrin molecule at concentration [**CuP**] in different solvents depends on the saturation concentration $[\mathbf{CuP}]_{sat}$ in that solvent. The chemical potential can therefore be written as:

$$\mu_{sol} = \mu_s + kT \ln [\mathbf{CuP}]_{rel} \tag{3.4}$$

where $[\mathbf{CuP}]_{rel}$ is the ratio between the actual and the saturation concentration. The description of self-assembled monolayers in terms of their relative concentration has been reported before[50,52], but formula 3.4 was not explicitly presented. The solvent dependence is thus proposed simply to be an extension of the aforementioned concentration dependence. This solvent dependence can most easily be appreciated from STM measurements performed on **CuP** at the decamethyltetrasiloxane/graphite interface. The solubility of **CuP** in this solvent is rather low ($\approx 10^{-6}$M). This solubility can be increased by increasing the temperature, but upon cooling **CuP** slowly precipitates. This process, however, takes several hours to complete and therefore yields a supersaturated solution. When such a supersaturated solution is brought onto the graphite surface, the molecules tend to form a large amount of the highest density polymorph (**S**) at the solid/liquid interface (Figure 3.10a). Decamethyltetrasiloxane can therefore be used to create and study the highest density polymorph at relatively low solute concentrations. Although the description in terms of the relative concentration qualitatively describes the observed behaviour, one should keep in mind that at thermodynamic equilibrium the chemical potentials of all different involved phases must be taken into account. Although the chemical potential of the solution phase is well-described by equation 3.4, the chemical potential of the monolayer might change

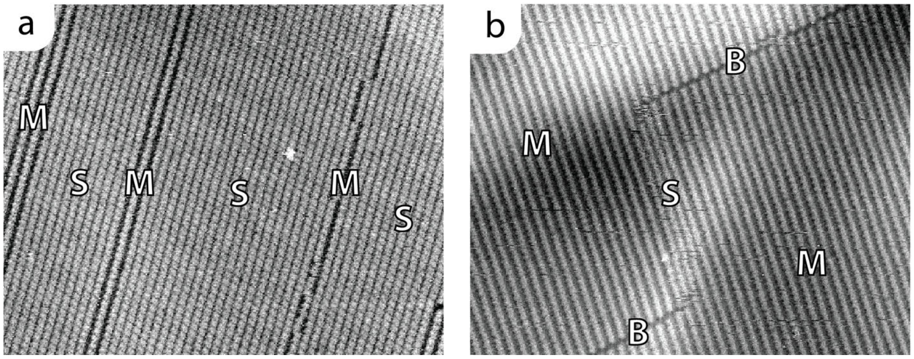

Figure 3.10: STM images of **CuP** at the interface of HOPG and solutions of decamethyltetrasiloxane (supersaturated) (a) and *n*-tetradecane at a concentration of 10^{-4}M (b). The low solubility of **CuP** in decamethyltetrasiloxane favors the formation of very **S**–rich surfaces. In the *n*-tetradecane solution, the **S**, **M** and **B** polymorphs can be identified. $V_{bias} = -890$ mV, $I_{set} = 7$ pA, 85 × 65 nm^2 (a) and $V_{bias} = 590$ mV, $I_{set} = 10$ pA, 90 × 75 nm^2 (b).

because of different interactions with a different supernatant solvent. Differences in the resulting dipole moment of the various polymorphs could, for instance, change the chemical potentials of the polymorphs as a function of the polarity of the used solvent. These matters have not been extensively studied and present an interesting opportunity for further investigations. Figure 3.10b shows an adlayer of **CuP** at the interface of HOPG and an *n*-tetradecane solution with a concentration of 10^{-4}M. The majority of the surface is covered with the **M** polymorph and the occasional **S** domain can be found at the endpoints of domains of **B**, showing that also in this solvent the same polymorphs are formed. The choice of solvent thus presents an alternative method to control the polymorphic composition of a sample and is particularly useful to create the high density **S** polymorph from solutions with low **CuP** concentrations.

3.2.5 Extension to other metal centers

Now that the structures **CuP** can form at the HOPG/solvent interface have been described the self–assembly behaviour of the same tetra-undecyl-porphyrin with different metal centers will be briefly discussed. Monolayers of the nickel derivative, **NiP**, on graphite have been studied in a wide range of concentrations in 1-octanoic acid and all four polymorphs that were observed for **CuP** could also be identified for this compound. The STM image in Figure 3.11 shows the **L**, **B**, **M** and **S** polymorphs

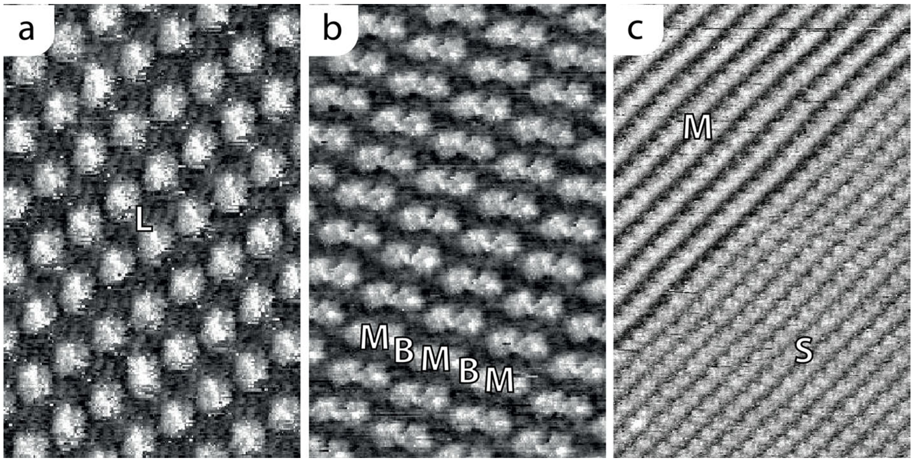

Figure 3.11: STM images of **NiP** at the 1-octanoic acid/HOPG interface. The self-assembly behavior is identical to that of **CuP**: at low concentrations (10^{-6} M) the **L** polymorph is formed (a), while at higher concentrations (10^{-5} M) **M** and **B** coexist (b). When the concentration is increased even further (10^{-3} M), domains of **S** are formed (c). $V_{bias} = -550$ mV, $I_{set} = 20$ pA, 15 × 22 nm^2 (a), $V_{bias} = 730$ mV, $I_{set} = 8$ pA, 15 × 22 nm^2 (b) and $V_{bias} = -720$ mV, $I_{set} = 10$ pA, 26 × 40 nm^2

formed by **NiP** at the HOPG/1-octanoic acid interface (Figure 3.11a and b) and the HOPG/decamethyltetrasiloxane interface (Figures 3.11c). The unit cell vectors in Table 3.2, are, within the experimental error, identical to those found for **CuP**. A survey of **2HP** and **ZnP** at the HOPG/*n*-tetradecane interface also revealed structures which were the same as those found for their copper–containing sibling. Figure 3.12 shows STM images of **ZnP** (a) and **2HP** (b) at the HOPG/*n*-tetradecane interface. The occurrence of the **M**, **S** and **B** polymorphs can be readily observed in both STM images. The unit cell vectors of these surface structure are summarized in Table 3.2, and within the experimental error they are also the same as the values determined for **CuP** and **NiP**. Given the limited accuracy of ambient STM, it is difficult to unambiguously determine whether unit cell vectors of adlayer structures formed by different species are exactly the same or merely highly similar. In this case it is not claimed that the unit cell vectors are the same, but that the whole unit cell vector system, including the shared unit cell vectors between the different polymorphs, is the same for the different investigated metalloporphyrins. The observation that the different metallo-porphyrins form the same surface structures opens possibilities to construct porphyrin monolayers containing multiple components. This property is more extensively discussed and exploited in Chapter 5 where multi-component monolayers of

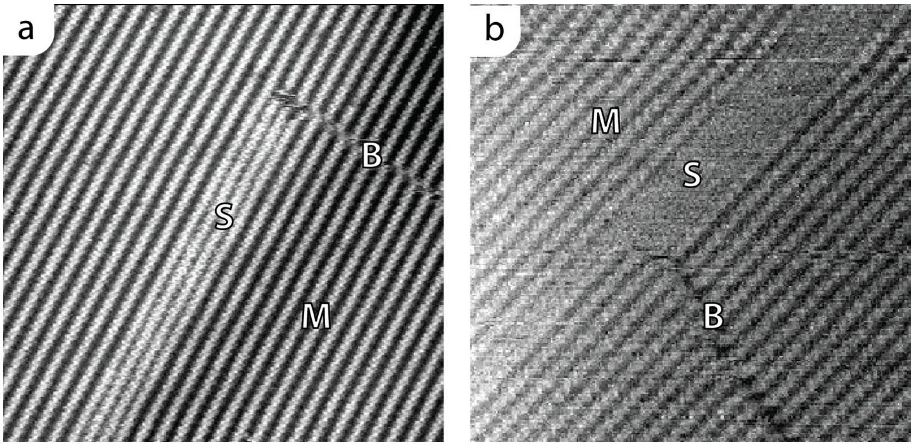

Figure 3.12: STM images of **ZnP** (a) and **2HP** (b) at the HOPG/n-tetradecane interface. Both porphyrins are found to form the **S**, **M** and **B** polymorphs which were also observed for **CuP**. 60 × 60 nm^2, V$_{bias}$ $= -720$ mV, I$_{set}$ $= 8$ pA (a) and 50 × 50 nm^2, V$_{bias}$ $= -640$ mV, I$_{set}$ $= 7$ pA (b)

MP will be described.

3.3 The relation between the overlayers and the graphite surface

The remainder of this chapter will mainly deal with the observation that some of the found polymorphs of **CuP** share unit cell vectors. To understand the polymorphic behavior in more detail, first the relationship between the vectors of the molecular overlayers and the HOPG substrate will be addressed by co-imaging the self-assembled monolayer with the underlying substrate. The balance between intermolecular forces between the **CuP** adlayer and the underlying HOPG surface and those within the self-assembled monolayer itself will be discussed subsequently, in order to asses the primary type of interactions responsible for the structure of the overlayer. The knowledge that will be acquired in these two steps will be applied, together with high resolution STM imaging, to propose the molecular conformations of the **CuP** adsorbates in the different surface structures, and, more specifically, for the different adsorption configurations.

Table 3.2: Summary of the unit cell vectors of the three 2–dimensional polymorphs (**S**,**M**,**L**) and the 1–dimensional structure (**B**) formed by **CuP**, **NiP**, **ZnP** and **2HP** on the HOPG surface. Values are reported as $mean \pm S.D.$ and the values are in nm. *N.D.* signifies that the values of the respective vector has not been determined.

	CuP		**NiP**		**ZnP**		**2HP**	
$\mathbf{l}_1$	1.74 ±0.08		1.74 ±0.15		ND		ND	
		76° ±5°		76° ±7°		ND		ND
$\mathbf{l}_2$	2.16 ±0.14		2.02 ±0.15		ND		ND	
		–		–		–		–
$\mathbf{b}_1$	1.92 ±0.09		2.00 ±0.20		ND		ND	
		71° ±4°		76° ±8°		ND		76° ±8°
$\mathbf{b}_2$=$\mathbf{m}_2$	2.05 ±0.05		2.08 ±0.10		2.07 ±0.10		2.05 ±0.10	
		79° ±4°		78° ±5°		79° ±7°		78° ±8°
$\mathbf{s}_1$=$\mathbf{m}_1$	1.26 ±0.05		1.24 ±0.10		1.24 ±0.10		1.21 ±0.10	
		68° ±4°		68° ±5°		69° ±8°		69° ±8°
$\mathbf{s}_2$	1.70 ±0.15		1.78 ±0.15		1.84 ±0.15		1.74 ±0.10	

3.3.1 The L polymorph

To accurately determine the dimensions of the unit cells of the different polymorphs, the molecular adlayers were co-imaged with the underlying graphite. These experiments were performed by switching between STM measurement parameters suitable for imaging the monolayer, *i.e.* a bias voltage of typically several hundreds of millivolts, and those suitable for imaging the HOPG, with typical bias voltage values of 2–5 mV. Not only does this procedure provide a very reliable internal calibration for the determination of the lengths and angles of the unit cells of the molecular layer, but also the relation of the unit cell to the underlying graphite lattice can be directly measured. A lattice was fitted over the graphite part of the image. Because of the small graphite unit cell size compared to those of the adlayer unit cells, the grid has a spacing of $2\mathbf{g}_1$ by $2\mathbf{g}_2$, in which $\mathbf{g}_1$ and $\mathbf{g}_2$ are two of the three equivalent lattice vectors of the HOPG surface as explained in Chapter 2. The double spacing is used for clarity. A molecular lattice was fitted to the adlayer half of the STM image and the graphite lattice was extended to overlay this part, so that unit cells of the overlayer can be obtained by determining the number of graphite unit cell vectors along each molecular vector as explained in Chapter 2. Because angles and distances are not directly measured in real-space, but determined as multiples of the graphite lattice vectors, this type of analysis is very robust with respect to thermal drift, since a constant drift will deform the imaged molecular lattice in the exact same way as the co–imaged graphite lattice. Although in real–space lengths and angles will be affected by drift, in graphite coordinates the vectors remain the same. The unit cells of the largest polymorph (**L**) have been determined by co–imaging the molecular overlayer of **CuP** with the underlying graphite (Figure 3.13).

From the STM image in Figure 3.13 it can be deduced that $\mathbf{l}_2$ has a large com-

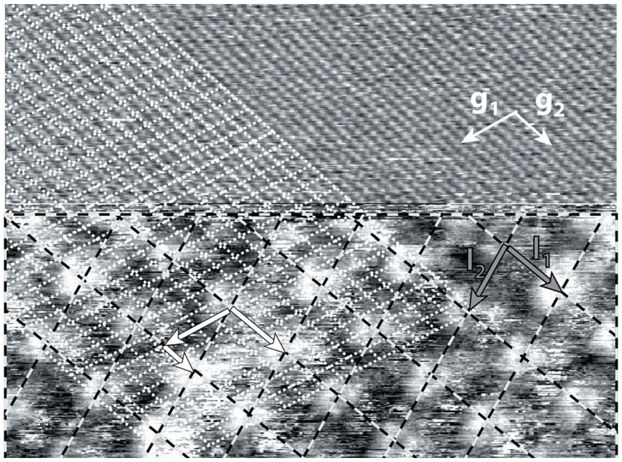

Figure 3.13: STM image showing the relationship of the unit cell vectors of the **L** polymorph and the underlying graphite lattice. The image is made by switching from experimental conditions suitable to image the overlayer (bottom half), to a bias voltage at which the underlying HOPG is probed (top part). Image parameters: 12 x 17 nm^2, V$_{bias}$ $= -770$ mV, I$_{set}$ $= 11$ pA (overlayer), V$_{bias}$ $= -5$ mV (HOPG).

ponent along one of the graphite lattice vectors ($\mathbf{g}_2$ in this choice of HOPG vectors) and just a small component along the other, $\mathbf{g}_1$, vector, making it nearly parallel to a $\langle 11\bar{2}0\rangle$ graphite direction. The other vector, $\mathbf{l}_1$, has large components along both graphite directions and it is not directed along any high symmetry axis of the substrate. The overlay method has been applied in 4 separate measurements of the **L** polymorph leading, to an average result of:

$$\mathbf{l}_1 = \begin{pmatrix} 7.9 \pm 0.3 \\ 5.7 \pm 0.3 \end{pmatrix}, \mathbf{l}_2 = \begin{pmatrix} -0.1 \pm 0.2 \\ 8.8 \pm 0.5 \end{pmatrix} \tag{3.5}$$

Which implies that that in real–space coordinates $\mathbf{l}_1 = 1.78 \pm 0.08$ nm and $\mathbf{l}_2 = 2.16 \pm 0.14$ nm, with an angle of 76°±5° between them, as was already mentioned in Section 3.2.

3.3.2 The M polymorph

The same procedure was used to determine the unit cell vectors of the **M** polymorph, and the results are shown in Figure 3.14. In this case the unit cell vector $\mathbf{m}_1$ is almost parallel to $\mathbf{g}_2 - \mathbf{g}_1$, which is a $\langle 1\bar{1}00\rangle$ graphite direction. Combining the results of 6

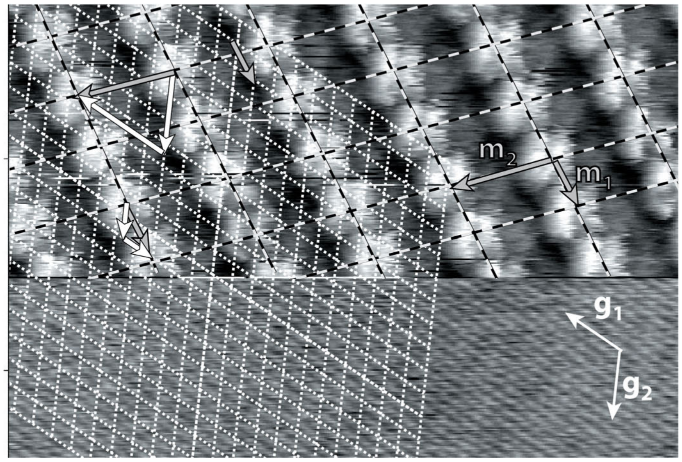

Figure 3.14: STM image showing the relationship of the unit cell vectors of the **M** polymorph (top part) and the underlying graphite lattice (bottom part). The image is made by switching between a bias voltage suitable for imaging the molecular overlayer and a lower voltage to image the underlying HOPG. Image parameters: 11 x 16 nm^2, $V_{bias} = -770$ mV, $I_{set} = 22$ pA (overlayer) and $V_{bias} = -4$ mV, $I_{set} = 22$ pA (HOPG).

separate measurements resulted in unit cell vectors of:

$$\mathbf{m}_1 = \begin{pmatrix} -2.9 \pm 0.1 \\ 3.0 \pm 0.1 \end{pmatrix}, \mathbf{m}_2 = \begin{pmatrix} 9.1 \pm 0.2 \\ 7.3 \pm 0.2 \end{pmatrix} \tag{3.6}$$

which means that $\mathbf{m}_1$=1.26±0.05 nm, at an angle of 79°±4° with respect to $\mathbf{m}_2$=2.05± 0.05 nm.

3.3.3 The B unit cell

Since larger domains consisting exclusively of **B** unit cells were never encountered on the HOPG surface, the unit cell vectors of the **B** surface structure have been determined in the limiting form of its occurrence. A packing consisting of a one–to–one ratio of lamellae of the **M** and **B** polymorphs, the **MB** packing.

Again the unit cell vectors have been determined by comparison with the lattice of the underlying graphite. The structure indeed contains rows of **M** with the same unit cell vectors as determined in Section 3.3.2. The value of the remaining vector, $\mathbf{b}_1$, is:

$$\mathbf{b}_1 = \begin{pmatrix} 0.2 \pm 0.2 \\ 7.7 \pm 0.3 \end{pmatrix}$$

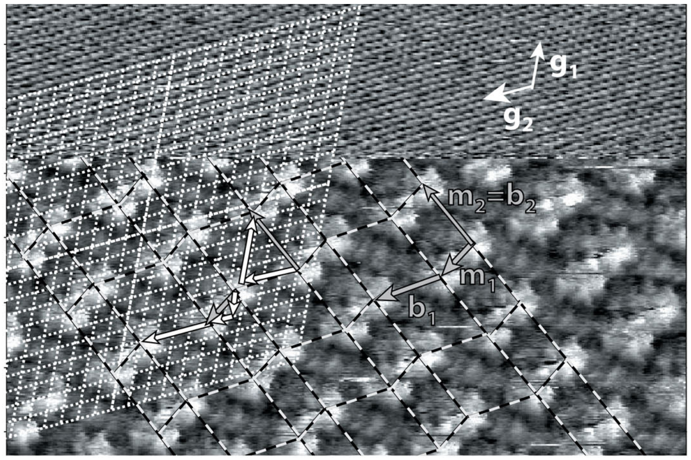

Figure 3.15: STM image in which a domain of the **MB** packing, the structure consisting of alternating rows of **M** and **B** unit cells, is co–imaged with the underlying graphite surface. In this domain every adsorbate is in an $\mathcal{MB}$ adsorption configuration. 21 × 15 nm^2, $V_{bias} = -760$ mV, $I_{set} = 10$ pA (overlayer) same but with $V_{bias} = -5$ mV (HOPG).

Which means that $\mathbf{b}_1$=1.92 ± 0.09 nm, at an angle of 71°±4° with $\mathbf{b}_2$. This $\mathbf{b}_1$ vector is parallel to the $\langle 11\bar{2}0\rangle$ direction of graphite.

3.3.4 The S polymorph

The structure of the **S** polymorph has not been determined by co-imaging it with the underlying graphite, but by direct measurement from tens of real-space and Fourier transformed images. Several, hitherto unsuccessful, attempts were made to co-image this polymorph with the underlying substrate, but these primarily lead to local desorption and temporal reorganisation of the area under investigation. Its unit cell vectors are $\mathbf{s}_2$=1.7 ± 0.1 nm and $\mathbf{s}_1$=1.3 ± 0.1 nm at an angle of 68°±4°. This unit cell has a surface area of 2.07±0.16 nm^2. Its shortest vector is, however, known with high accuracy from the fact that $\mathbf{s}_1 = \mathbf{m}_1$. The relation between the second unit cell vector of **S**, $\mathbf{s}_2$, and the HOPG lattice can be calculated using by transforming the real–space unit cell parameters to the HOPG unit cell vectors $\mathbf{g}_1$, $\mathbf{g}_2$, using the transformations described in Chapter 2. It is found that

$$\mathbf{s}_2 = \begin{pmatrix} 8.0 \pm 0.5 \\ 5.0 \pm 0.5 \end{pmatrix}$$

so that the relationship of this vector to those of the underlying substrate is known, although with a somewhat lower accuracy than those of the other unit cell vectors.

3.3.5 Interactions between the porphyrins and the graphite surface

Although the registry of the unit cell vectors of the molecular adlayer have now been expressed in terms of the lattice vectors of the HOPG surface, an explanation for the sharing of the unit cell vectors amongst the different polymorph structures has not yet been obtained. A possible explanation to explore, is whether the unit cell vectors are shared simply because there is commensurism of the overlayer with the HOPG substrate. In that case the coefficients of their unit cell vectors are integer multiples of the lattice vectors of the underlying substrate. This would imply that every **CuP** molecule is adsorbed at equivalent locations at the HOPG surface, *i.e.* at the same location within an HOPG unit cell. The central metal atom might, for instance, always be adsorbed at the center of an HOPG hexagon. Commensurism can thus put a large constraint on the possible unit cell vectors of the overlayers, since the molecules in the adlayer might only be allowed to adsorb at the vertices of a hexagonal grid with spacings of the HOPG lattice. One might propose that the coarse spacing of the HOPG lattice (0.246 nm) compared to the observed unit cell vectors (1.3–2.1 nm $\approx 5 - 8$ HOPG lattice vectors), puts such a large constraint on the possible unit cell vectors, that their sharing is a mere consequence of the limited number of possible commensurate adsorption positions. Unfortunately, the uncertainty in the determined unit cell coefficients of all the observed surface structures of **CuP** is too large to unambiguously determine whether they are integer multiples of the graphite lattice vectors or not. However, the frequent observation of so-called moiré patterns in the STM images of all found polymorphs indicates that they are not commensurate to the underlying HOPG surface (Figure 3.16). Besides the periodic structures of the unit cells of the three polymorphs, a superstructure can be observed in each of the three STM images: the apparent height of the molecules has variations over the surface, which are not random but repetitive over distances of several molecular unit cells. For example, if one focuses on the moiré pattern of the **M** polymorph, (Figure 3.16b), it can be seen that molecules of equal apparent height are found after translating over $7\mathbf{m}_1$ or $8\mathbf{m}_2$. This implies that the vectors of the molecular lattice deviate from being integer multiples of the graphite unit cell vectors by $\frac{1}{7} \approx 0.14$ and $\frac{1}{8} \approx 0.13$ HOPG lattice spacings for $\mathbf{m}_1$ and $\mathbf{m}_2$, respectively. These deviations correspond to about 50 pm in real–space. The superstructures are caused by the fact that the molecules within one period of the moiré pattern are adsorbed at slightly different locations of the unit cell of the underlying HOPG substrate. This causes a slight periodic variation in the coupling between the molecules and the HOPG, which affects the local tunneling probability and can therefore be seen as a periodic variation in the apparent height in STM images of such an overlayer. Such moiré patterns are

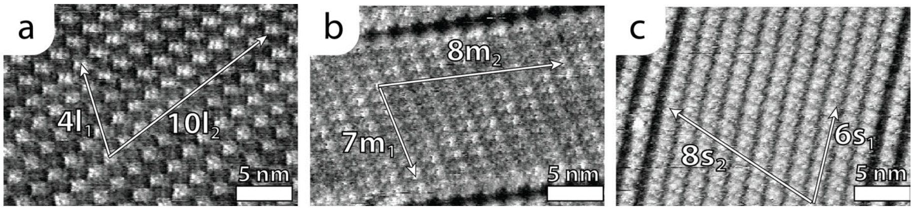

Figure 3.16: Three STM images of monolayers of **CuP** at the graphite/liquid interface, which reveal the occurrence of moiré patterns in the **L** polymorph (a), the **M** polymorph (b) and the **S** polymorph (c). The periodicity of the superstructure is depicted along the unit cell vectors of the three polymorphs. $V_{bias} = 740$ mV, $I_{set} = 7$ pA, 1-octanoic acid (a), $V_{bias} = 210$ mV, $I_{set} = 5$ pA, 1-octanoic acid (b) and $V_{bias} = -650$ mV, $I_{set} = 10$ pA, decamethyltetrasiloxane.

therefore direct evidence for molecular overlayers not being commensurate with the underlying graphite lattice[56]. From the observation that none of the moiré patterns of any of the polymorphs of **CuP** are parallel to any of the unit cell vectors of the overlayer, it can be deduced that none of these unit cell vectors is an integer multiple of the unit cell vectors of the underlying graphite lattice. The moiré patterns were not always observed in STM images of **CuP** monolayers; it is assumed that the non–commensurism is always present, but that the visibility of the moiré patterns strongly depends on the tunneling characteristics of the measurement, such as the bias voltage, the tunneling current and the atomic structure of the apex of the STM tip. Such a strong tip-dependent contrast has been observed more regularly for different forms of height contrast of **CuP** monolayers, and an in-depth treatment of this topic will be presented in Chapter 4. The occurrence of moiré patterns and the lack of commensurism that can be deduced from it contains important information about the delicate balance between interactions between **CuP** molecules within the monolayer, called *intra*–layer interactions, and interactions between the substrate and the monolayer, which are referred to as *inter*–substrate/layer interactions[57,58]. The interactions between the molecules of **CuP** within the layer the primary interactions are expected to be, primarily attractive, Van der Waals interactions and Pauli repulsion. The interactions between **CuP** and the underlying substrate involve π–π–interactions between the porphyrin ring and the extensive π–system of the HOPG surface[59,60], CH/π–interactions[60,61] between the aliphatic chains and the substrate and the ubiquitous Van der Waals interactions[62,63]. The apparent non-commensurate relationship between all the observed surface structures of **CuP** and the HOPG surface, indicates that there are no highly favourable adsorption sites on the HOPG surface; apparently the gain in interaction energy with the surface, resulting from the adsorption of **CuP** at a specific location, is rather low. The intra-layer interactions, *i.e.* the interactions between neighboring adsorbates, seem to be a much greater contributor to the specific structure of the molecules within the monolayers. The gain in *intra*–layer energy of the molecules by assuming a conformation and distance that maximizes the intermolecular Van der Waals interactions is apparently greater than the energy loss of the molecules upon assuming unfavourable adsorption positions on HOPG surface. The unit cell vectors of the **MP** adlayers are therefore not determined by the locations of specific adsorption sites on the surface, but by the relative locations of neighbouring porphyrins. The interaction of the **CuP** monolayer with the substrate is, however, not negligible since the molecular unit cell vectors still follow the 6-fold symmetry axes of the graphite surface, as do the alkyl tails that are adsorbed directly on the HOPG. The polymorphs described in this chapter are therefore not commensurate, nor fully incommensurate, but they are coincident with the underlying graphite. The HOPG induces preferential adsorption directions, but not preferential molecular adsorption sites. This implies that the HOPG does not enforce any coarsely spaced grid to which the **CuP** adsorbates must comply. Because of this, it is not expected that any polymorph-dependent physical and chemical behavior is governed by the adsorption site of a **CuP** molecule. Instead, it might be possible that any variation in the properties of a **CuP** adsorbate on the HOPG surface depends more on the locations at which its direct **CuP** neighbors are found. The term *adsorption configuration* will be used throughout this thesis to refer to the collection of relative locations at which the direct neighbors of a given **CuP** adsorbate are found. This term will be more extensively discussed in Section 3.4. The observation that the molecular layer is not commensurate to the substrate and that its molecular structure is governed by interactions between the adsorbates, is in contrast with that of many molecular monolayers formed on metallic surfaces, where the molecule–substrate interactions are dominant and site–specific compared to the molecule–molecule interactions, therefore leading to the formation of commensurate layers. In a review by Barlow *et al.*[64] the commensurism of many molecular layers on coinage metals is reviewed: for example, three different adlayer structures were found for tartaric acid on a Cu(110) surface in Ultra High Vacuum, all of which were found to be commensurate as a result of the strong interactions between the carboxylic acid groups of the tartaric acid molecules and the substrate, as was determined using Low Energy Electron Diffraction (LEED) and STM[65]. Also larger molecules, such as perylene-3,4,9,10-tetracarboxylic acid-3,4,9,10-dianhydride (PTCDA), can form strong chemisorptive bonds with a Ag(110) surface upon adsorbing with its molecular plane parallel to the surface, leading to the formation of a commensurate overlayer[64,66,67] and iron phthalycyanines which are closely related to the porphyrins studied here were found to form commensurate layers to metal surfaces such as Au(111)[68]. The lack of specific adsorption sites at the HOPG surface rules out the formation of strong and stiff covalent or coordinative bonds with, for instance, the central metal atom of the adsorbed porphyrins and the HOPG surface. The lack of specific adsorption sites for **CuP** molecules on the HOPG substrate, and the concomitant result that intra-layer forces thus primarily define the structure of the molecular overlayer, suggests that part of these intra-layer interactions must be shared among the different observed 2-dimensional polymorphs in case of the shared unit cell vectors. To facilitate the discussion on this matter, the concept of the adsorption configuration will be further explored in the following section.

3.4 From shared vectors to shared adsorption configurations

In this section the relationship between the relative locations of the direct neighbours of a **CuP** adsorbate and its molecular conformation will be explored. As was explained in Section 3.3.5, the interactions between the molecules in the self-assembled monolayer primarily govern the structure of the adlayer, as opposed to interactions between the adsorbates and the HOPG surface. Given the short range of the involved intermolecular interactions, compared to the lengths of the unit cell vectors, this would imply that the major contributor to an energy gain when molecules are assembled in a certain structure on the HOPG surface is the interaction an adsorbed **CuP** molecules has with its direct neighbors. In Section 3.3.5, the collection of the locations at which an adsorbates direct neighbours are located was defined as the *adsorption configuration*, and this term will be explained here in more detail. Figure 3.17a shows the same STM image as that in Figure 3.5, in which a domain of the **S** polymorph (left) borders a domain of the **M** polymorph. The seamless connection between the domains is caused by the fact that the $\mathbf{m}_1 = \mathbf{s}_1$ vector is shared between the unit cells of these two polymorphs. To emphasize the sharing of unit cell vectors, each different unit cell vector in the figures will be marked with a different color throughout the remainder of this chapter. The $\mathbf{m}_2$ unit cell vectors are colored green, while $\mathbf{s}_2$ vectors are indicated in blue. The shared $\mathbf{m}_1 = \mathbf{s}_1$ unit cell vectors are drawn in red. To more easily indicate with which unit cell vectors a given **CuP** molecule is connected to its neighbors, each porphyrin molecule is represented by a square with colored quadrants. The coloring of the quadrants indicates the unit cell vectors with which an adsorbate is connected to its four closest neighbouring porphyrin molecules. The usefulness of this notation is explained in Figure 3.17b, c and d for the case of **CuP** molecules at the border of an **M** and **S** domain. The molecules that are well within the **S** domain, and thus only have neighbouring molecules in this **S** domain, are marked $\mathcal{S}$, while molecules with only neighbors in the **M** domain are marked $\mathcal{M}$. Molecules at the border of the two domains, which thus have neighbours in both domains, are marked $\mathcal{MS}$. Some molecules have been numbered to aid the discussion, which will focus on the molecule labeled $\mathcal{MS}_2$. This molecule has eight direct neighbours, three of which are within the **S** domain ($\mathcal{S}_1$, $\mathcal{S}_2$, $\mathcal{S}_3$), three within the **M** domain ($\mathcal{M}_1$, $\mathcal{M}_2$, $\mathcal{M}_3$) and two at the border of the two domains ($\mathcal{MS}_1$ and $\mathcal{MS}_3$). Four of these eight neighbours $\mathcal{MS}_1$, $\mathcal{MS}_3$, $\mathcal{M}_2$ and $\mathcal{S}_2$, are connected to the central $\mathcal{MS}_2$ molecule by single **M** or **S** unit cell vectors: the molecule labeled

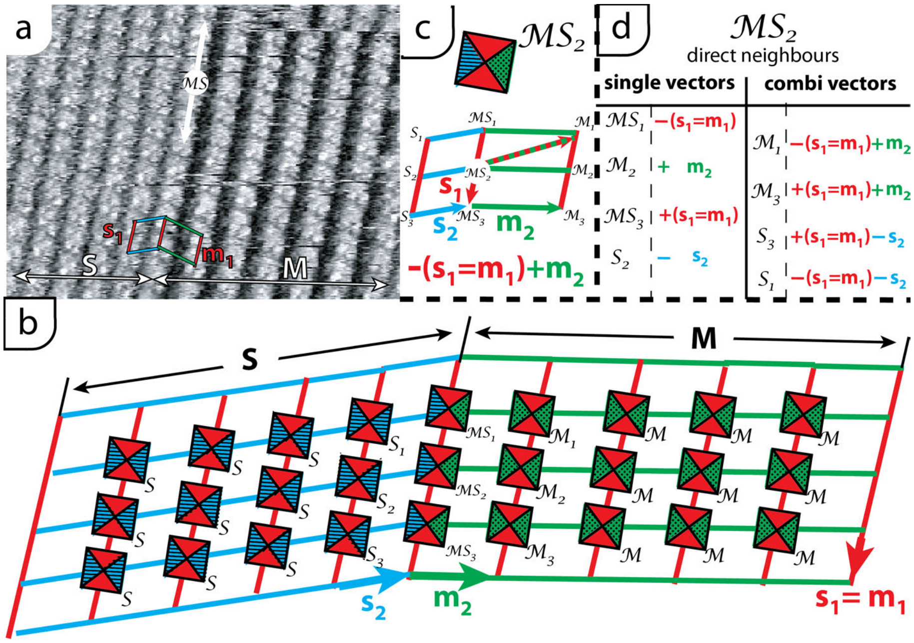

single vectors		combi vectors	
$\mathcal{MS}_1$	$-(s_1=m_1)$	$\mathcal{M}_1$	$-(s_1=m_1)+m_2$
$\mathcal{M}_2$	$+\ m_2$	$\mathcal{M}_3$	$+(s_1=m_1)+m_2$
$\mathcal{MS}_3$	$+(s_1=m_1)$	S_3	$+(s_1=m_1)-s_2$
S_2	$-\ s_2$	S_1	$-(s_1=m_1)-s_2$

Figure 3.17: STM image showing the coexistence of the **M** and **S** polymorphs formed by **CuP** on HOPG (a). A schematic representation of part of the STM image is drawn in image (b) in which the different unit cells are drawn in different colors. The $\mathbf{s}_1$ unit cell vector is drawn in blue, while the $\mathbf{m}_1$ vector is colored green and the vector that is shared between the **M** and **S** polymorphs ($\mathbf{s}_2 = \mathbf{m}_2$) is drawn in red. The colored squares represent porphyrin adsorbates and the color of the quadrants indicates through which unit cell vectors they are connected to their direct neighbors, as explained in the text. In image (c) it is shown that the vector connecting the molecule labelled $\mathcal{MS}_2$ to $\mathcal{M}_1$ is the sum of the vectors connecting it to $\mathcal{MS}_1$ and $\mathcal{M}_2$. The location of all direct neighbors of $\mathcal{MS}_2$ are summarized in image (d), from which it is apparent that the vectors connecting it to the four neighbours $\mathcal{MS}_1$, $\mathcal{M}_2$, $\mathcal{MS}_3$ and $\mathcal{S}_2$ completely define its adsorption configuration, since the positions of the other four neighbours are combinations of these vectors.

$\mathcal{MS}_2$ has four of its direct neighbors at $+(\mathbf{s}_1 = \mathbf{m}_1)$, $+\mathbf{m}_2$, $-(\mathbf{s}_1 = \mathbf{m}_1)$ and $-\mathbf{s}_2$, as is summarized in Figure 3.17d, in the colors corresponding to these unit cell vectors. The four quadrants of the square that represents the $\mathcal{M}_2$ molecule are also marked with the colours of these four vectors. The relative locations of these four neighbors, and the concomitant colouring of the quadrants also defines the locations of the other four neighbours of the molecule labeled $\mathcal{MS}_2$ (Figure 3.17c). The molecule marked $\mathcal{M}_1$ is found at $-(\mathbf{s}_1 = \mathbf{m}_1) + \mathbf{m}_2$, which is the sum of the vectors which connect $\mathcal{M}_2$ to its two neighbours *i.e.* $\mathcal{MS}_1$ and $\mathcal{M}_2$. The relative locations of the other neighbours can also be written as a combination of the four **M** and **S** unit cell vectors, as is demonstrated in Figure 3.17d. All direct neighbours of the molecule marked $\mathcal{MS}_2$ are thus defined by a combination of four **S** and **M** unit cell vectors, and its adsorption configuration is therefore also completely defined by the colouring of the four quadrants of its representing square. Molecules well within the domains of the **M** and **S** polymorphs, marked $\mathcal{M}$ and $\mathcal{S}$ respectively, can also be described by the combination of the four unit cell vectors that connect them to their direct neighbors. Throughout this thesis the term *adsorption configuration* will be used to refer to the relative locations at which the direct neighbours of a given porphyrin adsorbate are found. Calligraphic symbols ($\mathcal{L}$, $\mathcal{M}$, $\mathcal{MS}$, etc.) will be used to indicate adsorption configurations of molecules to avoid confusion with the bold face symbols (**M**, **S**, etc.) used for unit cells and domains. The adsorption configurations are also represented by the coloured squares in which the relative locations of four direct neighbours are explicitly indicated. From the schematic red coloured quadrants of the representing squares of **CuP** adsorbates in either an $\mathcal{M}$ or an $\mathcal{S}$ adsorption configuration, it can easily be seen that $\mathbf{m}_1 = \mathbf{s}_1$ is shared between the two polymorphs (Figure 3.5). Molecules in $\mathcal{M}$, $\mathcal{S}$ and $\mathcal{MS}$ adsorption configurations have two of their four closest neighbours at the same relative locations, which is indicated by the fact that their representing squares all have two quadrants coloured red. The other two closest neighbours are found at different vectors for the $\mathcal{M}$ and $\mathcal{S}$ adsorption configurations. A molecule at the border, which is in an $\mathcal{MS}$ adsorption configuration, has one of its other two neighbours in common with molecules in the $\mathcal{S}$ adsorption configuration and one with molecules in an $\mathcal{M}$ configuration, which can be quickly seen from the color patterns of the representing squares.

In Figure 3.18 the scope of the adsorption configurations is expanded to domains comprising the **M** and **B** surface structures. In the STM image in Figure 3.18a, a single lamella of **B** unit cells can be observed at the border between two large patches of the **M** polymorph. The molecules well within the patch of the **M** polymorph are in the $\mathcal{M}$ adsorption configuration, while the molecules that are in both **M** and **B** unit cells are in the $\mathcal{MB}$ adsorption configuration. The shared $\mathbf{m}_2 = \mathbf{b}_2$ unit cell vector is drawn in green, and the consequentially shared adsorption configuration between molecules in $\mathcal{M}$ and $\mathcal{B}$ adsorption configurations is emphasized by the green colored quadrants of their representing squares. The use of the term adsorption

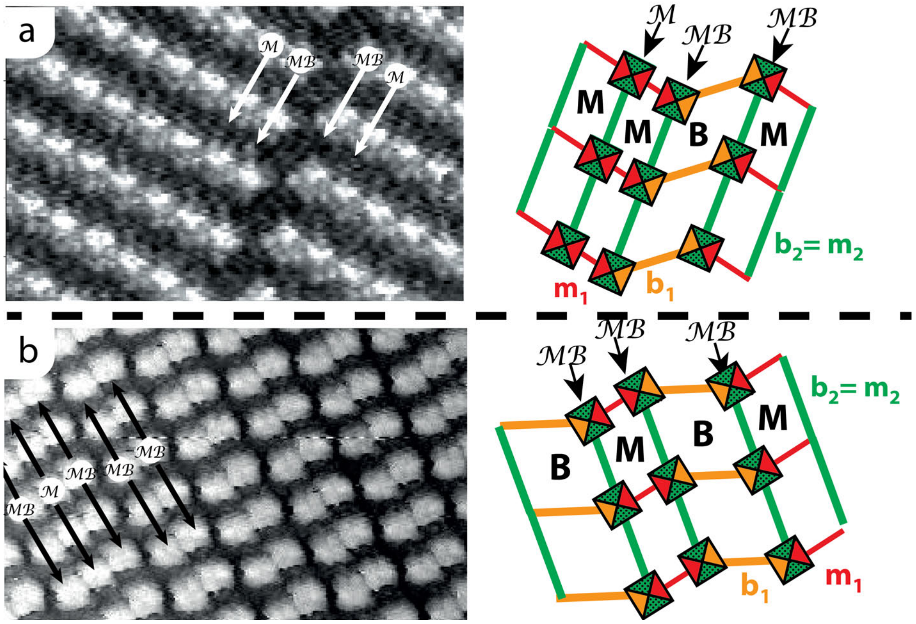

Figure 3.18: STM images showing the mixing of the **M** polymorph with the 1–dimensional **B** structure, formed by **CuP** on the HOPG/1-octanoic interface (left) and schematic representations of part of the STM image (right). Figure (a) shows the coexistence of the **M** and **B** structures and their sharing of the $\mathbf{m}_2 = \mathbf{b}_2$ unit cell vector. Figure (b) also shows the mixing of the **B** and **M** polymorphs, but with a much higher prevalence of the former. Molecules at the border of the different structures, which therefore truly are within both unit cells, are labeled $\mathcal{MB}$ in both (a) and (b). Molecules well within the **M** domain are labeled $\mathcal{M}$.

configuration empasizes the fact that molecules within an **M** domain, ($\mathcal{M}$), have different surroundings than molecules in an **B** lamella ($\mathcal{MB}$). In Chapter 4 it will be shown that the physical properties of **CuP** are different in $\mathcal{MB}$ and $\mathcal{M}$ adsorption configurations, as is apparent from differences in molecular contrast between them in images obtained from various scanning probe microscopy techniques. In Figure 3.18b, an STM image is shown in which the **M** and **B** surface structures occur in near one-to-one ratios. In a true one-to-one ratio domain (**MB**) every adsorbed **CuP** molecule is in an $\mathcal{MB}$ adsorption configuration. In the STM image in Figure 3.18b, some **CuP** adsorbates in the $\mathcal{M}$ adsorption configuration can also be observed within the majority of $\mathcal{MB}$ adsorbates. The relationship between the different molecular configurations is summarized in Figure 3.19. The porphyrins are depicted as squares which are drawn

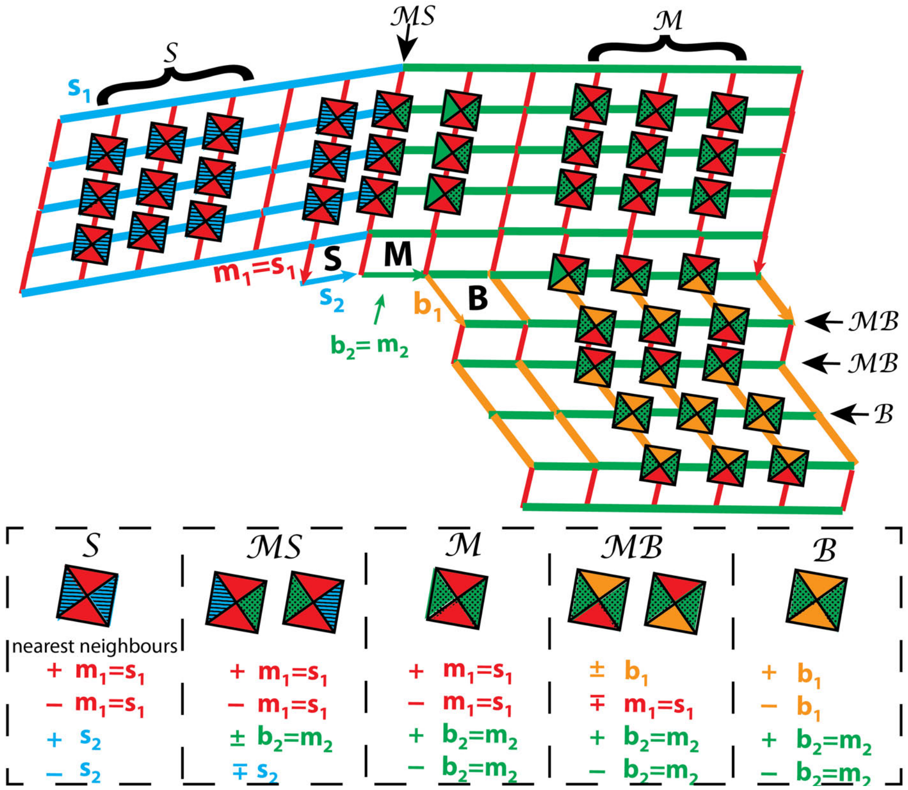

Figure 3.19: Schematic representation of **CuP** molecules in all possible adsorption configurations of the **B**, **M** and **S** polymorphs and at the borders of those domains (top part). Adsorbates in each of the five different adsorption configurations ($\mathcal{S}$, $\mathcal{MS}$, $\mathcal{M}$, $\mathcal{MB}$ and $\mathcal{B}$) are indicated and the coloring of the squares indicates the locations of the direct neighbours of the porphyrins in each adsorption configuration. The four unit cell vectors that connect a porphyrin in each conformation to its four nearest neighbors are given in the lower part of the schematic.

at the five possible adsorption configurations ($\mathcal{S}$, $\mathcal{MS}$, $\mathcal{M}$, $\mathcal{MB}$, $\mathcal{B}$) on a lattice in the top part of Figure 3.19, while in the bottom part the vectors at which their four closest neighbors are found are indicated. The colouring of the quadrants of the squares representing the porphyrins in different adsorption configuration signifies the parts of the adsorption configurations which are shared among the different polymorphs.

3.5 From shared adsorption configurations to shared molecular conformations

Now the different polymorphs formed by **CuP** on the HOPG surface have been discussed in both terms of their unit cells vectors and adsorption configurations, an attempt will be made to link the adsorption configuration and the shared unit cell vectors to the molecular conformations of the porphyrins adsorbates in the different adlayer structures.

3.5.1 Molecular conformation in the L polymorph

The first molecular structure under discussion is the largest polymorph, **L**. A high resolution STM image, together with the proposed molecular structure of **CuP** in the **L** polymorph, is shown in Figure 3.20. It should be noted that the monolayer domain shown in this image is the enantiomer of the domain from which previously the unit cell was determined (Figure 3.4a) . The unit cell vectors in Figure 3.20b are therefore obtained by mirroring and rotating the vectors from Table 3.3, using the operators described in Chapter 2:

$$\mathbf{R_{60}^{-1}M_y l}_1 = \begin{pmatrix} -5.7 \pm 0.3 \\ 7.9 \pm 0.3 \end{pmatrix}, \mathbf{R_{60}^{-1}M_y l}_2 = \begin{pmatrix} 8.8 \pm 0.2 \\ -0.1 \pm 0.2 \end{pmatrix}, \tag{3.7}$$

These unit cells are sketched in the STM image, the molecular structure and on the graphite lattice. The molecular conformation, with interdigitated alkyl chains, is highly similar to the one found by Chin *et al.*[47] for the $C_{19}H_{39}$ free base equivalent of **CuP**, as was shown in Figure 3.3a. In that case it was proposed, based on STM measurements and supported by DFT calculations, that the alkyl tails are slightly kinked upwards from the porphyrin ring when the porphyrins adsorb to the HOPG surface, and the bright lobes in their STM images were suggested to not only include the porphyrin macrocycle but also the kinked portion of the tails. This interpretation fits the STM data found for the **L** polymorph of **CuP** very well. The alkyl chains are adsorbed such that they align to the graphite $\langle 11\bar{2}0 \rangle$ directions, as do simple linear alkanes[69,70]. All four chains are thus adsorbed along the same graphite symmetry axis, which can be observed in both the STM image and the corresponding sketch of the molecular structure in Figure 3.20. The similar adsorption geometries of the

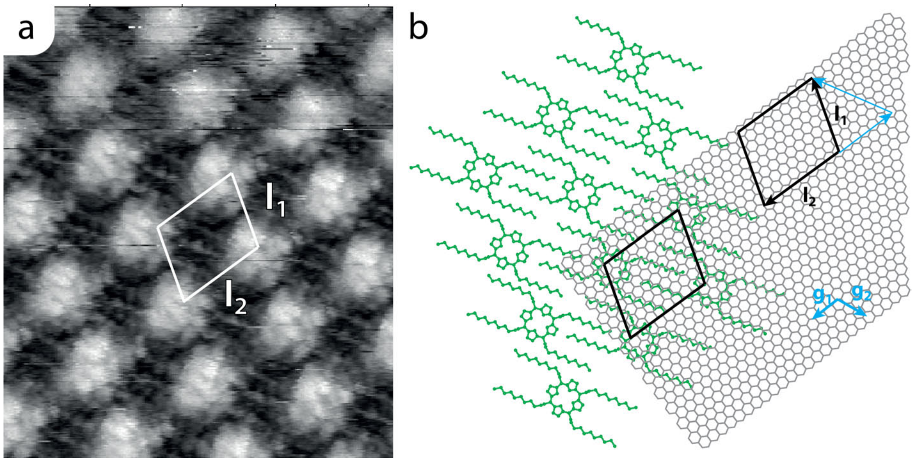

Figure 3.20: High resolution STM image of the **L** polymorph formed by **CuP** at the HOPG/1-octanoic acid interface (a) and a drawing of the molecular structure of this polymorph on top of part of a graphite lattice (b). The unit cell vectors are drawn in red on the STM image, the proposed molecular structure and the graphite lattice. $V_{bias} = 450$ mV, $I_{set} = 12$ pA, 8.5×9.5 nm^2.

adsorbed tails can be used to explain why the **a** unit cell vector, reported by Chin *et al.*, for the free base porphyrin with $C_{19}H_{39}$ tails is 2.17 ± 0.05 nm, and thus well within the range of the value of $= 2.16 \pm 0.14$ nm found for $\mathbf{l}_2$ of **CuP**. These vectors are not accidentally the same: when the proposed molecular structure in Figure 3.20 is closely examined, one can see the $\mathbf{l}_2$ unit cell vector, since it is nearly parallel to $\mathbf{g}_1$, has a negligible component along $\mathbf{g}_2$, the direction along which the tails are extended. Vector $\mathbf{l}_2$ therefore has almost no component along the alkyl chains and is thus not expected to be influenced by their length when the porphyrins are adsorbed in this conformation. The second unit cell vector for the free base porphyrin with $C_{19}H_{39}$ tails is larger than the value of the $\mathbf{l}_1$ vector of **CuP**, to allow for the accommodation of the longer alkyl tails. The fact that the tetra-*meso*-undecyl porphyrins studied here have a very similar surface structure as that reported for tetra-*meso*-nonadecyl porphyrins suggests that all *meso*-tetraalkylporphyrins with tail lengths ranging from $C_{11}H_{23}$ to $C_{19}H_{39}$ can form domains consisting of an **L** polymorph and moreover, that all these **L** unit cells have a unit cell vector close to the $\mathbf{l}_2$ vector found for **CuP**. However, care must be taken when data obtained for molecules functionalized with alkyl tails of an odd number of carbon atoms are extrapolated to molecules equipped with alkyl tails comprising an even number of carbon atoms, since odd—even effects have been shown to influence self-assembly behaviour at the solid/liquid interface in

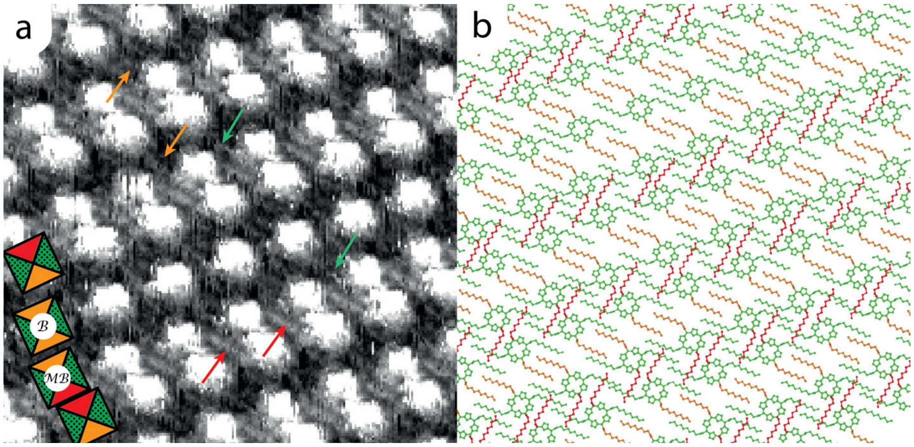

Figure 3.21: STM image of part of a **CuP** monolayer at the HOPG/1-octanoic acid interface (a) in which the porphyrins are adsorbed in $\mathcal{B}$ and $\mathcal{MB}$ adsorption configurations. The proposed molecular conformations are depicted in Figure (b) and the unit cell vectors are drawn in the schematic according to the values reported in Table 3.3. Image parameters: 17.5 × 17.5 nm^2, V$_{bias}$ $= -760$ mV, I$_{set}$ $= 25$ pA.

various ways[71]. It would therefore be interesting to investigate whether the porphyrin derivative with $C_{12}H_{25}$-alkyl tails, as reported by Visser *et al.*[48], also forms domains resembling the **L** polymorph at low concentrations of the supernatant solution, or that this behaviour is limited to porphyrins with tails containing of an odd number of carbon atoms.

3.5.2 Molecular conformations in the B, M and S polymorphs

As was argued in Section 3.3.5, the fact that the **B**,**S** and **M** polymorphs share unit cell vectors and thus have partially similar adsorption configurations, and because these unit cell vectors and adsorption configurations are largely determined by the interactions between different **CuP** adsorbates, it is proposed that the molecular conformations within the **B**, **S** and **M** surface structures are highly related. The molecular conformations in these structures will therefore be discussed collectively. Figure 3.21 shows a high resolution STM image and the proposed molecular conformations of **CuP** molecules in a domain in which the **B** and **M** polymorphs coexist. Molecules in this domain are in $\mathcal{MB}$ and $\mathcal{B}$ adsorption configurations, as indicated in Figure 3.21a. The molecular conformation of a **CuP** molecule in a $\mathcal{B}$ configuration is proposed to be similar to that of a molecule in the **L** polymorph. The unit cell vectors of these polymorphs show some resemblance and it is assumed that therefore also the molecular conformations are alike. From the STM image, all four alkyl tails appear to be extended along the same $\langle 11\bar{2}0\rangle$ graphite direction. These tails are drawn in orange and green in the schematic picture in Figure 3.21b, and some regions in the STM image, where they can most easily be observed, are indicated with green and orange arrows. The fact that the dimensions of the unit cell of the **B** polymorph are quite similar to that of the **L** polymorph forms the basis of the claim that the molecular conformations of the adsorbates in $\mathcal{B}$ and $\mathcal{L}$ adsorption configurations are similar. Because a **CuP** molecule in a $\mathcal{MB}$ adsorption configuration has the locations of three of its four closest neighbours in common with a **CuP** molecule in a $\mathcal{B}$ adsorption configuration it is suggested to have three of its for four alkyl tails adsorbed in a highly similar fashion as the alkyl chains of molecules in a $\mathcal{B}$ adsorption configuration (Figure 3.21): the green-coloured tails as well as one of the orange-coloured tails, are expected to retain highly similar conformations, while the fourth tail, which is colored red, is proposed to be adsorbed as a second layer on top of the green-coloured tails. The regions where the tails overlap, a few of which are indicated with red arrows in the STM image in Figure 3.21a, indeed appear higher than the regions where only tails are found that are directly adsorbed to the graphite. The increased apparent height caused by the bilayer of alkyl tails can more clearly be observed in Figure 3.22 where the area in between the porphyrin cores can be observed to be 30 pm higher in the **M** unit cells than in the unit cells of the **B** polymorph. The proposed relationship between the adsorption configuration and the molecular conformations extends beyond the $\mathcal{MB}$ and $\mathcal{B}$ configurations: when **CuP** molecules in an $\mathcal{MB}$ adsorption configuration are compared to molecules in an $\mathcal{M}$ adsorption configuration it is again suggested that the molecular conformations of three of the four tails are conserved, whereas the conformation of the fourth tail is changed. A high resolution STM image of an **M** domain and proposed molecular models of **CuP** in the $\mathcal{M}$ adsorption configuration is shown in Figure 3.23. It is proposed that the two green-coloured tails are adsorbed in a similar fashion as the green-coloured alkyl tails of **CuP** in $\mathcal{B}$ and $\mathcal{MB}$ adsorption configurations. This would explain the observed shared $\mathbf{m}_2 = \mathbf{b}_2$ unit cell vector between the **M** and **B** unit cells in a natural way. The red–coloured tails are proposed to be adsorbed in a similar fashion to those proposed for the $\mathcal{MB}$ conformation. The difference between a molecule in an $\mathcal{MB}$ conformation and a molecule in an $\mathcal{M}$ conformation is that the latter now has two tails adsorbed in conformations colored red, instead of just one. Locations of the STM image in Figure 3.23a where the overlapping tails may be most easily observed are indicated by red arrows. The adsorption geometry of the red-coloured tails deviates from that suggested by Visser *et al.*[48] for a similar porphyrin derivative with $C_{12}H_{25}$ alkyl chains. For that molecule it was proposed that only two of the four alkyl tails are adsorbed, while the other two are pointing away from the surface into the supernatant solution. The argument for that assumption was based on the fact that the unit cell is too small to accommodate all four alkyl tails on the HOPG surface. Although this reasoning seems sound, it is suggested for molecules of

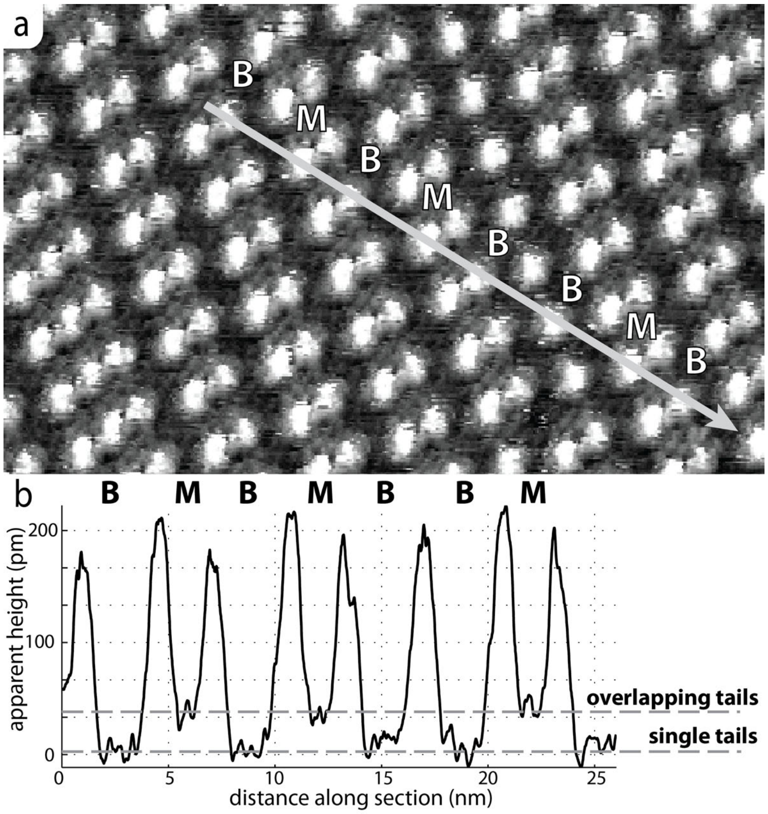

Figure 3.22: STM image (a) and cross section (b) showing the increased apparent height caused by the overlapping alkyl tails in the **M** unit cell compared to the **B** unit cell. Image parameters: 32 × 19 nm^2, V$_{bias} = -760$ mV, I$_{set} = 25$ pA.

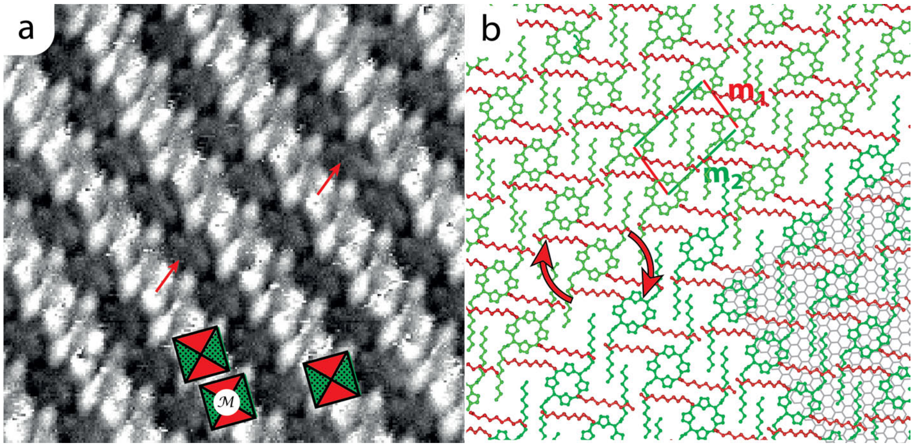

Figure 3.23: STM image of a domain of the **M** polymorph formed by **CuP** on the HOPG/1-octanoic acid interface with some schematic adsorption configurations drawn in (a) and a schematic of the proposed molecular conformations of **CuP** in the $\mathcal{M}$ adsorption configuration (b), in which the unit cell vectors are drawn according to the values in Table 3.3. Image parameters: 12×12 nm^2, V$_{bias} = -710$ mV, I$_{set} = 13$ pA.

CuP that the two non–fitting tails are partially adsorbed on top of the first layer of alkyl tails. Although the overlapping of alkyl tails of alkyl-functionalized molecules has not yet been reported in STM studies, the formation of an alkane bilayer has already been observed for long *n*-alkane molecules[72]. It was found that the apparent height of the bilayer in STM measurements can be indistinguishable from that of the alkane monolayer, which can be an explanation for the lack of height contrast in the STM images of regions where the tails were proposed to be adsorbed in the measurement of Visser *et. al.* In templating experiments, where molecular species adsorb as a second layer on top of a command layer of another species, alkyl tails were also found to adsorb on the aliphatic tails of layers of alkyl–functionalized molecules. The adsorption of hexakis(*n*-dodecyl)-*peri*-hexabenzocoronene (HCB-C_{12}) molecules on a template of *n*-$C_{50}H_{102}$ at the HOPG/*n*-tetradecane interface was reported by Piot *et al.*[73]. For this bicomponent layer, three different surface structures were found in which the six $C_{12}H_{25}$ alkyl tails are adsorbed in different conformations on the template. Den Boer *et al.*[54] reported the templating of **CuP** by a command layer of *p*-(hexadecyloxycarbonyl)phenylacetylene at the HOPG/*n*-phenyloctane interface. The reported bicomponent structure involved the adsorption of the alkyl tails of the **CuP** molecules on those of the template. These templating studies provide evidence that the adsorption of alkyl tails on alkanes or alkyl-functionalized molecules is in principle feasible. This suggests that also in the case that the alkyl tails originate from the same molecular species, the occurance of overlapping alkyl tails should be considered a viable option. In addition, since the occurrence of moiré patterns in monolayers of **CuP** sugggested that the primary forces governing the structure of the adlayer are those between the porphyrin adsorbates, the desorption of two alkyl tails seems unfavourable. These two tails would lose a substantial amount of Van der Waals interaction with the other alkyl tails and the adsorbed porphyrins.

It must be noted that the exact direction in which the second layer of alkyl tails is adsorbed is difficult to resolve from the STM images in Figure 3.23. These red-colored tails are drawn such that their connection to the porphyrin ring is rotationally equivalent by a four-fold rotation to the conformation of the green-coloured tails. A close comparison of the STM image in Figure 3.23a with the molecular drawing in Figure 3.23b might suggest that the red–coloured tails are more rotated in the direction indicated with by red arrows in Figure 3.23b. Due to the too low resolution, and, in addition, to the complex STM contrast of so many close and overlapping alkyl tails, this rotation cannot unambiguously be determined from the STM images. The exact adsorption geometry and conformation of these tails is expected to be an interplay of intramolecular within each alkyl chain and at the connection between the alkyl chain and the porphyrin core and intermolecular interactions between the alkyl tails of both layers. If the adsorption direction of the alkyl tails in the second layer would solely be be governed by the alkyl tails in the first layer, they would most likely be adsorbed at 60° angles with respect to the alkyl chains in the first layer. This leads to adsorption directions equivalent to the situation in which they would have been adsorbed directly to the HOPG surface. Such a geometry was proposed for the templated layer of hexakis(*n*-dodecyl)-*peri*-hexabenzocoronene (HCB-C_{12}) on *n*-$C_{50}H_{102}$[73] as well as that for the alkane bilayer[72]. To resolve these issues, extensive molecular modelling might be applied as part of future research.

The unit cell of the **S** polymorphs is even smaller than that of the **M** polymorph and the unambiguous determination of the conformation of molecules in the $\mathcal{S}$ configuration was found to be even more troublesome than for adsorbates in the $\mathcal{M}$ adsorption configuration. The proposed adsorption conformation of **CuP** molecules in the **S** polymorph is shown in Figure 3.24. The determination of the molecular conformation of the tetra-*meso*-undecylporphyrins is virtually impossible on the basis of the obtained STM images. It is again proposed that all tails are adsorbed instead of pointing in the supernatant solution, and that now two of the four tails are adsorbed on top of the other molecules rather than directly on the HOPG surface. These red-colored tails are proposed to be adsorbed in a similar fashion as was suggested for these tails in the **M** polymorph, because of the shared $\mathbf{m}_1 = \mathbf{s}_1$ unit cell vector between these two polymorphs. The blue-coloured tails, which are adsorbed directly on the HOPG surface, are proposed to be bent in the plane of the HOPG, because there is too little surface area to adopt a more extended conformation, as they did in the

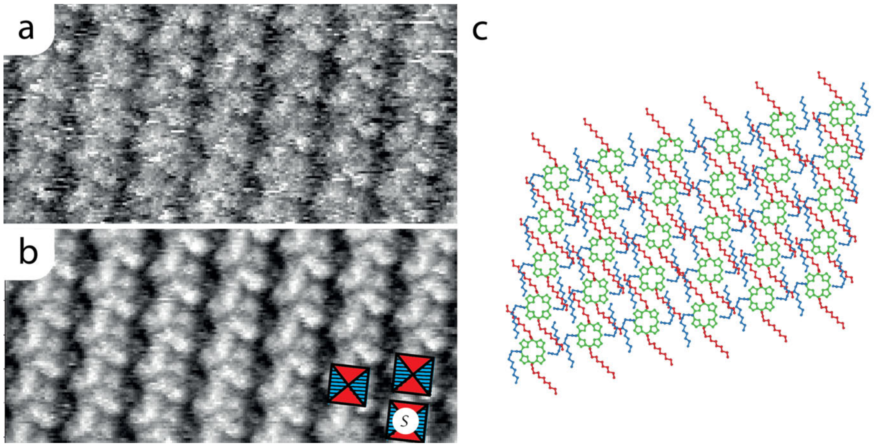

Figure 3.24: STM image of a domain of the **S** polymorph at the HOPG/decamethyltetrasiloxane interface (a), the same area enhanced by correlation averaging (b) and the proposed molecular conformations of molecules in the $\mathcal{S}$ adsorption configuration (c). The unit cell vectors are drawn in the schematic according to the values reported in Table 3.3 13 × 7 nm^2, V$_{bias} = -890$ mV, I$_{set} = 11$ pA.

M and **B** surface structures. This type of strongly bent conformation is expected to be unfavourable for the molecular adsorption energy, but it is the adsorption energy per unit of surface area, which is expected to be decisive for the formation of different surface structures[33]. Because the surface density of the **S** polymorph is 23 ± 10% higher than that of the **M** polymorph, the difference in surface free energy per unit area between these two polymorphs will be less than the difference in molecular adsorption energy caused by the less favourable molecular conformation of the alkyl tails in the **S** polymorph. The occurrence of bent alkyl tails has been proposed for other molecules upon self-assembly on a HOPG surface. STM data were reported for HCB-C_{12} molecules on a template of $C_{50}H_{102}$ and conformations were assumed in which the alkyl tails of the templated annulenes were bent[73]. Tahara *et al.* also reported bent aliphatic tails when alkyl- and alkoxy-functionalized dehydrobenzo[12]annulenes (DBAs) were adsorbed at the 1,2,4-trichlorobenzene/HOPG interface[74]. It is clear that there is great uncertainty in the conformations of the alkyl tails in the **M** polymorph and in particular of the alkyl tails in the **S** polymorph. In future investigations two main strategies may be employed to more accurately describe the adsorption geometry of the alkyl tails: STM in Ultra High Vacuum (UHV) at low temperatures, where their mobility and thermal motion is greatly reduced, and extensive molecular modeling using DFT, molecular mechanics or a combination of the two. Although the monolayers of **CuP** can be transferred to an UHV environment, as will be shown in Chapter 4.

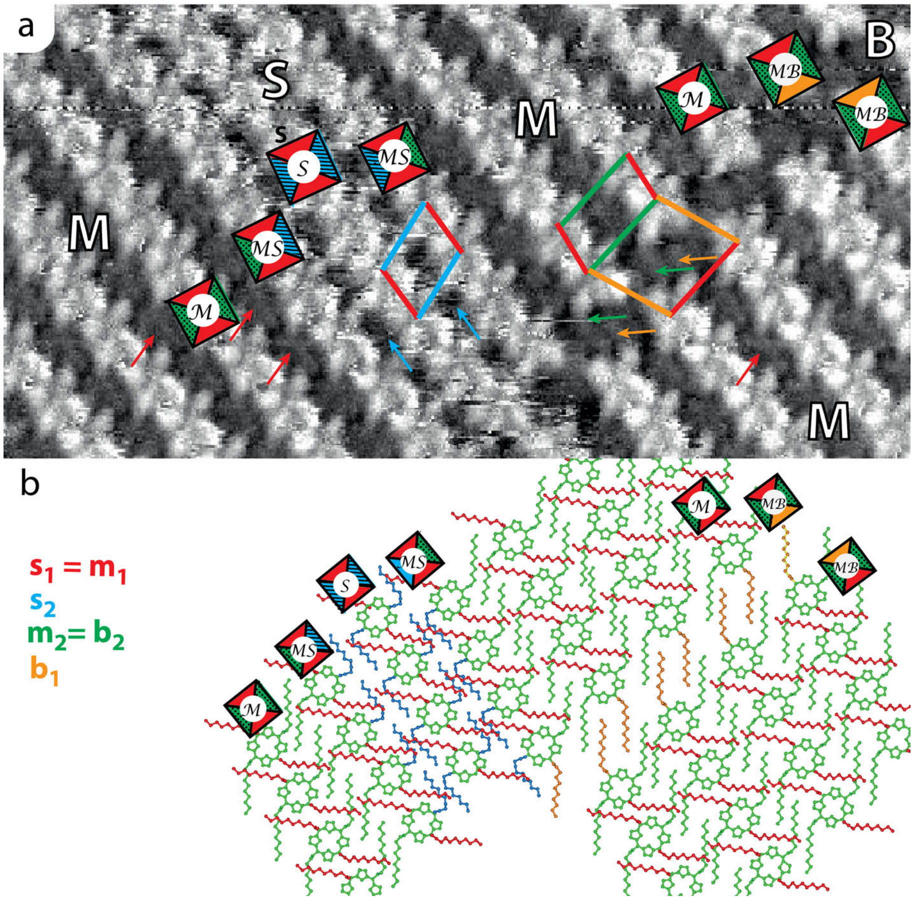

Figure 3.25: STM image in which molecules in the **M**, **B** and **S** surface structures can be observed (a) and a drawing of the proposed molecular structure of this layer (b). The adsorption configurations of some representative molecules are indicated on the same locations on both the STM image and the drawing of the molecular structures. Regions in which the alkyl tails can be most easily seen in the STM image are indicated by small arrows with colours corresponding to the colours used for different tails in the molecular structure drawing in (b). The molecular structure is drawn using the unit cell vectors reported in Table 3.3. 11.5 × 22.5 nm^2, V$_{bias} = -710$ mV, I$_{set} = 14$ pA

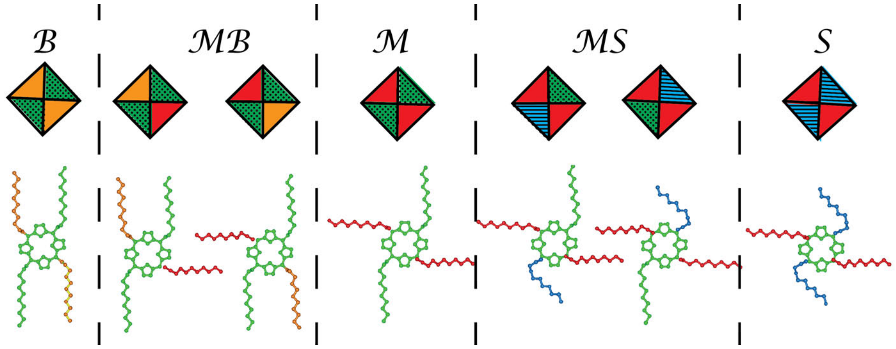

Figure 3.26: Drawings of the five proposed molecular conformations together with the squares representing the different adsorption configurations adopted by **CuP** on the HOPG surface.

An STM overview image in which the many relationships between the adsorption configurations and molecular conformations adopted by **CuP** at the HOPG surface can be observed is shown in Figure 3.25a. Besides the conformations corresponding to the previously shown $\mathcal{MB}$, $\mathcal{M}$ and $\mathcal{S}$ adsorption configurations, the conformation of porphyrins at the border of **M** and **S** unit cells, *i.e.* $\mathcal{MS}$, can be observed. The molecular conformation of this adsorption configuration is proposed to be a combination of the conformations of the $\mathcal{M}$ and $\mathcal{S}$ adsorption configurations. Two alkyl tails are proposed to have a highly similar conformation in both polymorphs (red) and also have the same conformation in the bordering, $\mathcal{MS}$ adsorption configuration, conformation. One alkyl tail is proposed to be strongly bent (blue), as proposed for alkyl tails in the **S** polymorph, and the other one in a more extended geometry (green), as observed in the **M** polymorphs. Regions in which the alkyl tails can be resolved are marked with arrows in the same color as that of the corresponding tails in the drawing in Figure 3.25b.

The relationship between the five stable adsorption configurations and the corresponding molecular conformations of **CuP** molecules in domains in which **B**, **M** and **S** coexist ($\mathcal{B}$, $\mathcal{MB}$, $\mathcal{M}$, $\mathcal{MS}$, $\mathcal{S}$), and their relationship to the adsorption configurations are summarized in Figure 3.26. The geometry of the four tails of a molecule in adsorption configuration $\mathcal{B}$ are proposed to be the same as for a **CuP** molecule in the **L** polymorph. All four tails are adsorbed in a symmetrically equivalent manner. Molecules at the border between a lamella of **B** unit cells, and a lamella of **M** unit cells (labeled $\mathcal{MB}$) have three tails adsorbed in the same conformation as those of molecules in an $\mathcal{B}$ adsorption configuration, and one tail in a different conformation (red). Another tail changes conformation upon going to an $\mathcal{M}$ configuration. When going from a $\mathcal{M}$ to an $\mathcal{S}$ adsorption configuration, one tail is proposed to change conformation in the bordering $\mathcal{MS}$ structure, and another one when going to the $\mathcal{S}$ configuration. In every step, three tails are thus proposed to retain their conformation, while the conformation of the other tail is proposed to change in correspondence with the change in adsorption configuration.

3.5.3 Discussion

In this chapter it was found that the different 2-dimensional polymorphs formed by **CuP** on graphite surfaces share some of their unit cell vectors. It was argued that partially similar molecular conformations of molecules of **CuP** in the different adsorption configurations underlie the partially shared adsorption configurations, and thereby the observed shared unit cell vectors. Even if the exact molecular conformations appear to be slightly different than reported, the underlying rational remains valid: **CuP** can form different polymorphs because of the conformational freedom of the alkyl tails in the adsorption process, and the sharing of the unit cell vectors between the different polymorphs is a result of partially shared molecular conformations. It should further be stressed that it is not claimed that the conformation of a given tail is solely responsible for the length of a unit cell vector and the angle with respect to the other unit cell vectors; the unit cell vectors arise from a complex interplay of forces between a molecule and all its direct neighbours and between the molecule and the underlying graphite. It is, however, claimed that the decisive difference between the unit cell vectors of the different polymorphs is the molecular conformation of the **CuP** molecules, of which the largest contribution is the conformational freedom of the alkyl tails. Furthermore it is claimed that some unit cell vectors of the different polymorphs are the same because part of the molecular conformation is the same. The alkyl tails are expected to be a major contributor to these similarities, but further investigation would be needed to determine which parts of the molecular structure of the adsorbates contributes to the sharing of the vectors. Besides extensive molecular modelling, an interesting expansion of the research on this matter would include the study of tetra-*meso*-alkyl derivatives in which a few of the four tails are replaced with shorter ones, in order to investigate with STM which, unit cell vectors are preserved. The formation of different polymorphs among which the conformation of the aliphatic tails of alkyl–functionalized molecules differs, has also been reported for the previously mentioned hexakis(n-dodecyl)-*peri*-hexabenzocoronene (HCB-C_{12}) on a templating monolayer of n-$C_{50}H_{102}$ at the HOPG/n–tetradecane interface[73]. Three different templated adlayer structures were formed on the same templating layer. Tahara *et al.*[74] reported the formation of five different polymorphs by alkyl- and alkoxy-functionalized bis(dehydrobenzo[12]annulene) (bisDBA) derivatives at the 1,2,4-trichlorobenzene/HOPG interface also resulting from conformational freedom of the alkyl chains. Although both these studies do not explicitly report shared unit cell

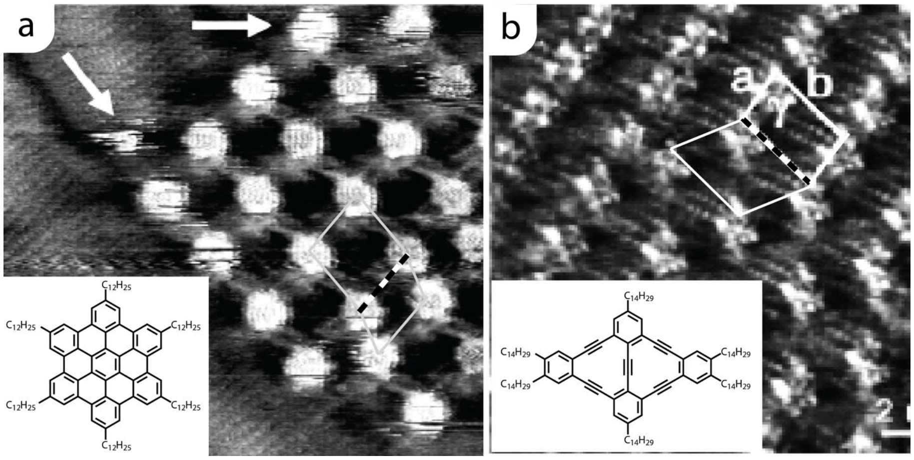

Figure 3.27: Two STM images from literature in which shared unit cell vectors (dashed) might be present, which we propose to result from shared conformations of the alkyl tails of these molecules. Image (a) shown as templated monolayer of hexakis(n-dodecyl)-*peri*-hexabenzocoronene (HCB-C_{12}) on layer of n-$C_{50}H_{102}$ at the HOPG/n-tetradecane interface as reported by Piot *et al.*[73]. The STM image in (b) shows part of a porous structure reported by Tahara[74] *et al.* for a bisdehydrobenzo[12]annulene (bisDBA) derivative with six $C_{14}H_{29}$ alkyl tails.

vectors, or the underlying shared conformations, careful investigation of the reported STM images shows that this mechanism might also be present in these cases. Two of these STM measurements are reproduced in Figure 3.27, in which the hereby proposed shared unit cell vectors indicated by the dashed line. Polymorphism with shared unit cell vectors might therefore be a more general property of alkyl-functionalized adsorbates. It is tentatively proposed that polymorphism caused by conformational freedom of alkyl tails, can lead to shared unit cell vectors whenever part of the molecular conformation is shared between molecules adsorbed in different surface structures. This is expected to be more prevalent for molecules in which the conformation of each tail is to a large extend independent from that of the others (*e.g* the stiffness of the porphyrin core of **CuP** allows the alkyl tails to assume different conformations without affecting the conformation of the other tails, for instance, by bending the porphyrin ring). Similar conformational decoupling mechanisms might underlie the self-assembly behavior of HCB-C_{12} and bisDBA in which the alkyl tails are also centred around stiff aromatic cores. To more precisely determine which molecular features underly the occurrence of shared unit cell vectors more research on a wider range of molecules would be needed. When this behaviour is better understood the use of shared unit cell vectors might be employed as a design parameter for self-assembled monolayers. For the creation of functional devices it is necessary to connect regions with different functionality and the shared unit cell vectors allow such connection in a stable, deterministic way, in contrast to adlayers of different species or different polymorphs in which the boundaries between different surface structures are stochastically formed and therefore difficult to control at the single molecule level.

3.6 Conclusions

In this chapter the surface structures formed by copper-tetra-*meso*-undecylporphyrins **CuP** were discussed. STM studies revealed three distinct 2–dimensional polymorphs (**L**, **M**, **S**) and one structure (**B**) that appears as 1–dimensional lamellae in coexistence with lamellae of the **M** polymorph. All unit cell vectors of the four surface structures **S**, **M**,**L** and **B** are summarized in Table 3.3. The ratio in which these polymorphs cover a given HOPG sample could be controlled by selection of the solvent and the concentration of **CuP** in the solution in which the monolayer was formed. From the observation of moiré patterns in the STM images of the monolayers, it was found that interactions between the porphyrin adsorbates are a more predominant factor governing the structure of the adlayers than the interaction of the molecules with the underlying graphite: the layers are coincident with the HOPG, implying that the HOPG dictates preferred adsorption directions of the **CuP** molecules, but not preferential adsorption positions. The research was expanded from **CuP** to the free-base and other metal derivatives of the same porphyrin scaffold, *i.e.* **NiP**, **ZnP** and **2HP**. These molecules formed the same 2-D polymorphs within experimental errors, and because all unit cell vectors of a given species are geometrically related to one another, it is proposed that the vectors are truly the same. This property is further exploited in Chapter 5 where monolayers comprising different **MP** derivatives will be examined.

The different surface structures formed by **CuP** were found to share unit cell vectors, and the term *adsorption configuration* was introduced to refer to the combination of unit cell vectors at which the four nearest neighbours of a given porphyrin adsorbate were found. The shared unit cell vectors between different adsorption configurations was explained by the proposing that part of the molecular conformations of molecules in different adjacent adsorption configurations is the same. This explanation is proposed here not only for alkyl-functionalized porphyrins, but it is suggested to explain the behaviour of a wider range of alkyl-functionalized molecules which can because of the shared molecular conformations self-assemble in different seamlessly connected 2-D polymorphs on a surface.

Table 3.3: Summary of the unit cell vectors of the three 2–dimensional polymorphs (**S**,**M**,**L**) and the 1–dimensional structure (**B**) formed by **CuP** on the HOPG surface. Values are reported as $mean \pm S.D.$

Polymorph	Vector	$\mathbf{g}_1$, $\mathbf{g}_2$	Length (nm)	Angle	Area (nm^2)
L	$\mathbf{l}_1$	$\begin{pmatrix} 7.9 \pm 0.3 \\ 5.7 \pm 0.3 \end{pmatrix}$	1.74 ± 0.08	$76^\circ \pm 5^\circ$	3.65 ± 0.30
	$\mathbf{l}_2$	$\begin{pmatrix} -0.1 \pm 0.2 \\ 8.8 \pm 0.5 \end{pmatrix}$	2.16 ± 0.14		
B	$\mathbf{b}_1$	$\begin{pmatrix} -0.2 \pm 0.2 \\ 7.7 \pm 0.3 \end{pmatrix}$	1.92 ± 0.09	$71^\circ \pm 4^\circ$	3.72 ± 0.26
	$\mathbf{b}_2 = \mathbf{m}_2$	$\begin{pmatrix} 9.1 \pm 0.2 \\ 7.3 \pm 0.2 \end{pmatrix}$	2.05 ± 0.05		
M	$\mathbf{m}_1 = \mathbf{s}_1$	$\begin{pmatrix} -2.9 \pm 0.1 \\ 3.0 \pm 0.1 \end{pmatrix}$	1.26 ± 0.05	$79^\circ \pm 4^\circ$	2.54 ± 0.12
	$\mathbf{m}_2 = \mathbf{b}_2$	$\begin{pmatrix} 9.1 \pm 0.2 \\ 7.3 \pm 0.2 \end{pmatrix}$	2.05 ± 0.05		
S	$\mathbf{s}_1 = \mathbf{m}_1$	$\begin{pmatrix} -2.9 \pm 0.1 \\ 3.0 \pm 0.5 \end{pmatrix}$	1.26 ± 0.05	$68^\circ \pm 4^\circ$	2.07 ± 0.16
	$\mathbf{s}_2$	$\begin{pmatrix} 8.0 \pm 0.5 \\ 5.0 \pm 0.5 \end{pmatrix}$	1.7 ± 0.15		

3.7 Outlook

Now the adlayer structures formed by **CuP** on HOPG/organic solvent, has been extensively described, influence of the polymorphs on the physical and chemical properties of the self-assembled monolayers can be investigated. In Chapter 5 the transformations of **CuP** monolayers upon changing the supernatant solvent will be discussed and the structural and dynamical properties of the monolayers, rather than the thermodynamical intricacies of the system, will be used to create multi–component monolayers. The influence of the different polymorphs on some of the local physical properties of the monolayers is subject of Chapter 4.The first steps towards investigation whether 2–dimensional polymorphism can be employed to tune chemical *i.e.* reactive properties of the molecular constituents of the monolayers is discussed in Chapter 6.

References

1. Drain C.M., Varotto A. and Radivojevic I. *Chem. Rev.*, 109 (5):1630–1658, **2009**
2. McMillin D.R. and McNett K.M. *Chem. Rev.*, 98 (3):1201–1219, **1998**
3. Liao M.S. and Scheiner S. *J. Chem. Phys.*, 117 (1):205–219, **2002**
4. Arasasingham R.D., He G.X. and Bruice T.C. *J. Am. Chem. Soc.*, 115 (18):7985–7991, **1993**
5. Collman J.P., Brauman J.I., Meunier B., Hayashi T., Kodadek T. and Raybuck S.A. *J. Am. Chem. Soc.*, 107 (7):2000–2005, **1985**
6. Biesaga M., Pyrzyńska K. and Trojanowicz M. *Talanta*, 51 (2):209–224, **2000**
7. Chinsky L., Turpin P., Alobaidi A.H.R., Bell S.E.J. and Hester R.E. *J. Phys. Chem.*, 95 (15):5754–5756, **1991**
8. Dougherty T., Kaufman J., Goldfarb A., Weishaupt K.R., Boyle D. and Mittleman A. *Cancer Res.*, 38 (8):2628–2635, **1978**
9. Kwong R.C., Sibley S., Dubovoy T., Baldo M., Forrest S.R. and Thompson M.E. *Chem. Mater.*, 11 (12):3709–3713, **1999**
10. Marée C.H.M., Roosendaal S.J., Savenije T.J., Schropp R.E.I., Schaafsma T.J. and Habraken F.H.P.M. *J. Appl. Phys.*, 80 (6):3381–3389, **1996**
11. Ambroise A., Kirmaier C., Wagner R.W., Loewe R.S., Bocian D.F., Holten D. and Lindsey J.S. *J. Org. Chem.*, 67 (11):3811–3826, **2002**
12. Jurow M., Schuckman A.E., Batteas J.D. and Drain C.M. *Coord. Chem. Rev.*, 254 (19-20, Sp. Iss. SI):2297–2310, **2010**
13. Li C., Ly J., Lei B., Fan W., Zhang D., Han J., Meyyappan M., Thompson M. and Zhou C. *J. Phys. Chem. B*, 108 (28):9646–9649, **2004**
14. Checcoli P., Conte G., Salvatori S., Paolesse R., Bolognesi A., Berliocchi A., Brunetti F., D'Amico A., Di Carlo A. and Lugli P. *Synth. Met.*, 138 (1-2):261–266, **2003**
15. Reid I., Zhang Y.F., Demasi A., Blueser A., Piper L., Downes J.E., Matsuura A., Hughes G. and Smith K.E. *Appl. Surf. Sci.*, 256 (3):720–725, **2009**
16. Beletskaya I., Tyurin V.S., Tsivadze A.Y., Guilard R. and Stern C. *Chem. Rev.*, 109 (5):1659–1713, **2009**
17. Otsuki J. *Coord. Chem. Rev.*, 254 (19-20):2311–2341, **2010**
18. Mohnani S. and Bonifazi D. *Coord. Chem. Rev.*, 254 (19-20):2342–2362, **2010**
19. Drain C.M., Batteas J.D., Smeauranu G. and Patel S. *Dekker Encyclopedia of Nanoscience and Nanotechnology*, 1 (1):3481–3502
20. Elemans J.A.A.W., Van Hameren R., Nolte R.J.M. and Rowan A.E. *Adv. Mater.*, 18 (10):1251–1266, **2006**
21. Beletskaya I., Tyurin V.S., Tsivadze A.Y., Guilard R. and Stern C. *Chem. Rev.*, 109 (5):1659–1713, **2009**
22. Palma C.A., Bonini M., Breiner T. and Samorì P. *Adv. Mater.*, 21:1383–1386, **2009**
23. Binnig G. and Rohrer H. *Helv. Phys. Acta*, 55 (6):726–735, **1982**
24. Lei S., Wang J., Dong Y.H., Wang C., Wan L.J. and Bai C.L. *Surf. Interface Anal.*, 34 (1):767–771, **2002**
25. Otsuki J., Nagamine E., Kondo T., Iwasaki K., Asakawa M. and Miyake K. *J. Am. Chem. Soc.*, 127 (29):10400–10405, **2005**
26. Yoshimoto S., Yokoo N., Fukuda T., Kobayashi N. and Itaya K. *Chem. Commun.*, (5):500–502, **2006**
27. Sugiura K., Tanaka H., Matsumoto T., Kawai T. and Sakata Y. *Chem. Lett.*, (11):1193–1194, **1999**
28. O'Sullivan M.C., Sprafke J.K., Kondratuk D.V., Rinfray C., Claridge T.D.W., Saywell A., Blunt M.O., O'Shea J.N., Beton P.H., Malfois M. and Anderson H. *Nature*, 469:72–75, **2011**
29. Lensen M.C., van Dingenen S.J.T., Elemans J.A.A.W., Dijkstra H.P., van Klink G.P.M., van Koten G., Gerritsen J.W., Speller S., Nolte R.J.M. and Rowan A.E. *Chem. Commun.*, (7):762–763, **2004**
30. Barth J.V., Costantini G. and Kern K. *Nature*, 437 (7059):671–679, **2005**
31. Lackinger M., Griessl S., Heckl W.A., Hietschold M. and Flynn G.W. *Langmuir*, 21 (11):4984–4988, **2005**
32. Lei S., Tahara K., De Schryver F.C., Van der Auweraer M., Tobe Y. and De Feyter S. *Angew. Chem. Int. Ed.*, 47:2964–2968, **2008**

33. Lei S., Tahara K., Tobe Y. and De Feyter S. *Chem. Commun.*, 46 (48):9125–9127, **2010**. 1359-7345

34. Miyake K., Hori Y., Ikeda T., Asakawa M., Shimizu T. and Sasaki S. *Langmuir*, 24 (9):4708–4714, **2008**

35. Samorì P., Engelkamp H., de Witte P., Rowan A.E., Nolte R.J.M. and Rabe J.P. *Angew. Chem. Int. Ed.*, 40 (12):2348–2350, **2001**

36. Elemans J.A.A.W., Lensen M.C., Gerritsen J.W., van Kempen H., Speller S., Nolte R.J.M. and Rowan A.E. *Adv. Mater.*, 15

37. Hill J.P., Wakayama Y. and Ariga K. *Phys. Chem. Chem. Phys.*, 8:5034–5037, **2006**

38. Lu J., Lei S.B., Zeng Q.D., Kang S.Z., Wang C., Wan L.J. and Bai C.L. *J. Phys. Chem. B*, 108 (17):5161–5165, **2004**

39. Burke S.A., LeDue J.M., Topple J.M., Fostner S. and Grutter P. *Adv. Mater.*, 21 (20):2029–2033, **2009**

40. Qiu X., Wang C., Zeng Q., Xu B., Yin S., Wang H., Xu S. and Bai C. *J. Am. Chem. Soc.*, 122 (23):5550–5556, **2000**

41. Satake A. and Kobuke Y. *Tetrahedron*, 61 (1):13 – 41, **2005**

42. Friedermann G.R., Halma M., Aparecida Dias de Freitas Castro K., Benedito F.L., G. D.F., Drechsel M.S., Mangrich A.S., das Dores Assis M. and S. N. *Appl. Catal. A*, 308:172 – 181, **2006**

43. Feiters M.C., Rowan A.E. and Nolte R.J.M. *Chem. Soc. Rev.*, 29 (6):375–384, **2000**

44. Chung T.D. and Anson F.C. *J. Electroanal. Chem.*, 508 (1-2):115 – 122, **2001**

45. Nanda A.K. and Kishore K. *Polymer*, 42 (6):2365 – 2372, **2001**

46. Shi C. and Anson F.C. *Inorg. Chem.*, 37 (5):1037–1043, **1998**

47. Chin Y., Panduwinata D., Sintic M., Sum T.J., Hush N.S., Crossley M.J. and Reimers J.R. *J. Phys. Chem. Lett.*, 2:62–66, **2011**

48. Visser J., Katsonis N., Vicario J. and Feringa B.L. *Langmuir*, 25 (10):5980–5985, **2009**

49. Gerritsen J.W., Boon E.J.G., Janssens G. and van Kempen H. *Appl. Phys. A Mater. Sci.*, 66 (Part 1 Suppl. S):S79–S82, **1998**

50. Gutzler R., Sirtl T., Dienstmaier J.F., Mahata K., Heckl W.M., Schmittel M. and Lackinger M. *J. Am. Chem. Soc.*, 132 (14):5084–5090, **2010**

51. Palma C.A., Bjork J., Bonini M., Dyer M.S., Llanes-Pallas A., Bonifazi D., Persson M. and Samorì P. *J. Am. Chem. Soc.*, 131 (36):13062–13071, **2009**

52. Kampschulte L., Werblowsky T.L., Kishore R.S.K., Schmittel M., Heckl W.M. and Lackinger M. *J. Am. Chem. Soc.*, 130 (26):8502–8507, **2008**

53. Yang Y. and Wang C. *Curr. Opin. Colloid Interface Sci.*, 14 (2):135 – 147, **2009**

54. den Boer D., Habets T., Coenen M.J.J., van der Maas M., Peters T.P.J., Crossley M.J., Khoury T., Rowan A.E., Nolte R.J.M., Speller S. and Elemans J.A.A.W. *Langmuir*, **2011**

55. Hulsken B., Elemans J.A.A.W., Gerritsen J.W., Khoury T., Crossley M.J., Rowan A.E., Nolte R.J.M. and Speller S. *New J. Phys.*, 11, **2009**

56. Hoshino A., Isoda S., Kurata H. and Kobayashi T. *J. Appl. Phys.*, 76 (7):4113–4120, **1994**

57. Hooks D.E., Fritz T. and Ward M.D. *Adv. Mater.*, 13 (4):227–241, **2001**

58. Last J.A., Hooks D.E., Hillier A.C. and Ward M.D. *J. Phys. Chem. B*, 103 (32):6723–6733, **1999**

59. Grimme S. *Angew. Chem. Int. Ed.*, 47 (18):3430–3434, **2008**

60. Linares M., Iavicoli P., Psychogyiopoulou K., Beljonne D., De Feyter S., Amabilino D.B. and Lazzaroni R. *Langmuir*, 24 (17):9566–9574, **2008**

61. Takahashi O., Kohno Y. and Nishio M. *Chem. Rev.*, 110 (10):6049–6076, **2010**

62. Tkatchenko A., Romaner L., Hofmann O.T., Zojer E., Ambrosch-Draxl C. and Scheffler M. *MRS Bull.*, 35 (6):435–442, **2010**

63. Chakarova-Käck S.D., Schröder E., Lundqvist B.I. and Langreth D.C. *Phys. Rev. Lett.*, 96 (14):146107–1,146107–4, **2006**

64. Barlow S.M. and Raval R. *Surf. Sci. Rep.*, 50 (6-8):201–341, **2003**

65. Lorenzo M.O., Haq S., Bertrams T., Murray P., Raval R. and Baddeley C.J. *J. Phys. Chem. B*, 103 (48):10661–10669, **1999**

66. Glöckler K., Seidel C., Soukopp A., Sokolowski M., Umbach E., Böhringer M., Berndt R. and Schneider W.D. *Surf. Sci.*, 405 (1):1 – 20, **1998**

67. Umbach E., Glöckler K. and Sokolowski M. *Surf. Sci.*, 402-404:20 – 31, **1998**

68. Cheng Z.H., Gao L., Deng Z.T., Jiang N., Liu Q., Shi D.X., Du S.X., Guo H.M. and Gao H.J. *J. Phys. Chem. C*, 111 (26):9240–9244, **2007**

69. Chen Q., Yan H.J., Yan C.J., Pan G.B., Wan L.J., Wen G.Y. and Zhang D.Q. *Surf. Sci.*, 602 (6):1256–1266, **2008**

70. Leunissen M.E., Graswinckel W.S., van Enckevort W.J.P. and Vlieg E. *Cryst. Growth Des.*, 4 (2):361–367, **2004**

71. Tao F. and Bernasek S.L. *Chem. Rev.*, 107 (5):1408–1453, **2007**

72. Watel G., Thibaudau F. and Cousty J. *Surf. Sci.*, 281 (1-2):L297–L302, **1993**

73. Piot L., Marchenko A., Wu J., Müllen K. and Fichou D. *J. Am. Chem. Soc.*, 127 (46):16245–16250, **2005**

74. Tahara K., Okuhata S., Adisoejoso J., Lei S., Fujita T., Feyter S.D. and Tobe Y. *J. Am. Chem. Soc.*, 131 (48):17583–17590, **2009**

CHAPTER 4

Polymorph dependent physical properties

4.1 Introduction

In Chapter 3 it was shown that tetra-*meso*-undecyl-porphyrins, **MP**, self–assemble at the HOPG/solvent interface and that they form several different 2-dimensional polymorphs. This chapter is concerned with the effect these different surface structures of **CuP** monolayers have on the physical properties of the **CuP** molecules. Understanding the relationship between the structure of a self-assembled monolayer and its physical properties allows one to fine tune these properties to optimize future devices and to use the same molecular building block for different functionalities. The influence of the different polymorphs and adsorption configurations on the physical properties of **CuP** were investigated using scanning tunneling microscopy (STM), non-contact atomic force microscopy (nc-AFM), scanning kelvin probe microscopy (SKPM) and tapping mode AFM (tm-AFM). The experimental environments in which the monolayers are examined, were expanded to include solvent free layers under ambient conditions as well as ultra-high vacuum (UHV). It will be shown that the different polymorphs in which **CuP** was found to self-assemble at the HOPG surface, have different electronic properties.

Polymorph dependent differences in physicochemical properties of self-assembled monolayers have been reported before. Burke *et al.* showed that the self–assembly into different polymorphs can affect the optoelectronic properties of 3,4,9,10-perylene tetracarboxylic dianhydride (PTCDA) molecules on a NaCl(001) surface substrate[1]. In etch pits they created on the NaCl surface the PTCDA molecules were found to form a more densely packed p2×4 adlayer structure than on terraces, on which the PTCDA molecules were found to adsorb in a p3×3 lattice. The photoinduced shift of the local contact potential difference (CPD) between the probe and the surface, as measured using non-contact AFM (nc-AFM) and scanning kelvin probe force microscopy (SKPM), was found to be different for the two adlayer structures upon irradiation with visible light. The optoelectronic properties of the monolayer were more bulk-like for the denser p2×4 structure and resembled those of the single molecules for the more weakly interacting p3×3 monolayers. The terminology used by Burke *et al.* nicely exemplifies that the density and thus the molecular surroundings of the PTCDA molecules are thought to constitute a direct and crucial influence on the properties of these monolayers. In another combined nc-AFM, SKPM study, Nikiforo *et al.*[2] reported that the free base porphyrin derivative 5,15-bis(2',6'-bis(3,3-dimethyl-1-butyloxy)phenyl)porphyrin can form two different surface structures, one in which the porphyrin ring is parallel to the underlying HOPG surface and one in which it is perpendicular to it. In the former case, in which the ring and the graphite surface are parallel, the surface work function of the adlayer/HOPG system is lowered by 50 mV as compared to bare HOPG. When the porphyrin ring is perpendicular to the surface, the work function is, however, the same as for clean HOPG. This shows that the work function of porphyrin monolayers on HOPG depends on the molecular orientation. Duhm *et al.*[3] showed, using ultraviolet photoadsorption spectroscopy (UPS) and X-ray photoelectron spectroscopy (XPS) that the ionization potentials of α,ω-dihexyl-sexithiophene (DH6T) and α-sexithiophene (6T) can change up to 600 meV, depending on whether they are lying flat on the Ag(111) surface or stand upright. Also for copper phthalocyanines (CuPc) a tilt-angle-dependent work function has been reported, based on X-ray studies[4,5]. These examples all assign differences in the properties of different surface structures to differences in the adsorption geometry, such as the tilt angle, of the individual adsorbates, rather than differences in the structure of the collective of adsorbates, as Burke *et al.* reported.

Comparison of the description by Burke *et al.* to the other examples given above, leads us to propose a dichotomy in the possible mechanisms underlying polymorph-dependent physicochemical properties of self-assembled monolayers. The example of Burke *et al.* suggests that, in their system, the difference in contact potential is caused by a collective property of the molecules in the polymorphs, while the other examples propose that the effect is caused by a change in adsorption geometry of the individual molecules. The question is thus whether any physical and chemical differences between the adsorbates in the different polymorphs are directly caused by direct intermolecular electronic interaction or that they are in principle differences in a single molecule property caused by the adsorption conformation of a molecule dictated by a certain polymorph. The former would present a collective property, while the second is the property of a single adsorbate, albeit induced by the presence of its neighbours.

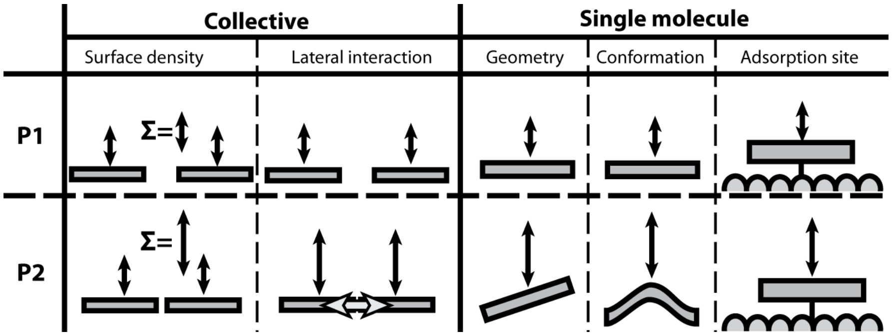

Figure 4.1: Overview of different interactions that could underlie differences in the physical properties of molecules in different polymorphs (P1, P2). A distinction is made between factors that are a collective property of the molecules in a certain polymorphs and factors that are a property of a single adsorbate. The physical property of a polymorph could simply be the sum of the interactions of the molecular constituents: a value which is higher for higher density polymorphs. Alternatively molecules in the different polymorphs might have different lateral intermolecular interactions, and thereby influence each others properties. At the single molecule level, adsorbates may be adsorbed at a height or angle to the underlying surface, have different molecular conformation or be adsorbed at a different site of the surface.

Several different interactions can be envisioned to influence the physical properties of an adsorbed molecule as a function of the polymorph it resides in. An overview of a selection of these interactions is presented in Figure 4.1. The influence of several potentially contributing factors is sketched for two hypothetical polymorphs, P1 and P2. The factors are split into those that stem from collective behavior of multiple adsorbates and factors that influence an adsorbate at the single molecule level. The first two interactions sketched in Figure 4.1, show how differences in the physicochemical properties could be caused by a collective property of the porphyrins in a polymorph, *i.e.* involving more than one adsorbate. In the simplest case the difference in physical properties of different polymorphs can be explained by a difference in the molecular surface density of the molecules in those polymorphs. A given physical property, such as the surface dipole moment or the total catalytic reaction rate, could simply be the sum of the interactions of several adsorbates over a given region. These interactions will then be proportional to the surface density of the polymorphs. Additionally, there may be lateral interactions between the adsorbates, and these intermolecular interactions could envisioned to be different for different relative positions of neighboring molecules. The physical properties are then not explained by the simple sum of the molecular interactions of individual adsorbates but an extra inter-molecular interaction should be taken into account. The collective properties by definition, require more than one adsorbate in a given polymorph to be of influence and changes in the local surface density or the locations of the nearest neighbors would have a profound influence on the local properties of the monolayer. Three options are presented that could influence the properties of the molecules in a self-assembled monolayer at the single molecule level. The first one summarizes the mechanisms proposed by Nikiforo *et al.*[2], Duhm *et al.*[3], Toader *et al.*[5] and Peisert *et al.*[4]. All these articles assign the polymorph dependent properties to a difference in the geometry of the molecular adsorbates with respect to the surface, such as the adsorpion height of the molecules, tilt angle or rotation in the plane of the substrate surface. A second possible mechanism are polymorph-dependent molecular conformations. Porphyrins are for example known to have distinct chemical and physical properties, which depend on the amount and type of bending of the porphyrin ring[6,7]. In different polymorphs the amount of bending might differ, thereby inducing changes in the physical or chemical properties of the molecules in the different polymorphs. A third possible mechanisms that might alter the physical and chemical properties of molecules adsorbed in different polymorphs is the difference in adsorption sites on the surface. The adsorption of molecules at different, specific adsorption sites might change their electronic coupling to the substrate and thereby influence their physical properties. This last option will not play a role for the polymorphs of **CuP**, since their monolayers formed on HOPG were found to be coincident to the graphite surface. This implies that within every single polymorph the adsorbates are already adsorbed at different sites with respect to the graphite. Although this might still influence the electronic properties of the porphyrins, as it to some extend does in the Moiré patterns itself, the influence is not polymorph dependent. The discussed options influence the adsorbate at the single molecule level, even though the differences are ultimately caused by 2–dimensional polymorphism. This implies that the effect would be present for a single molecule in the given geometry or conformation, irrespective of how this geometry or conformation is enforced on the molecule. Polymorphism is just a means to direct the adsorption of molecules in different geometries and in the accompanying conformations, but if one were able to place a single molecule in the desired conformation, *e.g.* via nanomanipulation or by trapping it in a specific nanoporous structure, one would observe the exact same change in physicochemical properties.

From biological systems it is known that both collective properties, as well as changes at the single molecule level, might alter the physical and chemical properties of porphyrins and other chromophores. The high quantum efficiency of the photosynthetic apparatus of the bacterium *Rhodospirillum photometricum* is mainly ascribed to the specific arrangement of the chromophores in the involved light harvesting complexes[8,9]. The observed spatial arrangement is thought to optimize the exciton transfer from one chromophore to the next, and is thus a collective property involving more than one molecule. Alternatively the properties of porphyrins

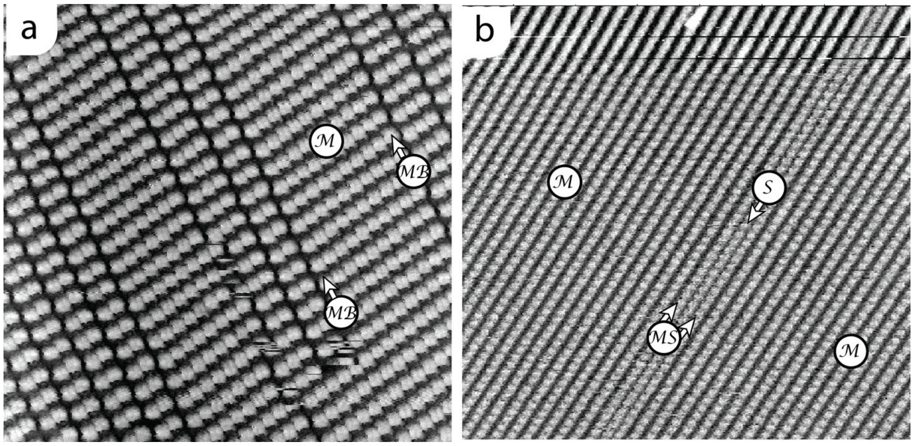

Figure 4.2: STM images of **CuP** monolayers at the HOPG/1-octanoic acid interface. In these images no difference in apparent height can be observed between porphyrin molecules residing in the different polymorphs, $\mathcal{M}$, $\mathcal{MB}$, $\mathcal{MS}$ and $\mathcal{S}$. Image parameters: $V_{bias} = -850\text{mV}$, $I_{set} = 10\text{pA}$, 50 × 50 nm^2 (a) and **CuP** at the HOPG/*n*-tetradecane interface $V_{bias} = -700\text{mV}$, $I_{set} = 6\text{pA}$, 70 × 70 nm^2 (b)

might be tuned by inducing structural changes at the single molecule level. A nice example of this is heme. This Fe-porphyrin derivative is employed to both bind and store oxygen, which it does in hemoglobin and myoglobin protein scaffolds, as well as to incorporate molecular oxygen into organic substrates, as it does in cytochrome P450. The ability to perform these two chemically quite distinct reactions is to a large extend caused by the protein scaffolds exerting a large degree of conformational control over the porphyrin macrocycle[6,7]. This shows that structural changes in an individual porphyrin can also cause differences in its physical and chemical properties. In this chapter we will explore these effects in monolayer structures. A variety of SPM methods will be used to establish a relationship between polymorphs, molecular conformations and electronic structures.

4.2 Apparent heights of the polymorphs in STM at the solid/liquid interface

The STM images in Figure 4.2 show self-assembled monolayers of **CuP** at the HOPG/1-octanoic acid (Figure 4.2a) and HOPG/n-tetradecane (Figure 4.2b) interfaces. Copper porphyrins adsorbed in $\mathcal{MB}$, $\mathcal{M}$, $\mathcal{MS}$ and $\mathcal{S}$ adsorption configurations, as explained in Chapter 3 can be identified. In these images, as in all the STM images shown in

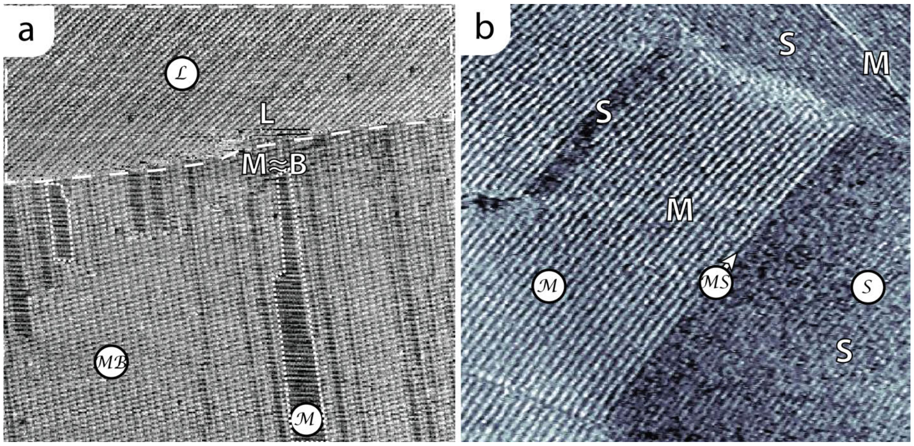

Figure 4.3: STM images of **CuP** at the HOPG/1-octanoic acid interface (a) and a monolayer created from a *n*-heptanic solution and imaged under ambient conditions (b). Although these monolayers are imaged using parameters well within the range of the previously used values, a difference in apparent height is visible between **CuP** molecules in the different adsorption configurations. In (a) it can be seen that porphyrins in the $\mathcal{M}$ adsorption configuration appear lower than **CuP** in $\mathcal{MB}$ and $\mathcal{L}$ adsorption configurations. The molecules in the $\mathcal{MS}$ and $\mathcal{S}$ adsorption configurations appear even lower than molecules in the $\mathcal{M}$ adsorption configuration as can be seen in image (b). Image parameters: $V_{bias} = -770$mV, $I_{set} = 7$pA, 180 × 180 nm^2 (a) and $V_{bias} = -450$mV, $I_{set} = 15$pA, 90 × 90 nm^2 (b)

Chapters 3 and 5, **CuP** molecules adsorbed in domains of the different polymorphs and thus in the different adsorption configurations, have nearly identical apparent heights: the apparent height of the porphyrin cores in the different adsorption configurations are indistinguishable. Similar to Figure 4.2 STM height differences between the different polymorphs are absent in the vast majority ($> 90\%$) of the STM images measured on monolayers of **CuP**. The situation is remarkably different in the other 10% of the STM images. The STM images displayed in Figure 4.3 show self-assembled monolayers of **CuP** on the HOPG surface in which the apparent height of the porphyrin cores strongly varies between the different polymorphs. The STM image shown in Figure 4.3a depicts a **CuP** monolayer at the HOPG/1-octanoic acid interface. It shows a domain of the **L** polymorph (top part, enclosed by the dashed line) as well as a domain consisting of linear arrays of **M** and **B** unit cells. The **CuP** molecules in the **M** domain appear lower than the same species adsorbed in both the **L** domain, and than molecules in $\mathcal{MB}$ adsorption positions. Molecules in the **S** polymorph ($\mathcal{S}$) or at the border between patches of the **M** and the **S** polymorphs ($\mathcal{MS}$)

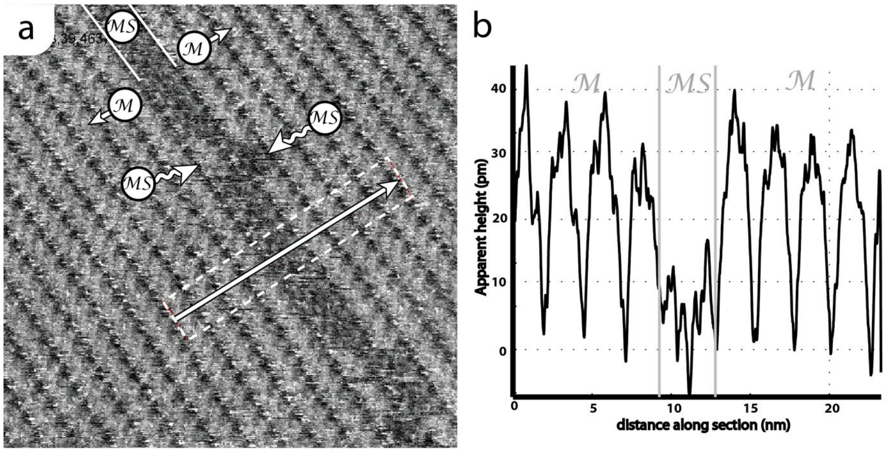

Figure 4.4: STM image of a **CuP** at the HOPG/*n*-tetradecane interface, displaying the lower apparent height of **CuP** in the $\mathcal{MS}$ adsorption configuration compared with those in $\mathcal{M}$ adsorption configurations. The molecules marked with wiggly arrows form a kink in the otherwise straight boundary between the **M** and **S** polymorphs, and show that the difference in apparent height is already present for two of molecules. A cross section taken along the arrow and averaged over the dashed rectangle is depicted in (b). Image parameters: $V_{bias} = -600$mV, $I_{set} = 8$pA, 40 × 40 nm^2.

in turn appear lower than molecules in $\mathcal{M}$ adsorption configurations. The imaging parameters with which these STM measurements were obtained, are well within the range of imaging parameters with which the STM images in the previous chapter were recorded, and the difference in apparent height can therefore not be attributed to a change in these experimental parameters. Rather than the image parameters, the chemical composition of the apex of the STM tip is suspected to be a decisive parameter in the visibility of the polymorph-dependent contrast. STM contrast has been reported to change[10,11], and even to reverse[12–14] upon changes of the chemical structure of the tip apex. The composition of the tip apex can change upon adsorption of atoms from the sample surface, as is commonly assumed to occur in STM measurements on metals[15], since the tip is in very close proximity to the surface and might occasionally come in contact with it. Besides atoms of the sample surface, other species may adsorb on to the tip and thereby influence the STM imaging contrast. The influence of different chemical species on the STM contrast is even been applied by intentionally chemically modify STM tips[14,16]. A more extensive description of the tip dependence of the polymorph dependent STM contrast is given in Appendix C

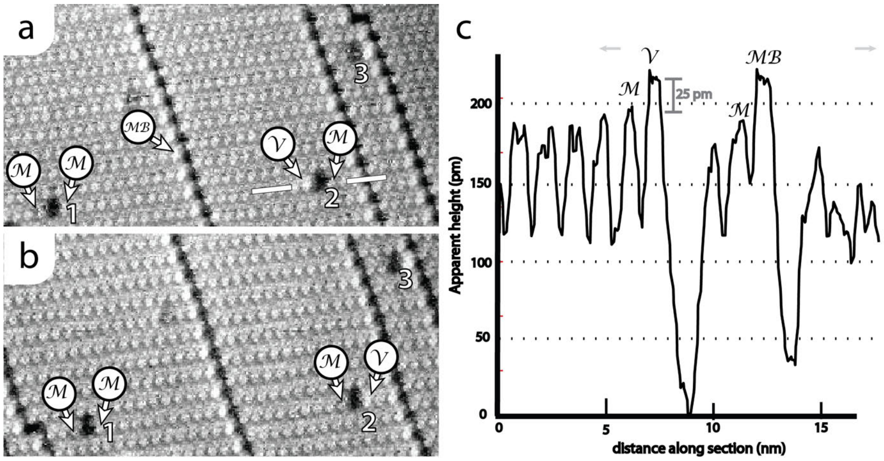

Figure 4.5: STM images (a,b) of **CuP** at the HOPG/octanoic acid interface depicting a domain comprising the **M** and **B** structures and three vacancies (1—3). A cross section taken along the marked line in Figure (a) is shown in Figure (c). At one side of vacancy 2 (left in (a) and right in (b)) a porphyrin adsorbate appears higher than the surrounding layer ($\mathcal{V}$). As is apparent from images (a) and (b) which were taken at the same location after a time interval of 2:15 minutes, the high feature can "hop" from one side of the vacancy to the other. $V_{bias} = -1350$mV, $I_{set} = 21$pA, 80 × 40 nm^2

Figure 4.4a shows another STM image of a domain of **CuP** in $\mathcal{MS}$ and $\mathcal{M}$ adsorption configurations. From the cross section in Figure 4.4b, which is averaged over the dashed area in Figure 4.4a and taken in the direction of the arrow, it can be observed that the apparent height difference between copper porphyrins in the $\mathcal{MS}$ and $\mathcal{M}$ polymorphs is ≈ 20 pm. An important observation can be made from the molecules marked with the wiggly arrows in Figure 4.4a . These molecules form kinks in an otherwise straight boundary between the **M** and **S** polymorphs. This shows that the polymorph-dependent contrast is already present in this small number of molecules and this suggests that the apparent height difference is a property of a single **CuP** molecule in a specific adsorption configuration, rather than being property of a large collection of molecules in a specific polymorph.

STM measurements, with which the apparent heights of **CuP** in a domain comprising of **M** and **B** unit cells can be quantified, are shown in Figure 4.5. This figure shows two consecutive STM images (Figure 4.5a and b), and a cross section (Figure 4.5c) taken between the markers in Figure 4.5a. From the cross section it can be deduced that molecules in the **B** lamellae, and thus in $\mathcal{MB}$ adsorption configurations, appear 20 pm higher than molecules in $\mathcal{M}$ adsorption configurations. Besides the **M** polymorph and the linear arrays of **B** unit cells, three vacancies (1—3) can be observed in the patches of the **M** surface structure. Two of the six porphyrin closest to these vacancies, also appear higher than molecules in the surrounding **M** patch. These apparently higher **CuP** molecules adjacent to a vacancy will be labeled $\mathcal{V}$ throughout this chapter. The fact that not all **CuP** molecules bordering the vacancies appear higher than molecules in the $\mathcal{M}$ adsorption configurations, provides a second clue that the surface structure dependent contrast is the property of a single adsorbed molecule rather than a property of the collective of adsorbates within a certain polymorph. A single vacancy, already induces a difference in apparent height for some of the neighboring porphyrin adsorbates: molecules bordering the vacancies in the $\pm\mathbf{m}_1$ direction, can appear at the height of the $\mathcal{MB}$ adsorbed molecule ($\mathcal{V}$) or at the height of a molecule in an $\mathcal{M}$ adsorption configuration. Close examination of the vacancy labelled "2" in Figure 4.5a shows that the high $\mathcal{V}$ can "hop" from one side of the vacancy to the other: in 4.5a the molecule at the left of this vacancy appears high ($\mathcal{V}$) while the right side appears as low as the molecules in the surrounding patch of the **M** polymorph ($\mathcal{M}$), and in Figure 4.5b this situation is reversed. Despite the identical molecular surroundings of these two situations, the molecules can appear at different apparent heights. This confirms that the effect is a single molecule rather than a collective property.

4.2.1 The role of molecular conformations

The molecular conformations of **CuP** on HOPG provide a good starting point to explain the differences STM contrast. A summary of the different apparent heights together with the adsorption configurations and the proposed molecular conformations is given in Figure 4.6. The molecular conformations of **CuP** shown here the $\mathcal{L}$, $\mathcal{B}$, $\mathcal{MB}$, $\mathcal{M}$, $\mathcal{MS}$ and $\mathcal{S}$ adsorption configurations were extensively discussed in Chapter 3. The relative positions of the four closest neighbors is tabulated in Figure 4.6. The approximate apparent heights of **CuP** in the different adsorption configurations, as measured with STM are depicted below the molecular drawings. The approximate apparent heights are given relative to adsorbates in the $\mathcal{M}$ adsorption configuration. It should be noted that the increased apparent height has not been observed for the $\mathcal{B}$ adsorption configuration, since this structure is only rarely observed. It is expected that it appears similarly to molecules in $\mathcal{MB}$ and $\mathcal{L}$ which have been observed to have similar, increased, apparent heights since it is proposed to have the same molecular conformation as adsorbed in the $\mathcal{L}$ configuration. First we focus on **CuP** molecules in the $\mathcal{M}$ adsorption position of the **M** polymorph. In STM measurements, this structure has an intermediate apparent height compared to the lower **S** and the higher **B** and **L** surface structures. Only a molecule well within a **M** domain, has this intermediate apparent height; molecules at the border between **M** and **S** ($\mathcal{MS}$) and at the boundary between **M** and **B** ($\mathcal{MB}$) have lower and higher apparent

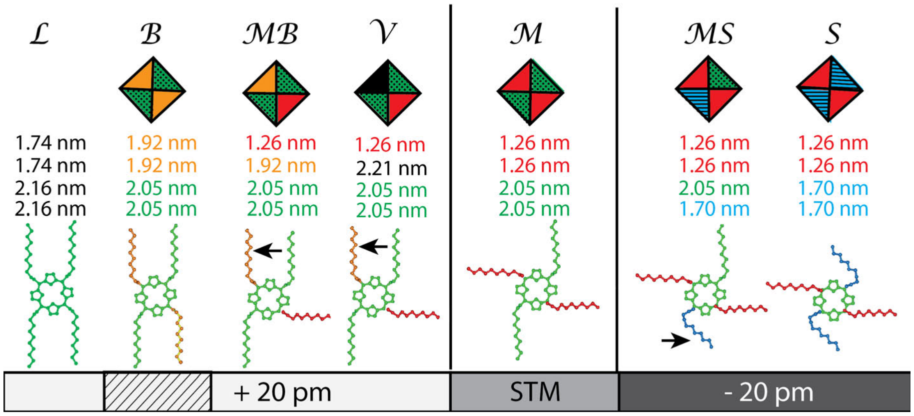

Figure 4.6: Summary of the apparent heights of **CuP** in STM, the corresponding adsorption configurations and the proposed molecular conformations that underlie these different apparent heights. Apparent heights are given in the bars below the molecular drawings. Values in the hatched sections have not been observed experimentally. In STM **CuP** molecules in $\mathcal{L}$, $\mathcal{MB}$, $\mathcal{V}$ and presumably those in $\mathcal{B}$ adsorption configurations appear 20 pm higher as those in $\mathcal{M}$ and **CuP** molecules in $\mathcal{MS}$ and $\mathcal{S}$ adsorption configurations appear 20 pm lower. The conformational changes of the tails are marked with arrows.

heights respectively. This implies that only a **CuP** adsorbate in an $\mathcal{M}$ configuration has the intermediate apparent height and changing one of its neighbors makes the adsorbed **CuP** molecule appear higher ($\mathcal{MB}$) or lower ($\mathcal{MS}$). The contrast does not substantially change between $\mathcal{MS}$ and $\mathcal{S}$ and between $\mathcal{MB}$ and $\mathcal{L}$. It is therefore proposed that a change in conformation of one decisive alkyl tail, alters the SPM contrast upon going from $\mathcal{M}$ to $\mathcal{MB}$ or $\mathcal{MS}$. These tails are marked with an arrow in Figure 4.6.

The hypothesis that differences in molecular conformations of the adsorbates are at the basis of the different SPM contrasts provides an elegant explanation for the observed "hopping" of the high $\mathcal{V}$ features adjacent to vacancies. Although the vacancies are occasionally encountered in low numbers in self-assembled **CuP** monolayers imaged under mild conditions they can be created in larger numbers by presenting the surface with a highly negative ($<$ -1000 mV) bias potential. The creation of these vacancies is discussed in more detail in Appendix B. Figure 4.7 shows two STM images recorded at the same area of a **CuP** monolayer at the HOPG/n-tetradecane interface recorded at a time-interval of 54 minutes. It shows a high density of artificially created vacancies. The majority of vacancies is characterized by a hole flanked by one bright feature ($\mathcal{V}$). Apart from one additional vacancy being formed (white circle), not a single vacancy has moved during this time period. The mobility of the vacan-

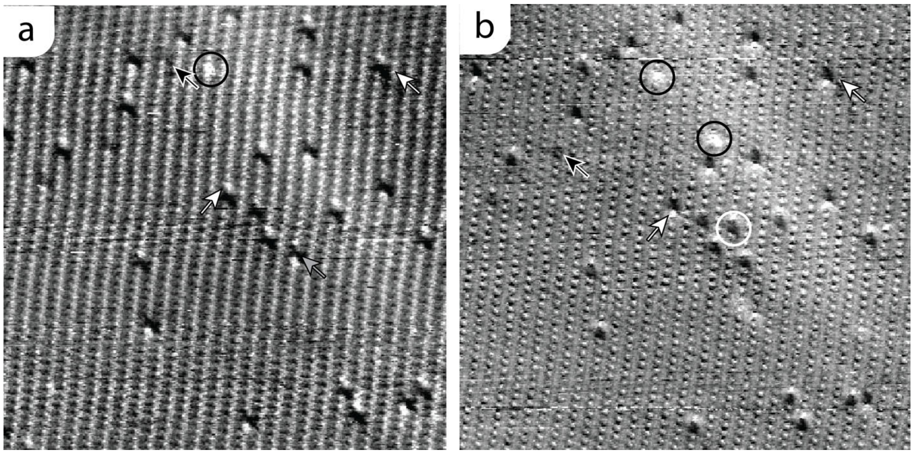

Figure 4.7: STM images of a **CuP** monolayer at the HOPG/*n*-tetradecane interface taken at a time interval of 54 minutes. The "hopping" of the high features adjacent to the vacancies can be seen V$_{bias} = -1335$ mV, I$_{set} = 35$ pA, 90 × 90 nm^2 (a,b)

cies themselves is thus very low. Further comparison shows that the high, $\mathcal{V}$, feature "hop" from one side of the vacancy ($\pm\mathbf{m}_1$) to the other ($\mp\mathbf{m}_1$). For instance for the vacancy marked with the white arrow in Figures 4.7a and b the high feature hops from top to bottom. A small number of vacancies has no high feature, an example of which is marked with a black arrow, or has bright features on both sides as indicated by the grey arrow. The high features marked with the black circles are thought to represent reduced **CuP** molecules (see Chapter 6). As discussed for Figure 4.5, the high feature adjacent to a vacancy in the **M** polymorph, is similar in apparent height to a **CuP** molecule in an $\mathcal{MB}$ adsorption position. Now we propose that molecules in these two adsorption configurations have similar apparent heights because they have similar molecular conformations, *i.e.* $\mathcal{MB} = \mathcal{V}$.

A quantitative analysis of the appearance the vacancies and of these high features in a series of 19 consecutive STM images, including those shown in Figure 4.7a and b, is given in Figure 4.8a. The chart shows that nearly equal amounts of the total of 803 observed, vacancies were found to have a high feature above (*i.e.* at $-\mathbf{m}_1$) or below ($+\mathbf{m}_1$) them: total of $82 \pm 9\%$ vacancies have a high feature at either side of it. The remainder contains vacancies with no higher-appearing neighboring molecule ($17 \pm 5\%$) and a very small fraction ($\approx 1\%$) is flanked by two bright **CuP** molecules. The proposed molecular conformations for **CuP** molecules surrounding a single vacancy are depicted in Figure 4.8b. The appearance of a molecule as a high feature is indicated by a grey dot on the corresponding molecule. In the simplest

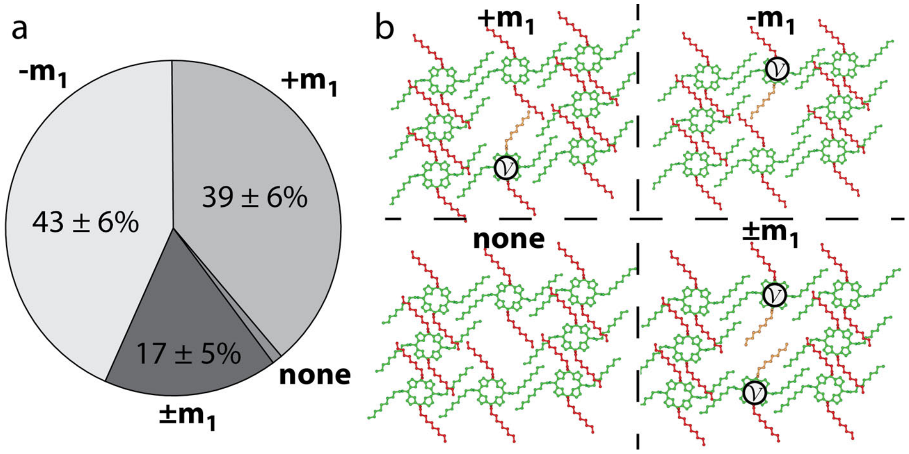

Figure 4.8: Pie chart (a) showing the percentage with which the high feature adjacent to a vacancy in a **CuP** monolayer appears at $+\mathbf{m}_1$, $-\mathbf{m}_2$, at both sides ($\pm\mathbf{m}_1$), and at neither sides (*none*). Image (b) shows the proposed molecular conformations for the four situations depicted in Figure (a).

case the molecules adjacent to the vacancy do not change conformation and remain adsorbed in exactly the same way as they would in a defect-free **M** domain. In such a situation, which is marked with "none" Figure 4.8a and b, none of the molecules adjacent to the vacancy appear as a high feature, as they all have the $\mathcal{M}$ adsorption configuration. However, the empty space of the vacancy can allow for one of the alkyl tails of an **CuP** molecule adjacent to the vacancy to change its conformation to one similar to the $\mathcal{MB}$ configuration. This is shown in Figure 4.8b, and labelled $+\mathbf{m}_1$ and $-\mathbf{m}_1$. A conformation at the vacancy to one similar to that of a molecule in an $\mathcal{MB}$ adsorption configuration would naturally explain the high degree of similarity between the apparent heights of these two adsorption configurations. The "hopping" of the high feature from $+\mathbf{m}_1$ to $-\mathbf{m}_1$ and *vice versa* is then simply the change of conformation of one of the porphyrins adjacent to the vacancy from a $\mathcal{V}$ conformation to the $\mathcal{M}$ conformations, together with the molecule on the opposite side of this vacancy changing from $\mathcal{M}$ to $\mathcal{V}$. The situation in which molecules at both $+\mathbf{m}_1$ and $-\mathbf{m}_1$ are in a $\mathcal{V}$ conformation is also sketched in Figure 4.8b. In Chapter 3 it was argued that the Van der Waals interaction between the alkyl tails in the monolayer is the main contributor to the structure of the monolayer. The occurrence of one high feature on one side of the vacancy is much more prevalent than the situation in which both sides occur bright and the situation in which none is bright. This suggests that the Van der Waals interaction for the molecules adjacent to a vacancy is apparently most favorable when just one adsorbate changes conformation to the $\mathcal{MB}$-like $\mathcal{V}$ conformation. Molecular modelling is required to quantify these energy differences. Although the high feature apparently "hops" from one side of the vacancy to the other, no **CuP** adsorbate changes its location on the surface. Instead the two porphyrins adjacent to the vacancy merely change the molecular conformations of their alkyl tails, which induces a change in the apparent height of the molecule.

In summary, it is proposed that the differences in apparent height between the polymorphs of **CuP** on HOPG are caused by differences in molecular conformation of adsorbates residing in these polymorphs. In different adsorption configurations the properties of the individual molecules are changed. The polymorphs, or more specifically, the locations of the neighbors of a given **CuP**, are therefore not the direct cause of the contrasts *but rather a means to induce conformational changes in the porphyrins adsorbates*. These conformation changes then lead to a change in the physical properties of the **CuP** molecules. In the next section it will be demonstrated by a combination of STM, AFM and SKPM that the variation in the apparent height between the different polymorphs is an electronic effect.

4.3 STM and AFM in air and vacuum

Hitherto, all studies on monolayers of **CuP** were concerned with the properties of these monolayers at the interface of HOPG and organic solvents. Although STM images can readily be taken at this interface, in order to extend the SPM studies to include Atomic Force Microscopy (AFM) it is more convenient to have access to the layers without any supernatant solvents. Such layers have been created from a heptanic solution of **CuP**. An HOPG sample was immersed in a 10^{-4} M heptanic **CuP** solution for half an hour, subsequently rinsed with clean heptane and dried in a gentle flow of nitrogen gas. Throughout this chapter these layers will be referred to as *dry* layers although no effort was made to ensure that no solvent molecules were left or that there was no water film adsorbed to the monolayer. An STM image of a dry layer prepared by this method is shown in Figure 4.9. The same structures as were reported for **CuP** at the HOPG/*n*-tetradecane, 1-octanoic acid, decamethyltetrasiloxane) interfaces can be identified. The polymorphic composition closely resembles those found when imaging a self-assembled **CuP** monolayer in a droplet of similar concentrations in *n*-tetradecane. Besides the **M**, **S** and **B** polymorphs, several holes can be observed in the monolayer. These holes could arise from a stronger preference for the formation of domains of the **S** polymorph under solvent free conditions, which would lead to a local increase in the occurrence of this denser polymorph and the concomitant shortage of **CuP** molecules elsewhere on the sample. They could also result from the excessive rinsing and accompanying desorption during the preparation of the monolayer. The formation of the holes was not examined in great detail.

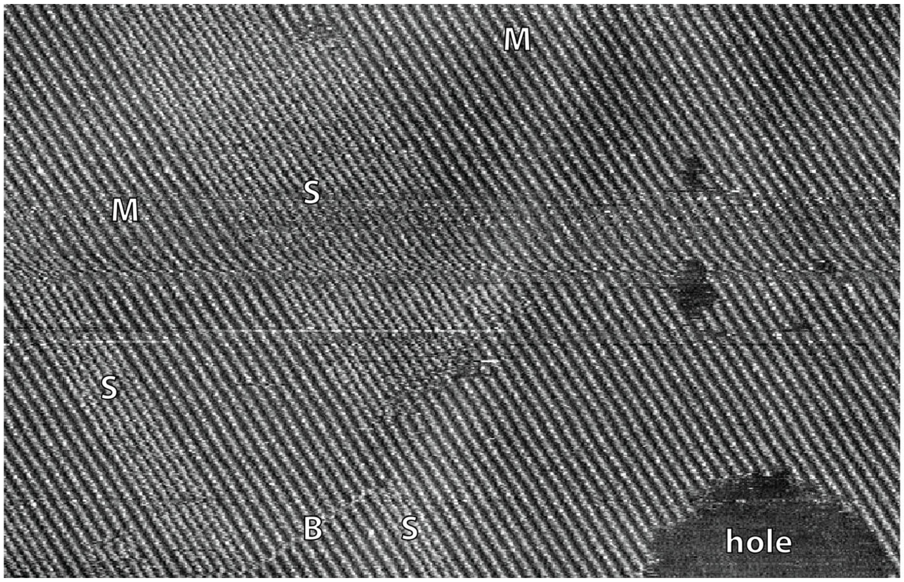

Figure 4.9: STM image of a self-assembled monolayer of **CuP** on HOPG created from a 10^{-4}M solution of **CuP** in *n*-heptane and imaged in air. The same **M**, **S** and **B** adlayer structures as were found at the HOPG/solvent interface can be identified. Some holes could also be observed in these dry layers. V_{bias}=-700mV, I_{set}=8 pA, 140 × 90 nm^2.

4.3.1 STM and nc-AFM in Ultra-high vacuum

Besides the aforementioned ambient conditions the layers can now also be studied Ultra–High Vacuum (UHV). An STM image of a **CuP** monolayer, created from a *n*-heptanic solution and imaged in UHV, is shown in Figure 4.10. Also in this case the same **B**, **M** and **S** surface structures can be identified. The polymorph-dependent height contrast is absent in this STM image. The number of STM images recorded in UHV is far lower than those recorded in ambient conditions and given the low occurrence of the polymorph-dependent contrast in STM, it is not known whether these apparent height differences are ever present in vacuum or not. Further studies would be required to assess the occurrence of the contrast in greater detail.

The STM image in Figure 4.10a was not recorded with a conventional STM tip. Rather, it was measured using a platinum coated AFM cantilever. This cantilever can be used for both STM and AFM measurements and thus allows one to apply both SPM techniques at the exact same location of the sample surface. An appropriate area was selected using non-contact AFM (nc-AFM) imaging, after which the tip was retracted, the oscillation of the cantilever was stopped and the tip was allowed to

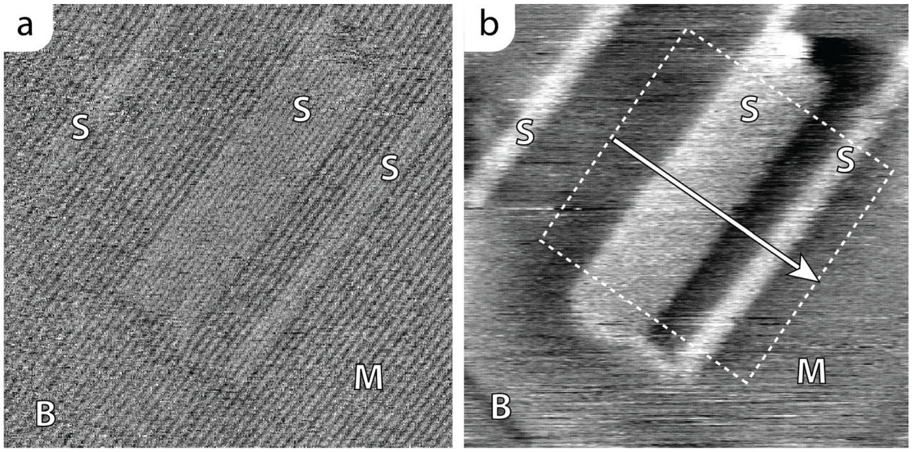

Figure 4.10: Ultra High Vacuum STM image (a) and nc-AFM image (b) of a self-assembled monolayer of **CuP** on HOPG. Figure (a) shows that the monolayers persist and that the same adlayer structures observed in liquid and are are present under vacuum conditions. Comparison between (a) and (b) clearly shows the apparent heights of the **M** and **S** polymorphs strongly differ in nc-AFM. The arrow indicates the direction in which the cross section shown in Figure 4.11 was taken. To reduce the noise, the cross sections within the dashed box were averaged. Image parameters: (a) V$_{bias}$=-800mV, I$_{set}$=50pA, 114 x 114 nm^2,(b) f_0=319.629kHz, =-310Hz, 114 x 114nm^2, V$_{bias}$=1000mV, MikroMasch NSC15Pt/NoAl. The images were recorded on a JEOL-JSPM4500A UHV SPM system.

re-engage with STM scan settings. After the STM measurements the tip was again retracted, the cantilever oscillation was restarted and an nc-AFM measurement was again performed. The switching between SPM modes allows for direct comparison between the apparent heights obtained using STM and those measured in AFM. This is demonstrated for a **CuP** monolayer in Figure 4.10a (STM) and b (nc-AFM). A remarkable difference between the contrast in the topography of the two polymorphs is immediately apparent: in nc-AFM the **S** polymorph appears much higher than the **M** polymorph. The difference between the apparent heights according to the two methods can more easily be seen in the cross sections shown in Figure 4.11. In this figure, two cross sections from the measurements shown in Figure 4.10, are depicted. The apparent height difference between the two polymorphs is found to be about 130 pm in nc-AFM while it is negligible in the corresponding STM measurement. The difference in apparent height in nc-AFM between the **M** and **S** polymorphs is an order of magnitude larger than it is whenever it appears in ambient STM measurements, and the contrast is reversed. Whereas in STM the **S** polymorph appears lower by

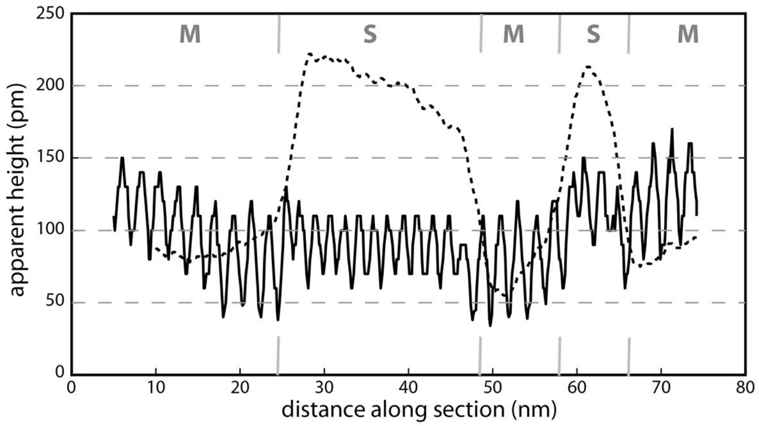

Figure 4.11: Averaged cross section from the STM and AFM images of Figure 4.10. The solid line represent the cross section in the STM image and the dashed line that of the same location in the nc-AFM image. The difference in apparent height between the **S** and **M** polymorphs is approximately 130 pm in the nc-AFM measurement while the **S** and **M** polymorphs in the STM cross section are at the same height.

about 20 pm than the **M** polymorph, in nc-AFM it appears approximately 100 pm higher. This observation strongly suggests that the observed apparent heights are not simply caused by different topographic heights.

Although the use of a platinum coated cantilever is very practical for the direct comparison between AFM and STM measurements, the thick, 25 nm, coating compromises nc-AFM resolution. Now the different polymorphs have been identified by comparison of STM and nc-AFM, sharper, uncoated AFM cantilevers can be used for further investigations. A higher resolution image, taken with a sharp cantilever is shown in Figure 4.12. The arrays of the **M** polymorph can clearly be identified, but the resolution in the direction of the shortest, shared, vector ($\mathbf{m}_1$) is still not high enough to identify individual molecules. Even with this higher resolution, no molecular resolution was obtained in the **S** polymorph. This suggests that the forces responsible for the increased apparent height of this polymorph in nc-AFM are of a long range nature. Even with the sharp Si tips, the **S** polymorph appears higher that the **M** packing, as can also be seen in the cross section shown in Figure 4.13. This demonstrates that the effect is not just caused by the interaction of the blunt AFM tip with a larger number of adsorbates in the higher surface density polymorph. Besides the **M** and **S** polymorphs, the linear arrays of **B** unit cells can be identified. This structure appears lower in nc-AFM than the **M** polymorph. Again, the appearance

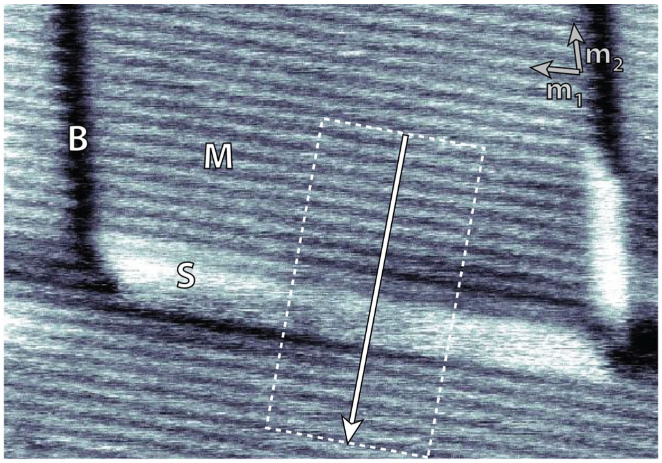

Figure 4.12: High resolution nc-AFM image of a monolayer of **CuP** on HOPG. The layer was made from a *n*-heptane solution and imaged in UHV. **M**, **S** and **B** are indicated. A cross section (see Figure 4.13) has been taken along the arrow, which has been averaged by the sections fitting in the dashed box. Image parameters:72 x 72nm^2,f_0=257.489kHz, =-53Hz, cantilever=MikroMasch NSC15/NoAl, V$_{bias}$=300 mV

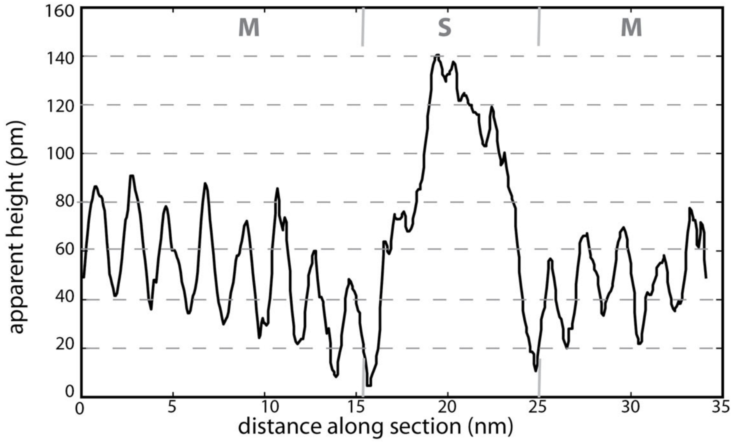

Figure 4.13: Cross section from the high resolution NC-AFM image of a monolayer of **CuP** on HOPG (Figure 4.12, as indicated by the box and arrow. Image parameters: 72 x 72nm^2,f_0=257.489kHz, =-53Hz, MikroMasch NSC15/NoAl cantilever.

of this structure is the opposite of the height contrast in ambient STM.

The fact that the polymorphs can now be identified by their height in nc-AFM allows one to search and identify the different polymorphs on large scale images with out the need of molecular resolution. Two such images are shown in Figure 4.14. These two images were obtained on two different samples of **CuP** on HOPG.

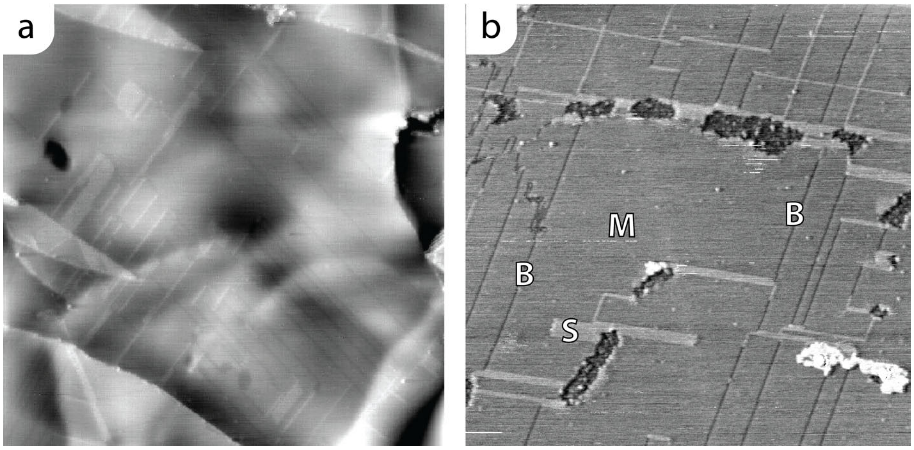

Figure 4.14: nc-AFM images presenting overviews of self-assembled **CuP** monolayers in UHV. 820×820 nm^2, MikroMasch NSC15Pt/NoAl, ${}_0$ =319.328 Hz, =-485Hz (a), 615×615 nm^2, MikroMasch NSC15Pt/NoAl, f_0 =359.653 Hz, =-487Hz (a)

4.3.2 Scanning Kelvin Probe Force Micoscopy

The contrast in Atomic Force Microscopy is a result of *forces* between the apex of the AFM tip and the sample surface. Of all the forces contributing to the contrast in AFM images such as Van der Waals forces, Pauli repulsion, dipole–dipole interaction, electrostatic interaction, *etc.*, one can be separated from the others: the electrostatic force that arises from differences in work function between the probe and the sample surface, the contact potential difference(CPD). In Scanning Kelvin Probe Microscopy (SKPM) the electrostatic force resulting from the CPD is compensated at each pixel of the AFM image. This is achieved by modulating the electrostatic force and adjusting the bias voltage such that the electrostatic force is completely cancelled. This implies that the difference in work function is not only measured: one locally corrects for it and thereby cancels the electrostatic forces between tip and sample at every location of the image. This yields, besides a map of the work function, an nc-AFM image which is closer to the "true" surface topography.

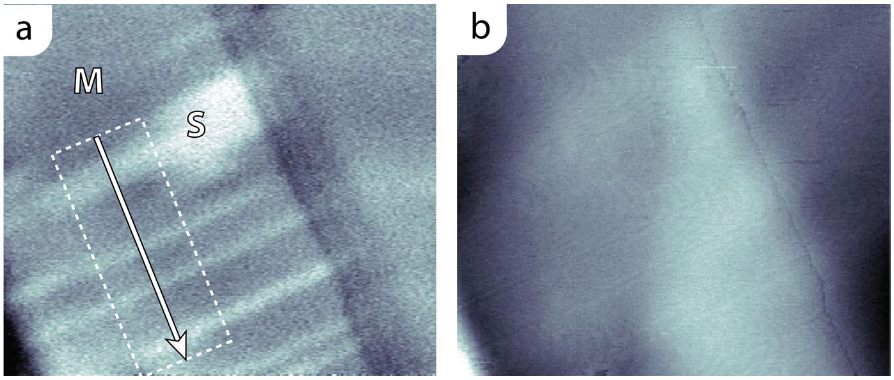

Figure 4.15: nc-AFM based Kelvin probe measurement consisting of a map of the local Contact Potential Difference (a) and a CPD-corrected topographic image (b). In the CPD image, the **S** polymorph appears higher than the surrounding **M** polymorph. In the topographic image it can be seen that, when compensating for the local CPD, the apparent heights of these two different polymorphs vanishes. Image parameters: 130 × 130 nm, $= 486$Hz, f_{mod}=1kHz, A_{mod}=1V, MikroMasch NSC15Pt/NoAl, the brighter the color in (a), the lower the CPD.

A SKPM CPD image of **CuP** monolayers on HOPG is shown in Figure 4.15a from which it is clear that the **S** and **M** polymorphs differ in contact potential. The simultaneously recorded height image shows the large topographical features, such as the graphite steps, but the height difference between the polymorphs is no longer present. This implies that the difference in contact potential between the polymorphs is responsible for the large height differences between them in nc-AFM. It is therefore proposed that the differences in physicochemical properties of the **CuP** adsorbates in the different polymorphs are of electronic origin. The contact potential difference is quantified in Figure 4.16. The work function difference is seen to be approximately 50 meV for the largest **S** domain. The smaller **S** domains show a lower value. Whether this is caused by lack of compensation for the CPD due to insufficient feedback or that it is an intrinsic property is not known and would require further research.

4.3.3 Ambient Tapping Mode AFM

The dry **CuP** monolayers were also studied using ambient tapping mode AFM (tm-AFM) with which the polymorph dependent contrast could also be observed, as is displayed in Figure 4.17. The sequence of the contrast is same as in the STM images at the solid/liquid interface, *i.e.* **B** > **M** > **S**, and thus inverted compared to the nc-AFM measurements performed in UHV. The magnitude of the contrast in

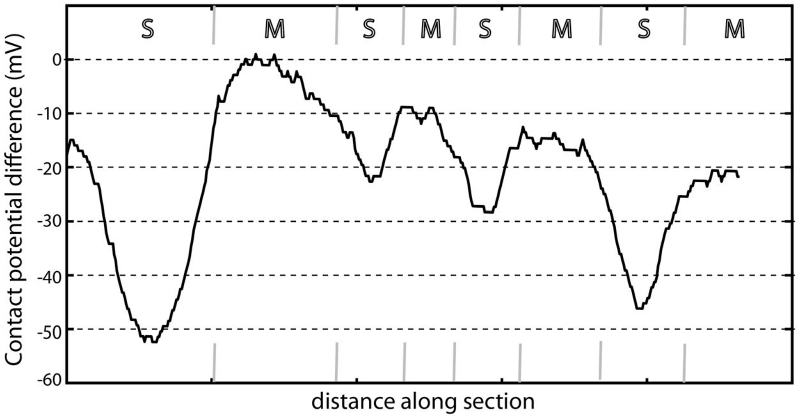

Figure 4.16: Cross section of the SKPM image in Figure 4.15a. The **S** polymorph has a -50 mV lower CPD with the cantilever than the surrounding **M** polymorph.

tm-AFM is the highest of all investigated techniques: molecules in the linear arrays of the **B** unit cell appear 500 pm higher than molecules residing within the **M** polymorph, while molecules in the **S** polymorph appear 300 pm lower. The pronounced polymorph-dependent contrast allows for identification of the different adlayer structures of **CuP** using the commonly used technique of tm-AFM, even at image sizes of several micrometers. This allows for faster and more elaborate investigation of the homogeneity of the layers and for the investigation of the layers for a wider range of possible applications such as the templating of protein crystal growth[17].

4.4 Physical origins of the polymorph dependent contrast

The height images acquired by any SPM technique display the superposition of the true topography of the sample and the variation of the probed in interaction over the sample surface. The fact that the different polymorphs have different apparent heights in, for instance, STM therefore suggests that the porphyrins are adsorbed at different heights above the surface, that there is a polymorph dependent difference in electronic levels of the adsorbates or a combination of these two options. Under the assumption that apparent height contrasts in nc-AFM have the same physical origin as those in STM, a significant difference in adsorption height between the polymorphs can be excluded. In the SKPM measurements the height differences vanish and all polymorphs are observed to have the same apparent height. Furthermore, differences in the adsorption height do not explain the large variation between the magnitudes

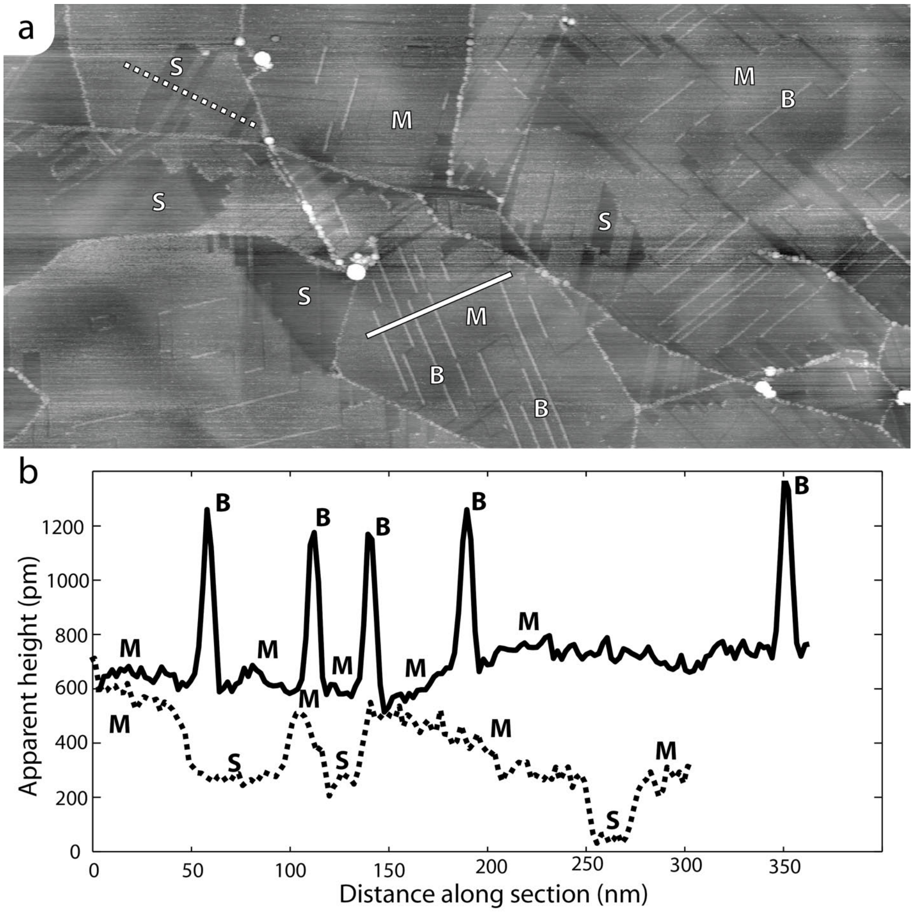

Figure 4.17: Ambient tapping mode AFM image of a dry **CuP** layer on HOPG, created from a heptanic solution (a) and two cross sections displaying the apparent height differences between the **M**, **S** and **B** adlayer structures (b). Image parameters: Veeco Nanoscope 4, Mikro Masch NSC 18 cantilever, 2.2 μm × 1.0 μm^2.

of the apparent heights in the different techniques and the contrast inversion between STM and nc-AFM measurements. It also does not explain why the contrast is only present in a 10% minority of the STM images. Electronic effects are the most likely cause for the polymorph dependent contrast in both STM and AFM. The next sections will be devoted to the exploration of the possible processes that lead to electronic differences between **CuP** adsorbates in the different polymorphs.

4.4.1 From tail conformation to altered electronic properties

In this chapter the different polymorphs of **CuP** were examined using a combination of scanning probe microscopy techniques (*i.e.* STM, nc-AFM, SKPM and tm-AFM) and the different polymorphs were found to have different apparent heights in these techniques. A summary of all observed SPM heights is given in Figure 4.18, from which it is apparent that the contrast not only differs in the magnitudes of the apparent heights between the different SPM techniques, but that the contrast is actually inverted between the different SPM techniques. Although **B** and **S** can both appear both higher or lower than **M**, the **M** polymorph is always the middle one. Therefore the apparent height of the porphyrin cores in this polymorph is used as reference value in Figure 4.18. Several mechanisms that alter the electronic properties of **CuP** at the single molecule level and which could be induced by conformational freedom of the alkyl tails, are depicted in Figure 4.19. Due to the conformations of the tails, the porphyrin core may be rotated in the plane of the graphite (Figure 4.19a), be tilted at different angles with respect to the graphite basal plane (Figure 4.19b) or be adsorbed at a different height with respect to the HOPG surface(Figure 4.19c). Although none of these mechanisms can be fully excluded as a contributor to the difference in electronic properties between the monolayers, these mechanisms seem inconsistent with the observed shared unit cells between the different polymorphs. An elegant alternative, which could explain both the imaging contrast while allowing for the shared unit cell vectors, is based on the non-planar distortion of the porphyrin ring as a result of the conformational freedom of the alkyl tails as sketched in Figure 4.19 d. This non-planar deformation of the porphyrin ring, as are the other proposed mechanisms in Figure 4.19 involve rearrangements of the atomic nuclei constituting the molecules. An alternative to atomic rearrangements are rearrangements of electrons. However purely electronic rearrangements are not sufficient to explain the differences in the electronic properties. The interaction between the porphyrins and the HOPG is exclusively due to dispersive Van der Waals forces and π–π interactions, and that the graphite surface terminated at its basal plane has no net dipole moment. Furthermore a purely electronic rearrangement does not explain why a single molecule can have different properties than its neighbors without any form of reciprocity, *e.g.* why molecules in $\mathcal{MB}$ adsorption configurations appear high, while their the directly neighboring porphyrins in $\mathcal{M}$ adsorption configurations do not seem to have even a

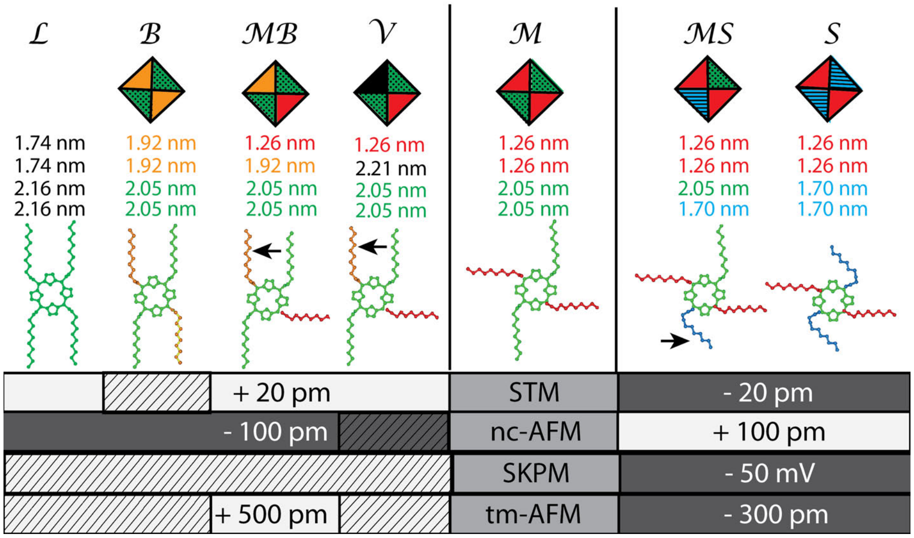

Figure 4.18: Summary of the apparent heights of **CuP** in STM, nc-AFM, tm-AFM and SKPM, the corresponding adsorption configurations and the proposed molecular conformations that underlie these different apparent heights. Apparent heights are given in the bars below the molecular drawings. Values in the hatched sections have not been observed experimentally. The conformational changes of the tails are marked with arrows.

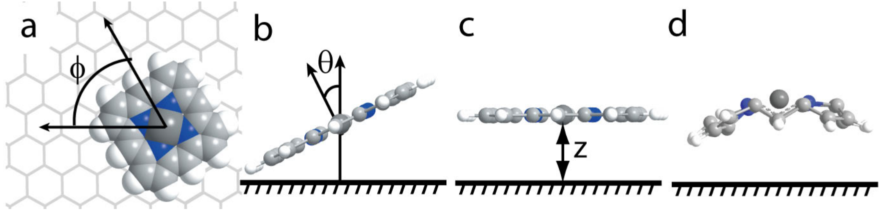

Figure 4.19: Schematic drawings of four possible mechanisms that could underlie the different apparent heights of **CuP** in different adsorption configurations, which would be apparent at the single molecule level. The sketch in (a) shows the rotation of the porphyrin core parallel to the HOPG surface. The drawings in (b) and (c) depict differences in the adsorption angle and the height of the porphyrin ring with the substrate surface respectively, while image (d) sketches non-planar distortion of the porphyrin macrocycle.

slight increase in their apparent heights.

Nonplanar deformations of the porphyrin macrocycle are known to influence various physical and chemical properties of the porphyrin such as solvation[18], intramolecular hydrogen bonding[19], redox potential[20,6,7], optical properties[20,6,7,21], spin delocalization[20], axial ligation[18,22,6] and π–π interactions[6]. In proteins these nonplanar distortions are found to fine-tune physical and chemical properties of porphyrin cofactors *in vivo* and to allow the same cofactor, *e.g.* heme, to be utilized for different chemical reactions[7,6]. The protein scaffold can thus induce and alter the nonplanar distortion of porphyrin rings. In synthetic porphyrins nonplanar macrocycle ring deformations have been induced by decoration the ring with a high number of sterically demanding substituents[23,24,20], by asymmetric distribution of substituents[23–27] and by altering the central metal atom[28]. It has also been reported that the porphyrin ring can deform upon adsorption to a surface[29,30]. Yokoyama *et al.*[29] reported that free base 5,10,15,20-tetrakis-(3,5-di-tertiary-butyl phenyl) porphyrin (**H_2-TBPP**) undergoes a saddle-shaped nonplanar deformation upon adsorption to the Au(111) surface. This deformation was caused by the tilting of the bulky 3,5-di-tertiary-butyl phenyl substituents. Brede *et al.*[30] reported that on different crystallographic planes of copper and depending on the phenyl periphery, CuTPP and CoTPP undergo different nonplanar distortions. It is here argued that the macrocycle of **CuP** undergoes polymorph dependent non-planar distortion. The possible deformations of the porphyrin macrocycle are described effectively as a linear combination of the deformations corresponding to the six lowest energy vibrational modes normal to the porphyrin ring[22,6,31,25,20]. These deformations, named *Saddle*, *Dome*, *Ruffle*, *Wave-x*, *Wave-y* and *Propellor*, are depicted in Figure 4.20. Two mechanisms might contribute to the differences in electronic properties that underlie differences in SPM contrast between the **CuP** polymorphs: the creation of a permanent dipole moment and shifting of the frontier orbitals. For free base porphyrins, which only have two-fold symmetry, the occurrence of a permanent dipole moment in the order of 1-2 Debye (3.3-6.6 10^{-30}Cm) was found for saddle-shaped porphyrin rings[27]. This dipole moment is due to the fact that the two central protons are tilted to the same side of the porphyrin ring in the saddle conformation and this is thus caused by the non-equivalence of the pyrrolenine (without N–H bond) and the pyrrole (with N–H bond) rings. In metalloporphyrins saddle-type deformations are not expected to lead to a permanent dipole moment orthogonal to the plane spanned by the four nitrogen atoms, since the metal center remains within the plane of the porphyrin (Figure 4.20a). In dome-type deformations, however, the metal center is pulled out of the plane of the porphyrins (see Figure 4.20b), and this type of deformation could lead to a permanent dipole moment upon adsorption. That nonplanar distortion can also shift the frontier orbitals is known from spectroscopic studies. The π–π^* adsorption band has been reported to undergo red shifts upon distortion of the porphyrin ring of several metalloporphyrins. A clear manifestation of the influence of the non-planarity on the frontier orbitals is

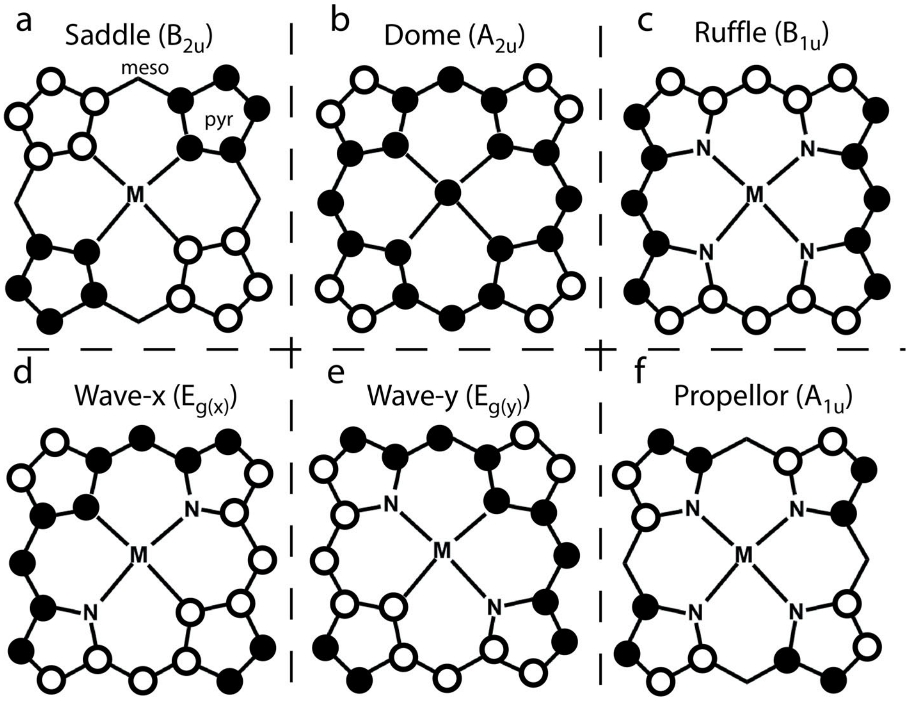

Figure 4.20: Schematic representations of the six lowest energy out-of-plane deformations of the porphyrin macrocycle . A black circle indicates that the respective atom has moved below the plane of the porphyrin, whereas a white circle indicates it moved upwards. Some atoms, such as the carbon atoms at the *meso* positions in the Saddle and the Propellor distortion, do not move out of the porphyrin plane. The corresponding symmetry labels of the porphyrin's D_{4h} group are indicated. Adapted from Song *et al.*[25]

the change of color upon protonation of a planar free base porphyrin[7]. The formed diacid is know to be non-planar and the destabilization of the π-system, primarily of the HOMO[32], leads to a smaller HOMO-LUMO gap. This smaller gap results in a red shift in the optical adsorption, thereby coloring the non-planar porphyrin diacid green, while the planar free base porphyrin is purple to red. The conformational freedom of the alkyl tails, which was also proposed to underlie the different polymorphs and the shared unit cell vectors of **CuP** monolayers on HOPG, is thus proposed to cause conformational changes in the structure of the porphyrin macrocycle such as non-planar distortion. This distortion is then thought to underlie the differences in electronic properties of the **CuP** adsorbates as is apparent from differences in apparent height between the porphyrins in the different polymorphs in STM and a different CPD in nc-AFM. In Chapter 3 it was proposed that the shared unit cell vectors exist because the conformations of the four alkyl chains are independent from each other. They are mechanically decoupled by the "stiff" porphyrin core. In Figure 4.20 it can be observed that in porphyrins exhibiting Saddle and Propellor distortions, the *meso* positions, at which the alkyl tails are attached, are not affected by these distortions. These two distortion modes would present a good starting point for further theoretical investigations since they explain both the conformational decoupling of the alkyl tails, as proposed in Chapter 3, and the changes in electronic properties caused by distortion of the ring.

4.5 Conclusions

In this chapter the self-assembled monolayers of **CuP** on HOPG were studied at the solid/liquid interface, as a dry layer under ambient conditions and in Ultra High Vacuum using a combination of scanning probe microscopy techniques. It was shown that the different polymorphs formed by **CuP** on the HOPG/1-octanoic acid have different apparent heights in STM, nc-AFM and tm-AFM. Comparison of the apparent heights obtained with the various SPM methods revealed that this contrast not caused by differences in the true height at which the **CuP** adsorbed to the HOPG surface. Kelvin Probe Microscopy showed that the different polymorphs have different contact potentials and that the differences in apparent height are of electronic origin. It was argued that the electronic differences between the different surface structures are already present at the single molecule level, rather than being a collective property. This implies that, the adsorption of a given **CuP** molecule in a domain of one of the polymorphs or, more precisely, in one of the adsorption configurations does not affect the electronic properties in a direct way. The difference in electronic properties are proposed to stem from the differences the conformations of the individual **CuP** molecules. A plausible mechanism with which the differences in the electronic properties of the adsorbates can be explained, is by assuming a different degree of nonplanar distortion of the porphyrin ring for **CuP** adsorbed in the different polymorphs. This distortion is ascribed to the conformational differences of the alkyl tails for the various polymorphs. Although without solid theoretical support these claims can not be completely proven, they present a consistent explanation for the observation that the properties are present at the single molecule level, that the polymorph-dependent contrast can differ for adsorbates with the exact same surroundings within the monolayer (*i.e.* $\mathcal{V}$ and $\mathcal{M}$), and that the contrast can be similar for adsorbates with different surroundings (*i.e.* $\mathcal{L}$, $\mathcal{B}$, $\mathcal{MB}$, $\mathcal{V}$). The combination of the high level of control over the **CuP** monolayer composition and the polymorph dependent physical properties of these layers presents a very powerful system for future nanoscale devices in which the properties thereby the functionality of the same molecular building block could be tuned locally by controlling the polymorphic structure.

References

1. Burke S.A., LeDue J.M., Topple J.M., Fostner S. and Grütter P. *Adv. Mater.*, 21 (20):2029–2033, **2009**
2. Nikiforov M.P., Zerweck U., Milde P., Loppacher C., Park T.H., Uyeda H.T., Therien M.J., Eng L. and Bonnell D. *Nano Lett.*, 8 (1):110–113, **2008**
3. Duhm S., Heimel G., Salzmann I., Glowatzki H., Johnson R.L., Vollmer A., Rabe J.P. and Koch N. *Nature Mater.*, 7 (4):326–332, **2008**
4. Peisert H., Biswas I., Knupfer M. and Chassé T. *Phys. Status Solidi B*, 246 (7):1529–1545, **2009**
5. Toader T., Gavrila G., Ivanco J., Braun W. and Zahn D.R.T. *Appl. Surf. Sci.*, 255 (15):6806–6808, **2009**
6. A. Shelnutt J., Song X.Z., Ma J.G., Jia S.L., Jentzen W., J. Medforth C. and J. Medforth C. *Chem. Soc. Rev.*, 27 (1):31–42, **1998**
7. Senge M.O. *Chem. Commun.*, 3:243–256, **2006**
8. Kudernac T., Lei S., Elemans J.A.A.W. and De Feyter S. *Chem. Soc. Rev.*, 38:402–421, **2009**
9. Scheuring S., Sturgis J.N., Prima V., Bernadac A., Lévy D. and Rigaud J.L. page 11293, **2004**
10. Ruan L., Besenbacher F., Stensgaard I. and Laegsgaard E. *Phys. Rev. Lett.*, 70 (26):4079–4082, **1993**
11. Hagelaar J.H.A., Flipse C.F.J. and Cerdá J.I. *Phys. Rev. B*, 78 (16):161405, **2008**
12. Calleja F., Arnau A., Hinarejos J.J., Vázquez de Parga A.L., Hofer W.A., Echenique P.M. and Miranda R. *Phys. Rev. Lett.*, 92 (20):206101, **2004**
13. Blanco J.M., González C., Jelínek P., Ortega J., Flores F., Pérez R., Rose M., Salmeron M., Méndez J., Wintterlin J. and Ertl G. *Phys. Rev. B*, 71 (11):113402, **2005**
14. Deng Z.T., Lin H., Ji W., Gao L., Lin X., Cheng Z.H., He X.B., Lu J.L., Shi D.X., Hofer W.A. and Gao H.J. *Phys. Rev. Lett.*, 96 (15):156102, **2006**
15. Hofer W.A. *Prog. Surf. Sci.*, 71 (5-8):147 – 183, **2003**. Proceedings of the IXth Symposium on Surface Physics, Trest Castle 2002
16. Nishino T., Buhlmann P., Ito T. and Umezawa Y. *Phys. Chem. Chem. Phys.*, 3:1867–1869, **2001**
17. van den Bruele F.J. *2D self-assembled structures on crystalline surfaces.* Ph.D. thesis, **2012**
18. Berezin D.B., Semeikin A.S. and Berezin M.B. *Russ. J. Phys. Chem.*, 83 (8):1315–1320, **2009**
19. S. Somma M., J. Medforth C., Y. Nelson N., M. Olmstead M., G. Khoury R. and M. Smith K. *Chem. Communun.*, (13):1221–1222, **1999**
20. Medforth C.J., Senge M.O., Smith K.M., Sparks L.D. and Shelnutt J.A. *J. Am. Chem. Soc.*, 114 (25):9859–9869, **1992**
21. Röder B., Büchner M., Rückmann I. and Senge M.O. *Photochem. Photobiol. Sci.*, 9 (8):1152–1158, **2010**
22. Jentzen W., Song X.Z. and Shelnutt J.A. *J. Phys. Chem. B*, 101 (9):1684–1699, **1997**

23. Senge M.O., Medforth C.J., Forsyth T.P., Lee D.A., Olmstead M.M., Jentzen W., Pandey R.K., Shelnutt J.A. and Smith K.M. *Inorg. Chem.*, 36 (6):1149–1163, **1997**

24. Senge M.O. *Chem. Commun.*, 47:1943–1960, **2011**

25. Song X.Z., Jentzen W., Jia S.L., Jaquinod L., Nurco D.J., Medforth C.J., Smith K.M. and Shelnutt J.A. *J. Am. Chem. Soc.*, 118 (51):12975–12988, **1996**

26. Senge M.O. *Acta Crystallogr., Sect. C: Cryst. Struct. Commun.*

27. Sazanovich I.V., Galievsky V.A., van Hoek A., Schaafsma T.J., Malinovskii V.L., Holten D. and Chirvony V.S. *J. Phys. Chem. B*, 105 (32):7818–7829, **2001**

28. Sparks L.D., Medforth C.J., Park M.S., Chamberlain J.R., Ondrias M.R., Senge M.O., Smith K.M. and Shelnutt J.A. *J. Am. Chem. Soc.*, 115 (2):581–592, **1993**

29. Yokoyama T., Yokoyama S., Kamikado T. and Mashiko S. *J. Chem. Phys.*, 115 (8):3814–3818, **2001**

30. Brede J., Linares M., Kuck S., Schwobel J., Scarfato A., Chang S.H., Hoffmann G., Wiesendanger R., Lensen R., Kouwer P.H.J., Hoogboom J., Rowan A.E., Bröring M., Funk M., Stafström S., Zerbetto F. and Lazzaroni R. *Nanotechnology*, 20 (27):799–804, **2009**

31. Cullen D., Desai L., Shelnutt J. and Zimmer M. *Struct. Chem.*, 12:127–136, **2001**

32. Senge M.O., Renner M.W., Kallisch W.W. and Fajer J. *J. Chem. Soc., Dalton Trans.*, pages 381–385, **2000**

CHAPTER 5

Structural transformations of **CuP** monolayers

5.1 Introduction

In the past decade, numerous studies have been reported that deal with the organization of potentially functional organic molecules in highly organized monolayer structures on surfaces[1,2]. In particular the spontaneous self-assembly of molecules at the solid/liquid interface has become a popular approach, since it involves relatively mild conditions, and allows for a wide range of molecules to be employed. Scanning Tunneling Microscopy (STM) is a powerful method to study the formation, structure and stability of such monolayers at the (sub)molecular level[3]. Only in recent years the first systematic STM studies have been performed to reveal the effect of the temperature and the concentration of the supernatant solution on the physisorption of molecules into monolayers at solid/liquid interfaces, and to elucidate the thermodynamics behind this process[4–9]. A detailed understanding of such factors, however, will be of paramount importance for the possible application of these self-assembled layers in future functional devices[10].

In Chapter 3 the different 2–dimensional polymorphs formed by metallo *meso*–5,10,15,20-tetraundecylporphyrins, **MP** (*i.e.* **ZnP**, **NiP**, **2HP** and **CuP**) on the HOPG surface, and their mutual geometric and conformational relationships in the monolayers were discussed. Three 2–dimensional polymorphs (**L**, **M** and **S**) were found, as well as one structure that was found only in linear arrays that coexisted with patches of **M** unit cells. This structure was named **B**, referring to its appearance as a boundary between adjacent patches of the **M** polymorph. These four structures

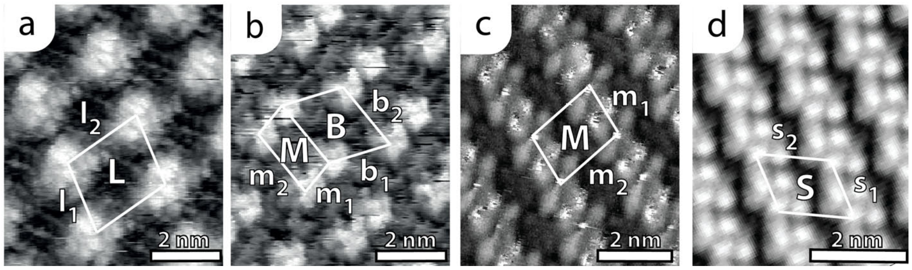

Figure 5.1: STM images showing the unit cells of the adlayer structures (**L**,**B**,**M**,**S**) found for **CuP** at the HOPG surface. The definitions of the unit cell vectors are indicated.

are again shown in Figure 5.1 for the most extensively studied metalloporphyrin, **CuP**. The fraction in which these surface polymorphs cover a given HOPG surface depends on the concentration of the solution in which the monolayers is formed: low concentration solutions ($\lessapprox 10^{-6}$ M) lead to the low density **L** polymorph, while increasingly high concentrations lead to the formation of domains comprising **M** and **B** unit cells in equal ratio (**MB**), domains completely covered with the **M** polymorph and the formation of the densest **S** surface structures. This concentration dependence was demonstrated for the formation of **CuP** monolayers on clean HOPG (0001) surfaces. This chapter is concerned with the transformation and adaptation of self-assembled **CuP** monolayers, to changes in the supernatant solution. It will be shown that the different 2-dimensional polymorphs of **CuP** at the solid/liquid interface can respond drastically different to a sudden change in the thermodynamics of the system, induced by an increase of several orders of magnitude in the **CuP** concentration in the supernatant solution.

Some STM studies on the time evolution of self–assembled monolayers[11–14]and of dynamics of molecules within molecular monolayers[13,15–18] have been reported in the literature. These studies range from the imaging of Ostwalt ripening at the solid/liquid interface[19–21] to nucleation processes of porphyrin monolayers on metallic surfaces in Ultra High Vacuum (UHV)[11]. In some cases, even dynamic processes within molecules, *i.e.* changes in conformation, have been imaged. De Feyter and coworkers reported on the dynamics of a multivalent six-legged molecule at the solid/liquid interface of which the individual legs were observed to desorb and readsorb[17]. The rotation of a single molecule in a supramolecular bearing was imaged in UHV[22] and in this environment also the tautomerization of a naphthalocyanine was imaged at low temperatures with sub-molecular resolution[23]. The study of dynamics of metal surfaces in UHV during growth[24], displaying step[25] and atom movement[26,27], and even during catalysis[28,29], is a highly developed field. However, to our best knowledge the description of single component physisorbed monolayers at

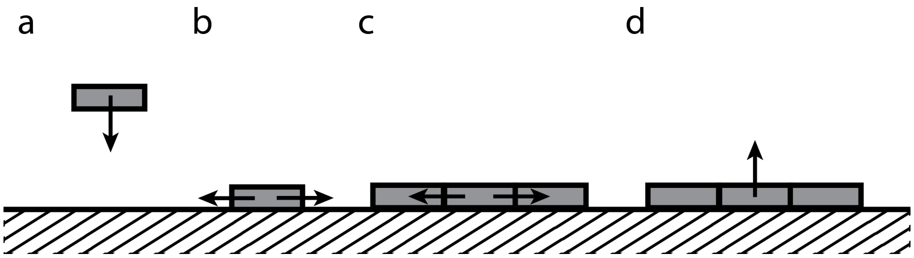

Figure 5.2: Sketch of the four most important processes involved in the formation and transformation of a self–assembled monolayer of porphyrin molecules: adsorption (a), lateral movement of a non-enclosed adsorbed porphyrin (b), movement of a porphyrin within a self–assembled monolayer (c), and desorption of a porphyrin from the monolayer (d).

the solid/liquid interface that adapt themselves to changing solute concentrations has never been studied in detail, and it will be shown in this chapter that a detailed understanding of the involved processes yields additional methods to control the surface structures of such monolayers.

The time–evolution studies presented in this chapter will focus on the mechanisms of transformation of the lower density surface structures (**L**, **B**) to the more tightly packed polymorphs (**M** and **S**) of monolayers of **MP**. Given that the surface density, and thereby the total number of molecules on the surface, increases when the surface fraction of the high density polymorphs becomes larger, the adaptation process must encompass additional adsorption of porphyrins from the supernatant solution and possibly the rearrangement of the already present physisorbed adsorbates. The key processes that can be envisioned to be involved with the formation and transformation of self–assembled monolayers, namely (i) adsorption of molecules from the supernatant solution, (ii) the lateral movement of individual unenclosed adsorbed molecules (*i.e.* not enclosed by neighbouring adsorbates), (iii) the movement of molecules within the self–assembled monolayer and (iv) the desorption of molecules from a self–assembled monolayer, are sketched in Figure 5.2. The contribution of these processes to the formation and, more importantly, to the *trans*formation of **MP** monolayers will be described. Initial experiments will focus on **CuP** monolayers at the HOPG/1-octanoic acid interface. The movement of molecules within the monolayer and the formation of specific defects, which turned out to be required for the self–assembled monolayers to establish thermodynamic equilibrium with the supernatant solvent, will be extensively discussed. Subsequently, the formation of bi–component **CoP**/**CuP** and **CoP**/**NiP** monolayers will be studied to test the proposed transformation mechanisms and to examine the influence of adsorbate desorption during the transformation processes.

5.2 Transformations of mixed B, M and S domains

When a clean HOPG surface is presented with a droplet of a 1-octanoic acid solution of **CuP** of a given concentration, a monolayer is formed within seconds. The adsorption process occurs too fast to be imaged with the Nijmegen Liquid STM, implying that both the adsorption of molecules from the solution to the HOPG surface, as well as the movement of single adsorbed molecules at the HOPG/1-octanoic acid interface occurs within seconds at room temperature. This high speed agrees well with the idea that the adsorption energy of **CuP** at the HOPG surface is strong but elastic, as was proposed in Chapter 3. It was concluded that there are no preferential adsorption sites for **CuP** on the HOPG/solvent interface, merely preferred adsorption directions. This would allow the individual molecules to slide over the gentle hillocks of the adsorption energy landscape rather than hopping from one deep adsorption valley to the next, as is often observed for adsorption on metal surfaces[30–36]. The structural transformation of an existing monolayer of **CuP** is orders of magnitudes slower than the initial monolayer formation. As was stated in Chapter 3, the **M** and **B** structures can coexist on a given terrace in virtually all ratios, ranging from 1:1 in the case of **MB** domains to domains that are completely comprised of the **M** polymorph. When the monolayer is created from a solution with a low **CuP** concentration (*i.e.* 10^{-6} M), low density **M≈B** domains are formed, as the one shown in Figure 5.3a. When, alternatively, a clean HOPG surface is exposed to a higher (10^{-4} M) concentration solution, large patches of the **M** polymorph are formed, which are only occasionaly intersected with a single row of **B** unit cells. This type of domains will be referred to as **M>B** and an example of such a domain is shown in the STM image in Figure 5.3b. The **B** unit cell, which has a surface area of 3.72 ± 0.23 nm^2, does not solely cover entire domains. The **M** unit cell has an area of 2.54 ± 0.12 nm^2 and thus an **MB** domain, in which both these unit cells occur in equal amounts, has an average unit cell area of 3.12 ± 0.26 nm^2. The fact that low density domains form at low concentrations of the supernatant solution, while the application of more concentrated solutions on bare graphite surfaces leads to higher density surface structures, seems to suggest that at any given concentration of the supernatant solution the self-assembled monolayer is in thermodynamic equilibrium with that solution. In this chapter it will be shown that this is not necessarily true and that it strongly depends on the arrangement of the molecules on the surface to what extend thermodynamic equilibrium can be obtained.

When a low density monolayer of **CuP**, prepared by presenting the graphite surface with a droplet of a solution with a concentration of 10^{-6}M, was subsequently exposed to a droplet of a 100-fold more concentrated solution (10^{-4}M), different domains of the monolayer appeared to adapt strikingly different to this new thermodynamic situation. The STM image in Figure 5.3c was recorded 16 hours after the addition of the 10^{-4}M solution. During this time the lower terrace has transformed

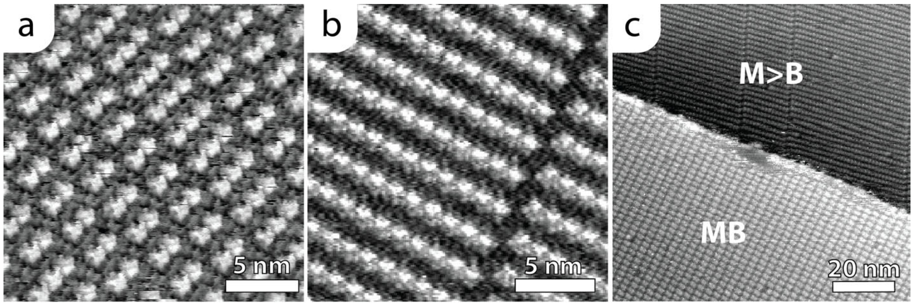

Figure 5.3: STM images of self-assembled monolayers of **CuP** at the HOPG/1-octanoic acid interface. The image in (a) shows an HOPG surface under a droplet with a **CuP** concentration of 10^{-6}M and the resulting monolayer consists of rows of **M** and **B** unit cells in a nearly equal ratio. The image in (b) shows a HOPG surface exposed to a 10^{-4}M solution which led to the formation of a monolayer consisting mainly of the **M** polymorph. The STM image in (c) was created by first exposing a clean HOPG surface to a 10^{-6}M and subsequently to a 10^{-4}M **CuP** solution. The image was recorded 16 hours after the addition of the higher concentrated solution and during this entire time, the higher lying terrace remained in a thermodynamically unfavourable, low density structure. Image parameters: V_{bias} = -1000 mV, I_{set} = 15 pA (a), V_{bias} = -760 mV, I_{set} = 10 pA (b) and V_{bias} =- 870 mV, I_{set} = 10 pA (c).

to a higher density, **M**>**B** domain, which is expected to form at this concentration, while the higher lying terrace remained completely unaltered (see section 5.2.3). This terrace is still covered with the low density **MB** structure. Because of the smaller fraction of **B** boundaries, the lower lying terrace is approximately 25% more dense than the higher terrace. This implies that up to 25% gain in surface density could have been obtained by the removal of the rows of the **B** unit cells on the upper terrace and the accompanying adsorption of additional **CuP** molecules from the supernatant solution. The observation that some of the initially formed low density domains persist for such a long time under a solution with a concentration at which higher density structures are thermodynamically much more favourable, indicates that physisorbed monolayers of **CuP** are not necessarily in thermodynamic equilibrium with the supernatant solution. To understand this phenomenon, the transformation of monolayers of **CuP** from low to high density domains was studied in more detail.

5.2.1 2-Dimensional defects

The time-evolution of a domain of **CuP** at the HOPG/1-octanoic acid interface, comprising **M** and **B** unit cells, is shown in Figure 5.4. The monolayer was first exposed to a 10^{-6}M droplet, and after it had been confirmed with STM that a monolayer had been formed, a more concentrated, 10^{-4}M, droplet was added. The STM image has been colored to indicate the two sublattices of the **M** polymorph, as is explained in Appendix A. The transformation of a mixed **M**≈**B** domain to a more dense **M**–domain not only requires the annihilation of the rows of the **B** unit cells, but also a redistribution of the molecules in **M** patches over the two sublattices, which will result in the local annihilation of one of the two sublattices. Since during this process the surface density increases, the changes in the 2-dimensional structure must be accompanied by adsorption of porphyrins from the supernatant solution. In Chapter 3 it was argued that linear arrays of **B** unit cells in a domain of the **M** polymorph should not be regarded as a defect, since they were found to be common and stable structures formed by **CuP** on the HOPG surface. The linear arrays of **B** unit cells in Figure 5.4 are, however, not perfectly straight, and several different defects can be identified in them. Some representative defects have been marked by ellipses in Figure 5.4a and b. Magnifications of the defects labeled 1, 3, 4 and 6 are displayed in Figure 5.4c without the sublattice colouring. The defects labeled 1—4 present kinks in the **B** boundaries. Defect 1 marks a single **CuP** molecule that crossed a **B**–boundary from one to the other sublattice. In the STM image of Figure 5.4b, recorded 15 minutes after that of Figure 5.4a, this defect has disappeared by the return of the molecule to the other sublattice, leaving a perfectly straight array of **B** unit cells. The kinks labeled 2—4 are more persistent than the single misplaced **CuP** adsorbate in defect 1. These kinks remain for longer times and move along the shared $\mathbf{m}_2 = \mathbf{b}_2$ vector over the sample surface, as can be seen in the STM images in Figure 5.4a and b. Defects 3 and 4 meet each other, causing a single **CuP** adsorbate to be fully surrounded by **B** unit cells, and therefore to reside in a $\mathcal{B}$ adsorption configuration. The defects responsible for the transformation of domains comprising a mixture of **M** and **B** unit cells (**M**,**B** are proposed to be of the type labeled 5 and 6). In these defects the two sublattices meet each other along the $\mathbf{m}_1$ direction *and* in the $\mathbf{m}_2 = \mathbf{b}_2$ direction. A. comparison between the STM images in Figure 5.4a and b, reveals that these defects have moved along the shared $\mathbf{b}_2 = \mathbf{m}_2$ unit cell vector, thereby increasing the surface density by the local annihilation of one of the sublattices. This process was studied in more detail, and the STM images and schematic drawings in Figure 5.5 show the removal of two rows of **B** unit cells and the enclosed **M** sublattice (blue), yielding a continuous patch of the red **M** sublattice. The annihilation defect (marked by the ellipse) moves upwards in this case. In the schematic drawings in Figure 5.5c it is proposed that in the course of the surface structure transformation, two molecules from the blue lattice (I, II) move to two of the three possible vacant positions (1—3) in the red lattice, implying that one additional porphyrin ($*$) must be adsorbed from the supernatant solution and inserted behind the progressing annihilation defect. In the solid ellipse in Figure 5.5b the movement of a **CuP** adsorbate from one to the other sublattice occurred during the scanning of this part of the image, since the molecule appears partially in the red-coloured and partially in the blue-coloured sublattice.

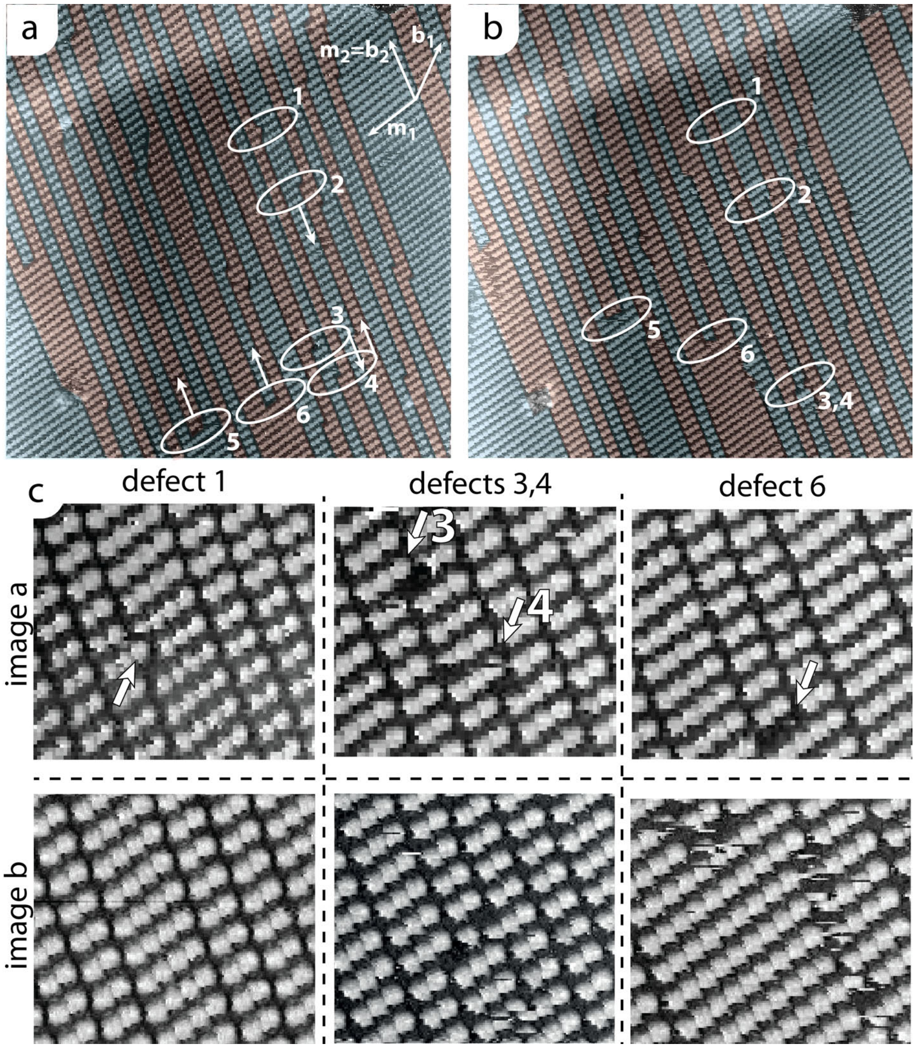

Figure 5.4: STM images taken at an interval of 15 minutes (a,b), in which the movement of several defects as well as transformations of **M** sublattices and **B** boundaries can be seen. Ellipses 2,3,4 show the movement of **B**–kinks along a row of **B** unit cells. The kinks in 3 and 4 meet and form a small 2–dimensional **B** structure. Ellipses 5 and 6 show the annihilation defect, in which two **M** sublattices meet along $\mathbf{m}_2 = \mathbf{b}_2$ and $\mathbf{m}_1$. The removal of **B** boundaries and the concomitant increase in surface density can be seen by comparison of images a and b. Defect 1 shows that single **CuP** molecules can cross a **B** boundary. This process is proposed to be at the basis of kink formation. The bottom rows show magnifications of the defects in ellipses 1,3,4 and 6. Image parameters: 125×125 nm^2, $V_{bias} = -850$ mV, $I_{set} = 10$ pA.

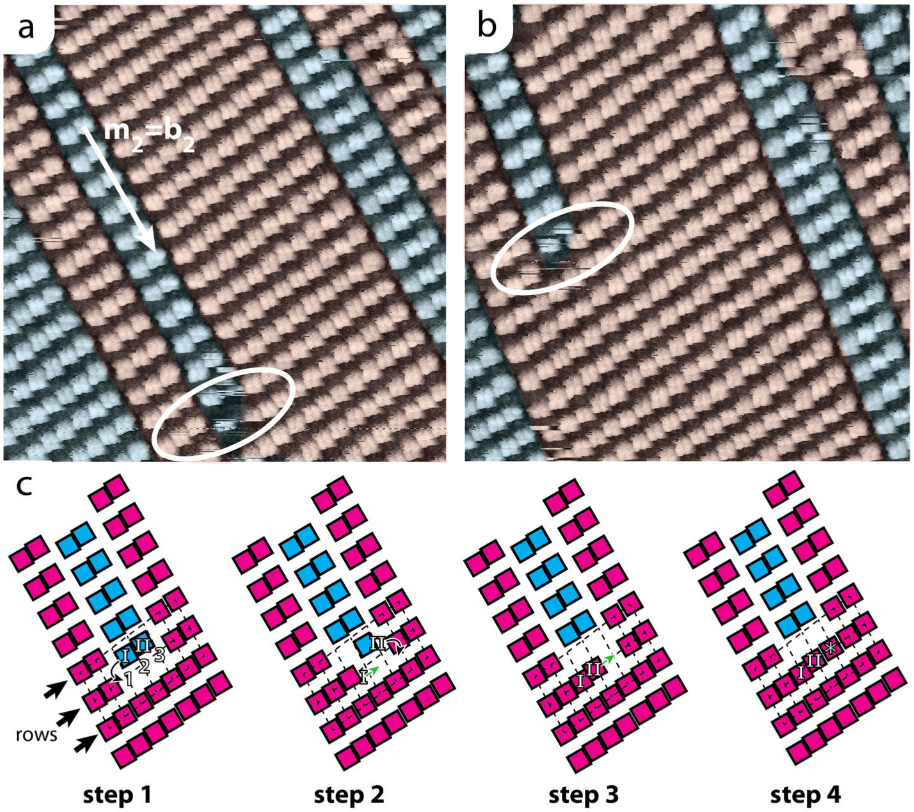

Figure 5.5: STM images stored at an interval of 2.3 minutes (a and b) in which the movement of an annihilation defect along $\mathbf{b}_2$ is shown in more detail and sketches of the different steps of the transformation process (c). The two sublattices are indicated by the red and blue colours. The area occupied by 2 molecules in the blue sublattice before the transformation (I and II) afterwards will accommodate 3 molecules in the red sublattice at the locations marked (1—3). One additional **CuP** ($*$) per annihilated row is therefore adsorbed during this process. Image parameters: 34×34 nm^2, $V_{bias} = -850$ mV, $I_{set} = 10$ pA.

It is proposed that the **CuP** molecules remain adsorbed during the transformation process and move in a 2-dimensional fashion to their new lattice positions. Step 1 of the transformation process is proposed to be the movement of one of the molecules of the blue sublattice (I) to one of the three positions of the red sublattice (1—3). After this transfer, this adsorbate is proposed to remain mobile and it can move to any of the three positions of the red sublattice (step 2). In step 3, the second molecule of the blue sublattice (II) is proposed to move to the red sublattice also remains mobile until in the final step an additional porphyrin from the supernatant solution is adsorbed with which the vacancy in the newly created row of the red sublattice is filled. It cannot be excluded that the adsorption of the additional porphyrin molecule actually occurs prior to the translation of molecule (II) to the red sublattice or that these two processes can occur in both sequences.

To prove this insertion mechanism, a second porphyrin species, **CoP**, was employed as a tracer molecule. The experiment is highly similar to those described above, but after imaging the formation of a monolayer in a droplet of a 10^{-6}M **CuP** solution, a droplet of a 10^{-3}M **CoP** solution was added to the supernatant solution. This method, in which molecules which are structurally very similar but which can also be distinguished by STM as a result of their different electronic properties, has been successfully applied at the solid/liquid interface before in studies of the dynamics of functionalized alkanes[15] and of alkyl–functionalized 1,3,5–tristyrylbenzene molecules[37]. **CoP** was chosen because in STM the half–filled d_{z^2} orbital of the Co center[38] can be easily recognized as a metal-centred protrusion[39–41], which means that this molecule can be easily discriminated from its copper sibling. The solution of **CoP** was added when a sufficiently large **M**>**B** domain of **CuP** was located by STM. The expected changes in the monolayer structure for the incorporation of **CoP** in a **CuP** **M**>**B** domain is sketched in Figure 5.6a and b. The copper porphyrins are all drawn grey, independent of the sublattice they are in. Upon monolayer transformation, the four porphyrins of the disappearing sublattice (marked in roman numerals) have to fill four of the five lattice sites (marked 1—5) of the enclosing **M** patch. This means that one of these lattice sites has to be occupied by a molecule from the supernatant solution. Because the concentration of **CoP** in the supernatant solution is a thousand–fold higher than that of **CuP**, the incorporated molecule will most likely be the cobalt species. The aforementioned variation in the process by which the four **CuP** molecules shift to the five possible new lattice positions, combined with the proposed mobility of the temporarily created vacancy, suggests a variation in the position of the newly inserted **CoP** molecule. This variation is sketched in Figure 5.6b where the **CoP** molecules are marked with yellow dots. Per newly created row of **M**, one **CoP** molecule is inserted, but it can be inserted in any of the five new lattice positions. The cobalt porphyrins are therefore expected to be arranged in a random pattern around a line (marked 'CL' in Figure 5.6b) which is parallel to common $\mathbf{m}_2 = \mathbf{b}_2$ unit cell vector and goes through the center of the annihilated

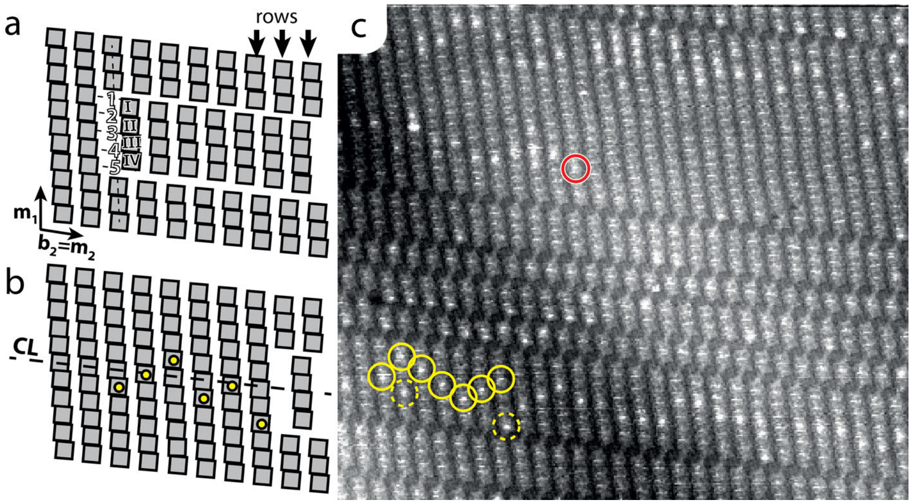

Figure 5.6: Schematic sketches (a,b) and STM image of a monolayer (c) showing the incorporation of **CoP** molecules in an existing layer of **CuP** by insertion in a annihilation defect.The layer was formed in a droplet of 10^{-6}M **CuP** in 1-octanoic acid, after which a droplet of 10^{-3}M **CoP** in the same solvent was added. The incorporation of **CoP** molecules (bright) can be observed and some of them are encircled for clarity. The characteristic erratic zig–zag patterns can most clearly be seen in the lower section of the image, by the yellow encircled porphyrins. The dashed yellow circles indicate some occurrences where a second molecule of **CoP** is present in the same row. The red encircled porphyrin probably marks the location of a annihilation defect at the moment the high **CoP** concentration reached the surface. For clarity the "rows" as intended in the text are indicated by black arrows and 'CL' marks the central line of the annihilated **M** sublattice. Image parameters: V_{bias} = 490 mV, I_{set} = 13 pA, 60 × 68 nm^2.

patch. The STM image in Figure 5.6c shows such an incorporation of **CoP** molecules in an existing **CuP** sublattice. The high features, some of which are encircled for clarity, are the inserted cobalt porphyrin molecules. These porphyrins indeed form an erratic zig–zag pattern with its central axis along the direction of the linear **B**–arrays. The mechanism described in Figure 5.5c and Figure 5.6a,b does not predict any correlation between the locations within each row, at which the molecule from the supernatant solution will be inserted, leading to the aforementioned random insertion pattern. The **CoP** inserts marked with the yellow circles in Figure 5.6c, however, seem to suggest a preference for the inserts to be shifted one lattice position from each other. This leads to a zig–zag-like pattern of the **CoP** inserts. Whether the interaction between the temporarily created vacancies or between the newly inserted

CoP species determines this behaviour will require further investigation. If the insertion process indeed occurred without any desorption of **CuP** molecules, but merely by a lateral redistribution of the adsorbed **CuP** molecules, one **CoP** molecule should have been adsorbed per annihilated row of **M** unit cells. However, in a number of rows more than one bright spot can be seen, some of which are marked with dashed yellow circles. This observation indicates that occasionally **CuP** molecules desorb during the transformation process and are replaced by a molecule from the solution phase. In the STM image in Figure 5.6c 956 **CuP** and 123 **CoP** adsorbates can be observed, indicating that the vast majority of the **CuP** molecules that moved to new lattice positions remained adsorbed to the HOPG during this movement. Even in the course of such a reorganization process, the adsorption at the HOPG surface and the interactions with their neighbouring adsorbates are strong enough for **CuP** to withstand desorption and the subsequent replacement by the 1000–fold more prevalent **CoP** porphyrins. The red circle in Figure 5.6c marks one end of the insertion pattern of **CoP** in this patch and is therefore proposed to indicate a location that was most likely occupied by an annihilation defect at the time that the highly concentrated **CoP** solution arrived at the interface. The observation that the well-defined incorporation of **CoP** molecules in an existing monolayer of **CuP** predominantly occurs via insertion in annihilation defects presents evidence that desorption of **MP** from HOPG is slow, that the adsorption of individual molecules is fast when they have a location to adsorb, and that the layer is not necessarily in thermodynamic equilibrium with the solution at all times. If it were in equilibrium, the surface composition would much more reflect the high **CoP**/**CuP** ratio present in the solution.

5.2.2 The formation of the S polymorph

The density of **CuP** monolayers can further increase by the formation of the **S** polymorph. This process can be observed in Figure 5.7, where a monolayer, formed on HOPG from a 10^{-5}M **CuP** solution in 1-octanoic acid, was exposed to a saturated ($\approx 10^{-2}$ M) solution of the same species. In Figure 5.7a many patches of the two **M** sublattices (blue and red) can be seen. Over time (Figures 5.7b, and c), these patches transform in a manner similar to the mechanism described in section 5.2.1 for the annihilation of the **M** sublattices. Patches of the **S** polymorph (yellow) form at locations where the two different **M** sublattices meet along the $\mathbf{b}_2 = \mathbf{m}_2$ direction. The location of these newly formed patches suggests that the same annihilation defect that was at the basis of the transformation of mixed **M**/ **B**–domains is also responsible for the formation of the **S** polymorph, which explains why the densest (**S**) polymorph is predominantly encountered in close proximity to the least dense (**B**) surface structure.

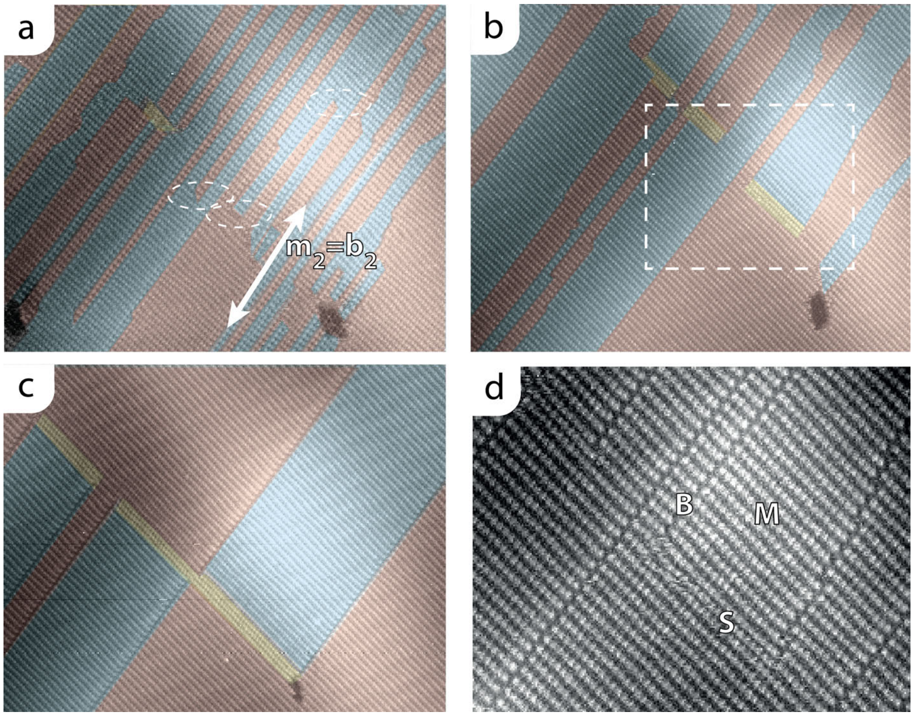

Figure 5.7: (a-c) STM images of **CuP** at the HOPG/1-octanoic acid interface taken at times $t_a = 0$ (a), $t_b = 23$ min. (b), and $t_c = 3$h and 20 min. (c). The initial layer was formed from a solution with a **CuP** concentration of 10^{-5}M, after which a droplet with a **CuP** concentration of 10^{-3}M was added. Patches of the **S** polymorph (yellow) are formed at the same annihilation defect from which the **M** sublattices (red/blue) anneal. The image in (d) is a magnification of the marked region in (b). Image parameters: 150×150 nm^2, $V_{bias} = -710$ mV, $I_{set} = 14$ pA.

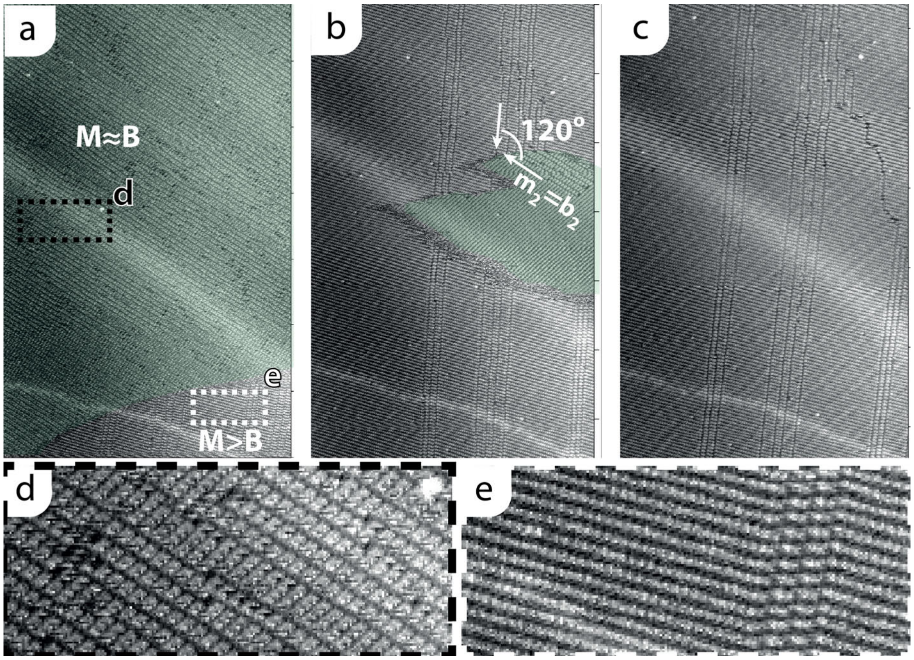

Figure 5.8: Series of three STM images (a–c) of a **CuP** monolayer at the HOPG/1-octanoic acid interface stored at intervals of 15 minutes (a,b,c). Within this time, the low density (uncolored) **M**$\approx$**B** domain disappears at expense of the denser **M**$>$**B** (green) domains. Magnifications of the marked rectangular areas in image (a) are given images (d) and (e). Both the **M**$\approx$**B** domain (d) and the **M**$>$**B** domains (e) are shown. The directions of the $\mathbf{m}_2 = \mathbf{b}_2$ vectors of both domains are depicted in image (b). Image parameters: 225×350 nm^2, $V_{bias} = -870$ mV, $I_{set} = 10$ pA

5.2.3 The transformation of rotational domains

In regions where 2-dimensional defects are plentiful, such as at the border between two rotational domains, in which the molecular lamellae are aligned along rotationally equivalent directions of the graphite substrate, the adaptation to a new thermodynamic situation occurs readily. An example of such a fast transition is shown in Figure 5.8. The STM image in Figure 5.8a shows two domains of **CuP** at the HOPG/1-octanoic acid interface. The surface area shown in this image, which is the same as that in Figure 5.3c, but 16 hours earlier, was imaged after the addition of the highly concentrated **CuP** solution to the layer formed from a low density solution. This low density **M**$\approx$**B** structure that formed from the initial, low concentration, solution can be more easily identified in the magnification shown in Figure 5.8d. The **M**>**B** domain in the lower right corner of Figure 5.8a (uncoloured, magnification in Figure 5.8e) has an approximately 20% higher density than the **M**≈**B** domain. The domains of the monolayer are oriented along different, equivalent, crystallographic directions of the HOPG substrate (Figure 5.8b) . The boundary between the domains is rough and very dynamic, which is ascribed to the high mobility of individual, not fully enclosed **CuP** molecules. This reduces the amount of interactions that fixate the **CuP** molecules at their lattice positions, which is proposed to lead to a higher mobility. The high density domain rapidly grows at the expense of the lower density (green) domain, (Figures 5.8a and b), and after 30 minutes the whole terrace is covered by the higher density domain (Figure 5.8c). The different steps of this transformation to the high density polymorphs, which must have included the adsorption of additional molecules of **CuP** from the solution phase and most likely the lateral movement of molecule at the boundaries of the domains, thus occur fast. This observation once again emphasizes that the low speed of the transformation of domains that are poor in defects is not limited by slow adsorption or the intrinsically slow movement of single adsorbates on the HOPG surface, but by the 2-dimensional movement of specific defects.

5.2.4 Formation of the annihilation defect

In this section it is investigated how and under which boundary conditions these defects are formed. Some of the annihilation defects, which were proposed to lead to the transformation of low density **M**≈**B** domains to higher density **M** and **S** domains, might be formed immediately when the layer is formed or during the fast growth of rotational domains, as shown in section 5.2.3. Other 2-dimensional processes might also be responsible for the creation of some of these annihilation defects. In Figure 5.4 it could be observed that, besides the annihilation defects kinks are present in the otherwise straight, rows of **B** unit cells. Two STM images of domains in which many of the linear **B** arrays are strongly kinked are shown in Figure 5.9. Some of these kinks are marked with black arrows for clarity. In the dashed ellipse in Figure 5.9b it can be observed that when the two strongly kinked boundaries at opposite sites of the same sublattice (blue in this image) meet, an annihilation defect is formed. In this mechanism, which may only be one of several mechanisms via which this defect can be formed, the formation thus requires the existence of kinks in the linear **B**-arrays. The kinks themselves are proposed to form when molecules from the sublattice on one side of the array of **B**-unit cells, cross to the other side, which is sketched in Figure 5.10a. and was observed earlier in the STM image in Figure 5.4 (defect 1). In that case a single porphyrin molecule had crossed the adjacent **B**-boundary, which apparently led to a less favourable situation, given the fact that the molecule quickly returned to its original position. It can, however, be envisioned that when a series of

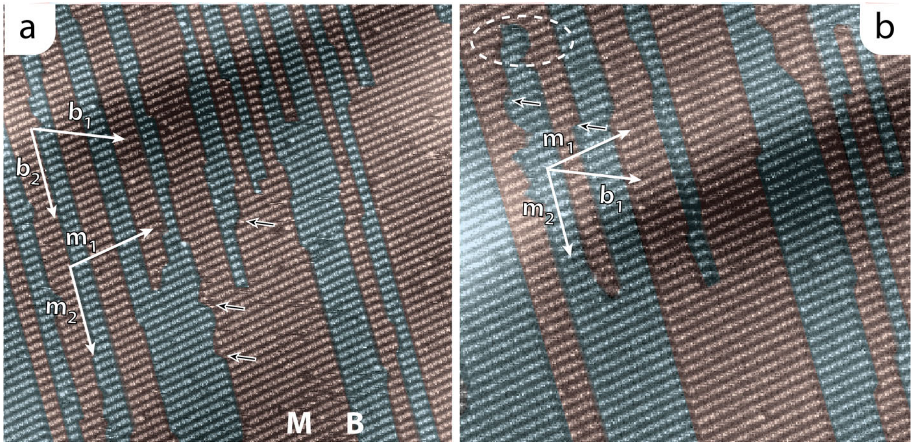

Figure 5.9: Two STM images showing defects in the linear **B** polymorph. The black arrows indicate kinks in the **B** boundaries. The dashed white ellipse highlights the annihilation defect that is formed when two kinked **B** boundaries on adjacent sides of a **M** sublattice meet. Image parameters: 120×120 nm^2,V$_{bias} = -830$ mV, $I_{set} = 15$ pA.

adjacent **CuP** molecules cross the same **B** boundary in a short period of time, a kink defect is formed, as is sketched in Figure 5.10.

There might be specific boundary conditions under which such a process can occur, which is schematically drawn in Figure 5.10a where the creation of kinks along a **B** boundary, in the middle of a molecular domain (*i.e.* far from any defects in the underlying substrate or rotationally symmetric domains), would lead to a surface structure in which the adsorbed **CuP** molecules become too closely spaced. The locations in which this occurs are marked with a "$\times$". These adsorption configurations are proposed to be energetically unfavorable, due to a too small spacing between adjacent rows. This process can therefore not occur without inducing desorption of these adsorbates. Near step edges of the HOPG substrate, however, such a situation, in which molecules are forced to assume too close spacings, does not necessarily have to occur, as is schematically depicted in Figure 5.10b. Here, the strongly kinked boundary is drawn such that it terminates at a step edge of the HOPG substrate. The periodic structure of the layer is already imperfect at such a substrate defect and the energy penalty of a situation in which the kinked boundaries continue until they meet such a surface defect, might therefore be minimal.

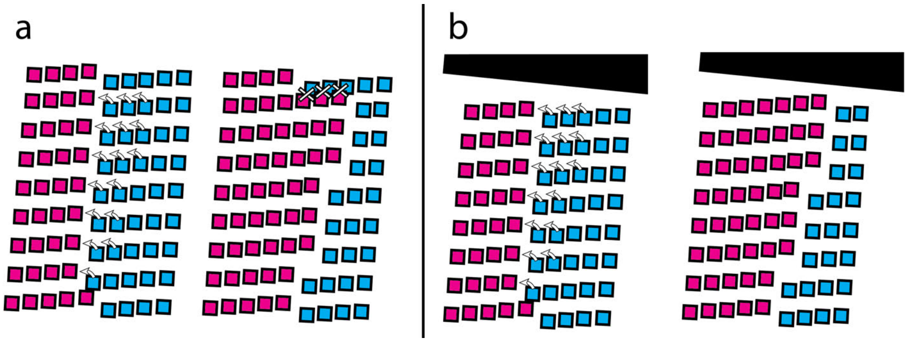

Figure 5.10: Schematic representation of the formation of **B** kinks by **CuP** molecules crossing a **B** boundary as it would occur far from any steps in the HOPG substrate (a) and near a step edge (b). It can be seen that the formation of a kink in the middle of a domain leads to some closely spaced **CuP** adsorbates which might render this process highly unfavorable. At the edge of a domain, for instance at a step in the graphite surface, such unfavourable spacings are not expected and the formation of kinks might therefore occur at these and other surface defects.

5.2.5 Kinetic trapping

The proposed mechanism for the formation of annihilation defects from meandering kinked **B** arrays provides an explanation for the observation that the higher lying terrace in Figure 5.3c was unable to form the annihilation defects that were proposed to be at the basis of the transformations that increase the surface density of **CuP** monolayers. The time evolution of the monolayer leading up to the STM image in Figure 5.3c is shown in Figure 5.11. The terraces are now colored to indicate the two different **M** sublattices. The transformation of the low density 1-dimensional **B**–arrays that border the different **M** sub–lattices according to the mechanism described above takes several hours to complete. In the image in Figure 5.11c, which was taken approximately 16 hours after the addition of the 10^{-3}M solution of **CuP** to the surface, the higher, uncolored, terrace is still covered with a domain of the **MB** structure, in which rows of **M** and **B** unit cells occur in equal ratios. A magnification of the terrace covered with the **MB** domain is shown in Figure 5.11d. In contrast to the lower lying terrace, which slowly adapted to the new thermodynamic situation, the **MB** domain remained completely unaltered. It is apparently impossible to form the necessary kinks needed to form annihilation defects in this domain. This conclusion might seem counter-intuitive. Since kinks in arrays of the **B** unit cells were proposed to be required of the formation of the annihilation defects and the **MB** domain contains the highest amount of these **B**-arrays possible, one expects a high probability

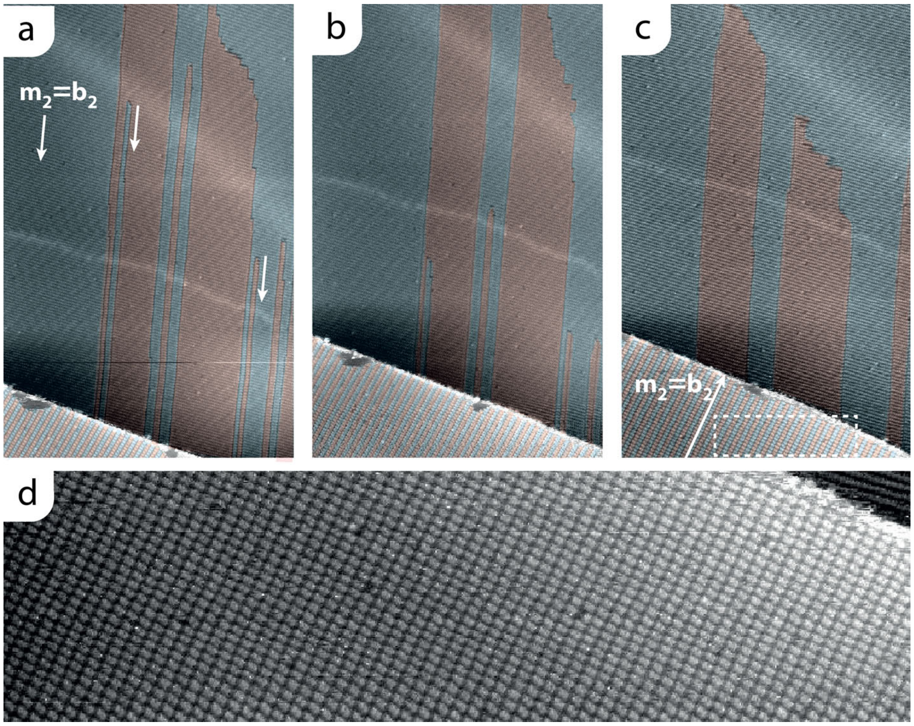

Figure 5.11: STM images taken 4 hours (a), 8,5 hours (b) and 16 hours (c) after the image in Figure 5.8c. The lower HOPG terrace (colored in blue and red), has a monolayer structure comprising mostly of the **M** polymorph whereas the uncoloured terrace is trapped in a **MB** structure. The arrows mark direction of the common unit cell vector of the **M** and **B** polymorphs, which is the direction along which the annihilation defects propagate. A magnification of the area within the dashed white rectangle in (c) is shown in (d). Image parameters: 225×350 nm^2, $V_{bias} = -870$ mV, $I_{set} = 10$ pA.

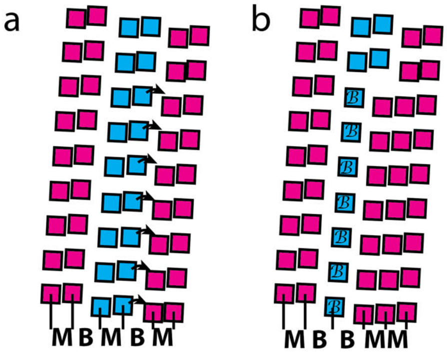

Figure 5.12: Schematic representation of **CuP** molecules crossing between the two different sublattices in a domain which consists of equal ratios of rows of the **M** and **B** unit cells (**MB**).

for the formation of kinks and annihilation defects. The **MB** structure, however, is a special case, since it presents the limiting form of the occurrence of the **B** unit cells: structures more rich in **B**, in which **CuP** molecules would have to be adsorbed in $\mathcal{B}$ adsorption configurations, should be regarded as defects, as was argued in Chapter 3 The formation of kinks in **MB** domains inevitably leads to the formation of energetically unfavourable 2–dimensional **B** patches, as is shown in Figure 5.12, and although the formation of a high enough number of kinks to initiate polymorph transformation it is proposed to occur far less readily than in domains with a higher fraction of **M** unit cells. The difficulty in creating the annihilation defects makes that these domains cannot adapt to changes in the thermodynamic situation and that they are thus kinetically trapped in low density adlayer structures.

5.3 Evolution of domains of the L polymorph

Domains of the **L** polymorph of **CuP** have an even lower surface density than the **MB** domains discussed in the previous section, and it is therefore interesting to investigate how these domains respond to an increase in the **CuP** concentration of the supernatant solution. An example of the kinetic trapping of low density **L** domains of **CuP** monolayers is shown in the STM image in Figure 5.13. In this image a domain, covered mostly with the **M** polymorph and intersected by some rows of **B** unit cells (labeled **M**>**B**), coexists with two **L** domains on different HOPG terraces. Before the recording of this image, the surface was exposed to a high concentration (10^{-4}M) **CuP** solution, so the **M**>**B** domain is expected to be thermodynamically

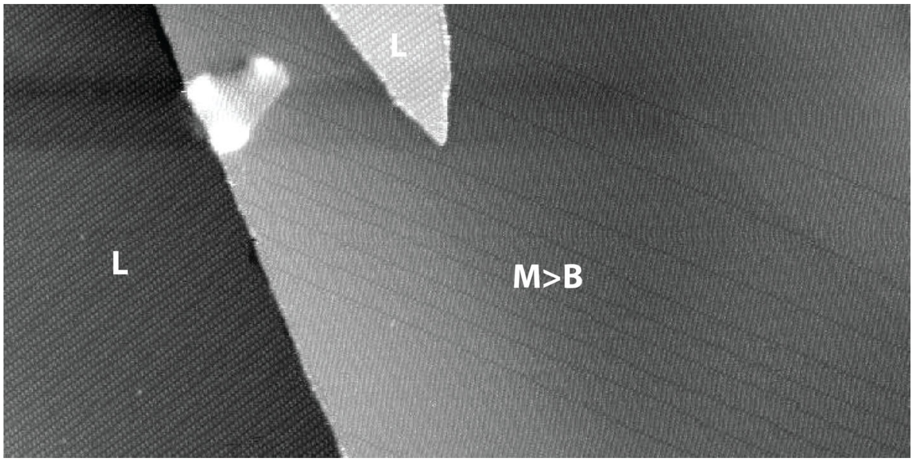

Figure 5.13: STM image of a **CuP** monolayer at the HOPG/1-octanoic acid interface. Three different HOPG terraces are present, one covered with a domain which mainly consists of the **M** polymorph of CuP, intersected by some rows of **B** unit cells (**M**>**B**), and the other two terraces having overlayers consisting of the much lower density **L** polymorph. Image parameters: 375×195 nm^2, $V_{bias} = -750$ mV, $I_{set} = 7$ pA.

more favorable than the **L** polymorph. However, the terraces covered with the **L** polymorph seem unable to adapt to the new thermodynamic situation. In view of the discussion in the previous section, this inability is proposed to be due to the absence of defects in the trapped **L** domains, but in this case the nature of the defects has not yet been identified. This is because the transition from **L** to **M**>**B** occurs too suddenly and too fast to be observed with STM. The final result of the reorganization of **MP** adsorbates assembled in the **L** polymorph into higher density polymorphs has been observed with STM. After a proposed kinetic barrier has been overcome, the transformation from **L** to **M** was found to occur at similarly short time scales as the annealing of rotational domains. To gain more insight in the transformation from **L** to the higher density surface polymorphs **CoP** was again employed as a molecular tracer. The results of these experiments can be observed in Figure 5.14 for a **NiP** monolayer, to which a high concentration (10^{-3}M) **CoP** solution in 1-octanoic acid was added. In Figure 5.14a the terrace is still fully covered with the low density **L** polymorphs of **NiP**, whereas 5 minutes later only a small patch of this **L** polymorph remains (top left corner of Figure 5.14b, marked with the arrow). The remaining terrace is covered with the **M** and **B** surface structures. A high resolution image of the newly formed domain is shown in Figure 5.14c. The **CoP** adsorbates again appear higher than **NiP** because of their half-filled d_{z^2} orbital. The STM image from which

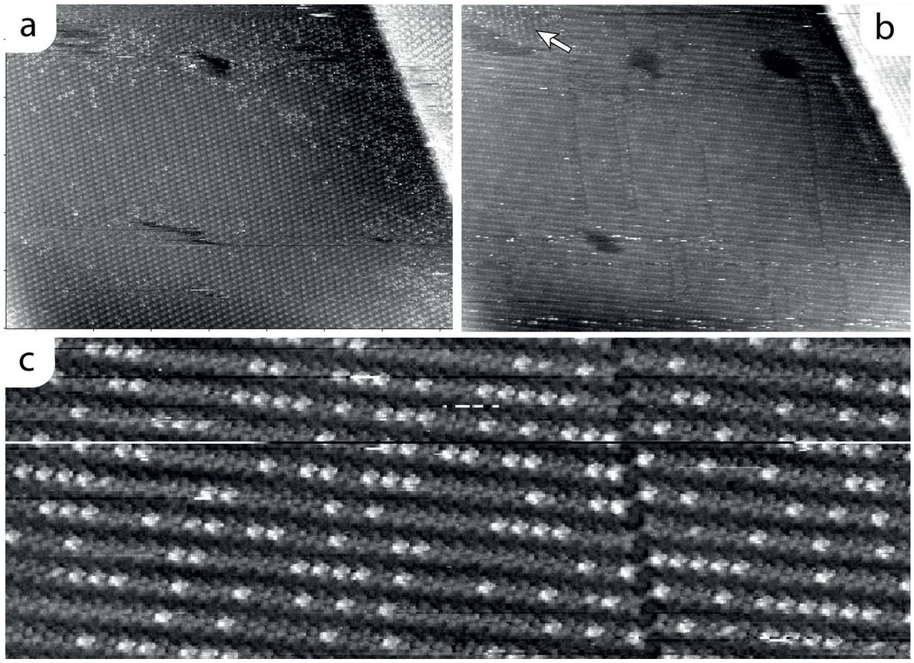

Figure 5.14: Series of STM images displaying the transformation of an **L** domain of **NiP** at the HOPG/1-octanoic acid interface (a) to a more dense **M**,**B** domain (b) and the concomitant insertion of **CoP** as a marker. The image in (b) is stored 5 minutes after that in (a). In the top left corner of (b) (marked with the arrow), a small patch of the **L** polymorph can still be observed. The image in (c) shows a higher resolution image of the newly formed **M**>**B** domain. Image parameters: 155 × 110 nm^2, I_{set} = 15 pA, V_{bias} = -450 mV (a and b), 25 × 60 nm^2, I_{set} = 5 pA, V_{bias} = -650 mV (c).

the magnification in Figure 5.14c is cropped contains 1337 **MP** molecules, of which 615 (46%) are **CoP** and 722 **NiP**. Given the difference in density between the initial **L** and the final **M** polymorphs the same surface area would have had to be covered by 930 **NiP** molecules in the original domain of the **L** polymorph. Without any desorption of the **NiP** adsorbates, 407 **CoP** molecules would have had to be adsorbed from the supernatant solution to compensate for the increase in surface density, neglecting the small fraction ($< 1\%$) of **NiP** in the final supernatant solution. The difference between these predicted values (**NiP** = 930, **CoP** = 407) and the ones actually observed (**NiP** = 722, **CoP** = 615) indicates that 208 (=22%) of the **NiP** adsorbates have desorbed during the transformation from the **L** to the **M** polymorph, and were replaced by **CoP** molecules from the solution phase. This implies that 78% of the molecules comprising the initial **L** domain remain adsorbed during the transformation process.

5.4 Nanoscale manipulation

Thusfar the dynamics and kinetic stability of metallo-porphyrin monolayers were studied at the HOPG/1-octanoic interface with minimal disturbance by the STM tip. No substantial differences in surface structure could be observed between areas that were imaged during long periods of time and areas that were not yet imaged, only to be imaged at the final stages of an experiment. Although so far it cannot be fully excluded that the presence of the tip has unintentionally affected the monolayer, hitherto no effort was made to control or employ this interaction. Nanomanipulation with the STM tip, however, provides a valuable tool to locally "shave away" adsorbed porphyrin molecules, in order to create vacancies and other surface defects. This nanoshaving is performed by scanning the surface with the tip at a short distance *i.e.* using high tunneling currents of $\gtrapprox$ 300 pA and/or low bias voltages of $\lessapprox$ 5 mV. At these conditions the tip ploughs through the monolayer and thereby causes desorption of part of the **CuP** molecules. This section is devoted to the response of a **CuP** monolayer which is intentionally locally disturbed by the removal of molecules through such shaving with the STM tip. Nanoscale manipulation of molecular adlayers by an STM tip has already been reported for the movement of individual molecules[42], for the nanoscale separation of enantiomers of a racemic mixture[43], and for inducing tautomerization[23] and chemical reactions[44]. "Shaving", has been demonstrated by Scudiero *et al.*[45].

The STM images in Figure 5.15 shows that in a **M**>**B** domain the tip–induced desorption of **CuP** molecules leads to the formation of additional rows of the **B** unit cells. After the STM image in Figure 5.15a had been recorded, nanoshaving was performed in the area marked by the dashed square. The result of this shaving operation is visible in the solid square in Figure 5.15b. Subsequently, a second shaving operation was performed at the location the dashed square of the STM image in Figure 5.15b. The result of this manipulation can be observed in the solid square in Figure 5.15c. The coloring of the sublattices emphasizes the fact that not only more **B**–boundaries are created by the shaving procedure, but also that porphyrin molecules are redistributed over the two different **M** sublattices. This type of shaving thus locally reverses the transformation of **M**,**B** domains to higher density domains.

A different situation is depicted in Figure 5.16. The same shaving procedure is employed, but this time on a **CuP** monolayer created from, and still exposed to a solution with a 10^{-3}M **CuP** concentration. The initially formed layer consists primarily of the **M** polymorph with smalls amount of both the **B** and **S** structures. The white square in Figure 5.16a marks the area where the shaving operation will be performed and the exact shaving pattern is shown in Figure 5.16b. The shaving was performed by alternating the bias voltage between -750 mV (indicated with a dashed

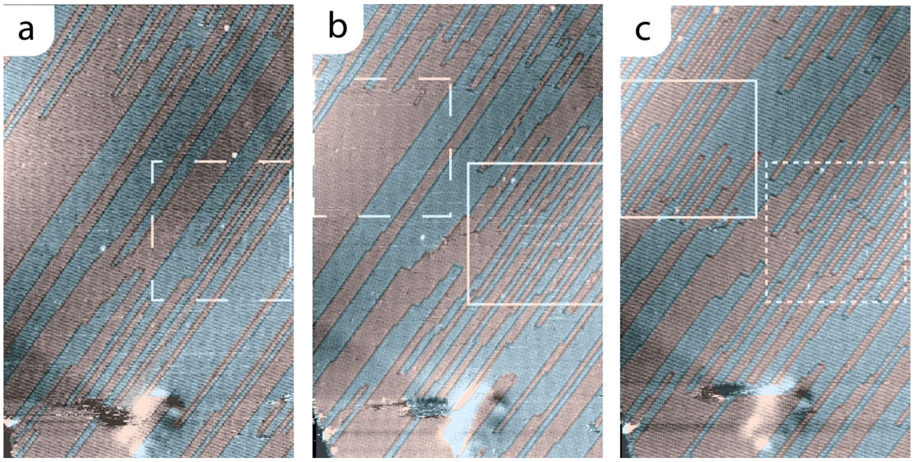

Figure 5.15: STM images of a monolayer **CuP** at the HOPG/1-octanoic acid interface, showing an example of nanoscale manipulation. After image (a), the dashed square was scanned with a low bias voltage ($V_{bias} = -25$ mV) and a high tunnelling current $I_{set} = 300$ pA) to perform nanoshaving. The same area is indicated by a solid square in image (b). After recording this image, a second shaving experiment was performed at the location of the dashed square. The result of the first (dotted square) and second (solid square) shaving can be seen in image (c). Image parameters: I_{set} = 30 pA, V_{bias} = -820 mV, 150 × 240 nm^2

section in the bar at the right side of the image), and -5 mV (solid sections). This STM image, in which the slow scan direction is upwards, shows that immediately after (=above) shaving, more **B** boundaries are formed, some of which are indicated by arrows. This implies that, as was also observed in the case of Figure 5.15, the surface density is locally lowered and arrays of **B**-unit cells are created. A remarkable difference with the previous experiment is observed in the STM image of the same area immediately after the shaving (Figure 5.16c): besides a line of the low density **B** polymorph, an extended patch of the densest polymorph (**S**) has formed outside of the shaving area. The initial tip-induced desorption of molecules has thus led to the additional adsorption of molecules in the resulting monolayer structure, and therefore the nanoscale fabrication of lower density structures has resulted in the formation of higher density polymorphs. It is proposed that the shaving locally led to the desorption of molecules and a concomitant creation of the necessary 2–dimensional defects, from which the formation of the high density **S** polymorph could occur. Given the slow intrinsic exchange of **CuP** adsorbates with those in the supernatant, it is unlikely that the formation of annihilation defects would have occurred spontaneously

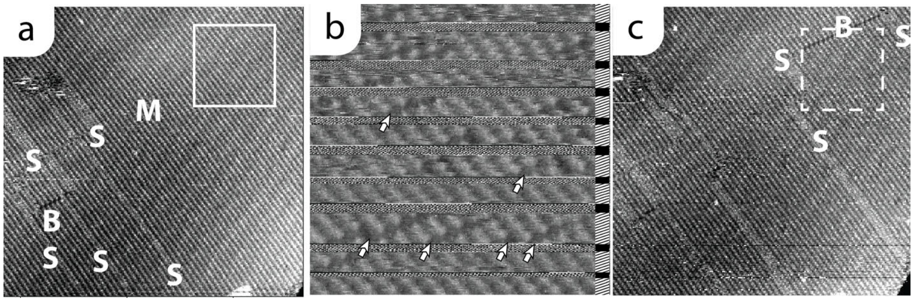

Figure 5.16: STM images of **CuP** at the HOPG/1-octanoic acid interface. A terrace of **B**, **M** and **S** was imaged in a 10^{-3}M solution. After image a the image displayed in b was recorded in the area marked by the white square. In this image the bias potential was repeatedly switched between $V_{bias} = -750$ mV (dashed bar) and $V_{bias} = -5$ mV (solid bar). The slow scan direction is upwards and it can be seen that after (=above) shaving, **B** structures appear. Image c shows that at these high concentrations the creation of **B** boundaries leads to the formation of the high density **S** polymorph, because the necessary annihilation-defects where hereby formed. Image parameters: V_{bias} = -740 mV, I_{set} = 18 pA, 140 × 180 nm^2 (a,c)

on the virtually defect-free region of the **M** polymorph on which the shaving operation was performed. It has therefore been shown that surface defects can be locally created using nanomanipulation and that this can lead to the formation of lower density polymorphs or higher density polymorphs, depending on the concentration of **CuP** in the supernatant solution. The surface morphology can thus be manipulated on the nanoscale in a controlled way, by combining the locality of tip–induced desorption and the choice of the concentration of molecules of **CuP** in the droplet in which the manipulation is performed.

Besides changing the polymorphic composition of a **CuP** monolayer, nanomanipulation could also be used to locally change the molecular composition of **MP** monolayers. To this end, nanoshaving was applied to a surface covered with a **CuP** adlayer, which was subsequently exposed to a solution which was very rich in **CoP**. The intention of this procedure was to replace adsorbed **CuP** molecules with **CoP** molecules from the supernatant solution. This so-called "nanografting" method is very commonly applied in Atomic Force Microscopy[46]. Nanografts of different thiol species chemisorbed to an Au(111) surface can be constructed very reliably and reproducibly[47,48]. In a study by Takami *et al.* part of an alkyl-functionalized porphyrin/phthalocyanine double decker monolayer was locally replaced by a simple pththalocyanine, also equipped with aliphatic tails[49].

First, a **CuP** monolayer was prepared at the *n*-tetradecane/HOPG interface. Ap-

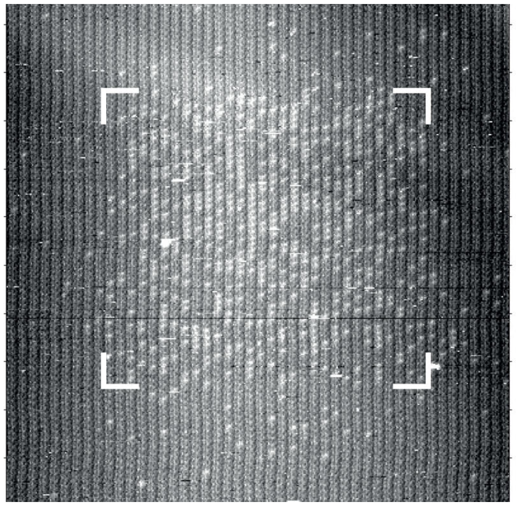

Figure 5.17: STM image of a mixed monolayer of **CuP** and **CoP** showing an area rich in **CoP** molecules (protrusions) which is created by making a nanograft in a previously formed layer of **CuP** at the HOPG/*n*-tetradecane interface. The nano–shaving was performed in the region within markers. Image parameters:V_{bias} = 800 mV, I_{set} = 8 pA 110 × 110 nm^2. Shaving was performed at V_{bias} = -3 mV

plying a concentration of 10^{-4}M, domains of primarily the **M** polymorph are formed. Several droplets of a solution of **CoP** in *n*-tetradecane with a concentration of 10^{-3}M were subsequently added, and in the marked square in the STM image in Figure 5.17 a scan was made with the tip in close proximity to the surface, because of the low bias voltage (-3 mV). The molecules that are removed by nano–shaving at this voltage are replaced by molecules from the supernatant solution. Because this solution has a much higher **CoP** than **CuP** content, a substantial number of cobalt porphyrins is inserted in the existing monolayer. Within the shaved area, 525 of the 1410 **MP** adsorbates (37%) are the **CoP** species, while outside this region only 71 of the 2209 (3%) porphyrins are the apparently higher **CoP** species which clearly demonstrates that the substitution was tip-induced. This method demonstrates that spontaneous desorption of molecules from adlayers of **CuP** is very slow, and adsorption of molecules from the solution phase is fast. In the surface area of the newly grafted patch, the **CuP** / **CoP** ratio resembles that of the supernatant solution more than that of the surrounding layer, because of the forced desorption induced by the nanoshaving procedure.

5.5 Monolayer dynamics in UHV

Thus far this chapter was only concerned with the study of the dynamics of **MP** monolayers at the solid/liquid interface. **CuP** monolayers were also stable on HOPG in ultrahigh vacuum (UHV), as has been shown in Chapter 4. An interesting expansion of this work is therefore to study the dynamics of **CuP** monolayers on HOPG in UHV with the aim to investigate the role of the solvent. A dry **CuP** monolayer was prepared by immersing a freshly cleaved HOPG substrate in a heptanic **CuP** solution for several minutes, after which the solution was removed and the sample was excessively rinsed with clean heptane to remove excess **CuP**, dried in a nitrogen flow and subsequently inserted in the vacuum chamber of our Jeol UHV SPM system. Figure 5.18 shows STM images of a **CuP** monolayer in this environment. When the STM image in Figure 5.18a is compared with that in Figure 5.18b, which was stored 14 minutes later, one can see that the **CuP** monolayer is still dynamic at the HOPG/UHV interface. In the STM image in Figure 5.18b it can be observed that after some of the **CuP** have rearranged along the direction of the white arrow. The molecules are again adsorbed in the same **M** and **S** polymorphs as were found at the solid/liquid interface. This observation indicates that the surface structures found for **CuP** on the graphite are intrinsically governed by porphyrins and the HOPG surface, and not by any particular HOPG/solvent interface. In Chapter 3 it was already demonstrated that the same polymorphs form at the interface between HOPG and a variety solvents, *i.e.* decamethyltetrasiloxane, 1-octanoic acid, *n*-tetradecane and *n*-heptane. The observation that the same surface structures are present and transform into each other in UHV implies that the observed surface polymorphs are not mere remnants of those formed during the formation of the monolayer at the HOPG/*n*-heptane interface, but that these surface structures are also the preferred surface structures that form in UHV after reorganisations within the monolayer. The thermodynamic constraints in UHV are of course different than at the solid/liquid interface, since the adsorption of additional **CuP** molecules is not possible in this situation and desorption is expected to be slower than in solution, if not completely absent.

With the help of the polymorph–dependent nc-AFM contrast measurements, which were presented in Chapter 4, the adaptation of the **CuP** monolayers to tip-induced disturbances, has been studied in UHV (Figure 5.19). After the nc-AFM image of a monolayer of **CuP** on HOPG shown in Figure 5.19a was recorded, holes were created by performing contact-mode AFM approximately in a 100 × 100 nm^2 area marked with the solid white square. After this nano-shaving procedure the area marked with the white dashed square was studied over time. In Figure 5.19 these two holes, created by the AFM cantilever, can be observed. Over time these two holes merge into one larger hole. Rather than having scraped away **CuP** molecules, which would subsequently pile up at the edges of the region at which the shaving was performed, the

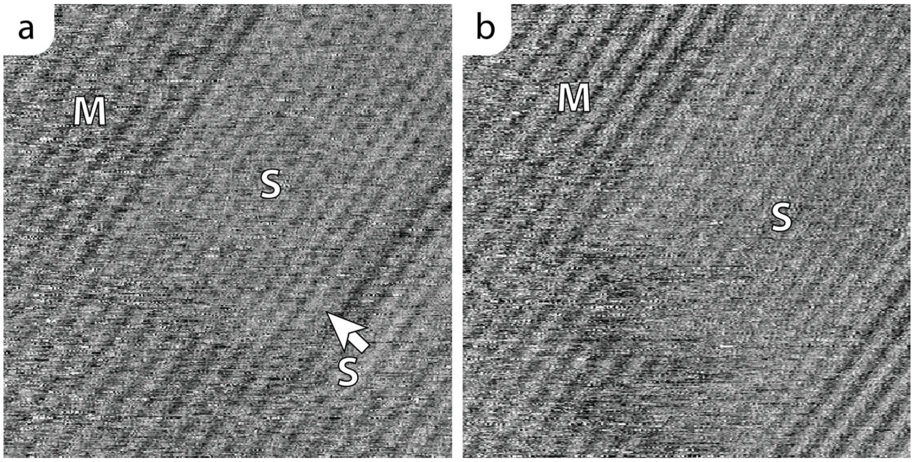

Figure 5.18: Two STM images of a **CuP** monolayer at the HOPG/UHV interface taken at a time interval of 14 minutes. These images show that the movement of **CuP** molecules (along white arrow) at the HOPG surface also occurs in ultra high vacuum and are therefore an intrinsic property of the 2–D layer, not requiring desorption or adsorption. The layer was prepared from a heptanic **CuP** solution. $I_{set} = 9$pA, $V_{bias} = -1000$mV, 50×50 nm^2 (a), idem but $I_{set} = 20$ pA (b).

holes can be observed to be surrounded by 2-dimensional patches of the **S** polymorph. The excess of **CuP** molecules in the surrounding layer, which has arisen from the local removal of **CuP** adsorbates from the holes, has thus led to the transformation of part of the monolayer from the **M** polymorph into the densest **S** polymorph. Both the STM and the nc-AFM measurements in UHV therefore present further evidence that the transformation of **MP** monolayers occurs in a 2-dimensional fashion, and does not require exchange of molecules with the solution phase or any other form of desorption.

5.6 Conclusion

This chapter has shown how different 2-dimensional polymorphs of **MP** molecules at the HOPG/ liquid interface form and transform into each other. The transformation of **MP** monolayers at room temperature is characterized by fast adsorption of **MP** molecules from the supernatant solution, a high mobility of individual adsorbed, unenclosed porphyrins, low mobility of molecules within the self–assembled monolayer, and limited desorption from the graphite surface. Because the desorption of porphyrin adsorbates is nearly absent, nearly all changes in surface structure involves

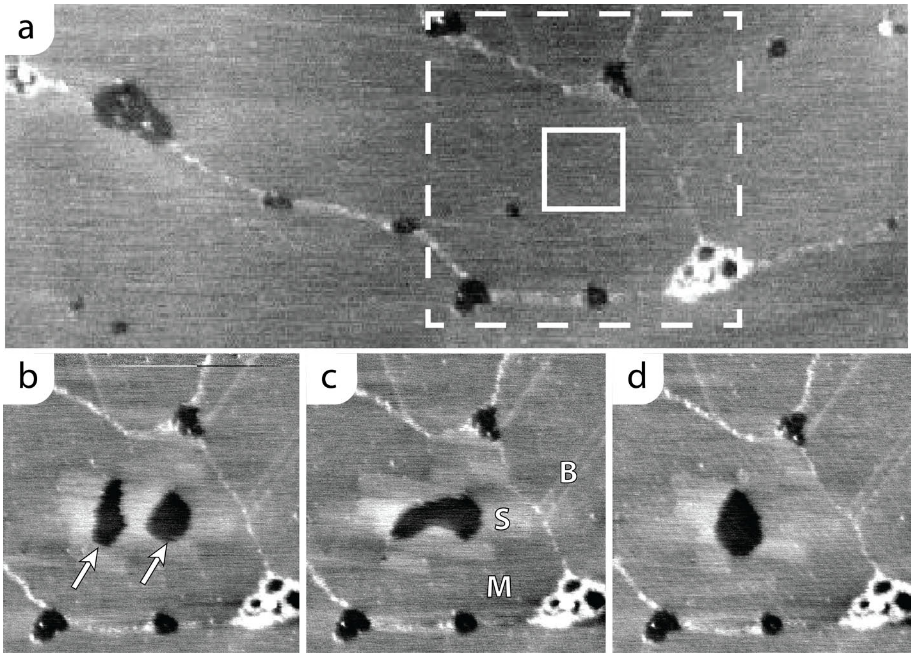

Figure 5.19: Series of nc-AFM images of a **CuP** monolayer at the HOPG surface. After the measurement in image (a) was performed, a contact AFM measurement was performed in the area marked with the white solid square. The result of this manipulation is shown in image (b). Two holes (white arrows) formed in the domain which consisted previously exclusively of the **M** polymorph, the formation of patches the **S** polymorph around the can be seen. Over time the two holes diffuse, forming one nearly circular hole as can be seen in (c) and (d) which are recorded 13 and 54 minutes after image (b) respectively. Image parameters: 1×1 nm^2, $\nu_0 = 142.228$ kHz, (a) 420×420 nm^2, $\nu_0 = 142.228$ kHz, $\Delta\nu = 240$ Hz (b,c,d).

2-dimensional movement of the adsorbed species. In order for a **CuP** monolayer to be able to adapt to changing concentrations of the supernatant solution, the presence of specific 2-dimensional defects is required. In the absence of such defects, a domain of a **MP** monolayer may be completely unable to adapt to changing thermodynamic situations and this explains why some low density domains can persist in thermodynamically unfavourable situations for more than 16 hours. These studies show that these physisorbed monolayers are not necessarily in thermodynamic equilibrium with the supernatant solution. Because the transformation of monolayers of **CuP** requires the presence of certain surface defects, the initial formation of the layer, which occurs within seconds, may determine the surface structure for hours or days. This study has demonstrated that, even for physisorbed molecules, which are only bound by Van der Waals and π–π interactions, and which in principle could always exchange molecules with the solution, thermodynamic equilibrium may not be reached on the time scale of the experiment, or on time-scales required for future bottom–up nanofabrication. Nanomanipulation, *i.e.* shaving away part of a self-assembled monolayer by the STM tip, can be used to reverse or accelerate transformations of **MP** monolayers. Local control over the monolayer structure can be obtained by combining nanoscale manipulation with an appropriate choice of the concentration and composition of the supernatant solution. Molecular tracers, *i.e.* different species of **MP** with STM contrast that is easily distinguishable from the species from which the monolayer was created, were employed to further study the behavior of **MP** monolayers. In particular insertion mechanisms responsible for the annealing of low density **M≈B** to higher density **M** domains has been studied using these tracers. The observation that the composition of a monolayer created by the addition of a second **MP** species to an existing monolayer does not reflect the molecular composition of the new supernatant solution provides further evidence that self–assembled monolayers of **MP** at the HOPG/liquid interface are not necessarily in thermodynamic equilibrium with the supernatant solution. The fact that previously adsorbed molecules are not replaced when a solution of a second, different molecule, is introduced, has more often been observed in the case of alkyl–functionalized porphyrins and phthalocyanines[49], and the second species could only be induced by locally nanografting in the previously formed monolayer as was already described in section 5.4. These findings suggest that the important role of kinetics for the stability of alkyl–functionalized adsorbates at the solid/liquid interface may be more general than for the tetra–undecylporphyrins studied here. These findings are relevant in view of the recently aroused interest in the thermodynamics of self–assembled monolayers at the solid/liquid interface[10,5,6,8]. Before correlating the appearance of a self–assembled monolayer to thermodynamic parameters like the concentration of the supernatant solution, the nature of the solvent, and the temperature, one has to ascertain in the first place that the monolayer is able to reach thermodynamic equilibrium with its supernatant solution. The dynamics of **CuP** were not only studied at the solid/liquid interface but also in UHV. As expansion of the work in Chapter 3, in which it was shown that the same **MP** forms the same polymorphs at the interfaces of HOPG and different supernatant solutions, it is shown here that upon disturbance of a monolayer of **CuP** at the HOPG/UHV interface, the same polymorphs are again formed, which provides further evidence that the observed polymorphs are an intrinsic property of **MP** molecules on a HOGP substrate and that transformations of the structures of these layers occurs in a 2-dimensional fashion without the need for desorption and adsorption of **MP** molecules.

5.7 Outlook

A natural extension of this work is to investigate the behavior of the self–assembled monolayers of tetraundecyl porphyrins at different temperatures. The effect of thermal annealing of molecular layers at the solid/liquid interface could be studied prior to[50] or even during[4,34] STM imaging. Given the high melting points of both 1-octanoic acid and *n*-tetradecane of 17 °C and 6 °C respectively, shorter alkanes may need to be employed as a solvent to study the layers at lower temperature. The melting point of *n*-heptane, for instance, is -90 °C and since **CuP** monolayers have been demonstrated to form in this solvent, this seems to be an appropriate choice for initial experiments. In the controlled atmosphere of the Nijmegen Liquid STM[51–53], necessary to prevent water condensation at these temperatures, the adaptation to enable measurements at these low temperatures should be feasible. This would allow for a wide range of temperatures at which STM studies could be performed, yielding further insight in the kinetics and thermodynamics of layer formation and transformation. Because the dynamics of individual molecules occurs fast on the measurement time–scale of the used scanning tunneling microscope, additional information could be obtained by employing faster video–rate STMs, capable of capturing tens of images per second[54,55,34]. These speeds, in combination with the lower temperatures may be sufficient to image the molecular dynamics step by step and even visualize the underlying changes in conformation of the alkyl chains. An additional interesting question to be answered in future research is to what extend desorption of parts of the adsorbates plays a role during dynamic structural processes: does the entire **CuP** molecule, *i.e.* porphyrin core and all four tails, stay adsorbed during the entire process or do some tails temporarily desorb? These questions could be answered using an STM capable of imaging with higher frame rates, or at lower temperatures. Finally, employing the kinetics of the self-assembled monolayers to create multicomponent monolayers, could be expanded to more than two **MP** species and even to the inclusion of other molecular species in existing layers of **MP**. Not only will this lead to more insight in the formation and transformation of physisorbed monolayers, but also to the expansion of the toolbox for the creation of nanoscale molecular devices. The inclusion of a second **MP** species in an existing **MP** monolayer has been introduced in this chapter merely as a means to track individual molecules during the dynamics of self–assembled monolayers. The formation of monolayers of more than one component is, however, interesting in its own right and it can be of crucial importance for the bottom-up fabrication for nanoscale devices[56–58]. The formation of multicomponent 2-dimensional crystals has been a topic of extensive investigation[50,59,60] and structures comprising up to four components have been reported[61]. In this chapter it was shown that mixed **CoP**/**CuP** and **CoP**/**NiP** monolayers can be fabricated by employing the kinetic properties of the initially formed monolayer. It was furthermore shown that with the help of nanografting **CoP** molecules can be locally inserted in an existing **CuP** monolayer. Most multi–component surface structures reported in literature are prepared by presenting the surface with a single solution containing a mixture of the constituting components. The sequential application of different components as employed in this chapter has primarily been used for templating studies, in which a self–assembled monolayer is used as a command layer to guide the adsorption of a second layer of a different molecule[62] or, in the case of porous host—guest complexes, where components are bound inside a preformed cavity[56,63,60]. Some studies have explicitly reported that the sequence in which different components were added to the system was unimportant to the outcome of the self-assembly process[61,62], showing that the eventually obtained surface structures presented the thermodynamically most stable configurations. Although the formation of a bi–component monolayer could be achieved by presenting the surface with a single solution containing a mixture of the two different porphyrin species, and this strategy has been proven successful in several studies[59], this method can have an important limitation. The preparation of the monolayers in a single step, from a single solution, provides a ratio of the molecules adsorbed on the surface which will only depend on the thermodynamic intricacies of the two species in solution and on the surface. The ratio will thus be governed by the chemical potentials of the involved species, with the most accessible experimental parameter being the concentration of each species in the dissolved phase. A disadvantage of this might is the entire sample surface will be covered with structures comprising the same component ratio. This might be beneficial for the preparation of actual devices but it is not always practical for single–molecule level studies in which the influence of the physical and chemical properties adsorbed species on one another is investigated. Interesting investigations include the influence of locally induced charge on the electronic properties of neighboring molecules[64] and studies of catalytic reactions that involve more than one surface–bound molecule, such as the catalytic epoxidation of alkenes by **MnP**, which was proposed to involve two surface—bound porphyrins to split molecular oxygen[52], or cascade reactions[65,66] in which the product of one catalyst is the substrate for the next. To reliably perform these studies it is more convenient to be able to control surface self-assembly in such a way that ratio of the different components strongly varies over the surface, since this allows for the examination of the mutual influence and distance of the two components on the same sample, in the same supernatant solution, with the same concentration, the same surrounding atmosphere, at the same temperature and even in the same STM images. This will greatly increase reliability of such single–molecule level studies.

References

1. Gomar-Nadal E., Puigmartí-Luis J. and Amabilino D.B. *Chem. Soc. Rev.*, 37 (3):490–504, **2008**
2. Love J.C., Estroff L.A., Kriebel J.K., Nuzzo R.G. and Whitesides G.M. *Chem. Rev.*, 105 (4):1103–1169, **2005**
3. Elemans J.A.A.W., Lei S. and De Feyter S. *Angew. Chem. Int. Ed.*, 48 (40):7298–7332, **2009**
4. Gutzler R., Sirtl T., Dienstmaier J.F., Mahata K., Heckl W.M., Schmittel M. and Lackinger M. *J. Am. Chem. Soc.*, 132
5. Lei S., Tahara K., De Schryver F.C., Van der Auweraer M., Tobe Y. and De Feyter S. *Angew. Chem. Int. Ed.*, 120 (16):3006–3010, **2008**
6. Lei S., Tahara K., Tobe Y. and De Feyter S. *Chem. Commun.*, 46:9125–9127, **2010**
7. Palma C.A., Bjork J., Bonini M., Dyer M.S., Llanes-Pallas A., Bonifazi D., Persson M. and Samor{‘i P. *J. Am. Chem. Soc.*, 131 (36):13062–13071, **2009**
8. Kampschulte L., Werblowsky T.L., Kishore R.S.K., Schmittel M., Heckl W.M. and Lackinger M. *J. Am. Chem. Soc.*, 130 (26):8502–8507, **2008**
9. Marie C., Silly F., Tortech L., Müllen K. and Fichou D. *ACS Nano*, 4:1288, **2010**
10. Palma C.A., Bonini M., Breiner T. and Samorì P. *Adv. Mater.*, 21 (13):1383–1386, **2009**
11. Yanagi H., Mukai H., Ikuta K., Shibutani T., Kamikado T., Yokoyama S. and Mashiko S. *Nano Lett.*, 2 (6):601–604, **2002**
12. Rabe J.P. and Buchholz S. *Phys. Rev. Lett.*, 66 (16):2096–2099, **1991**
13. Wang D., Wan L.J. and Bai C.L. *Mater. Sci. Eng., R*, 70 (3-6):169 – 187, **2010**
14. Samorì P., Müllen K. and Rabe J.P. *Adv. Mater.*, 16 (19):1761–1765, **2004**
15. Stevens F. and Beebe T.P. *Langmuir*, 15 (20):6884–6889, **1999**
16. Piot L., Marchenko A., Wu J., Müllen K. and Fichou D. *J. Am. Chem. Soc.*, 127 (46):16245–16250, **2005**
17. Xu H., Minoia A., Tomović Z., Lazzaroni R., Meijer E.W., Schenning A.P.H.J. and De Feyter S. *ACS Nano*, 3 (4):1016–1024, **2009**
18. Gesquière A., Abdel-Mottaleb M.M., De Feyter S., De Schryver F.C., Sieffert M., Müllen K., Calderone A., Lazzaroni R. and Brédas J.L. *Chem. Eur. J.*, 6 (20):3739–3746, **2000**
19. Florio G.M., Klare J.E., Pasamba M.O., Werblowsky T.L., Hyers M., Berne B.J., Hybertsen M.S., Nuckolls C. and Flynn G.W. *Langmuir*, 22 (24):10003–10008, **2006**
20. Hibino M., Sumi A. and Hatta I. *Thin Solid Films*, 273 (1-2):272 – 278, **1996**
21. Lackinger M., Griessl S., Kampschulte L., Jamitzky F. and Heckl W.M. *Small*, 1 (5):532–539, **2005**
22. Gimzewski J.K., Joachim C., Schlittler R.R., Langlais V., Tang H. and Johannsen I. *Science*, 281 (5376):531–533, **1998**
23. Liljeroth P., Repp J. and Meyer G. *Science*, 317 (5842):1203–1206, **2007**
24. Pleth Nielsen L., Besenbacher F., Stensgaard I., Laegsgaard E., Engdahl C., Stoltze P., Jacobsen K.W. and Nørskov J.K. *Phys. Rev. Lett.*, 71 (5):754–757, **1993**
25. Speller S., Heiland W., Biedermann A., Platzgummer E., Nagl C., Schmid M. and Varga P. *Surf. Sci.*, 331-333 (Part 2):1056 – 1061, **1995**. Proceedings of the 14th European Conference on Surface Science
26. van Houselt A. and Zandvliet H.J.W. *Rev. Mod. Phys.*, 82 (2):1593–1605, **2010**
27. Saedi A., van Houselt A., van Gastel R., Poelsema B. and Zandvliet H.J.W. *Nano Lett.*, 9 (5):1733–1736, **2009**
28. Hendriksen B.L.M. and Frenken J.W.M. *Phys. Rev. Lett.*, 89 (4):046101, **2002**
29. Besenbacher F. and Nørskov J.K. *Prog. Surf. Sci.*, 44 (1):5 – 66, **1993**
30. Weckesser J., Barth J., Cai C. and M˙*Surf. Sci.*, 431 (1-3):168 – 173, **1999**

31. Wahl M., von Arx M., Jung T.A. and Baiker A. *J. Phys. Chem. B*, 110 (43):21777–21782, **2006**
32. Schunack M., Linderoth T.R., Rosei F., Lægsgaard E., Stensgaard I. and Besenbacher F. *Phys. Rev. Lett.*, 88 (15):156102, **2002**
33. Schunack M., Petersen L., Kühnle A., Lægsgaard E., Stensgaard I., Johannsen I. and Besenbacher F. *Phys. Rev. Lett.*, 86 (3):456–459, **2001**
34. Tansel T. and Magnussen O.M. *Phys. Rev. Lett.*, 96 (2):026101, **2006**
35. Eichberger M., Marschall M., Reichert J., Weber-Bargioni A., Auwärter W., Wang R.L.C., Kreuzer H.J., Pennec Y., Schiffrin A. and Barth J.V. *Nano Lett.*, 8 (12):4608–4613, **2008**
36. Weckesser J., Barth J.V. and Kern K. *Phys. Rev. B*, 64 (16):161403, **2001**
37. Schull G., Ness H., Douillard L., Fiorini-Debuisschert C., Charra F., Mathevet F., Kreher D. and Attias A.J. *J. Phys. Chem. C*, 112 (36):14058–14063, **2008**
38. Liao M. and Scheiner S. *J. Chem. Phys.*, 117:205–219, **2002**
39. Barlow D.E., Scudiero L. and Hipps K.W. *Langmuir*, 20 (11):4413–4421, **2004**
40. Scudiero L., Barlow D.E., Mazur U. and Hipps K.W. *J. Am. Chem. Soc.*, 123 (17):4073–4080, **2001**
41. Suto K., Yoshimoto S. and Itaya K. *J. Am. Chem. Soc.*, 125 (49):14976–14977, **2003**
42. Jung T.A., Schlittler R.R., Gimzewski J.K., Tang H. and Joachim C. *Science*, 271 (5246):181–184, **1996**
43. Böringer M., Morgenstern K., Schneider W.D. and Berndt R. *Angew. Chem. Int. Ed.*, 38 (6):821–823, **1999**
44. Hla S.W., Meyer G. and Rieder K.H. *ChemPhysChem*, 2 (6):361–366, **2001**
45. Scudiero L. and Hipps K.W. *J. Phys. Chem. C*, 111 (47):17516–17520, **2007**
46. Xu S. and Liu G.y. *Langmuir*, 13 (2):127–129, **1997**
47. te Riet J., Smit T., Gerritsen J.W., Cambi A., Elemans J.A.A.W., Figdor C.G. and Speller S. *Langmuir*, 26 (9):6357–6366, **2010**
48. te Riet J., Smit T., Coenen M.J.J., Gerritsen J.W., Cambi A., Elemans J.A.A.W., Speller S. and Figdor C.G. *Soft Matter*, 6, **2010**
49. Takami T., Ye T., Pathem B.K., Arnold D.P., Sugiura K.i., Bian Y., Jiang J. and Weiss P.S. *J. Am. Chem. Soc.*, 132 (46):16460–16466, **2010**
50. Kong X.H., Deng K., Yang Y.L., Zeng Q.D. and Wang C. *J. Phys. Chem. C*, 111 (26):9235–9239, **2007**
51. Hulsken B., Elemans J.A.A.W., Gerritsen J.W., Khoury T., Crossley M.J., Rowan A.E., Nolte R.J.M. and Speller S. *New J. Phys.*, 11 (8):083011, **2009**
52. Hulsken B., Van Hameren R., Gerritsen J.W., Khoury T., Thordarson P., Crossley M.J., Rowan A.E., Nolte R.J.M., Elemans J.A.A.W. and Speller S. *Nature Nanotech.*, 2 (5):285–289, **2007**
53. Hulsken B., Gerritsen J. and Speller S. *Surface Science*, 580 (1-3):95 – 100, **2005**
54. Rost M., Crama L., Schakel P., van Tol E., van Velzen-Williams G., Overgauw C., ter Horst H., Dekker H., Okhuijsen B., Seynen M., Vijftigschild A., Han P., Katan A., Schoots K., Schumm R., van Loo W., Oosterkamp T. and Frenken J. *Review of Scientific Instruments*, 76 (5):053710, **2005**
55. Fleming A., Kenton B. and Leang K. *Ultramicroscopy*, 110 (9):1205 – 1214, **2010**
56. Wan L.J. *Acc. Chem. Res.*, 39 (5):334–342, **2006**. PMID: 16700532
57. Ciesielski A., Palma C.A., Bonini M. and Samorì P. *Adv. Mater.*, 22 (32):3506–3520, **2010**
58. Surin M. and Samorì P. *Small*, 3 (2):190–194, **2007**
59. Suto K., Yoshimoto S. and Itaya K. *J. Am. Chem. Soc.*, 125 (49):14976–14977, **2003**
60. Perdigão L.M.A., Perkins E.W., Ma J., Staniec P.A., Rogers B.L., Champness N.R. and Beton P.H. *J. Phys. Chem. B*, 110 (25):12539–12542, **2006**
61. Adisoejoso J., Tahara K., Okuhata S., Lei S., Tobe Y. and De Feyter S. *Angew. Chem. Int. Ed.*, 121 (40):7489–7493, **2009**
62. den Boer D., Habets T., Coenen M. J. J. v.d.M.M., Peters T.P.J., Crossley M.J., Khoury T., Rowan A.E., Nolte R.J.M., Speller S. and Elemans J.A.A.W. *Langmuir*, 27 (6):2644–2651, **2011**

63. Ruben M., Payer D., Landa A., Comisso A., Gattinoni C., Lin N., Collin J.P., Sauvage J.P., De Vita A. and Kern K. *J. Am. Chem. Soc.*, 128 (49):15644–15651, **2006**

64. Piva P.G., DiLabio G.A., Pitters J.L., Zikovsky J., Rezeq M., Dogel S., Hofer W. and Wolkow R. *Nature*, 435 (7042):658–661, **2005**

65. Bruggink A., Schoevaart R. and Kieboom T. *Org. Process Res. Dev.*, 7 (5):622–640, **2003**

66. Wasilke J.C., Obrey S.J., Baker R.T. and Bazan G.C. *Chem. Rev.*, 105 (3):1001–1020, **2005**

CHAPTER 6

Tip-induced electrochemical reactions of **CuP**

6.1 Introduction

Scanning tunneling microscopy (STM) allows for the study of chemical reactions at the single molecules level[1]. As has been demonstrated by Hulsken *et al.* the catalytic properties of metalloporphyrins can be studied with submolecular resolution at the solid/liquid interface[2]. The catalytic epoxidation of alkenes by a monolayer of Mn(III)-porphyrins at the Au(111)/n-tetradecane interface could be imaged *in situ* using STM. However, the identification of the different intermediate species involved, including those caused by changes in oxidation state of the Mn center, was to some extend based on circumstantial evidence. In that work the identification of reactive single molecule Mn(IV)=O complexes was based on the distribution of these species on the surface as dictated by the stoichiometry of the oxygen atoms which originated from a homolytic dissociation of O_2. Reflectance UV-Vis measurements on the catalytic monolayer confirmed the assignment of the intermediates, this technique however averages the behaviour of many molecules due to its limited lateral resolution. Although these experiments convincingly demonstrated that STM is a useful tool to investigate known catalytic reactions, one would ultimately like to characterize chemical species on a surface directly by STM. This ability would allow the elucidation of unknown reaction mechanisms by unambiguously identifying hitherto unknown intermediate species, which is particularly important if the reactivity of adsorbed molecules differs from that of the molecules in solution, or if the reactivity is altered by different adsorption sites or adsorption configurations. In this respect, Hieringer *et al.* recently demonstrated that the affinity of metalloporphyrins for axial ligands is strongly affected by the covalent bonds that the central metal can form with silver substrates[3]. Just like the differences in physical properties of the various polymorphs of **CuP**, which were topic of Chapter 4, the chemical and reactive properties of **CuP** might depend on the exact adsorption configuration of physisorbed molecules on the surface, and only by the unambiguous identification of reactive species and intermediates can one try to fully understand and eventually exploit such behaviour.

The main feature that underlies the catalytic activity of Mn–, Co–and Fe–porphyrins, is that these metal centers can adopt several oxidation states. The metal center of Mn–porphyrins, for instance, is able to obtain Mn(II), Mn(III), and Mn(IV) oxidation states[4]. Not all porphyrin metal centers share this possibility, and Cu(II), Zn(II), Al(III) and V(IV)O, do not have the ability to adopt different metal centered oxidation states[5,6]. Besides the possibly rich collection of oxidation states of the central transition metal, the π–system of an aromatic porphyrin ligand can be oxidized and reduced twice. This means that every metalloporphyrin has at least five possible oxidation states: $\mathbf{P}^{2-}$, $\mathbf{P}^{1-}$, $\mathbf{P}^{0}$ (or simply **P**), $\mathbf{P}^{1+}$ and $\mathbf{P}^{2+}$. Also the free base derivative, **2HP**, can have these oxidation states[7]. Although, in principle, the ring-centered redox behaviour is the same for all metalloporphyrins, the energies at which the different oxidation states are formed, which are reflected by the redox potential, may be shifted. Such a shift is observed for porphyrins of which the metal center can be oxidized or reduced multiple times, which leads to high electrical charges on the metal center and thereby to coulomb repulsion of the additional electrons or holes of consecutive, ring-centered, reductions or oxidations[5]. The possible redox states of porphyrins have been extensively studied by DFT calculations[6] and electrochemical experiments[5,7–11]. It has also been reported that different redox states of adsorbed porphyrins can be distinguished with the help of STM[12–15]. This makes STM a valuable tool to investigate the electrochemistry of porphyrins and the reactive properties that stem from these different oxidation states.

Given the fact that copper porphyrins do not have metal-centered oxidation states, their electrochemistry is less complicated than that of, for instance, manganese porphyrins. Only oxidations and reductions of the porphyrin ring species are expected for **CuP**, while the metal stays in its native Cu(II) oxidation state. An overview of the different redox species of **CuP** is given in Table 6.1. It can be observed that the only oxidations and reductions of Cu porphyrins are the ones on the π–system of the porphyrin ring, despite the fact that Cu porphyrins have an unpaired electron on the copper center. **CuP** is thus paramagnetic and its single unpaired spin resides in an orbital with primarily $d_{x^2-y^2}$ character. Density functional theory (DFT) calculations, performed on unfunctionalized metalloporphyrins, support these experimental findings[6]. As stated above, Cu porphyrins thus give rise to the simplest electrochemical behaviour possible for metalloporphyrin species, and for this reason they have been chosen for the STM studies on reactivity described in this chapter. Even free base

Table 6.1: Overview of the oxidation states of **CuP** as reported in literature[16]. The reported values are the half-wave potentials at whicmymolecCuPh the given species is formed. The experiments were performed in dichloromethane (CH_2Cl_2) and benzonitrile (PhCN) and in both cases the supporting electrolyte was tetrabutylammonium perchlorate (TBAP). The electrochemical formation of **Cu(II)P**$^{2-}$ occurs at a more reductive potential than the reduction of dichloromethane[17], and can therefore not be observed in this solvent.

Species	V$_{redox}$, (*vs* SCE) CH_2Cl_2, 0.1M TBAP	V$_{redox}$ (*vs* SCE) PhCN, 0.1M TBAP
Cu(II)P^{2-}	*outside window*	-1.91
Cu(II)P^{1-}	-1.42	-1.43
Cu(II)P^{0}	*native*	*native*
Cu(II)P^{1+}	0.82	0.81
Cu(II)P^{2+}	1.19	1.17

porphyrins have more complex electrochemical behaviour because of their ability to be protonated[11,18,19] or metallated[18]. The porphyrin core of the free base analogue furthermore has only two–fold symmetry, unlike **CuP** which is four–fold symmetric like the other metalloporphyrins. Since this symmetry will be reflected in the orbital structure and thus appearance in STM images[20], comparison with other metalloporphyrins is therefore expected to be more straightforward for **CuP** than for **2HP**. A final consideration in choosing **CuP** over other porphyrins with a non–electro–active metal center such as, for instance, **ZnP**, is the much lower affinity of **CuP** for axial ligands[21,22]. The binding constants of nitrogen ligands, such as pyridine, to copper porphyrins are about 10^5 times lower than those to zinc porphyrins[21]. Such a binding of axial ligands, including coordinating solvents, could further complicate the identification by STM of surface-bound porphyrins that exist in different oxidation states. Not only has the coordination of axial ligands been reported to alter the appearance of adsorbed Zn–porphyrins in STM[23], it is also known to shift the redox potentials of the π–system centered oxidation states[10]. The combination of these two factors make data interpretation cumbersome, both from a microscopical and an electrochemical perspective.

In summary, **CuP** is an excellent choice to investigate, with the help of STM, the electrochemical behaviour and appearance of the porphyrin–ring system common to all metalloporphyrins. Besides this potential of **CuP** to act as a reference system, it is also interesting to investigate its electrochemical reactivity in its own right. Copper tetraphenylporphyrin (CuTPP) has been reported to be a molecular semiconductor[24] like the related copper phthalocyanine[25,26]. The charge transport through these molecules, whether it regards electrons or holes, is closely related to the formation of anions and cations, respectively. Copper–porphyrin derivatives have also been investigated as photosensitzers which can, upon optical excitation create highly reactive oxygen species that can destroy tumors.[27–29]. This process is believed to rely on the creation of a porphyrin cation from the neutral, excited molecule, which exemplifies the potential importance of the understanding the electrochemical processes at a fundamental level. Finally, it would be of great interest to investigate whether the polymorph dependent electronic properties of **CuP** alter the oxidation states of these molecules to such an extend that the **CuP** displays a different electrochemical response when adsorbed in the different polymorphs and adsorption configurations. Such polymorph dependent reactivity may allow for tuning of the electrochemical and reactive properties at the single–molecule level.

6.2 STM studies of CuP at reductive potentials

First, the behaviour of **CuP** molecules at the HOPG/1-octanoic acid interface at negative surface potentials was studied. At negative surface potential there is a highly negative electric charge at the surface under the porphyrin adsorbates. The transfer of an electron from this negatively charged electron to a porphyrin adsorbate would reduce this molecule. Figure 6.1 shows a domain consisting of **M** and **B** polymorphs. The structural evolution of these domains, as was extensively discussed in Chapter 5, can be seen in Figure 6.1a and b, which show the annihilation of some rows of the **B** unit cells and a reduction in the amount of **M** sublattices. After the image in Figure 6.1b had been recorded, the tip was retracted by 2 nm and then the bias voltage between tip and sample was changed from -825 mV to -3850 mV for a duration of 300 μs, after which it was restored to the original bias voltage. The location of the tip where the voltage pulse was applied is marked by the "×" in Figure 6.1b. Since the negative bias voltage is applied to the sample, the HOPG surface has been at highly reductive potentials during the voltage pulse. The third STM image (Figure 6.1c) shows that this negative voltage pulse has created several "dots" with increased apparent heights, near the location where it was applied. These dots appear approximately 100 pm higher than the surrounding unaffected porphyrin adsorbates. The result of a similar pulse on a domain of the **L** polymorph of **CuP** is shown in Figure 6.2. On the reductive pulse has lead to the occurence of similar **CuP** adsorbates with increased apparent heights, showing that this behaviour is not specific to any of the surface polymorphs. The individual **CuP** molecules can clearly be distinguished in this image, and it can be observed that the entire porphyrin ring of the affected porphyrin molecules appears higher than that of their neighboring adsorbates. These results are in line with the fact that reductions of **CuP** are centered at the π–system, rather than on the metal. An increased apparent height of the entire

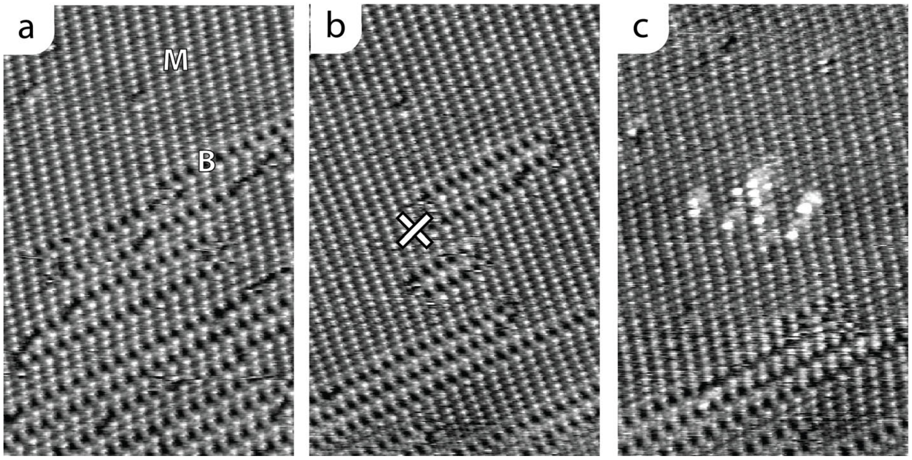

Figure 6.1: Three STM images at the same location on a domain comprising **M** and **B** unit cells of a **CuP** monolayer at the HOPG/1-octanoic acid interface. After image (b) a voltage pulse (-3850 mV, 300 μs, tip retracted by 2 nm) was given at the location marked with "×". The result of the pulse can be seen in image (c). Image parameters (a,b,c): 40 × 60 nm^2, I_{set} = 3 pA, V_{bias} = -820 mV.

porphyrin ring was also observed for reduced ZnTPP molecules at the Au(111)/0.1M $HClO_4^-$ interface in an electrochemical STM (ECSTM), as was reported by Yoshimoto *et al.*[12]. Also for magnesium porphyrins at an oxidized NiAl surface the anion appears with an increased apparent height of the entire porphyrin ring[30,31].

6.2.1 The proposed formation of $Cu(II)P^{1-}$ and $Cu(II)P^{2-}$

Close inspection of the cross section in Figure 6.2, reveals that three distinct species, which can be distinguished by their apparent heights. The majority of the surface is still covered by the species appearing lowest (≈ 100 pm apparent height difference between the ring and the alkyl tail regions). Since this species is the most prevalent on the surface, it is expected to correspond to the native $\mathbf{Cu(II)P^0}$ molecule. Besides this species, two species with an increased apparent height (≈ 175 pm and ≈ 200 pm apparent height difference between the alkyl chains and the porphyrin rings, respectively) can be observed. Some of these species are encircled in the STM image of Figure 6.2 and marked with arrows in the corresponding cross section. Since these species are generated by a pulse with a reductive surface potential, it is proposed that the higher **CuP** species have been reduced from $\mathbf{Cu(II)P^0}$ to $\mathbf{Cu(II)P^{1-}}$ or $\mathbf{Cu(II)P^{2-}}$. The **CuP** molecules with an apparent height of ≈ 175 pm, some of which

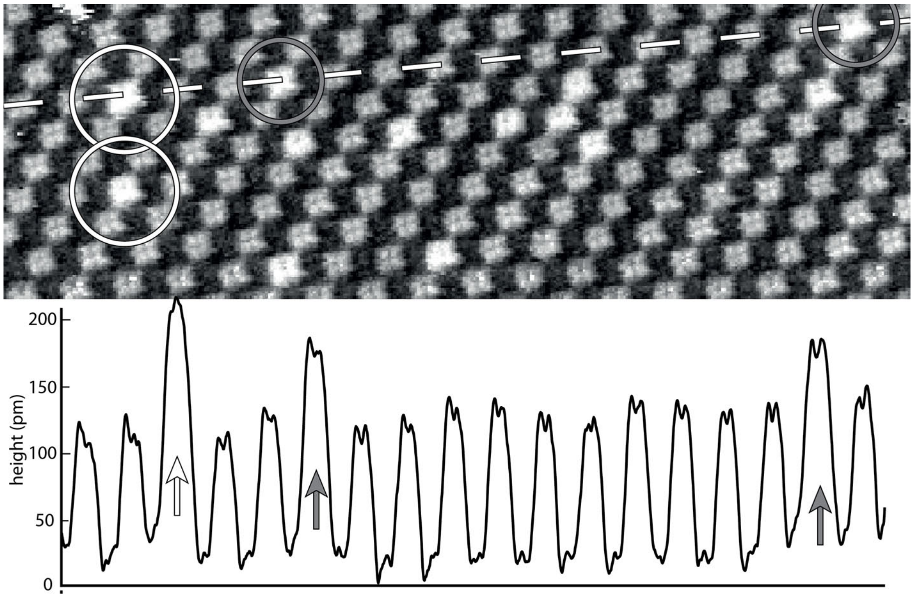

Figure 6.2: High resolution STM image(top) and cross section (bottom) of a **L** domain of a **CuP** monolayer at the HOPG/1-octanoic acid interface after application of a negative voltage pulse. **CuP** molecules with three different apparent heights can be identified. These are assigned to **Cu(II)P**$^{1-}$(encircled grey), **Cu(II)P**$^{2-}$ (encircled white) and the native **Cu(II)P**^{0} species (unmarked). Image parameters: 38 × 13 nm^2, $I_{set} = 2$ pA, V_{bias} = -600 mV.

are encircled in grey, are proposed to be the mono–anionic $\mathbf{Cu(II)P^{1-}}$ species, and those with an apparent height of ≈ 200 pm (encircled in white) the dianionic species $\mathbf{Cu(II)P^{2-}}$. Evidence for these assignments is based on their formation mechanism. The formation of the mono-anionic species $\mathbf{Cu(II)P^{1-}}$ results from the single-electron reduction of the neutral $\mathbf{Cu(II)P^{0}}$ species:

$$\mathbf{Cu(II)P^{0}} + e^{-} \longrightarrow \mathbf{Cu(II)P^{1-}} \tag{6.1}$$

It has been reported, based on cyclic voltammetry, that the formation of the dianion, $\mathbf{Cu(II)P^{2-}}$, occurs by a consecutive single–electron reduction of $\mathbf{Cu(II)P^{1-}}$,

$$\mathbf{Cu(II)P^{1-}} + e^{-} \longrightarrow \mathbf{Cu(II)P^{2-}} \tag{6.2}$$

This implies that the formation of $\mathbf{Cu(II)P^{2-}}$ occurs via the formation of $\mathbf{Cu(II)P^{1-}}$ rather than by a single two–electron reduction process, which are proposed to occur for other porphyrin species, such as free base porphyrins in very acidic environments[32]. Since the formations of both the monoanion and the dianion do not require any additional chemical reactions it is therefore expected that reductive pulses applied on a given region of the monolayer, yield the creation of monoanions from which dianions are formed in a second reduction step. The STM image in 6.3a shows a **M>B** domain of **CuP** after a reductive pulse. Both the proposed anionic and dianionic species can be identified. After the STM image in Figure 6.3a had been recorded, a second reductive voltage pulse was applied at the center of the region in the image, after which image 6.3b was recorded. After the pulse both the number of anions (not marked) and dianions (encircled) had increased. Of the 436 neutral $\mathbf{Cu(II)P^0}$ species visible in the marked region in the STM image in Figure 6.3a, 2 (0.5%) are reduced to the dianion, whereas an additional dianion in Figure 6.3b originates from 1 of the 23 (4%) monoanions that were already present. This implies that the probability that a dianion is formed from an existing mono-anion is an order of magnitude larger than that it forms from a neutral **CuP** adsorbate. After the recording of the STM image in Figure 6.3b, the same surface area was continuously scanned at the same bias voltage of V_{bias} =- 750 mV for 30 minutes. The last image of this measurement series is depicted in Figure 6.3c, and no significant changes in the amount or location of the reduced **CuP** adsorbates can be observed. After the recording of this image, another reductive voltage pulse was applied in the center of the image and the resulting STM image, which is recorded 2 minutes later, is shown in Figure 6.3d. The region within the marked rectangle in image 6.3c contains 460 molecules, of which 36 are mono–anions and 3 dianions. The same region in Figure 6.3d contains 39 mono–anions and 10 di–anions. From the previously existing 421 neutral species, a mere 2 (0.5%) were transformed to the dianionic form, whereas 6 of the previously existing 36 $\mathbf{Cu(II)P^{1-}}$ entities (16.5%) are reduced to the dianion. The origins of the newly formed dianions are summarized in Table 6.2. From this table it is clear that the probability of formation of the highest features from a monoanion is up to 30 times higher than formation from a neutral **CuP** molecule which supports our assumption that this species is the dianionic $\mathbf{Cu(II)P^{2-}}$ species. Despite the voltage pulse, none of the 3 existing dianions was transformed to another species, although one existing dianion (marked $*$) crossed a **B** boundary and thereby left the marked region. It is proposed that, in agreement with the voltammetric studies reported in literature, the formation of the dianions always occurs as two consequtive single–electron reductions, but during the pulse both steps may occur rapidly after each other on the same molecule, leading to an apparent single step transformation from the neutral species to the dianion. During such a pulse many high energy electrons pass the monolayer in a short time, making consecutive reductions possible, which make the two-electron reduction appear as a single step process.

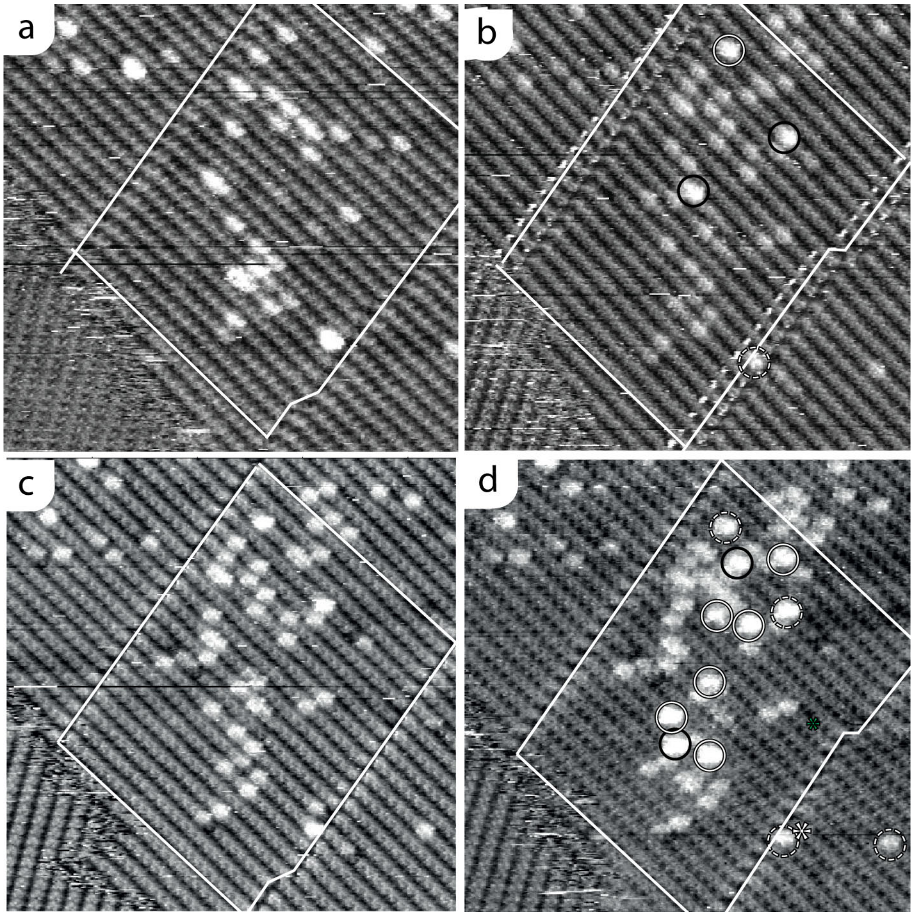

Figure 6.3: STM image (a) of monolayer of **CuP** at the HOPG/1-octanoic acid interface after a single reductive pulse (-3850 mV, 0.3 ms) which has led to the proposed formation of reduced **CuP** adsorbates. After the image in (a, t = 0), a second pulse of the same duration and magnitude was applied in the center of the imaged region, the result of which is shown in the STM image in (b, t = 10 min.). $\mathbf{Cu(II)P^{2-}}$ entities that already existed before the second pulse was applied, are marked with dashed circles. $\mathbf{Cu(II)P^{2-}}$ adsorbates that are formed from a previously neutral molecule ($\mathbf{Cu(II)P^{0}}$) are marked with a black circle, and dianions that are formed from the mono–anion are encircled in white. No additional pulses were applied between images (b) and (c, t = 31 min.) after which a third pulse was applied of which the result can be observed in (d, t = 34 min.). Image parameters (a,b,c,d): 40 × 40 nm^2, I_{set} = 5 pA, V_{bias} =- 750 mV

Table 6.2: Overview of the fate of the **CuP** adsorbates after the reductive pulses applied between the STM images in Figure 6.3 (a) and (b) and between the STM images in Figures 6.3 (c) and (d). The observed number of each of the precursors (**Cu(II)P^{0}** and **Cu(II)P^{1-}**) within the marked region is given, as well as how many of these were converted to the **Cu(II)P^{2-}** dianion as a result of the pulses.

	Figures 6.3 a,b		**Figures 6.3 c,d**	
Precursor	# Precursor present	# **Cu(II)P^{2-}** formed	# Precursor present	# **Cu(II)P^{2-}** formed
Cu(II)P^{0}	436	2 (0.5%)	421	2 (0.5%)
Cu(II)P^{1-}	23	1 (4%)	36	6 (16.5%)

6.2.2 Reoxidation of the anions

If the assignment of the aformentioned species to ring-centered anions is correct, it should be possible for them to revert back to their native **Cu(II)P^{0}** state. Reductions of the π-system of porhyrins have been reported to be electrochemically reversible[16], implying that no chemical reaction is expected to accompany the electrochemical reduction step which could prevent the species from returning to its native, neutral state. In the two consecutive STM images in Figure 6.4 the spontaneous reoxidation of two dianions can be observed. These images were recorded with a time interval of 1.5 minutes during which no pulses or bias voltage changes were applied. The dianionic porphyrin marked with a dashed circle is reoxidized to the monoanionic form, which implies that a single electron reduction step has occurred, as expected from the mechanism reported in the literature[16]. The dianion marked in the solid circle, however, decays in an apparent two–electron oxidation to the neutral species. The previous explanation for the apparently simultaneous two-electron reduction, namely the high current density during the pulse, does not explain this phenomenon, as it is observed during normal scanning with moderate bias voltages and currents. A more extensive discussion on this matter will be given in Section 6.3.

The oxidation of **Cu(II)P^{2-}** species has also been monitored over a longer time period. First, a large amount of reduced **CuP** species was created by applying 9 identical −3850 mV voltage pulses in an equally spaced 3×3 grid in the region enclosed by the rectangle in the STM image in Figure 6.5a. Both monoanions (grey circles) and dianions (white circles) can be identified, although the resolution is too poor to accurately count the former. In the STM images in Figure 6.5b and c which have been recorded 60 and 177 minutes after the STM image in Figure 6.5a, respectively, a clear decrease in the number of the high **Cu(II)P^{2-}** spots can be observed.

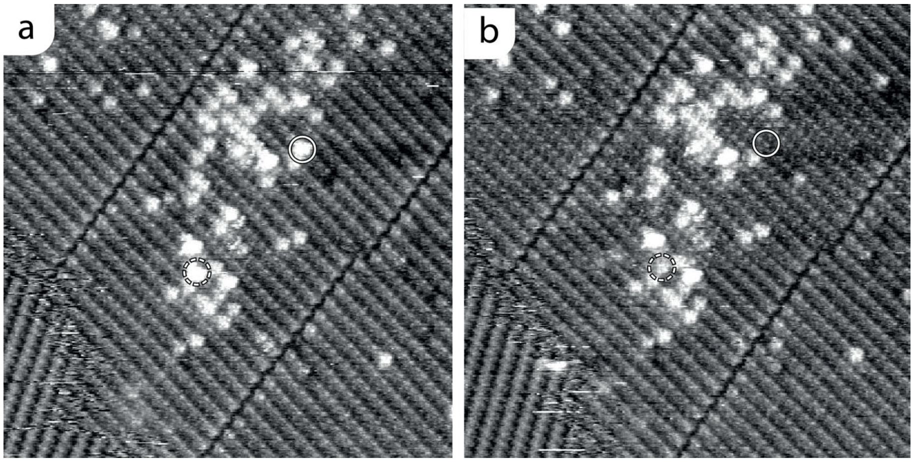

Figure 6.4: Two STM images taken at a time interval of 1.5 minutes in which the fate of dianionic **Cu(II)P**$^{2-}$ species at the HOPG/1-octanoic acid interface can be observed. The **Cu(II)P**$^{2-}$ molecule marked with the solid circle decays to the native **Cu(II)P**^{0} species, while the molecule marked with the dashed circle reoxidizes to the **Cu(II)P**$^{1-}$ monoanion. Image parameters: 40 × 40 nm^2, I_{set} = 5 pA, V_{bias} = -750 mV.

This decrease is quantified in the graph in Figure 6.5d. From this graph it is derived that the average lifetime of the **Cu(II)P**$^{2-}$ state is about 90 minutes. This value should be treated with some caution because the region where the two rotational domains meet (between the dashed lines in Figure 6.5b) is depleted from all reduced molecules quickly. This depletion might not be the result of oxidation, but of desorption of **CuP** molecules at the dynamic boundary between the two domains. That the observed oxidation behaviour does not merely reflect the natural decay of the dianions is supported by the fact that the re-oxidation over time can be well fitted with a straight line, while an exponential decay would have been expected for such uni-molecular process and its corresponding first order reaction kinetics[33]. The obtained lifetime of the **Cu(II)P**$^{2-}$ species does, however, yield an order of magnitude estimation of this decay process. The same area can be seen in the STM image in Figure 6.5e which has been recorded 20 hours after the image in Figure 6.5a. The image in Figure 6.5e shows that the monolayer now comprises only **Cu(II)P**^{0} and **Cu(II)P**$^{1-}$ species. Although the exact decrease in the number of mono–anions cannot be determined due to the poor resolution in the beginning of the measurement series, and the lateral diffusion of the molecules by processes described in Chapter 5, it is the average lifetime of the **Cu(II)P**$^{1-}$ species is orders of magnitudes larger (>20 hours) than that of **Cu(II)P**$^{2-}$. This experiment demonstrates that the spon-

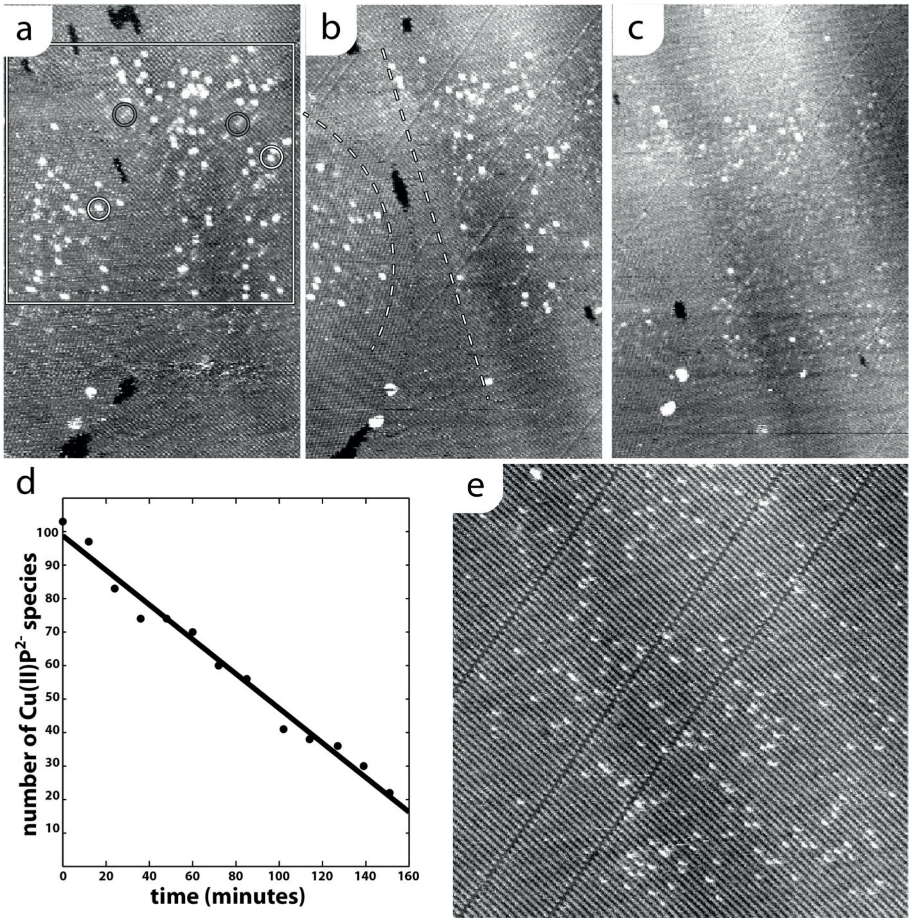

Figure 6.5: Three consecutive STM (a,b,c) images taken $t_a = 0$, $t_b = 60$ min. and $t_c = 177$ min. in which the oxidation of **Cu(II)P^{2-}** species over time can be monitored. The STM image in (e) is taken at the same location at t_e = 20 hrs. The decay of **CuP^{2-}** species over time, as obtained from analysis of a series of STM images including those shown in (a), (b) and (c) is plotted in (d). Image parameters: (a,b,c) 130 × 200 nm^2, I_{set} = 3 pA, V_{bias} = -750 mV. (e) 120 × 120 nm^2, I_{set} = 10 pA, V_{bias} = -750 mV

taneous reduction of the monoanionic $\mathbf{Cu(II)P^{1-}}$ species is slow. The process can be accelerated by external stimuli, which was demonstrated by the fact that the application of a positive voltage pulse could result in the re-oxidiation of the $\mathbf{Cu(II)P^{-1}}$ species to the neutral $\mathbf{Cu(II)P^{0}}$ (Figure 6.6). Immediately after the STM image in Figure 6.6a had been recorded, a single positive voltage pulse (2250 mV, 450 μs) was applied in the center of the scanned area. Directly after this pulse the STM image in Figure 6.6b was recorded. The time interval between the storage of the two images is 3 minutes. Of the 64 reduced **CuP** adsorbates present in the STM image in Figure 6.6a, 31 (48%) are re-oxidized and therefore no longer visible as apparently high features in Figure 6.6b. The cross section shows that the re-oxidized adsorbates (indicated by "×") cannot be distinguished from the **CuP** molecules that were not affected by any of the applied pulses, and it is therefore proposed that indeed the native $\mathbf{Cu(II)P^{0}}$ species can be regenerated upon applying a positive voltage pulse to the anionic species. This fact shows that upon reduction of **CuP**, no processes occur that irreversibly alter the chemical nature of the copper porphyrin, such as demetallation or hydrogenation of the porphyrin ring. The slow decay of charged porphyrin species adsorbed to a surface without external stimulation, has been reported by He *et al.*[14,32], who investigated the redox behaviour of free base tetrapyridyl porphyrins (2HTPyP) at the Au(111)/0.1M H_2SO_4 interface in an electrochemical STM. These porphyrins were observed to remain in voltage induced redox states for more than ten minutes. This slow electrochemical reaction was ascribed to the fact that in the highly acid electrolyte they used, protonation of the the free base porphyrin occurs as a result of the change in redox state. In this case the reduction reaction is therefore only quasi–reversible. This process is only possible for free base porphyrins since they can be protonated reversibly. If such a protonation process were to occur in the case of the copper porphyrins studied here, it would inevitibily lead to demetallation of the porphyrin and does therefore not agree with the fact that the created porphyrin anions can be transformed back to the native **CuP** species, by applying positive voltage pulses. It is therefore proposed that the extremely slow re-oxidation of the reduced species of **CuP** at the HOPG/1-octanoic acid interface has a different origin.

6.3 Explanation of the slow re-oxidation

In electrochemical studies of porphyrin solutions all reductions and oxidations of **CuP** have been reported to be reversible[16], which implies that upon moving the electrode potential back below the threshold values for oxidation or reduction, the porphyrins quickly return to their native redox states. The STM studies presented in this Chapter, however, show that the reduced species generated by voltage pulses do not return to their native $\mathbf{Cu(II)P^{0}}$ state within several hours. The lifetime of the the dianionic $\mathbf{Cu(II)P^{2-}}$ species was found to be approximately 90 minutes, whereas the monoanionic $\mathbf{Cu(II)P^{1-}}$ species even remained in its reduced state for over 20 hours. In

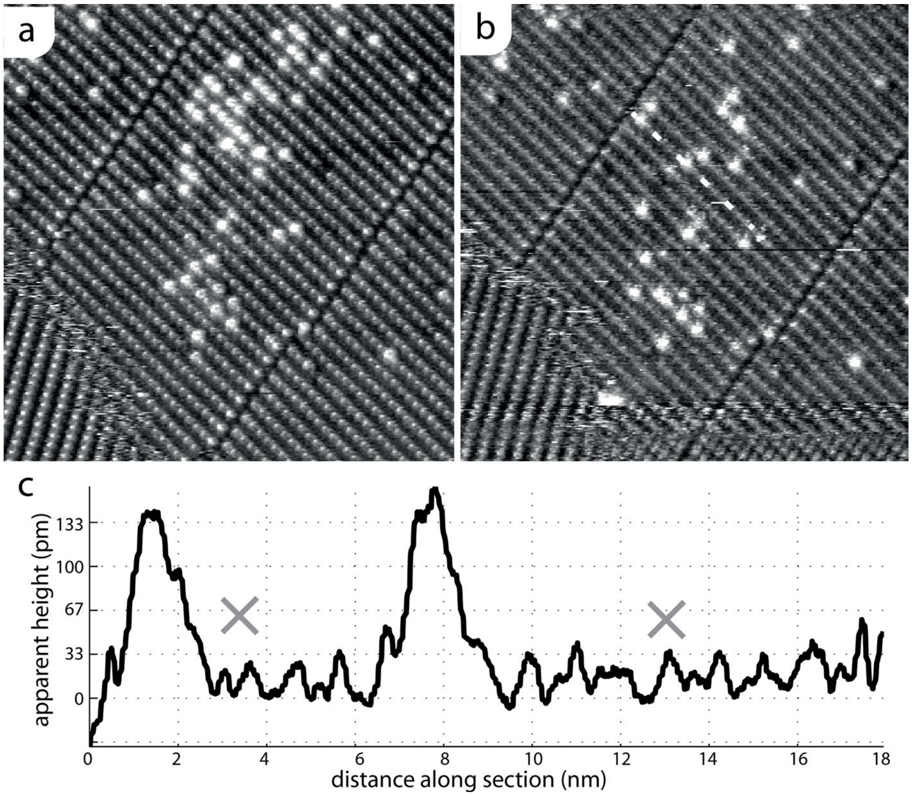

Figure 6.6: STM images of **CuP** at the HOPG/1-octanoic acid interface. Between the two STM images a positive voltage pulse (2250 mV, 450 μs) was applied at the center of the imaged region. The re-oxidation of the anionic and dianionic $\mathbf{Cu(II)P^{1-}}$, $\mathbf{Cu(II)P^{2-}}$ species to $\mathbf{Cu(II)P^{0}}$ can be observed as the disappearance of the higher features. A cross section along the dotted line in (b) is given in (c). The locations marked with "×" indicate reduced **CuP** adsorbates that were re-oxidized in (b) as a result of the positive voltage pulse. Image parameters: (a,b) 40 × 40 nm^2, I_{set} = 5 pA, V_{bias} = -750 mV

Chapter 3 it was shown that monolayers of **CuP** are not commensurate to the underlying HOPG substrate. From this it was deduced that there are no strong covalent bonds between the adsorbates and the graphite surface. The weak nature of the bonds between **CuP** and the HOPG presumably implies weak electronic coupling between the two and this allows for the extended existence of the reduced species. The weak coupling might, however not be sufficient to explain the slow re-oxidation processes and two additional mechanisms are proposed that might explain the apparent differences between the behavior of **CuP** in voltammetric experiments and at the interface between HOPG and apolar solvents. Firstly, it is known that the basal plane of HOPG is remarkably inert with respect to electron transfer[34–37]. It has even been suggested that the electron transfer rate at the graphite basal plane is six orders of magnitude slower than at step edges and that the complete voltammetric response of a basal-plane HOPG electrode is solely the result of to defects like step edges, even when less then 1% of the surface consists of such defects[34]. The electrochemical irreversibility of the redox reactions of **CuP** molecules adsorbed to the HOPG basal plane could therefore be due to the extremely slow electron transfer across this electrode. Although thermodynamically the anions should reoxidize to the neutral species, this process is kinetically limited by the slow electron transfer across the electrode. It can at this stage not even be excluded that the decay of the reduced porphyrin species does not occur *via* electron transfer across the HOPG surface at all, but rather that this electron is transferred to the scanning STM tip or to molecules of the surrounding 1-octanoic acid solvent. A second factor that might explain the apparent difference in redox behaviour of **CuP** at the surface is a possible difference in the planarity of the porphyrin macrocycle upon adsorption, as was proposed in Chapter 4 by the adsorption of the alkyl tails to the graphite surface It has been reported that a nonplanar distortion of porphyrins can alter their redox potentials and even the nature of the formed oxidation and reduction species, *i.e.* whether 1-electron or 2-electron oxidations occur and whether these oxidations take place the metal centre or the porphyrin ring[38,39]. Possibly such a the difference in planarity of adsorbed porphyrins and those dissolved in the electrolytic solutions also influences the reversibility of the electron transfer reactions. To further assess these factors STM studies would need to be expanded to include porphyrin derivatives equipped with different functional groups at their periphery which would enhance or decrease the amount of porphyrin ring distortion.

6.4 Apparent heights of the reduced species

Although there can be confidence that the same electrochemical processes occur when negative voltage pulses are applied in different experiments, it is important to note that the observed apparent heights and even the apparent widths of the anionic species vary significantly per measurement and even per image. The reported apparent height

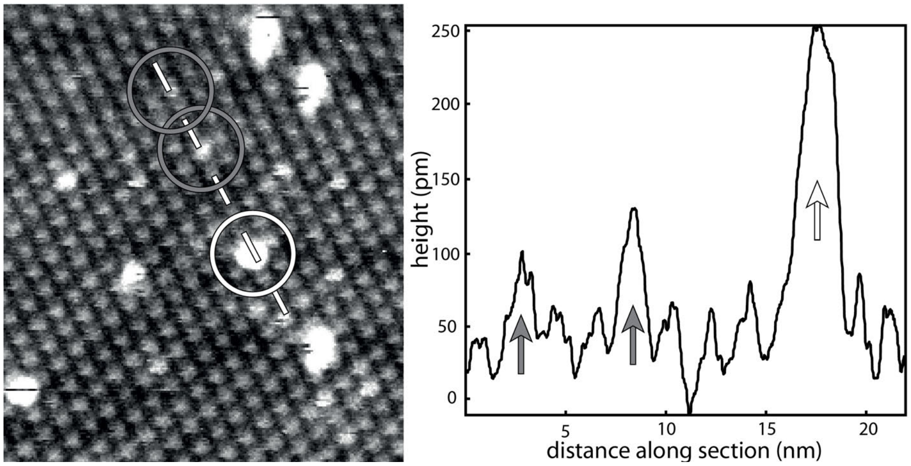

Figure 6.7: STM image and cross section of a **L** domain of a **CuP** monolayer at the HOPG/1-octanoic acid interface. Three distinct species can be identified on the basis of their apparent heights: besides the native **CuP** species, two brighter species can be identified in the image (left) and the corresponding cross section (right). These two species are proposed to be the mono-anionic **Cu(II)P**$^{1-}$ with apparent height of $\approx$ 80-100 pm, and the dianionic **Cu(II)P**$^{2-}$ species with an apparent height of $\approx$ 220 pm. Image parameters: 32 × 37 nm^2, I_{set} = 3 pA, V_{bias} = -750 mV.

values should therefore only be taken as a rough estimate and ability to unambiguously identify the redox state of a single adsorbate, without reference molecules, will require much more detailed investigations. To illustrate these problems, an STM image containing reduced **CuP** species is shown in Figure 6.7 with **Cu(II)P**$^{1-}$ species marked in grey and **Cu(II)P**$^{2-}$ in white. The apparent height of the mono–anion is now $\approx$ 80–100 pm while the dianion appears to be $\approx$ 220 pm high, which is different from the $\approx$ 175 pm and $\approx$ 200 pm found for the same species in Figure 6.2. Furthermore, the dianions species appears much wider than the width of one porphyrin ring, presumably due to tip–sample convolution. The images in Figures 6.2 and 6.7 were taken on different samples and with different STM tips. Since the latter are prepared by manually cutting a piece of PtIr wire, a variation in sharpness and the concomitant height contrast and the extent of tip–sample convolution could be expected. Within a single experiment, however, a change of the state of the apex of the STM tip has similar effects on the apparent heights of the reduced species, as can be seen in Figure 6.8. The two STM images in that figure were obtained at a time interval of 3 minutes. Although the scanning parameters, the scan speed and scan size, are the same, all species in Figure 6.8b appear higher than before the tip change

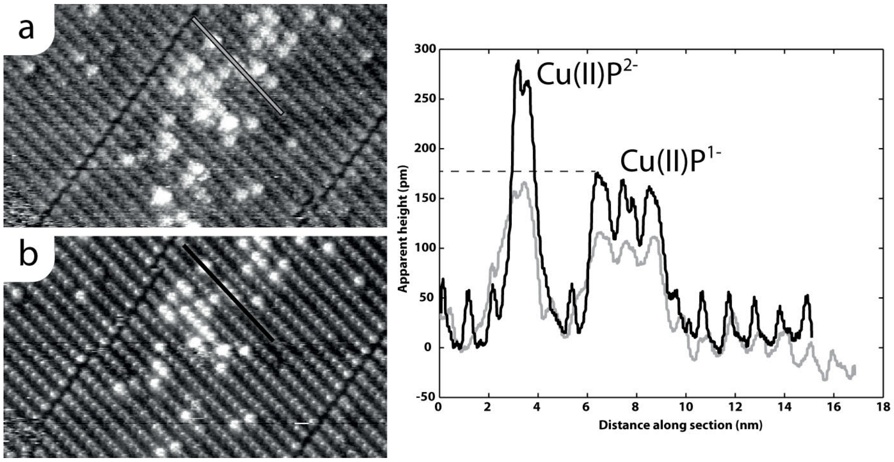

Figure 6.8: STM images (a,b) of **CuP** recorded at a time interval of 3 minutes and cross sections from these images (c) in which the tip dependence of the apparent heights of the different reduced **CuP** species at the HOPG/1-octanoic interface can be observed. The most striking difference is that the apparent height of **Cu(II)P**$^{\mathbf{1-}}$ of image (b), which is 175 pm, is higher than that of a **Cu(II)P**$^{\mathbf{2-}}$ species in image (a), which is 160 pm. Image parameters: (a,b) 50 × 26 nm^2, I_{set} = 5 pA, V_{bias} = -750 mV.

has occured (Figure 6.8a), despite the fact that before and after the tip–change the molecules were molecularly resolved, showing that the effect is not simply a matter of imaging resolution. Upon the tip change, the apparent height of the neutral **Cu(II)P**$^{\mathbf{0}}$ species increased from about 25 pm in image 6.8a, to 50 pm in Figure 6.8b, that of **Cu(II)P**$^{\mathbf{1-}}$ from 100 pm to 175 pm and of **Cu(II)P**$^{\mathbf{2-}}$ from about 160 pm to 275 pm. After the tip–change the apparent height of **Cu(II)P**$^{\mathbf{1-}}$ (175 pm) is thus greater than the apparent height of **Cu(II)P**$^{\mathbf{2-}}$ before the tip change (160 pm), demonstrating that unambiguous determination of the redox state of a single porphyrin adsorbate is cumbersome. The exact nature of the apex of the STM tip seems to have a profound influence on the appearance of the reduced porphyrin species. In Chapter 4 it was already proposed that the state of the STM tip is a crucial parameter in the visibility of polymorph-dependent contrasts. Also in the case of reduced porphyrin adsorbates, it is proposed that chemical changes in the nature of the STM tip apex, such as adsorption of a **CuP** molecule, or changes in the crystallographic orientation of the atoms near the apex can greatly influence the STM contrast.

All the variations in appparent height of **CuP** monolayer on HOPG that have been reported thusfar can be observed in the STM image in Figure 6.9, in which the monoanion (single circle) and the dianion (double circle) can be identified as

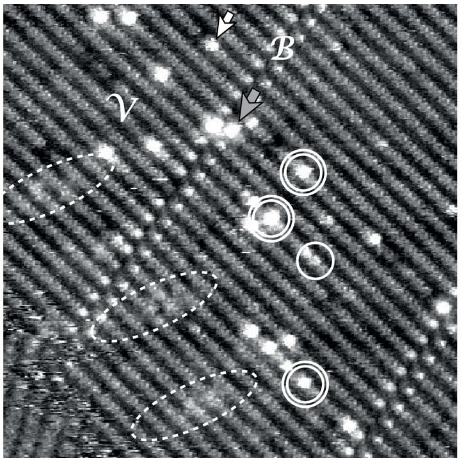

Figure 6.9: STM image of a monolayer of **CuP** at the HOPG/1-octanoic acid interface, displaying the complexity of the apparent height of the **CuP** adsorbates when the surface is covered with **Cu(II)P^0** (unmarked), **Cu(II)P^{1-}** (circle) and **Cu(II)P^{2-}** (double circle). Also the moiré patterns (dashed ellipses) and the polymorph-dependent contrast are visible. The white arrow marks a **CuP** molecule which might appear high because it is in a $\mathcal{V}$ adsorption configuration or in one of the two reduced forms. The molecule marked by the gray arrow is in a $\mathcal{B}$ adsorption configuration and in a reduced form, but since it is unknown whether these two contrasts are additive, it is not known if it is a monoanion or a dianion. Image parameters: 40 × 40 nm^2, I_{set} = 10 pA, V_{bias} = -950 mV

well as the increase in apparent height of **CuP** when it resides in a **B** unit cell ($\mathcal{B}$) or next to a vacancy ($\mathcal{V}$). These states can unambiguously be identified, but the molecule marked by the gray arrow is both reduced and in a **B** unit cell, making it very difficult to determine whether it is a monoanion or a dianion. Furthermore the regions in the dashed ellipses show an increase in apparent height that coincides with the moiré pattern of this domain but appears even higher. This observation suggests that charge transfer, needed for the reductions, more easily occurs at bright regions of the moiré patterns where a stronger electronic coupling of the molecules to the HOPG is expected. Besides the many mechanisms contributing to the signature of **CuP** molecules in self–assembled monolayers on HOPG, also the dynamics of the monolayer (see Chapter 5) make it difficult to image the same molecules in the same, undisturbed, domain for a long time. Further studies on the reactivity of metalloporphyrins might therefore benefit from switching the focus to porphyrins with longer ($>C_{17}H_{35}$) alkyl tails. This limits the amount of polymorphs and thereby reduces the amount of STM contrast mechanisms. The appearence of the different

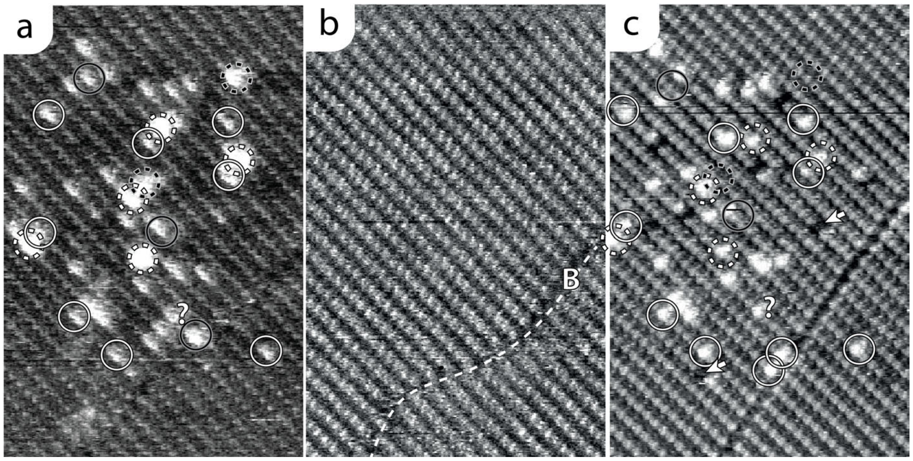

Figure 6.10: Consequtive STM images of the same location of a **CuP** monolayer at the HOPG/1-octanoic acid interface, recorded at negative (a,c) and positive (b) bias voltages. It can be observed that the reduced species, clearly visible in image (a) at negative bias, are invisible at positive bias in image (b). In (c) the bias voltage was switched back to negative polarity. Image parameters: 30 × 45 nm^2, I_{set} = 4 pA, V_{bias} = -750 mV (a,c) idem but V_{bias} = +750 mV (b).

CuP anions also depends on the imaging parameters, as is illustrated in Figure 6.10. At positive bias voltages (Figure 6.10b), the reduced species cannot be distinguished from their neutral couterparts, although they have continuously been present, as can be deduced from the fact that after switching back to negative bias voltages (Figure 6.10), most of the high features are still located at the same locations as before the change in bias voltage. In fact 29 of the 32 monoanions have remained at the same location while 3 have decayed to the neutral species. Of the 6 observed $\mathbf{Cu(II)P^{2-}}$ adsorbates, 4 seem to have undergone a single oxidation step to the $\mathbf{Cu(II)P^{-}}$ anion, while 2 seem to have decayed to the neutral species.

In summary, great care must be taken when different measurements of these reactive species are compared and it is proposed that is is nearly impossible to unambiguously identify a single redox species based on its appearance in STM at the solid/liquid interface. One needs to compare its apparent height and its apparent width with those of species of which the redox state is known and the appearance of that redox state in STM is well understood. This stresses the importance of incorporating molecules with simple and well-known redox behavior, as an internal standard when the behaviour of more reactive species at the solid/liquid interface is studied. When the properties of **CuP** are understood they can well be used for that purpose,

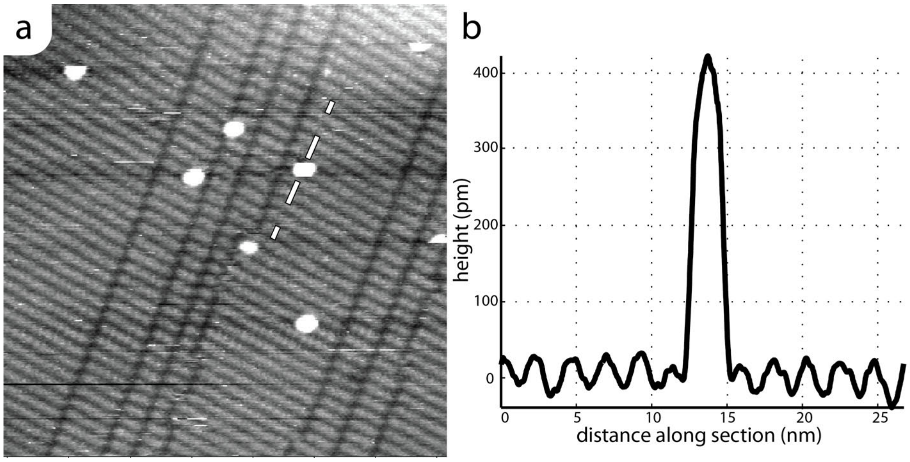

Figure 6.11: STM image (a) of a monolayer of **CuP** at the HOPG / interface recorded while scanning at a large positive bias potential, and a cross section through one of the protrusions that can be observed to form at these potentials (b). Image parameters: 75 × 75 nm^2, I_{set} = 9 pA, V_{bias} = +1650 mV

since they exhibit the simplest possible redox behavior of all metalloporphyrins and can be mixed with other, more complicated **MP** species, in a single monolayer as was shown in Chapter 5.

6.5 STM studies of CuP at oxidative potentials

The behavior of **CuP** at oxidative surface potentials has also been studied, albeit not as thoroughly as the behavior at negative potentials. When pulses of up to +5 V were applied to a monolayer of **CuP** at the HOPG/1-octanoic acid interface, no different porphyrin species could be observed, but whether they are not formed, or merely do not show different STM contrast at the bias voltages used is not known. However, when the surface was scanned with a high positive bias voltage ($\gtrsim$1200 mV) very high features were generated (Figure 6.11). Although it cannot be excluded that these are simply cations of **CuP** such as $\mathbf{Cu(II)P^{1+}}$ or $\mathbf{Cu(II)P^{2+}}$, their apparent height of 400 pm, compared to 50 pm of the other neutral species and 250 pm of the dianion, suggests that they are dimeric species. Copper porphyrins are known to form dimers upon oxidation to the monocation[40], and they are stable[41] and could be isolated[42]. These so–called mixed–valence π–cation radical dimers have been reported to be formed by dimerisation of a cation and a neutral copper octaethylporphyrin[40]:

$$\mathrm{Cu}(II)OEP + \mathrm{Cu}(II)OEP^{+} \longrightarrow [\mathrm{Cu}(II)OEP^{+/2}]_2 \tag{6.3}$$

The hole (*i.e.* missing electron) caused by the oxidation is thus shared over the two porphyrin rings of the involved porphyrins. The species was not only found for copper porphyrins but also for Zn, Pd, Ni and VO. It could be envisioned that after the oxidation of an adsorbed **CuP** molecule, a second, neutral porphyrin from the solution phase dimerizes with the adsorbate. Although the formation of such a dimer in STM is only proposed tentatively here, the fact that it might form and that it could also form in case of other metalloporphyrins makes it an important process to investigate in more detail. The lifetimes of these feature was found to be around 10 minutes. Their stability of might be explained by the formation of the dimeric species, which prevents the oxidized species from reducing to the neutral species, but the slow electron transfer across the HOPG surface might also be a crucial factor for long lifetime of the cations.

6.6 Conclusion

The redox chemistry of **CuP** molecules has been investigated at the HOPG/1-octanoic acid interface. The behaviour of these species upon presenting the surface with a negative, reductive, voltage pulse seems to be understood. Two new different signatures that were formed in the STM images, were assigned to the monoanionic $\mathbf{Cu(II)P^{1-}}$ and the dianionic $\mathbf{Cu(II)P^{2-}}$ species. The latter has an average lifetime of 90 minutes, whereas the former was found to be stable for more than 20 hours. It was shown that upon applying consecutive reductive voltage pulses at the same location of the surface, dianionic species are primarily formed from monoanions that were already present in the layer. This observation is in agreement with the mechanism reported in the literature that the $\mathbf{Cu(II)P^{2-}}$ species is formed *via* two consecutive single-electron reductions of a native $\mathbf{Cu(II)P^{0}}$ species. Both anions could be reverted back to the native species by applying positive voltage pulses. No distinction in apparent height could be made between molecules that had been reduced and reoxidized and those that had been in the neutral state throughout the experiment. This observation suggests that the chemical nature of the **CuP** adsorbates is not irreversibly altered by the voltage pulses. The fact that in the absence of pulsing the formed redox species are persistent for such a long time (hours to days) does not correspond well to the electrochemical reversibility reported about these porphyrins in the solution phase. A tentative explanation, for which indications can be found in the literature but that would require further investigation, is that the electron transfer across the HOPG surface is limiting the decay of the charged species. Finally it was reported that when the surface was scanned at a large positive bias voltage, features with an apparent height of up to 400 pm were created. These species are identified as radical cation dimers, but it can not yet be excluded that they are simple single cationic species. So far, no correlation has been found between the different surface structures, (*i.e.* the adsorption conformation and the adsorption configuration) and the redox properties of the **CuP** adsorbates. Although it would be very interesting to investigate the polymorph dependence of the formation of these high features, the amount of data gathered in these studies is not sufficient to support such claims. The influence of the tip state on the visibility (see section 6.4) and possibly on the formation of these features require a large amount of data on carefully prepared monolayers to justify these claims. Chapter 5 provides the required methodology to prepare monolayers with a large variation of different polymorphs. With such monolayers the polymorph dependence of the formation of the bright dots can be studied at the exact same interface, using the exact same tip, to minimize differences in experimental conditions. More extensive studies are necessary to be able to determine whether the formation, decay or chemical nature of the formed redox species are altered as a result of their adsorption in a particular surface polymorph. An electrochemical STM (EC-STM) was developed to perform these experiments under more controlled electrochemical conditions. The development of this EC-STM is described in Chapter 7.

References

1. Hla S.W., Meyer G. and Rieder K.H. *ChemPhysChem*, 2 (6):361–366, **2001**
2. Hulsken B., Van Hameren R., Gerritsen J.W., Khoury T., Thordarson P., Crossley M.J., Rowan A.E., Nolte R.J.M., Elemans J.A.A.W. and Speller S. *Nature Nanotech.*, 2 (5):285–289, **2007**
3. Hieringer W., Flechter K., Kretschmann A., Seufert K., Auwärter W., Barth J., Görling A. and Steinrück H-P G.J. *J. Am. Chem. Soc.*, 133:6206–6222, **2011**
4. Friedermann G.R., Halma M., Dias de Freitas Castro K.A., Benedito F.L., Doro F.G., Drechsel S.M., Mangrich A.S., Assis M.D. and Nakagaki S. *Appl. Catal., A*, 308:172–181, **2006**
5. Fuhrhop J.H., Kadish K.M. and Davis D.G. *J. Am. Chem. Soc.*, 95 (16):5140–5147, **1973**
6. Liao M.S. and Scheiner S. *J. Chem. Phys.*, 117:205–219, **2002**
7. Kadish K.M. and Morrison M.M. *J. Am. Chem. Soc.*, 98 (11):3326–3328, **1976**
8. Renner M. and Fajer J. *J. Biol. Inorg. Chem.*, 6:823–830, **2001**
9. Kadish K.M. and Morrison M.M. *Bioinorg. Chem.*, 7 (2):107 – 115, **1977**
10. Lin Chia L., Fang May Y. and Cheng Shu H. *J. Electroanal. Chem.*, 531 (2):155 – 162, **2002**
11. Langhus D.L. and Wilson G.S. *Anal. Chem.*, 51 (8):1139–1144, **1979**
12. Yoshimoto S., Tsutsumi E., Suto K., Honda Y. and Itaya K. *Chem. Phys.*, 319 (1-3):147 – 158, **2005**
13. Tao N.J. *Phys. Rev. Lett.*, 76 (21):4066–4069, **1996**
14. He Y. and E. B. *Angew. Chem. Int. Ed.*, 46:6098–6101, **2007**
15. Yuan Q., Xing Y. and Borguet E. *J. Am. Chem. Soc.*, 132 (14):5054–5060, **2010**
16. Kadish K.M., Ou Z., Zhan R. and Khoury T. E.W.C.M.J. *J. Porphyrins Phthalocyanines*, 14:866–876, **2010**
17. Bard A.J. and Faulkner L.R. *Electrochemical methods: Fundamentals and applications.* 2nd edition
18. Hai N.T.M., Furukawa S., Vosch T., De Feyter S., Broekmann P. and Wandelt K. *Phys. Chem. Chem. Phys.*, 11:5422–5430, **2009**

19. Wilson G.S. and Peychal-Heiling G. *Anal. Chem.*, 43 (4):550–556, **1971**

20. Liljeroth P., Repp J. and Meyer G. *Science*, 317 (5842):1203–1206, **2007**

21. Szintay G. and Horváth A. *Inorg. Chim. Acta*, 324 (1-2):278 – 285, **2001**

22. Szintay G. and Horváth A. *Inorg. Chim. Acta*, 310 (2):175–182, **2000**

23. Visser J., Katsonis N., Vicario J. and Feringa B.L. *Langmuir*, 25 (10):5980–5985, **2009**

24. Reid I., Zhang Y., Demasi A., Blueser A., Piper L., Downes J.E., Matsuura A., Hughes G. and Smith K.E. *Appl. Surf. Sci.*, 256 (3):720 – 725, **2009**

25. Schwieger T., Peisert H., Golden M.S., Knupfer M. and Fink J. *Phys. Rev. B*, 66:155207, **2002**

26. Peisert H., Knupfer M., Schwieger T., Auerhammer J.M., Golden M.S. and Fink J. *J. Appl. Phys.*, 91:4872–4878, **2002**

27. Strahan G.D., D. L., Tsuboi M. and Nakamoto K. *J. Phys. Chem.*, 96 (15):6450–6457, **1992**

28. Mojzes P., Chinksy L. and Turpin P.Y. *J. Phys. Chem.*, 97 (18):4841–4847, **1993**

29. L. C., Turpin P.Y., Alobaida A.H.R., Bell S.E.J. and Hester R.E. *J. Phys. Chem.*, 95 (15):5754–5756, **1991**

30. Wu S.W., Ogawa N., Nazin G.V. and Ho W. *J. Phys. Chem. C*, 112 (14):5241–5244, **2008**

31. Wu S.W., Ogawa N. and Ho W. *Science*, 312 (5778):1362–1365, **2006**

32. Ye T., He Y. and Borguet E. *J. Phys. Chem. B*, 110 (12):6141–6147, **2006**

33. Atkins P. *Physical Chemistry.* 6th edition, **1998**

34. Davies T.J., Hyde M.E. and Compton R.G. *Angew. Chem. Int. Ed.*, 44 (32):5121–5126, **2005**

35. Hallam P.M. and Banks C.E. *Electrochem. Commun.*, 13 (1):8–11, **2011**

36. Cline K.K., Mcdermott M.T. and Mccreery R.L. *J. Phys. Chem.*, 98 (20):5314–5319, **1994**

37. Banks C.E. and Compton R.G. *Anal. Sci.*, 21 (11):1263–1268, **2005**

38. A. Shelnutt J., Song X.Z., Ma J.G., Jia S.L., Jentzen W., J. Medforth C. and J. Medforth C. *Chem. Soc. Rev.*, 27 (1):31–42, **1998**

39. Kadish K.M., Van Caemelbecke E., D'Souza F., Medforth C.J., Smith K.M., Tabard A. and Guilard R. *Inorg. Chem.*, 34 (11):2984–2989, **1995**

40. Scheidt R.W., Buentello K.E., Ehlinger N., Cinquantini A., Fontani M. and Laschi F. *Inorg. Chim. Acta*, 361 (6):1722 – 1727, **2008**

41. Brancato-Buentello K.E., Kang S.J. and Scheidt W.R. *J. Am. Chem. Soc.*, 119 (12):2839–2846, **1997**

42. Scheidt W.R., Brancato-Buentello K.E., Song H., Reddy K.V. and Cheng B. *Inorg. Chem.*, 35 (26):7500–7507, **1996**

CHAPTER 7

Development of an EC-STM

7.1 Introduction

In Chapter 6 it was demonstrated that by applying negative or positive bias voltages and voltage pulses to self-assembled monolayers of **CuP** at the HOPG/1-octanoic acid interface, species with different apparent heights could reversibly be created. It was argued that the different species are created by the copper porphyrins being able to adopt different redox states, and it was proposed that at negative surface bias potentials **CuP** is reduced to its mono- and dianion, while at positive bias potentials oxidized species are formed. Many other STM studies on monolayers of porphyrin and related macrocyclic dyes have reported the existence of species with different apparent heights. The number of different experimental conditions under which these species are formed, as well as the number of proposed explanations, is quite large. Hulsken *et al.*[1,2] and Den Boer *et al.*[3] have reported that derivatives of manganese porphyrins display features with different apparent heights, because these porphyrins can catalytically dissociate molecular oxygen. The intermediates of this reaction are proposed to appear with increased or decreased apparent heights. The studies of Hulsken and Den Boer were performed using ambient STM at the Au(111)/*n*-tetradecane and the HOPG/1-octanoic acid interfaces respectively. A similar explanation has been given by Hipps *et al.* for the occurrence of species with increased apparent heights in monolayers of cobalt octaethyl porphyrin at the HOPG/*n*-phenyloctane interface[4]. Visser *et al.* attributed the formation of species with increased apparent height in self-assembled monolayers of Zn-porphyrins at the HOPG/*n*-tetradecane to the binding of 3-nitropyridine ligands that were added to the solution[5]. The works of den Boer, Hulsken, Visser and Hipps thus all propose explanations involving the binding of additional chemical species. Wu *et al.* performed STM and STS experiments in UHV and attributed the switching between different heights of Mg–porphyrins at an alumina–covered NiAl surface to the reduction of these molecules[6,7]. A completely different mechanism was proposed for the voltage–induced creation of species with different apparent heights of AlCl–phthalocyanines on a graphite surface in UHV. The existence and switching between two different species were explained by the Cl ion of the molecule switching between being bound to the Al metallocenter above the flat–lying macrocycle to being bound below this phthalocyanine ring[8]. The authors proposed that switching between these two configurations could be caused by either electron–induced molecular flipping of the entire AlCl–phthalocyanine molecule or to "atom-tunneling" of the Cl atom through the plane of the macrocycle.

These studies show that in a conventional STM it can be difficult to assess the role of electron transfer processes in the formation of species with different height signatures. The use of a so-called electrochemical STM (EC-STM) allows for more elaborate control over the electrochemical processes occurring at the sample surface, as well as at the STM tip while it images the surface with submolecular or atomic resolution. Using EC-STM, an electrochemical reduction was proposed to underly apparently high features observed for ZnTPP molecules at the Au(111)/0.1 M $HClO_4^-$ interface[9]. In another EC-STM study Ye *et al.*[10] also proposed an electrochemical reduction for free base tetrapyridyl porphyrins at the Au(111)/0.1 M H_2SO_4 interface but in conjunction with protonation by the highly acidic sulphuric acid electrolyte. The EC-STM studies provide great certainty about the involvement of electron transfer reactions in these particular studies, but the conditions with which these experiments were performed differ greatly from those in UHV and at the interface of HOPG with apolar solvents. In fact all aforementioned STM studies of porphyrin monolayers were performed under a wide range of different experimental conditions, on a range of different surfaces and with different metallo–porphyrin and phthalocyanine derivatives. The small amount of overlap between the different studies makes generalization of the results difficult.

To unambiguously elucidate the chemical nature of all these apparently higher porphyrin adsorbates, it is hereby proposed that the formation of the higher species should be investigated in an electrochemical STM, in which charge transfer processes and concomitant chemical reactions can be assigned with great certainty. This motivated us to develop an STM operating in an electrochemical cell (EC-STM) which will be described in this chapter.

7.2 Design and construction of the EC-STM

An electrochemical scanning tunneling microscope was designed and built as part of this project. The design is based on the Nijmegen Liquid-cell STM[1,11] and the EC-STM design by Wandelt *et al.*[12] Several adaptations were made to transform a conventional STM into an EC-STM. Besides the addition of a bipotentiostat to control the electrochemical potentials and currents in the setup, a new liquid-cell had to be designed and additional electrodes had to be selected.

7.2.1 Potentiostatic control

In principle electrochemistry can be performed by simply applying an electrical voltage between two electrodes that are submerged in an electrolytic solution[13]. This situation is sketched in Figure 7.1a. For consistency with the discussion below these two electrodes will be referred to as the "sample", which is the electrode to be studied, and the "counter electrode", CE. The sample electrode is in the literature also often referred to as the " working electrode" , WE. At certain voltages between the two electrodes, electrochemical, also called redox reactions, can occur at both electrodes. In the example in Figure 7.1a an oxidation reaction occurs at the sample electrode, which implies that the electrons are abstracted from the red_1 species and transferred across this positively charged electrode. The potential required to drive this reaction does not only depend on the sample electrode but, because the electrical current across this electrode must be balanced by an opposite current through the counter electrode, it also depends on the electrochemical reaction that occurs at the CE. An oxidation reaction at the sample electrode can only occur if a reduction reaction, involving an electrochemical current of equal magnitude but opposite sign, can occur at the counter electrode and *vice versa*. This is not necessarily the opposite chemical reaction as the one that occurs at the sample surface, as indicated by the use of different indices (red_1, red_2, ...). The composition of the counter electrode might change during the course of the experiment. As a direct result of the electrochemical reactions that necessarily occur at the counter electrode for current to flow inside the cell, deposition or etching might occur at this electrode which might alter the electrochemical state of the CE. Because the voltage and current through the sample surface are both supplied by the same electrode, there is no stable reference for the electrochemical potential of the sample surface. This implies that whether electrochemical reactions can occur also depends on the nature and conditions of the CE. The solution to these problems is to employ a three-electrode setup controlled by a potentiostat (Figure 7.1b). In addition to the sample electrode and the counter electrode (CE), a third electrode is introduced to the system. This reference electrode (RE) will be used as the voltage reference for the sample surface. The electrochemical potential of the sample surface will be defined relative to this electrode. In contrast to the two-electrode setup described above, this potential is not maintained by simply

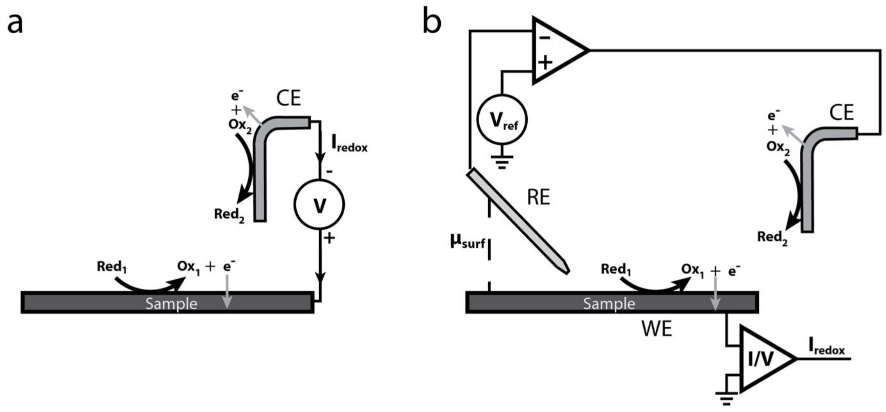

Figure 7.1: Schematics to illustrate the shortcomings of an electrochemical cell comprising two electrodes (a) and the improvements arising from the use of a three-electrode setup (b). To perform electrochemical reactions in a two-electrode electrochemical cell, a voltage is applied between the two electrodes. If the applied voltage is such that an oxidation reaction can occur at one of the two electrodes (*i.e.* the sample) and a reduction at the other, counter electrode (CE) or *vice versa*, a current will flow between the electrodes and the redox reactions at both electrodes can proceed. In a two-electrode setup, both electrodes are equivalent and a redox reaction can only occur at one electrode if the required current is balanced by a reaction of opposing sign at the other electrode. In a given experiment one is typically only interested in the processed occurring at a single, well-defined sample electrode, and the fact that the processes at the second electrode influence the behaviour of the sample electrode complicates the experiment. In a three-electrode setup the electrochemical potential of the sample surface is set relative to a stable reference electrode (RE). This electrode is kept currentless so that no electrochemical processes can occur at its surface. Any currents needed to balance those of the reactions occurring at the sample electrode are supplied by a third, counter electrode (CE) . Using a feedback loop the potential of this electrode is adjusted such that the potential difference between RE and the sample corresponds to the value chosen by the user.

adding a voltage source between RE and the sample. Instead, the potential difference between the grounded sample and RE is applied via a feedback circuit. This feedback circuit basically works as a simple op-amp[14]. The reference electrode is connected to the negative input of this op-amp and the desired potential of this electrode, with respect to the grounded sample electrode, is connected to the positive terminal. The output of the op-amp is connected to CE. An ideal op-amp will drive the output to whatever voltage is needed to equalize the potentials at its two inputs and no currents flow through the inputs themselves. The fact that the inputs remain currentless is very convenient as it ensures that no current can flow through the reference electrode and hence that no electrochemical reactions can occur there. The current is supplied by the CE electrode instead. The output of the op-amp will apply a potential at this electrode and thereby drive the necessary current through it, such that the RE will be at the selected potential, V_{ref}, with respect to the sample. The electrochemical potential, which will be referred to as μ, of the sample is thus

$$\mu_{sample} = \mu_{\mathrm{RE}} - V_{ref} \tag{7.1}$$

If the electrochemical potential of the reference electrode is known, because it has been calibrated against a known redox couple or it is a known redox couple in thermodynamic equilibrium itself, the electrochemical potential of the surface can be chosen using this equation. The currents required for any reactions occurring at the electrochemical potential of the surface will be supplied by the counter electrode.

7.2.2 EC-STM

An electrochemical STM is the combination of the potentiostatically controlled three-electrode setup and an STM. Such a device would allow for the investigation of carefully controlled electrochemical processes occurring at the sample with molecular or atomic resolution. Besides the electrochemical potential of the sample surface, the potentiostat also has to control the potential of the tip, both to prevent electrochemical reactions from occurring at the tip as well as to provide the bias voltage needed for the STM measurements. An overview of the different currents and potentials in the EC-STM is schematically depicted in Figure 7.2a. Using a bipotentiostat, which is an extension of the aforementioned potentiostat, the potentials of the tip and the surface can be controlled independently. A schematic overview of the EC-STM is given in Figure 7.2b. Instead of the sample, the tip is now put at virtual ground, because this is the most sensitive part of the device. This means that

$$V_{tip} = 0V \tag{7.2}$$

The potential difference between the tip and the sample is controlled by applying a bias voltage, V_{bias}, relative to the ground level of the tip. Relative to this ground

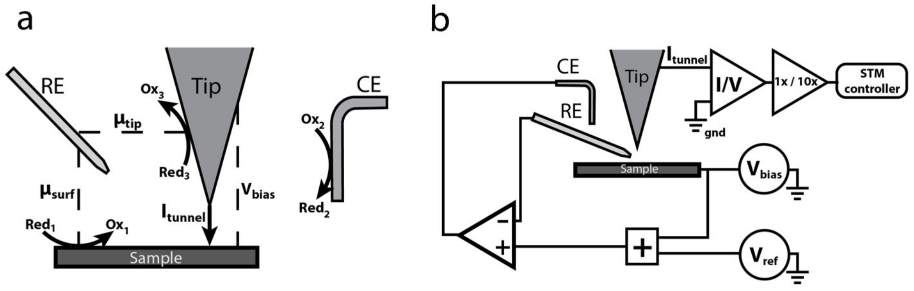

Figure 7.2: Schematic representation of the potentials present and currents flowing in an EC-STM (a), and a schematic picture of the bipotentiostatic control of the EC-STM (b). In (a) it is sketched that three electrical potentials define the processes in this setup: μ_{surf}, the potential between the sample and the reference electrode (RE) defines which electrochemical processes occur at the sample surface. The potential between the tip and the reference electrode (RE), μ_{tip}, defines which electrochemical processes occur at the tip, and V$_{bias}$, the potential between tip and sample, determines the energy levels between which tunneling can occur, like in a conventional STM. Any two of these potentials can be chosen independently and the third is then determined by the values of the other two. The electrochemical reactions at tip and sample require or produce electrical currents. The potentiostat adjusts the potential of the counter electrode (CE) such that these currents are balanced and the cell remains electrically neutral.

level the potential of the sample is thus given by:

$$V_{sample} = V_{bias} \tag{7.3}$$

The potential of the reference electrode, RE, relative to the ground of the system is given by

$$V_{\mathrm{RE}} = V_{bias} + V_{ref} \tag{7.4}$$

These voltages are all given with respect to the tip, which is at virtual ground. This is convenient from an electronic point of view and this is how these voltages are controlled by the bipotentiostat. To understand the electrochemical reactions that occur in the EC-STM, however, the voltages can more easily be expressed with respect to the known, or at least constant, electrochemical potential of the reference electrode μ_{RE}.

$$\mu_{sample} = \mu_{\mathrm{RE}} - V_{ref} \tag{7.5}$$

$$\mu_{tip} = \mu_{\mathrm{RE}} - (V_{bias} + V_{ref}) \tag{7.6}$$

Three potentials are important for the operation of the EC-STM: V_{bias}, μ_{sample}, μ_{tip}. And, as can be deduced from the equations above, these are not independent, but related to each other by

$$V_{bias} = \mu_{sample} - \mu_{tip} \tag{7.7}$$

This implies that any two of these potentials can be freely chosen by the operator, and the third one is then defined by the values of the other two. In the most common type of experiment, the electrochemical potential of the sample is the most important variable, since it determines which processes will occur at the surface of interest. This value is thus chosen without any constraints to match the electrochemical potential at which the process of interest is supposed to occur. The other two potentials are then chosen such that no unwanted electrochemical reactions occur at the tip[15] and that tunneling between tip and sample yields the desired STM contrast. This is accomplished by selecting a suitable combination of μ_{tip} and V_{bias}.

7.2.3 Additional electrodes

As described above, two additional electrodes (*i.e.*, besides the tip and the sample) are employed for full bipotentiostatic control: a reference electrode (RE), which constitutes a stable electrochemical reference potential to which all other potentials are compared, and a counter electrode (CE), which supplies the currents to balance those resulting from the electrochemical reactions at the tip and sample to ensure charge neutrality. Although a simple platinum[16,17] or silver[18,19] wire could be used as reference electrode, which is commonly done in many EC-STM studies, this does not provide a true, stable reference point, since the platinum wire does not constitute an immutable thermodynamic equilibrium with the surrounding electrolyte. Such a reference electrode is therefore commonly referred to as a *quasi*-reference electrode. When, for instance, material from the electrolyte adsorbs on the platinum reference electrode in the course of the experiment, its potential may change. This makes comparison during time-consuming experiments and between different experiments cumbersome, and in general the reference electrode has to be calibrated at the end of the experiment by determining its potential versus a known redox couple, such as ferrocenium/ferrocene[20]. The use of a true reference electrode therefore has clear advantages in stability and accuracy. A commercial **LF-1** Ag/AgCl reference electrode[21] was employed for this purpose. This leak-free reference electrode by *Innovative Instruments* can be used in both aqueous and organic electrolytes, as the junction that separates the Ag/AgCl couple from the measurement electrolyte is highly conductive but not porous and therefore no mixing occurs between the KCl electrolyte in the electrode and the measurement system. A platinum strip with a total geometric surface are of approximately 8 cm^2 was used as CE. This strip was bent in a circular way and placed along the inner wall of the liquid cell.

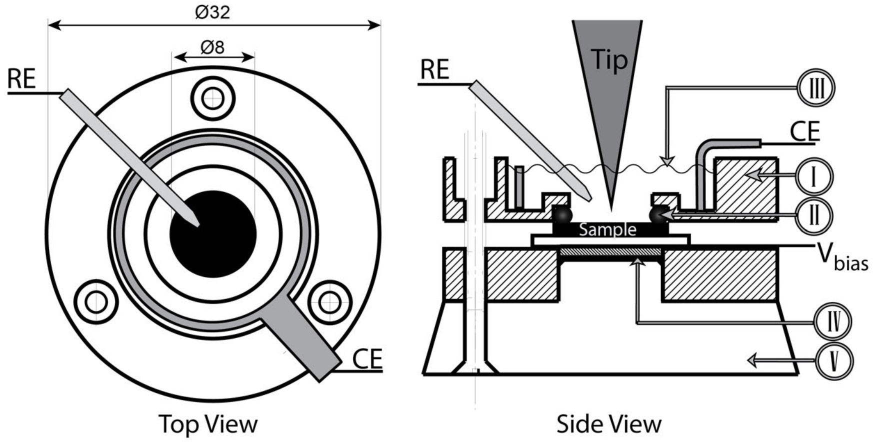

Figure 7.3: Schematic top view and side view of the liquid cell of the EC-STM that was constructed as part of this project. The circularly symmetric liquid-cell (I) is made out of PEEK and is placed over a the sample and a seal is made between the two using a Kalrez O-ring (II) . The sample is mounted onto a metal puck through which V_{bias} is applied. A thin disc of mica (IV) is used to electrically insulate the sample from the stainless steel base (V). After the tip is coarsely approached to the sample, the liquid-cell is filled with an electrolyte (III). Besides the tip and the sample, a Pt counter electrode (CE) and a reference electrode (RE) are immersed in the electrolyte solution. The indicated dimensions are in mm.

7.2.4 Liquid Cell

The design of the liquid cell of the Nijmegen Liquid-Cell STM as developed by Hulsken[1] is not suitable for use in an electrolytic environment. In that design the samples are mounted on a metallic disk, which supplies the bias voltage to the sample through top contacts. The bias voltage is supplied to this disk via a platinum wire that is mounted in the liquid and contacts the metallic from the bottom. This implies that besides the sample, the whole metallic disk and the platinum wire used for the contacting are at bias potential. The surface area of the metallic disk and the contacts is much larger than that of the samples under investigation: in terms of geometric area the difference in surface area would be merely five times larger than that of the sample, but the machined surfaces of the different parts are extremely rough compared to the atomically flat surfaces under investigation, which makes the effective electrochemically active area of the former even larger. This difference in surface area makes it impossible to electrochemically characterize the sample surface, as the electrochemical current of the sample constitutes only a minute part of the total electrochemical currents, which are dominated by electrochemical reactions at the larger sample holder surfaces. The second problem is that these undesired electrochemical reactions at the sample holder surfaces create contaminants, which pollute the carefully cleaned measurement solution. The current to drive the reactions at the sample electrode needs to be counterbalanced by an equal but opposite current at the counter electrode, and this doubles the rate of contamination caused by an oversized sample electrode. A new liquid-cell (figure 7.3) was therefore designed, underneath which the sample is mounted *via* an O-ring of the highly inert polymer Kalrez (DuPont Elastomers). The cell itself was constructed out of polyether ether ketone (PEEK), which is a stiff and chemically inert polymer. This material can withstand all commonly used aqueous electrolytes, as well as a wide range of organic solvents. The top part is pressed down on the O-ring and the sample, using three screws to ensure a leak-tight fit.

7.2.5 Coated tips

Although many protocols have been described in the literature to create coated STM tips suitable for EC-STM measurements[22–25], and even though some effort was made to reliably produce such tips, all measurements on the EC-STM have been performed using commercially available, apiezon wax coated platinum tips (N9804A, N9803A, Agilent Technologies).

7.3 Testing the EC-STM

As a benchmark system to test the performance of the EC-STM, measurements were performed on the electrodeposition of copper on gold. The Au(111) surface was imaged in a solution of 0.1 M H_2SO_4 containing 50 mM $CuSO_4$. When the sample potential is lowered to -400V (vs. 3.4 M KCl) Cu^{2+}(aq) from the electrolyte solution is electrochemically reduced to Cu^0(s) which forms deposits at the Au(111) surface. This process can be seen in Figure 7.4. The observed deposition mode is in agreement to that reported by Kolb *et al.*[26] who also reported the formation of crystallites rather than smooth layer-by-layer growth.

7.4 Outlook

A natural extension of this work, is to use the developed EC-STM to study the monolayers of **CuP** on HOPG. After investigating and understanding the electrochemical behaviour and the appearance of the different redox species of this metallo-porphyrin, porphyrin derivatives with more complex redox behaviour, such as Mn– and Co–porphyrins could be studied next. These studies might elucidate which features are

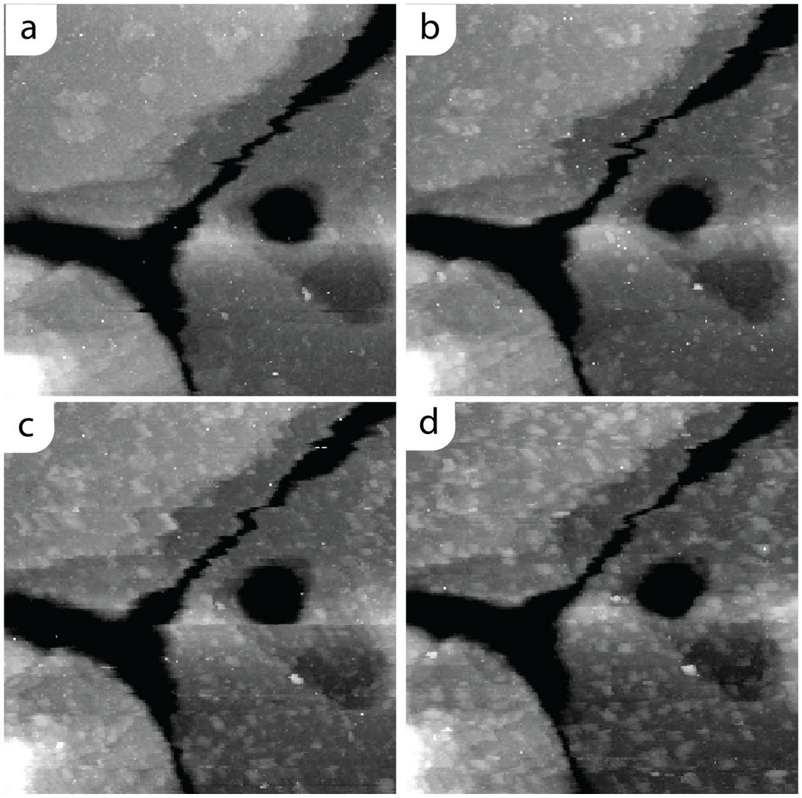

Figure 7.4: Series of EC-STM images depicting the electrodeposition of metallic copper on a Au(111) surface in an electrolyte containing 0.1 M H_2SO_4 and 50 mM $CuSO_4$. The copper is deposited in nanometer sized particles, rather than *via* smooth layer-by-layer growth, which is in agreement with the deposits reported by Kolb *et al.*[26]. Image parameters. (a) V_{tip}= + 300 mV, V_{surf}= + 80 mV, V_{bias}= - 220 mV, I_{set} = 0.72 nA, T = 0. (b) V_{tip}= + 50 mV, V_{surf}= - 300 mV, V_{bias}= - 350 mV, I_{set} = 0.83 nA, T = 44 min., (c) V_{tip}= + 50 mV, V_{surf}= -300 mV, V_{bias}= - 350 mV, I_{set} = 1.4 nA, T = 66 min and V_{tip}= + 50 mV, $V_{surface}$= -300 mV, V_{bias}= - 350 mV I_{set} = 1.4 nA, T = 88 min. 350 × 350 nm^2. A platinum strip and a commercial **LF-1** Ag/AgCl leak-free electrode were used as counter and reference electrode, respectively.

common to all porphyrins and which are specific to each metallo-center. Simultaneously, the study of voltage–induced high features in **CuP** monolayers should be extended to UHV, since by performing studies in UHV one can be certain to exclude the involvement of solvent molecules, atmospheric gasses or impurities.

References

1. Hulsken B. *STM in Liquids*. Ph.D. thesis, **2008**
2. Hulsken B., Van Hameren R., Gerritsen J.W., Khoury T., Thordarson P., Crossley M.J., Rowan A.E., Nolte R.J.M., Elemans J.A.A.W. and Speller S. *Nat. Nanotech.*, 2 (5):285–289, **2007**
3. den Boer D. *Reactivity of single molecules at a solid/liquid interface*. Ph.D. thesis, **2012**
4. Friesen B.A., Bhattarai A., Mazur U. and Hipps K.W. *J. Am. Chem. Soc.*, 134 (36):14897–14904, **2012**
5. Visser J., Katsonis N., Vicario J. and Feringa B.L. *Langmuir*, 25 (10):5980–5985, **2009**
6. Wu S.W., Ogawa N. and Ho W. *Science*, 312 (5778):1362–1365, **2006**
7. Wu S.W., Ogawa N., Nazin G.V. and Ho W. *J. Phys. Chem. C*, 112 (14):5241–5244, **2008**
8. Li Huang Y., Lu Y., Niu T.C., Huang H., Kera S., Ueno N., Wee A.T.S. and Chen W. *Small*, 8 (9):1423–1428, **2012**
9. Yoshimoto S., Tsutsumi E., Suto K., Honda Y. and Itaya K. *Chem. Phys.*, 319 (1-3):147 – 158, **2005**
10. Ye T., He Y. and Borguet E. *J. Phys. Chem. B*, 110 (12):6141–6147, **2006**
11. Gerritsen J.W., Boon E.J.G., Janssens G. and van Kempen H. *Appl. Phys. A: Mater. Sci. Proc.*, **1998**
12. Wilms M., Kruft M., Bermes G. and Wandelt K. *Rev. Sci. Instrum.*, 70 (9):3641–3650, **1999**
13. Bard A.J. and Faulkner L.R. *Electrochemical methods, fundamentals and applications*. John Wiley & Sons inc., second edition, **2001**
14. Horowitz P. and Hill W. *The art of electronics*. Cambridge University Press, second edition, **2006**
15. Wilms M., Broekmann P., Stuhlmann C. and Wandelt K. *Surf. Sci.*, 416 (1-2):121 – 140, **1998**
16. Gasparotto L.H.S., Borisenko N., Bocchi N., Zein El Abedin S. and Endres F. *Phys. Chem. Chem. Phys.*, 11:11140–11145, **2009**
17. Atkin R., Borisenko N., Druschler M., El Abedin S.Z., Endres F., Hayes R., Huber B. and Roling B. *Phys. Chem. Chem. Phys.*, 13:6849–6857, **2011**
18. Pobelov I.V., Li Z. and Wandlowski T. *J. Am. Chem. Soc.*, 130 (47):16045–16054, **2008**
19. Tao N.J. *Phys. Rev. Lett.*, 76:4066–4069, **1996**
20. Gagne R.R., Koval C.A. and Lisensky G.C. *Inorg. Chem.*, 19 (9):2854–2855, **1980**
21. Innovative Instruments, Inc, http://www.2in.com. *Leak-Free Reference Electrode LF-1*
22. Bach C.E., Nichols R.J., Meyer H. and Besenhard J.O. *Surf. Coat. Technol.*, 67 (3):139 – 144, **1994**
23. Zhang B. and Wang E. *Electrochim. Acta*, 39 (1):103 – 106, **1994**
24. Vasilic R., Vasiljevic N. and Dimitrov N. *J. Electroanal. Chem.*, 580 (2):203 – 212, **2005**
25. Abelev E., Sezin N. and Ein-Eli Y. *Rev. Sci. Instrum.*, 76 (10), **2005**
26. Nichols R.J., Kolb D.M. and Behm R.J. *J. Electroanal. Chem. Interfac. Electrochem.*, 313 (1-2):109 – 119, **1991**

APPENDIX A

Sublattices in **M**,**B** domains

Besides sharing one of their unit cell vectors, another interesting relationship exists between the unit cell vectors of **B** and **M**, which is illustrated in figure A.1. The patches of the **M** polymorph are separated from each other by **B** boundaries. Two different unit cell lattices are drawn on top of the STM image, both of which are spanned by $\mathbf{m}_1$ and $\mathbf{m}_2$. The red/yellow lattice connects the centers of all porphyrins in every other **M** patch (red) while the blue/green lattice connects the centres of all porphyrins on the other patches(blue). Every other patch is on the same sublattice, independent of the width (*i.e.* the number of **M** unit cells along $\mathbf{m}_1$) of the patch. A domain comprising **M** and **B** unit cells can therefore be considered to consist of two different sublattices. By crossing a **B** boundary, one moves from one to the other sublattice. The two sublatices are shifted from each other by $\mathbf{b}_1$. By crossing a second **B** boundary, a sublattice is entered which is on the same unit cell grid as the first one. This relation between the sublattices implies that there is not only a relationship between $\mathbf{m}_2$ and $\mathbf{b}_2$, which were found to be identical, but that also $\mathbf{b}_1$ is not independent from $\mathbf{m}_1$ and $\mathbf{m}_2$. This relationship can be most easily seen in the schematic in the dashed ellipse in figure A.1. By starting at a molecule on the red grid and translating over $4\mathbf{m}_1 + \mathbf{m}_2$ the same location is reached as by taking a path consisting of $\mathbf{b}_1 + \mathbf{m}_1 + \mathbf{b}_1$. Therefore:

$$4\mathbf{m}_1 + \mathbf{m}_2 = 2\mathbf{b}_1 + \mathbf{m}_1 \tag{A.1}$$

which implies that:

$$\mathbf{b}_1 = \frac{3\mathbf{m}_1}{2} + \frac{\mathbf{m}_2}{2} \tag{A.2}$$

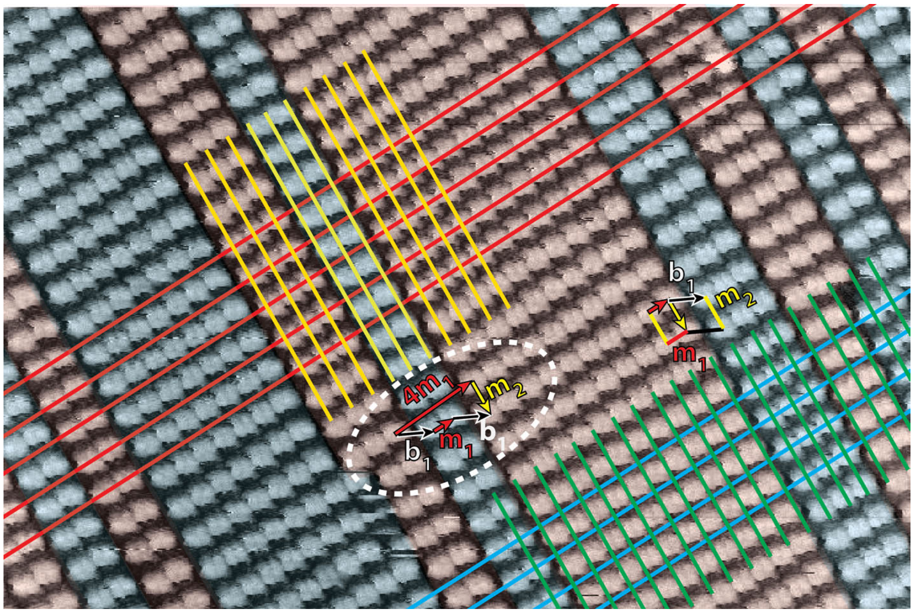

Figure A.1: STM image of the adlayer formed by **CuP** at the HOPG/1-octanoic acid interface. Frequent mixing of **M** and **B** unit cells can be seen. The drawn grid is spanned by lines along the $\mathbf{m}_1$ vector (red) and lines along the $\mathbf{m}_2 = \mathbf{b}_2$ vector (blue). The porphyrins in every other domain of **M** lie exactly on top of a vertex of the lattice, whereas the porphyrins in the other half of the domains are found in between these vertices. The schematic in the dashed white oval shows the relationship between the $\mathbf{m}_1$, $\mathbf{m}_2$ and $\mathbf{b}_1$ unit cell vectors of the **B** and **M** structures. Starting at the leftmost molecule in this schematic and translating over $4\mathbf{m}_1 + \mathbf{m}_2$ takes one to the same location as the path $\mathbf{b}_1 + \mathbf{m}_1 + \mathbf{b}_1$. Image parameters: $I_{set} = 9$ pA, $V_{bias} = -850$ mV, 55 × 35 nm^2.

Filling out the previously obtained unit cell vector of **M** yields

$$\mathbf{b}_{1,eqA.2} = \frac{3}{2}\begin{pmatrix}-2.9\\3.0\end{pmatrix} + \frac{1}{2}\begin{pmatrix}9.1\\7.3\end{pmatrix} = \begin{pmatrix}-0.2\\8.2\end{pmatrix}$$

in which $\mathbf{b}_{1,eqA.2}$ is the value of the $\mathbf{b}_1$ unit cell vector as determined from equation A.2 Including its errors this value is indeed within the range of the previously determined value:

$$\mathbf{b}_{1,eqA.2} = \begin{pmatrix}-0.2 \pm 0.2\\8.3 \pm 0.2\end{pmatrix} = \begin{pmatrix}0.2 \pm 0.2\\7.7 \pm 0.3\end{pmatrix} = \mathbf{b}_{1,Ch3}$$

Where $\mathbf{b}_{1,Ch3}$ is the experimentally determined unit cell vector as presented in Chapter 3 The fact that $\mathbf{b}_1$ is a linear combination of $\mathbf{m}_1$ and $\mathbf{m}_2$, with coefficients that are multiples of $\frac{1}{2}$, and the resulting fact that the patches of **M** in a domain consisting of **M** and **B** can be considered to lie on two sublattices shifted by $\mathbf{b}_1$ turned out to be a determining factor in the formation and the dynamics of the different surface structure formed by **CuP** at the HOPG/liquid interface as were discussed in Chapter 5. Although, undoubtedly, there is a physical or chemical reason for the unit cells vectors of the **M** and **B** to be so closely related to each other, and considerable effort was made to identify the underlying mechanism, no plausible explanation for this behaviour has hitherto been found. The existence of the two sublattices and the underlying algebraic connection between the unit cell vectors is therefore simply posed as a peculiarity of this particular system.

APPENDIX B

Creation of vacancies in **CuP** monolayers

The formation of vacancies in monolayers of **CuP** can be induced by applying highly negative ($<$ -1000 mV) bias voltages between tip and sample while scanning. In this figure two STM images can be seen, of which the first (figure B.1a) is recorded at a bias voltage of about $+500$ mV. The lower apparent height of the **S** patch as compared to the **M** polymorph, is already present at this voltage, but no vacancies can be identified. The second image (figure B.1b) , which is taken at the same location on the sample, is measured using a voltage of -1200 mV. At this voltage several vacancies have been formed. It is thus suggested that this large amount of vacancies is not a property a native **CuP** monolayer, but that they arise at highly negative surface potentials ($\lesssim -1000\,\mathrm{mV}$). The fact that the vacancies form at highly negative voltages suggests voltage- or electric field-assisted desorption of **CuP** molecules. Whether this desorption process merely involves the alignment of native, *i.e.* neutral **CuP**, species to the very strong ($\gtrsim 10^9$ V/m) electric field between the tip and the sample, or that the actual desorption step is preceded by an electrochemical reduction of oxidation step, which would create a charged porphyrin species, as is topic of Chapter 6, is not yet been investigated.

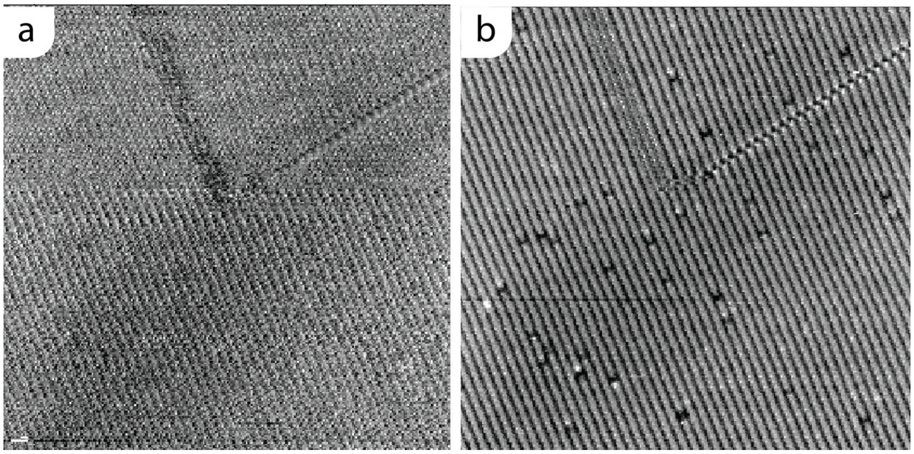

Figure B.1: STM images of a **CuP** monolayer at the HOPG/1-octanoic acid interface. Image (a) was recorded at a moderately positive bias voltage and shows a monolayer free of point defects. Lowering the bias voltage to strongly negative values (b) induces the creation of molecular vacancies. $V_{bias} = 515$ mV, $I_{set} = 13$ pA, 90 × 90 nm^2 (a), $V_{bias} = -1200$ mV, $I_{set} = 10$ pA, 90 × 90 nm^2 (b)

APPENDIX C

Visibility of the polymorph dependent STM contrast

In Chapter 4 it was described that the polymorph dependent contrast is not always present in STM images and it was argued that the visibility of this contrast is not due to the choice of the imaging parameters, since the images presented in this chapter in which the polymorph dependent height differences could be observed were recorded with imaging conditions well within the range of values used in Chapter 3. The result of a more systematic investigation of the influence of the scan parameters on the STM contrast is depicted in figure C.1. These measurement show that within the bias voltage range at which stable STM images could be obtained at the HOPG/*n*-tetradecane interface, *i.e.* from -1200 mV to + 1000 mV, no apparent height difference between the **S** and **M** polymorph could be made visible by variation of the bias voltage. Although the scan parameters might still play a minor role in the appearance of the STM height contrast it is proposed that the apex of the STM tip plays a much more crucial role in the visibility of the polymorph dependent STM contrast. The important role of the STM tip can be observed in the STM images in figure C.2 in which the state of the tip changes within the STM images. The scan lines in which tip changes occur are marked with arrows. In the top part of figure C.2a, which shows a domain comprising **CuP** in $\mathcal{M}$ and $\mathcal{MB}$ adsorption configurations, an apparent height difference exists between the **M** and **B** polymorphs. After the tip change marked with an asterisk, the STM contrast disappeared. Similar behavior can be observed in the STM image in figure C.2b which shows the coexistence of the **M** and **S** polymorphs. Depending on the STM tip porphyrin molecules adsorbed in the **S** polymorph appear lower than porphyrins in the **M** polymorph (lower third) or practically absent (top third).

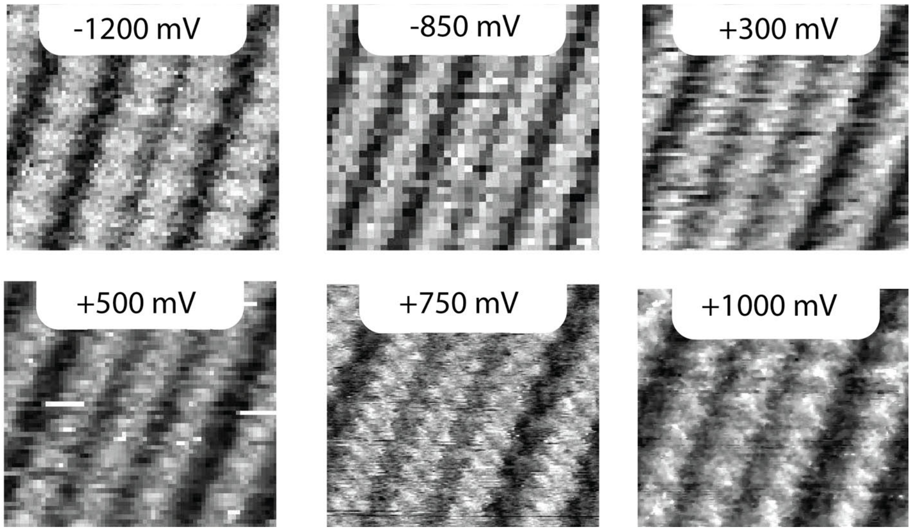

Figure C.1: STM images of the **M** and **S** polymorphs of a **CuP** monolayer at the HOPG/*n*-tetradecane interface performed at different bias voltages, demonstrating that even when using bias voltages up to ± 1000 mV, the polymorph dependent STM contrast does not depend on the bias voltage. I_{set}=8pA.

These measurements were performed at the HOPG/1-octanoic acid interface but the importance of the tip state has also been observed in UHV as is shown in figure C.3. Although the polymorph dependent contrast has not been observed in these measurements, the fact that a tip-change spontaneously alters the STM contrast illustrates that the polymorph dependent contrast is difficult to reproduce at will. It can also be observed that the presence of the Moiré pattern in the STM image depends on the state of the tip (Figure C.3b). Only with certain tip states can the four leaf clover of the porphyrin clearly be identified, as can be see in image C.3d. The difference between image C.3c and d shows the difficulty of obtaining accurate apparent heights: in image C.3c the height difference between the alkyl tails is much larger than that in C.3d. Images in STM, like in any other SPM technique, are caused by interactions between the sample surface and the apex of the probe. This implies that imaging contrast depends, not only on the chemical and electronic structures of the sample, but also on those of the tip and the mutual interactions between the two[1]. STM contrast has been reported to change[2,3], and even to reverse[4–6] upon changes of the chemical structure of the tip apex. The composition of the tip apex can change upon adsorption of atoms from the sample surface, as is commonly assumed to occur in STM measurements on metals[1], since the tip is in very close proximity to

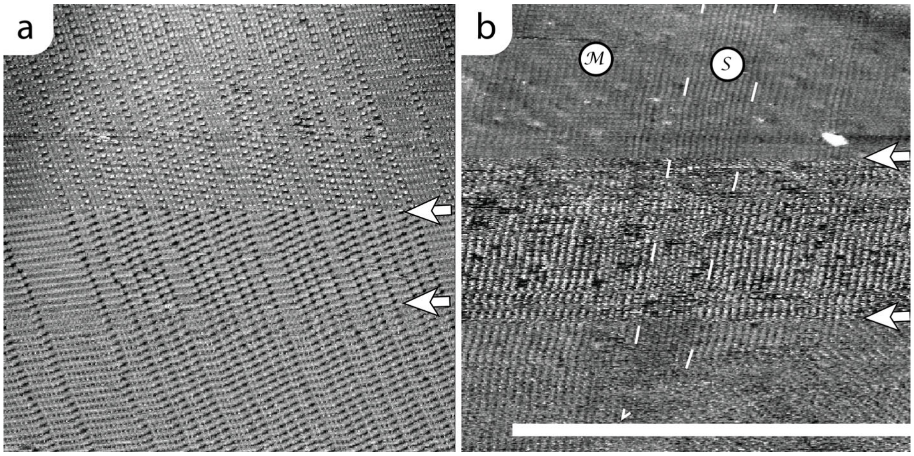

Figure C.2: STM images of **CuP** at the HOPG/1-octanoic acid interface in which the apparent height between the different polymorphs can be seen to depend on the state of the STM tip. Tip changes are indicated by a arrow next to the scan line in which the change occurs. Image (a) shows a domain of **M** and **B** while (b) shows two rotational domains both comprising **M** and **S** unit cells. $V_{bias} = -1820$mV, $I_{set} = 19$pA, 120×120 nm^2, downscan (a) $V_{bias} = -820$mV, $I_{set} = 10$pA, 110×110 nm^2, upscan (b)

the surface and might occasionally come in contact with it. Besides atoms of the sample surface, other species may adsorb on to the tip and thereby influence the STM imaging contrast. Oxygen atoms are reported to adsorb on the apices of metal tips[5,4], as do other gases such as NO[3]. The influence of different chemical species on the STM contrast is even been applied by intentionally chemically modify STM tips. Nishino *et al.* investigated the chemical modification of gold tips by different thiophenol derivatives, and they reported that a tip covered with the hydrogen bond-donor 4-mercaptobenzenesulphonic acid interacts with the hydrogen bond acceptors of the $CH_3(CH_2)_{20}COO(CH_2)_{16}OH$ molecules (*i.e.* the carboxylate and hydroxy moieties) constituting the investigated monolayer, and can thereby distinguish between these parts and the rest of the molecule[7]. Similar results were obtained by functionalizing gold tips with 4-mercaptobenzoic acid and the use of these tips for the imaging of self-assembled monolayers of ethers on HOPG. Not only chemisorbed species, such as thiols on gold, were shown to alter STM contrast, the physisorption of perylene on a tungsten tip also changed the appearance of perylenes adsorbed to the Ag(110) surface from protrusions to depressions[6]. Given the covalent nature of the graphite substrate, it is unlikely that single carbon atoms adsorb on the PtIr tips used in this research, but the adsorption of graphite flakes cannot be excluded to be an important

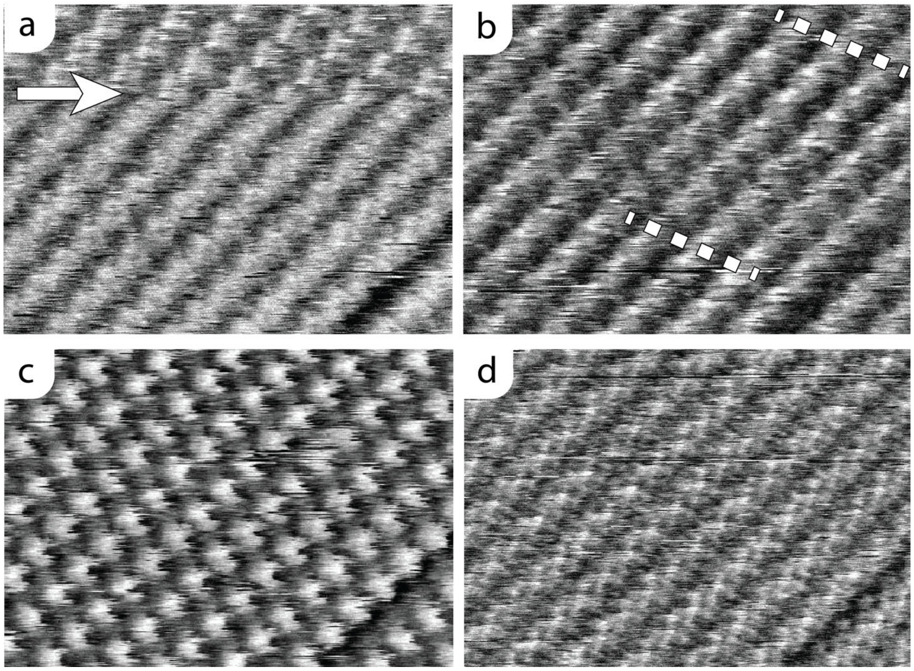

Figure C.3: Four STM images acquired in UHV on the same area of a **S** domain of a **CuP** monolayer on HOPG created from a heptanic solution. The images show the influence of the STM tip on the contrast. A tip change can be seen in image (a). This change is marked by the arrow. After another tip change the Moiré pattern becomes apparent as can be seen in image (b). A period of the Moiré pattern is marked by the dashed lines. The influence of the state of the STM on the height ratio between the alkyl tails and the porphyrin core can be seen in figures (c) and (d). The four leaf clover of the porphyrin core can most easily be observed in image (d). All images where acquired with the same bias voltage and setpoint current.13 × 18 nm, V_{bias}=700 mV, I_{set}=100 pA.

influence on the STM image contrast of **CuP** monolayers on HOPG. Since the increased contrast between the different polymorphs was observed in different solvents, the adsorption of a solvent molecule, of which 1-octanoic acid is the most likely candidate, can be excluded. The fact that contrast-altering tip-changes also occur in UHV also supports the fact that the tip changes are not caused by the surrounding medium. The adsorption of water[8,9] or atmospheric gasses such as O_2[10–12] or CO_2[13] on the tips apex and the resulting change in local dipole moment and work function can not be excluded in ambient measurements and at the solid/liquid interface. Not only might these molecules themselves adsorb to the apex, since platinum is a potent catalyst[10,8,14], both unpolarized[10] as well as under electrochemical conditions[8], reaction products of these molecules, such as atomic oxygen, OH-radicals and atomic hydrogen might form and alter the chemical and electronic structure of the tip. It can also not be excluded that the contrast switches are a consequence of the structure of the PtIr alloy itself: which of the two constituents presents the apex atom might be of influence to the STM contrast, as might the crystallographic adsorption site of the apex atom. For different crystallographic surfaces of a given solid the work function can differ[15], for instance due to a different surface dipole, and such effect could influence the electronic structure of the apex atom. A more thorough combined experimental and theoretical analysis is required to unambiguously determine the crucial factors that underlie differences in STM contrast in general and the polymorph dependent apparent height differences in particular.

References

1. Hofer W.A. *Prog. Surf. Sci.*, 71 (5-8):147 – 183, **2003**. Proceedings of the IXth Symposium on Surface Physics, Trest Castle 2002
2. Ruan L., Besenbacher F., Stensgaard I. and Laegsgaard E. *Phys. Rev. Lett.*, 70 (26):4079–4082, **1993**
3. Hagelaar J.H.A., Flipse C.F.J. and Cerdá J.I. *Phys. Rev. B*, 78 (16):161405, **2008**
4. Calleja F., Arnau A., Hinarejos J.J., Vázquez de Parga A.L., Hofer W.A., Echenique P.M. and Miranda R. *Phys. Rev. Lett.*, 92 (20):206101, **2004**
5. Blanco J.M., González C., Jelínek P., Ortega J., Flores F., Pérez R., Rose M., Salmeron M., Méndez J., Wintterlin J. and Ertl G. *Phys. Rev. B*, 71 (11):113402, **2005**
6. Deng Z.T., Lin H., Ji W., Gao L., Lin X., Cheng Z.H., He X.B., Lu J.L., Shi D.X., Hofer W.A. and Gao H.J. *Phys. Rev. Lett.*, 96 (15):156102, **2006**
7. Nishino T., Buhlmann P., Ito T. and Umezawa Y. *Phys. Chem. Chem. Phys.*, 3:1867–1869, **2001**
8. Anderson A.B., Neshev N.M., Sidik R.A. and Shiller P. *Electrochim. Acta*, 47 (18):2999 – 3008, **2002**
9. Fisher G.B. and Gland J.L. *Surf. Sci.*, 94 (2-3):446 – 455, **1980**
10. Michaelides A. and Hu P. *J. Am. Chem. Soc.*, 123 (18):4235–4242, **2001**. PMID: 11457189
11. Vassilyev Y.B., Khazova O.A. and Nikolaeva N.N. *J. Electroanal. Chem. Interfac. Electrochem.*, 196 (1):105 – 125, **1985**
12. Marković N.M., Schmidt T.J., Stamenković V. and Ross P.N. *Fuel Cells*, 1 (2):105–116, **2001**
13. Bellows R.J., Marucchi-Soos E.P. and Buckley D.T. *nd. Eng. Chem. Res.*, 35 (4):1235–1242, **1996**
14. Wells P. and Wilkinson A. *Top. Catal.*, 5:39–50, **1998**
15. Ishii H., Sugiyama K., Ito E. and Seki K. *Adv. Mater.*, 11 (12):972–972, **1999**

Summary

This thesis describes the structure and properties of self-assembled monolayers of 5,10,15,20-tetraundecylporphyrinato copper (**CuP**) at the interfaces of highly oriented pyrolytic graphite (HOPG) and a range of organic solvents, as well as at HOPG surfaces in ultra high vacuum (UHV). The scanning tunneling microscopy STM studies in Chapter 3 revealed three distinct 2–dimensional polymorphs (**L** (large), **M** (medium), **S** (small)) and one structure, **B** (boundary), that appears as 1–dimensional lamellae in coexistence with lamellae of the **M** polymorph. The ratio in which these polymorphs cover a given HOPG sample could be controlled by selection of the solvent and the concentration of **CuP** in the solution in which the monolayer was formed, with higher concentrations leading to the formation of higher density surface structures. From the observation of moiré patterns in the STM images of the monolayers, it was found that interactions between the porphyrin adsorbates are a more predominant factor governing the structure of the adlayers than the interaction of the molecules with the underlying graphite. The different surface structures formed by **CuP** were found to share unit cell vectors, and the term *adsorption configuration* was introduced to refer to the combination of unit cell vectors at which the four nearest neighbours of a given porphyrin adsorbate were found. The sharing of unit cell vectors between different adsorption configurations was proposed to be the result of part of the molecular conformations of molecules in different adjacent adsorption configurations being the same. The research was expanded from **CuP** to the free-base and other metal derivatives of the same porphyrin scaffold, *i.e.* **2HP**, **NiP**, and **ZnP**. All these molecules formed the same 2-D polymorphs within experimental errors, and because all unit cell vectors of a given species are geometrically related to one another, it is proposed that the vectors are truly the same.

The influence of the 2-dimensional polymorphism on the physical properties of the porphyrin adsorbates was the topic of Chapter 4. The self-assembled monolayers of **CuP** on HOPG were studied at the solid/liquid interface, as dry layers under ambient conditions and in UHV using a combination of scanning probe microscopy techniques. It was shown that the different polymorphs formed by **CuP** on the HOPG surface have different apparent heights in STM, noncontact atomic force microscopy (nc-AFM) and tapping mode atomic force microscopy (tm-AFM). Comparison of the apparent heights obtained with the various SPM methods revealed that this contrast was not caused by differences in the true height at which the **CuP** molecules adsorbed to the HOPG surface. Scanning kelvin probe microscopy (SKPM) showed that the different polymorphs have different contact potentials and that the differences in apparent height are of electronic origin. The difference in electronic properties is proposed to stem from the differences in the conformations of the individual **CuP** molecules. These conformations were proposed to lead to a different degree of non-planar distortion of the porphyrin ring of **CuP** adsorbed in the different polymorphs.

STM studies on dynamical transitions from low density to higher density polymorphs, were the topic of Chapter 5. The transformation of **CuP** monolayers at room temperature is characterized by fast adsorption of porphyrin molecules from the supernatant solution, a high mobility of individual adsorbed, unenclosed porphyrins, low mobility of molecules within the self–assembled monolayer, and limited desorption from the graphite surface. Because the desorption of porphyrin adsorbates is nearly absent, nearly all changes in surface structure involves 2-dimensional movement of the adsorbed species. In order for a **CuP** monolayer to be able to adapt to changing concentrations of the supernatant solution, the presence of specific 2-dimensional defects is required. In the absence of such defects, a domain of a metal porphyrin **MP** monolayer may be completely unable to adapt to changing thermodynamic situations, and this explains why some low density domains can persist in thermodynamically unfavourable situations for more than 16 hours. These studies showed that these physisorbed monolayers are not necessarily in thermodynamic equilibrium with the supernatant solution. Because the transformation of monolayers of **CuP** requires the presence of certain surface defects, the initial formation of the layer, which occurs within seconds, may determine the surface structure for hours or days. Nanomanipulation, *i.e.* shaving away part of a self-assembled monolayer by the STM tip, can be used to reverse or accelerate transformations of **MP** monolayers. Local control over the monolayer structure can be obtained by combining nanoscale manipulation with an appropriate choice of the concentration and composition of the supernatant solution. Molecular tracers, *i.e.* different species of **MP** with STM contrast that is easily distinguishable from the species from which the monolayer was created, were employed to further study the behavior of **MP** monolayers. In particular insertion mechanisms that are responsible for the annealing of low density **M**≈**B** to higher density **M** domains have been studied using these tracers. The dynamics of **CuP** were also studied in UHV. It was shown that upon disturbance of a monolayer of **CuP** at the HOPG/UHV interface, the same polymorphs are again formed, which provides further evidence that the observed polymorphs are an intrinsic property of **MP** molecules on a HOGP substrate and that transformations of the structures of these layers occurs in a 2-dimensional fashion without the need for desorption and adsorption of **MP** molecules.

The formation of different redox species of **CuP** at the HOPG/1-octanoic acid interface by voltage pulses applied with an STM tip was described in chapter 6. Two new signatures that were observed in the STM images, were assigned to the monoanionic $\mathbf{Cu(II)P^{1-}}$ and the dianionic $\mathbf{Cu(II)P^{2-}}$ species. Both these anions could be reverted back to the native species by applying positive voltage pulses. No distinction in apparent height could be made between molecules that had been reduced and reoxidized and those that had been in the neutral state throughout the experiment. This observation suggests that the chemical nature of the **CuP** adsorbates is not irreversibly altered by the voltage pulses. The fact that in the absence of pulsing the formed redox species are persistent for such a long time (hours to days) does not correspond well to the electrochemical reversibility reported for these porphyrins in the solution phase. A tentative explanation for this observation is that the electron transfer across the HOPG surface is limiting the decay of the charged species. Finally it was reported that when the surface was scanned at a large positive bias voltage, features with an apparent height of up to 400 pm were created. These species were identified as radical cation dimers, but it could not yet be excluded that they are single cationic species.

To unambiguously elucidate the chemical nature of all these apparently higher porphyrin adsorbates, the formation of the higher species should be further investigated in an electrochemical STM, in which charge transfer processes and concomitant chemical reactions can be assigned with greater certainty. An electrochemical scanning tunneling microscope (EC-STM) was therefore designed and built as part of this project (Chapter 7). Several adaptations were made to the Nijmegen Liquid Cell STM to transform it into an EC-STM. Besides the addition of a bipotentiostat to control the electrochemical potentials and currents in the setup, a new liquid-cell was designed and additional electrodes were selected. As a benchmark system to test the performance of the EC-STM, measurements were performed on the electrodeposition of copper on gold. The Au(111) surface was imaged in a solution of 0.1 M H_2SO_4 containing 50 mM $CuSO_4$. When the sample potential was lowered to -400mV (vs. 3.4 M KCl) Cu^{2+}(aq) from the electrolyte solution was electrochemically reduced to Cu^{0}(s) which formed deposits at the Au(111) surface. The observed deposition mode is in agreement with the mechanism reported in the literature.

Samenvatting

Dit proefschrift beschrijft de structuur en eigenschappen van zelf-geassembleerde monolagen van 5,10,15,20-tetraundecylporfyrinato koper (**CuP**) op de grensvlakken van grafiet (HOPG) met een scala aan organische oplosmiddelen, en op grafietoppervlakken in ultrahoog vacuum (UHV). Met behulp van Scanning Tunneling Microscopie (STM) is in Hoofdstuk 3 aangetoond dat **CuP** zich in drie verschillende 2-dimensionale en in één 1-dimensionale oppervlakte structuur op het grafietoppervlak kan rangschikken. Deze verschillende oppervlakte structuren, ook wel polymorfen genoemd, worden in het proefschrift respectievelijk **L**, van *Large*, **M**, van *Medium*, **S**, van *Small* en **B**, van *Boundary* oftewel *Grens*, genoemd, omdat het meest in het oog springende verschil tussen de eerste drie de grootte van hun eenheidscellen is, en de laatste alleen voorkomt als grens tussen twee domeinen van de **M** polymorf. Door het oplosmiddel en de concentratie van **CuP** moleculen in dat oplosmiddel te variëren, kon de verhouding waarmee deze verschillende polymorfen voorkomen op een grafietoppervlak, gestuurd worden. Een hogere concentratie van moleculen in de oplossing leidt tot een hogere concentratie, dat wil zeggen een hogere dichtheid, op het oppervlak, en andersom. Uit het feit dat Moiré patronen konden worden waargenomen in de STM metingen van de monolagen, is afgeleid dat de wisselwerking tussen de geadsorbeerde moleculen een grotere invloed heeft op de structuur van de monolagen dan de wisselwerking tussen de geadsorbeerde moleculen en het grafietoppervlak. Van de verschillende oppervlaktestructuren die door **CuP** gevormd worden is ontdekt dat ze onderling eenheidscelvectoren delen, en de term *adsorptieconfiguratie* is geïntroduceerd om de verzameling van eenheidscelvectoren te beschrijven waarmee een gegeven **CuP** molecuul op het oppervlak aan zijn naaste buren gekoppeld is. Gedeeltelijk gedeelde moleculaire conformaties zijn voorgesteld als verklaring voor de gedeelde eenheidscelvectoren tussen de verschillende adsorptieconfiguraties. Naast de porfyrine met koper als metaalcentrum, is het project uitgebreid met onderzoek naar de gerelateerde vrije base **2HP** en naar hetzelfde porfyrineligand maar met zink (**ZnP**) en nikkel (**NiP**) als metaal centrum. Binnen de meetonnauwkeurigheid vormden al deze moleculen dezelfde oppervlaktestructuren en aangezien alle eenheidscelvectoren van een gegeven porfyrinevariant gelijksoortige geometrische relaties met elkaar hebben, is gesteld voor dat deze vectoren inderdaad hetzelfde zijn.

De invloed van de 2-dimensionale polymorfen op de fysische eigenschappen van de geadsorbeerde porfyrines was het onderwerp van Hoofdstuk 4. Hier zijn de zelfgeassembleerde monolagen van **CuP** bestudeerd op het grensvlak van grafiet met verschillende oplosmiddelen, als *droge* lagen in atmosferische lucht, en in UHV. Dit onderzoek is gedaan met een scala aan verschillende scanning probe microscopen. Er is aangetoond dat de verschillende polymorfen van **CuP** verschillende schijnbare hoogtes hebben wanneer ze in kaart gebracht worden met STM, met non-contact atomaire kracht microscopie (nc-AFM) en met tapping mode AFM (tm-AFM). Vergelijking van de met de verschillende methoden verkregen resultaten liet zien dat de schijnbare hoogteverschillen niet veroorzaakt werden door een daadwerkelijk hoogteverschil van de porfyrine-adsorbaten in de verscheidene oppervlaktestructuren. Scanning Kelvin Probe Microscopie (SKPM) toonde aan dat de verschillende polymorfen een andere contactpotentiaal hebben en dat derhalve de schijnbare hoogteverschillen een elektronische oorzaak hebben. De voorgestelde verklaring is dat de verschillen in elektronische eigenschappen worden veroorzaakt door verschillen in de moleculaire conformaties van de individuele geadsorbeerde moleculen. Deze conformaties zouden dan leiden tot een verschillende mate van vervorming van de porfyrinering in de verschillende polymorfen.

STM onderzoek aan de overgang van polymorfen met een lage dichtheid naar structuren met een hogere dichtheid waren het onderwerp van Hoofdstuk 5. Bij kamertemperatuur wordt deze overgang gekenmerkt door een snelle adsorptie vanuit de vloeistof, hoge beweeglijkheid van afzonderlijke, niet ingesloten moleculen op het oppervlak, een lage beweeglijkheid van moleculen in de monolagen en slechts beperkte desorptie van het oppervlak naar de bovenstaande vloeistof. Gezien het feit dat desorptie van porfyrine moleculen vrijwel afwezig is, gaan alle overgangen tussen de verschillende polymorfen gepaard met 2-dimensionale reorganisatie van de geadsorbeerde moleculen. De aanwezigheid van specifieke defecten in de koperporfyrinemonolagen is nodig om het mogelijk te maken dat de structuur van deze laag zich aanpast aan de concentratie van de moleculen in de bovenstaande vloeistof. Zijn deze specifieke defecten afwezig, dan kan het zijn dat een domein van een porfyrinemonolaag zich niet kan aanpassen aan veranderende thermodynamische omstandigheden. Dit verklaart waarom structuren met een lage dichtheid, welke zich bevinden onder een oplossing met een hoge concentratie van **CuP**, zich gedurende perioden van meer dan 16 uur niet aanpassen, ondanks de ongunstige thermodynamica. Dit onderzoek heeft dus aangetoond dat deze gefysisorbeerde monolagen niet noodzakelijkerwijs in thermodynamisch evenwicht zijn met de bovenstaande oplossing. Aangezien voor de transformatie van **CuP** monolagen de aanwezigheid van bepaalde defecten noodzakelijk is, kan de initiële vorming van de laag, die over het algemeen slechts enkele seconden in beslag neemt, de structuur van deze monolaag voor uren of zelfs dagen vastleggen. Nanomanipulatie in dit geval het met de STM tip een gedeelte van de monolaag afscheren, kan worden gebruikt om de transformatie tussen de verschillende structuren in de monolaag te versnellen of ongedaan te maken. De lokale manipulatie die met de STM-tip kan worden uitgeoefend kan worden gecombineerd met de keuze van concentratie en samenstelling van de oplossing waaronder het oppervlak zich bevindt. Traceermoleculen, dat wil zeggen andere soorten porfyrines die met STM eenvoudig te onderscheiden zijn van de koperporpfyrines, zijn gebruikt om het gedrag van deze monolagen verder te bestuderen. Met name het insertiemechanisme dat verantwoordelijk is voor de overgang van domeinen met een lage dichtheid (**M**≈**B**) naar domeinen die volledig uit de **M** polymorf bestaan, en dus een hogere dichtheid hebben, is met traceermoleculen in detail bestudeerd. De dynamica van **CuP** moleculen is ook bestudeerd in UHV. Er is aangetoond dat in een **CuP** monolaag op het grensvlak van grafiet en vacuüm zich wederom dezelfde polymorfen vormen. Dit levert aanvullend bewijs dat de waargenomen polymorfen een intrinsieke eigenschap van de **CuP** moleculen op het grafietoppervlak zijn en dat de transformatie tussen de verschillende polymorfen zich hoofdzakelijk in twee dimensies afspeelt, zonder dat daarbij moleculaire desorptie en adsorptie een grote rol spelen.

De vorming van verschillende redoxtoestanden van **CuP** op het grensvlak van grafiet en 1-octaanzuur door middel van spanningspulsen met de STM-tip is beschreven in Hoofdstuk 6. Twee van deze toestanden werden toegekend aan het monoanion $\mathbf{Cu(II)P^{1-}}$ en het dianion $\mathbf{Cu(II)P^{2-}}$. Beide anionen konden geoxideerd worden tot de neutrale begintoestand door middel van het geven van positieve spanningspulsen. Er kon geen onderscheid gemaakt worden tussen moleculen die achtereenvolgens gereduceerd en geoxideerd werden en moleculen die gedurende de gehele meting in neutrale toestand gebleven waren. Deze observatie suggereert dat de chemische structuur van de **CuP** moleculen niet onomkeerbaar veranderd is door de spanningspulsen. In de afwezigheid van verdere spanningspulsen bleven de geadsorbeerde moleculen verrassend lang, uren tot dagen, in hun gereduceerde toestanden, en dit wijkt af van de elektrochemische reversibiliteit die voor deze porfyrines gerapporteerd is wanneer de moleculen in oplossing zijn. Een mogelijke verklaring hiervoor is dat de elektronenoverdracht door het grafietoppervlak de beperkende factor is bij het verval van de geladen deeltjes. Tenslotte is in dit hoofdstuk beschreven dat wanneer de **CuP** monolaag gescand werd bij een hoge positieve spanning, er deeltjes ontstonden met een schijnbare hoogte van tot wel 400 pm. Deze deeltjes zijn vermoedelijk radicaalkation -dimeren, maar het kan nog niet uitgesloten worden dat het hier enkelvoudige kationische deeltjes betreft.

Om ondubbelzinnig uitsluitsel te kunnen geven over de chemische aard van al deze verschillende toestanden zou de vorming van dit soort schijnbaar hogere porfyrines onderzocht moeten worden met een elektrochemische STM (EC-STM). In dit type microscoop kunnen de ladingsoverdracht en eventuele bijbehorende chemische reacties met grotere zekerheid worden toegewezen. Om die reden is een EC-STM ontworpen en gebouwd als onderdeel van dit project (zie Hoofdstuk 7). Er zijn hiervor verscheidene aanpassingen gedaan aan de Nijmeegse vloeistof cel-STM. Naast de toevoeging van een bipotentiostaat om de elektrochemische potentialen en stromen te regelen, is een nieuwe vloeistofcel ontworpen en gebouwd en zijn verschillende additionele elektroden geselecteerd. Om de prestaties van de EC-STM te testen, zijn is de elektrodepositie van koper op goud in beeld gebracht. Het Au(111) oppervlak is gemeten in een oplossing van 0.1 M H_2SO_4 met daarin 50 mM $CuSO_4$. Het verlagen van de potentiaal van het oppervlak tot -400mV (vs. 3.4 M KCl) leidde ertoe dat Cu^{2+}(aq) uit de oplossing elektrochemisch gereduceerd werd tot metallisch koper. De waargenomen depositie-modus komt overeen met de resultaten uit de literatuur.

List of Publications

1. M. J. J. Coenen, M. Cremers, D. den Boer, F. J. van den Bruele, T. Khoury, M. Sintic, M. J. Crossley, W. J. P. van Enckevort, B. L. M. Hendriksen, J. A. A. W. Elemans, and S. Speller. Little exchange at the liquid/solid interface: defect-mediated equilibration of physisorbed porphyrin monolayers. *Chem. Commun.*, **2011**. *47*, 9666–9668.

2. M. J. J. Coenen, D. den Boer, F. J. van den Bruele, T. Habets, K. A. A. M. Timmers, M. van der Maas, T. Khoury, D. Panduwinata, M. J. Crossley, J. R. Reimers, W. J. P. van Enckevort, B. L. M. Hendriksen, J. A. A. W. Elemans, and S. Speller. Polymorphism in porphyrin monolayers: the relation between adsorption configuration and molecular conformation. *Phys. Chem. Chem. Phys.*, **2013**. *15*, 12451–12458.

3. M. J. J. Coenen, T. Khoury, M. J. Crossley, B. L. M. Hendriksen, J. A. A. W. Elemans, and S. Speller. Nanostructuring of self-assembled monolayers: local manipulation under global control. *submitted*.

4. M. J. J. Coenen, M. van der Maas, T. Habets, B. L. M. Hendriksen, S. Speller, and J. A. A. W. Elemans. Controlling the apparent height of copper porphyrins by voltage pulses: conductance switching observed under room temperature liquid and low-temperature UHV conditions. *manuscript in preparation*.

5. M. J. J. Coenen, M. van der Maas, T. Habets, S. Vasnyov, B. L. M. Hendriksen, S. Speller, and J. A. A. W. Elemans. Guiding the electronic properties of self-assembled porphyrin monolayers using polymorph controlled molecular conformations. *manuscript in preparation*.

6. P. Schön, M. Görlich, M. J. J. Coenen, H. A. Heus, and S. Speller. Nonspecific protein adsorption at the single molecule level studied by atomic force microscopy. *Langmuir*, **2007**. *23*, 20, 9921–9923.

7. A. B. C. Deutman, C. Monnereau, M. Moalin, R. G. E. Coumans, N. Veling, M. Coenen, J. M. M. Smits, R. de Gelder, J. A. A. W. Elemans, G. Ercolani, R. J. M. Nolte, and A. E. Rowan. Squaring cooperative binding circles. *Proc. Natl. Acad. Sci. USA*, **2009**. *106*, 26, 10471–10476.

8. D. den Boer, M. J. J. Coenen, M. van der Maas, T. P. J. Peters, O. I. Shklyarevskii, J. A. A. W. Elemans, A. E. Rowan, and S. Speller. Electron transport through CO studied by gold break junctions in nonpolar liquids. *J. Phys. Chem. C*, **2009**. *113*, 15412–15416.

9. J. A. A. W. Elemans, S. J. Wezenberg, M. J. J. Coenen, E. C. Escudero-Adàn, J. Benet-Buchholz, D. den Boer, S. Speller, A. W. Kleij, and S. De Feyter. Axial ligand control over monolayer and bilayer formation of metal-salophens at the liquid-solid interface. *Chem. Commun.*, **2010**. *46*, 2548–2550.

10. J. te Riet, T. Smit, M. J. J. Coenen, J. W. Gerritsen, A. Cambi, J. A. A. W. Elemans, S. Speller, and C. G. Figdor. AFM topography and friction studies of hydrogen-bonded bilayers of functionalized alkanethiols. *Soft Matter*, **2010**. *6*, 3450–3454.

11. D. den Boer, T. Habets, M. J. J. Coenen, M. van der Maas, T. P. J. Peters, M. J. Crossley, T. Khoury, A. E. Rowan, R. J. M. Nolte, J. A. A. W. Elemans, and S. Speller. Controlled templating of porphyrins by a molecular command layer. *Langmuir*, **2011**. *27*, 6, 2644–2651.

12. D. den Boer, M. J. J. Coenen, J. A. A. W. Elemans, and S. Speller. STM of Chemistry at the solid liquid interface. *In: Encyclopedia of Nanoscience and Nanotechnologie, American Scientific Publishers*, **2011**. *ISBN: 1588831590.*

13. D. den Boer, O. I. Shklyarevskii, M. J. J. Coenen, M. van der Maas, T. P. J. Peters, A. E. Rowan, J. A. A. W. Elemans, and S. Speller. Mechano-catalysis: cyclohexane oxidation in a silver nanowire break junction. *J. Phys. Chem. C*, **2011**. *115*, 16, 8295–8299.

14. G. Salassa, M. J. J. Coenen, S. J. Wezenberg, B. L. M. Hendriksen, S. Speller, J. A. A. W. Elemans, and A. W. Kleij. Unusually strong cooperative self-assembly of a bimetallic salen complex visualized at the single-molecule level. *J. Am. Chem. Soc.*, **2012**. *134*, 16, 7186–7192.

15. H. Gorter, M. J. J. Coenen, M. W. L. Slaats, M. Ren, W. Lu, C. J. Kuijpers, and W. A. Groen. Toward inkjet printing of small molecule organic light emitting diodes. *Thin Solid Films*, **2013**. *532*, 11–15.

Curriculum Vitae

Martinus (Michiel) Jacobus Johannes Coenen werd geboren op 18 december 1981 te Venray. In 2000 behaalde hij zijn VWO diploma aan het Raayland College in diezelfde plaats, waarna hij begon aan zijn studie Algemene Natuurwetenschappen aan de Katholieke Universiteit Nijmegen, de huidige Radboud Universiteit. In 2006 behaalde hij zijn doctoraalexamen met een gecombineerde afstudeerstage binnen de afdeling Supramoleculaire chemie van Prof. Dr. R.J.M. Nolte en de Scanning Probe Microscopy Group van Prof. Dr. S.E. Speller. In die laatste onderzoeksgroep begon hij in 2006 aan zijn promotieonderzoek waarvan de resultaten in dit proefschrift beschreven staan. Sinds 2011 is Michiel werkzaam bij TMC Physics B.V. te Eindhoven. Via TMC is hij eerst korte tijd gedetacheerd is geweest bij Océ Technologies b.v. in Venlo en sinds maart 2012 werkt hij als onderzoeker binnen het Holst Centre te Eindhoven. Hier doet hij onderzoek naar het inkjetprinten van organische electronica.

Dankwoord

Eindelijk, mijn proefschrift is vrijwel af, rest mij alleen nog een aantal personen te bedanken. Allereerst wil ik mijn promotor Prof. Dr. Sylvia Speller bedanken. Bedankt voor het feit dat ik jouw groep mijn promotieonderzoek mocht doen. Je hebt de SPM-groep inmiddels verlaten en ik wens je heel veel succes met je nieuwe groep in Rostock. Dr. Bas Hendriksen wil ik bedanken voor de vele wetenschappelijke discussies en zijn bijdragen aan dit proefschrift en de daaruit voortgekomen en nog voortkomende artikelen. Rest mij van het rijtje (co-)promotoren nog Dr. Hans Elemans. Hans, zonder jou was dit proefschrift er nog steeds niet geweest, het overgrote deel van het correctiewerk van dit manuscript heb jij voor je rekening genomen en ook bij het schrijven van de artikelen was en ben je onmisbaar. Ik bewonder de ongelooflijke hoeveelheid werk die je in een gemiddelde week verzet en ik hoop dat je ook in de toekomst in Nijmegen je eigen onderzoek kunt blijven doen. Verder wil ik de leden van de manuscriptcommissie Prof. dr. Alan E. Rowan, Dr. Meike A. Stöhr en Prof. dr. Elias Vlieg bedanken voor het plaatsnemen in de commissie en de snelle beoordeling van mijn proefschrift. I would like to thank Prof. dr. Maxwell J. Crossley, Prof. dr. Jeffrey R. Reimers, Dr. Tony Khoury and Dwi Panduwinata of the University of Sydney for their supply of porphyrin molecules and the fruitful collaboration. Naast de porfyrines heb ik ook nog een aantal experimenten gedaan aan salenen. Hoewel ik daar niets van in het proefschrift heb opgenomen wil ik Dr. Sander J. Wezenberg, Prof. dr. Arjan W. Kleij en Giovanni Salassa van het Institute of Chemical Research of Catalonia (ICIQ), in Tarragona, Spanje bedanken voor de samenwerking en onze gezamenlijke publicaties.

Albert, Tonnie, Jan H. en Jan G. en Pieter wil ik bedanken voor hun bijdragen aan de ontwikkeling van de EC-STM en alle andere technische ondersteuning tijdens mijn promotieonderzoek. Marilou, Marie-Louise en Riki, bedankt voor alle hulp bij alle administratieve rompslomp en natuurlijk voor alle door jullie georganiseerde borrels en feestjes.

Twee studenten hebben bijgedragen aan het werk in dit proefschrift, Koen en Melissa. Jullie hebben je allebei beziggehouden met een klein zij-projectje van mijn onderzoek: *zelf-geassembleerde monolagen van porfyrines op grafiet*, terwijl ik mij zelf vooral bezig hield met monolagen van salenen en het bouwen van een EC-STM. Jullie resultaten waren erg interessant, maar we begrepen er destijds nog niet veel van. Na jullie stages was het mijn plan nog eventjes wat metinkjes te doen en wat laatste openstaande vragen te beantwoorden, zodat de porpfyrines één hoofdstuk van mijn proefschrift zouden vullen. *Wat* metinkjes werden *veel* metinkjes en het beantwoorden van wat laatste openstaande vragen bleek meerdere hoofdstukken op te leveren. Ondanks jullie onmisbare werk zijn er maar een paar van jullie metingen in het uiteindelijke proefschrift beland: troost je met de gedachte dat van de experimenten waar ik ten tijde van jullie afstudeerstages mee bezig was, er niet één de eindstreep heeft gehaald.

Verder natuurlijk mijn dank naar de collega-aio's, studenten en post-docs van de SPM-groep: Joost, Joris, Fresia, Duncan, Serhiy, Natascha, Lucian, Guillaume, Edgar, Sondes, Delphine, Monique, Dwi, Tim, Jonas, Oleg, Fieke, Martijn, Roman, Peter en Nico voor alle samenwerking en voor de goede sfeer in het Nanolab. Minko en Thomas, bedankt voor de ellenlange wetenschappelijke en niet-wetenschappelijke discussies, het voetballen en voor het feit dat jullie mijn paranimfen willen zijn.

Om historische redenen is de SPM-groep altijd nauw verbonden geweest met de SSI-groep. In het begin kwam die verbondenheid nog tot uiting met een gezamenlijk wetenschappelijk colloquium, maar later werd het teruggebracht tot de meest essentiële academische activiteiten: koffiepauzes, afdelingsuitjes, (glühwein) borrels en tafelvoetbal. Chris, Roman, Steven, Jeroen, Johan d. J., Johan M., Sasha, Fred, Dima, Sergiy, Daniel, Loïc, Marina, Weizhe, Andrei, Alexei en Theo; het was gezellig.

Inmiddels ben ik al een tijdje weg bij de Radboud Universiteit en in dienst bij TMC Physics. Alle TMC'ers, TNO'ers, en Holstianen met wie ik het genoegen heb samen te mogen werken, bedankt. Ook wil ik Richard en zijn meisjes (zowel Hanneke en je dochtertjes thuis, als die waarmee ik binnen Océ met veel plezier heb samengewerkt) even bedanken. Richard, dank je wel dat je me op weg hebt geholpen binnen zowel de academische wereld als in het bedrijfsleven.

Voorts ben ik Dr. Paul van Gerven erkentelijk voor het feit dat hij de verdediging van mijn proefschrift niet heeft trachten tegen te houden ondanks het feit dat ik niet aan de nieuwe regels voldoe; 100 kg bankdrukken tussen het lekenpraatje en de oppositie zit er helaas niet meer in. Verder bedankt voor alle uren die we (lang geleden) samen op het sportcentrum hebben doorgebracht, de biertjes en de verontrustende hersenspinsels die nog steeds met enige regelmaat mijn kant op komen.

Mark, Jasper, Margot, Dennis en Judith, bedankt voor de vele gezellige potjes pool.

Tom, Erik en Martijn wil ik bedanken voor de stapavonden en hun onaflatende bereidheid mij tegen een zeer schappelijk tarief aan kleingeld te leren Zwikken en Klaverjassen.

Vincent, Denise, Bram, Yorma en Arend, bedankt voor het klimmen, skieën, de bordspelletjes, het civven en alle andere ontspannende activiteiten.

Marc en Nienke, Niels en Eveline en Steven en Lianne, bedankt voor de langste vriendschappen die ik heb, een enkele al vanaf de peuterspeelzaal. Ondanks het feit dat we elkaar soms lange tijd niet zien, is het altijd weer als vanouds.

Ik wil ook nog even stilstaan bij het mooiste dat ik aan mijn tijd in de SPM-groep heb overgehouden: Jelena. Je kwam in de groep als aio, terwijl ikzelf nog bezig was met mijn afstudeerstage. De buit was dus eigenlijk al binnen voordat ik aan mijn promotieonderzoek begon, en ik had me dus een hoop werk kunnen besparen. Bedankt voor alle mooie momenten en voor alle reizen die we samen gemaakt hebben, bedankt ook voor het feit dat je nooit echt vuur spuwt, ondanks het feit dat je blik om zeven uur 's ochtends doet vermoeden dat je daar wel toe in staat bent, voor het feit dat je me geïntroduceerd hebt in de mooie wereld van het tango-dansen, en dat je me daarna geïntroduceerd hebt in de nog mooiere wereld van het niet-meer-tango-dansen. Ik hoop dat we samen nog veel moois mogen meemaken. Ook een welgemeend *hvala* aan jouw familie en vrienden, voor de vakanties die we in Montenegro hebben door gebracht en voor al hun bezoeken naar Nederland.

Tenslotte wil ik ook mijn eigen familie bedanken. Ad en Eny (als we thuis een zin beginnen met *Pap*, of *Mam* betekent het meestal niet veel goeds) bedankt voor alles wat jullie me hebben meegegeven, zowel alle materiële en financiële zaken als jullie opvoeding, wijze raad (met mijn auto als recent hoogtepunt), de gezelligheid thuis en alle vrijheid jullie me altijd gegeven hebben. De Wilhelminastraat in Venray voelt ook nog steeds als thuis, zeker als daar weer nieuwe culinaire probeersels op tafel staan. Bedankt ook voor alle steun tijdens mijn promotie, zeker op de momenten dat het allemaal even tegen zat. Ook mijn zus en broer, Jacqueline en Maarten, bedankt. Hoewel we alledrie heel verschillend zijn, verbaast het me altijd hoeveel we met elkaar gemeen hebben. Met name ons gedeelde gevoel voor humor, of gebrek daaraan, waardeer ik zeer.

Allemaal nogmaals bedankt!

Michiel Coenen